ADVANCED STEEL CONSTRUCTION

An International Journal

Volume 17 Number 4

December 2021

CONTENTS

Website: *http://www.hkisc.org*
ISSN 1816-112X
Science Citation Index Expanded, Materials Science Citation Index and ISI Alerting
Cover: Long-Span Steel Footbridge of the Wings II, Designed by using Second-Order Direct Analysis
e-copy of IJASC is free to download at "www.ascjournal.com" in internet and mobile apps.

ADVANCED STEEL CONSTRUCTION

VOL.17, NO.4 (2021)

ADVANCED STEEL CONSTRUCTION

an International Journal

ISSN 1816-112X

Volume 17 Number 4 *December 2021*

ADVANCED STEEL CONSTRUCTION
an international journal

Advanced Steel Construction
an international journal

ISSN 1816-112X

Science Citation Index Expanded, Materials Science Citation Index and ISI Alerting

Cover: Long-Span Steel Footbridge of the Wings Ⅱ, Designed by using Second-Order Direct Analysis
e-copy of IJASC is free to download at "www.ascjournal.com" in internet and mobile apps.

General Information
Advanced Steel Construction, an international journal

Aims and scope

The International Journal of Advanced Steel Construction provides a platform for the publication and rapid dissemination of original and up-to-date research and technological developments in steel construction, design and analysis. Scope of research papers published in this journal includes but is not limited to theoretical and experimental research on elements, assemblages, systems, material, design philosophy and codification, standards, fabrication, projects of innovative nature and computer techniques. The journal is specifically tailored to channel the exchange of technological know-how between researchers and practitioners. Contributions from all aspects related to the recent developments of advanced steel construction are welcome.

Subscription inquiries and change of address. Address all subscription inquiries and correspondence to Member Records, IJASC. Notify an address change as soon as possible. All communications should include both old and new addresses with zip codes and be accompanied by a mailing label from a recent issue. Allow six weeks for all changes to become effective.

The Hong Kong Institute of Steel Construction
HKISC
c/o Department of Civil and Environmental Engineering,
The Hong Kong Polytechnic University,
Hunghom, Kowloon, Hong Kong, China.
Tel: 852- 2766 6047 Fax: 852- 2334 6389
Email: *ceslchan@polyu.edu.hk* Website: *http://www.hkisc.org/*
ISSN 1816-112X
Science Citation Index Expanded, Materials Science Citation Index and ISI Alerting

ISSN 1816-112X

Science Citation Index Expanded, Materials Science Citation Index and ISI Alerting

Advanced Steel Construction
an international journal

VOLUME 17 NUMBER 4 December 2021

Technical Papers

Advanced Steel Construction – Vol. 17 No. 4 (2021) 331–339
DOI:10.18057/IJASC.2021.17.4.1

NUMERICAL ANALYSIS AND EVALUATION OF EFFECTIVE SLAB WIDTH OF COMPOSITE CONTINUOUS BEAMS WITH SEMI-RIGID JOINT

Abdesselam Bahaz [1, *], Salah Amara [1], Jean-Pierre Jaspart [2] and Jean-François Demonceau [2]

[1] *Structures Rehabilitation and Materials Laboratory (SREML), Amar Telidji University of Laghouat, Algeria*
[2] *Urban and Environmental Engineering (UEE) Department, University of Liege, Belgium*
** (Corresponding author: E-mail: a.bahaz@lagh-univ.dz)*

ABSTRACT

The characterization of the structural behavior of composite beams is directly affected by the determination of the effective slab width. Various codes propose their own definitions of the effective width based on the beam span and the slab width parameters. However, the evaluation of the effective width may be influenced by other parameters. The aim of this work is to determine the most important factors affecting effective width for continuous composite beams with semi-rigid joints using numerical simulations. A three-dimensional finite element model of a composite continuous beam using explicit-solver available in ABAQUS is developed. The proposed model is validated through comparisons to available experimental results. A modified model is proposed based on the so-validated model to study the influence of the composite beam-column joint stiffness on the effective width. Then, both numerical models are used to perform an extensive parametric study to investigate the influence of various parameters on the estimation of the effective slab width. The influence of slab width, the shear connection degree, and composite joint stiffness are particularly analyzed to find out the most important parameters influencing the effective width so that simplified equations for the calculation of the effective slab width are proposed.

ARTICLE HISTORY

Received: 13 March 2021
Revised: 21 May 2021
Accepted: 24 May 2021

KEYWORDS

Composite beams;
Effective width;
Numerical analysis;
Semi-rigid joints;
Shear-lag

1. Introduction

Composite steel-concrete continuous beams have been widely used in bridges and high-rise buildings in recent years because they consist of taking advantage of both materials. The effective slab width affects the determination of the section properties of composite beams, which is assumed in their calculation. The concept of effective slab width allows accounting for the shear-lag phenomenon developing in the concrete slab, which occurs due to shear deformation in the slab plan when the longitudinal strain of a slab portion away from the steel beam is smaller than that in the portion close to the steel beam [1]. Many design codes [2–4] specify their effective widths for composite beams by considering the beam's span as the most important parameter influencing the effective width. However, they ignore the effect of the degree of shear connections and the initial stiffness of the beam-to-column composite joints on the effective slab width. Amadio et al. [5] conducted numerical analyses on the cantilever and simply supported composite beams to study the influence of shear connections deformability and loading level on the evaluation of effective widths. They presented a simple modification of the Eurocode [2] formula to estimate the effective width of composite beams subjected to hogging bending moments [6]. Salama et al. found that the beam span and the slab width significantly affect the effective width. Two formulas were proposed to calculate the effective width at the serviceability and ultimate states for simply supported composite beams [7]. Yuan et al. [1] proposed a simplified design formula for computing the effective width of the cantilever and simply supported beams based on two theoretical models. A parametric study was carried out to study the effect of concrete slab thickness, beam span, and slab width on evaluating the effective width. Lasheen et al. found that the slenderness ratio of the steel beam and the width-to-span ratio affect the effective width and loading level [8]. Two equations were provided to calculate the effective width at service and ultimate load states for simply supported composite beams. Al-Sherrawi et al. [9] performed a three-dimensional linearly elastic finite element analysis to study the effect of the interaction degree on the concrete slab's stress distribution in a composite continuous beam under concentrated loads.

Most of the existing studies [1, 5–16] concerning the definition of the effective width are based on cantilever or simply supported beams. However, continuous beams or semi-continuous beams (i.e., beams with semi-rigid joints at their extremities) are regularly met in buildings; in these beams, regions subjected to sagging and hogging bending are identified. Thus, composite joint stiffness and reinforcement ratio in the hogging bending region should be taken into account to evaluate the effective slab width. This paper investigates the effect of shear connection degree η, slab width b_s, and composite joint stiffness $S_{j,ini}$ on the effective slab width of composite continuous and semi-continuous beams. In the next section, the definition of the effective width will be briefly reminded. Then, in Section 3, the numerical modeling assumptions will be presented, and the validation of the numerical model through comparisons with experimental results will be demonstrated in Section 4. In Section 5, a parametric study is conducted with the so-validated numerical model. Finally, the obtained results are discussed in Section 6, and conclusions are drawn in Section 7.

2. Effective width definition

Due to the shear-lag effect, longitudinal stress along the transverse direction of the concrete slab has a non-uniform distribution. The effective width b_e is defined as the equivalent slab width having a constant stress distribution across it and sustaining stress equal to the maximum stress applied to the slab considering the actual stress distribution, so the Bernoulli assumption applies. Accordingly, the magnitude of the constant stress in the effective width is taken as equal to the peak longitudinal stress in the slab at the slab-beam junction, as shown in Fig. 1. As a result, the mathematical definition of effective width is:

$$b_e = \frac{\int_0^{b_s} \sigma_x dz}{(\sigma_x)_{\max}} \tag{1}$$

where:
b_e is the effective width;
b_s is the concrete slab width;
σ_x represents the normal stress in the slab at the top surface in the longitudinal direction.
$(\sigma_x)_{\max}$ represents the maximum normal stress for $0 \le z \le b_s$.

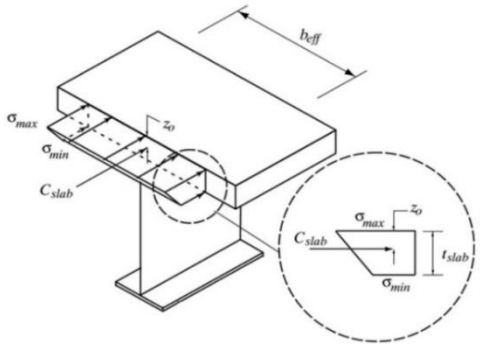

Fig. 1 Effective slab width definition for a hogging moment section [10]

In the presented study, the effective widths have been predicted using Eq. (1) and solving the integral. These calculations were carried out using MATLAB® [17] and an approximate method based on the trapezoidal rule.

3. Finite element modeling assumptions

The objective is to simulate the behavior of continuous and semi-continuous composite beams using the ABAQUS software [18]. Due to symmetry in geometry, loading, and boundary conditions, just one-quarter of the investigated beams are modeled, as shown in Fig. 2 and Fig. 3. A linear reduced integration quadrilateral shell element (S4R) is used to model the concrete slab and the steel beam. This element allows us to obtain a good prediction of the steel beam behavior and, in particular, of local buckling effects [19] and have a computationally efficient model involving a limited number of degrees of freedom. Steel reinforcing bars are modeled as smeared layers with constant thickness in the shell element. The load-slip behavior of shear studs is simulated using a nonlinear connector element "Cartesian + Align," which connects a beam flange node with a slab node at the steel-to-concrete interface where the shear connectors are located, as shown in Fig. 3. In the direction perpendicular to the beam axes, a rigid connection is assumed (the uplift is neglected), while the slip-load behavior in the direction parallel to the beam axis is derived from the nonlinear elastic law proposed by Aribert [20], as follows:

$$Q = Q_{\max}(1-e^{-0.7\gamma})^{0.56} \tag{2}$$

where:

γ and Q are the relative slip between the slab and the steel beam and the shear force, respectively (see Fig. 4). The maximum shear studs' resistance $Q_{\max}$ is calculated according to Eurocode 4 [2].

3.1. Material models

By specifying the nominal stress-strain relationship, which is calculated using Yun et al. [21] proposed bilinear plus nonlinear hardening material model, material nonlinearity is included in the finite element model. The obtained true stress and strain relationships are tabulated in ABAQUS [18]. A concrete damaged plasticity (CDP) method is selected to define the plastic behavior of the concrete; hence an elastic-plastic behavior including strain-softening can be defined. The CDP model proposed by Carreira et al. [22] is adopted for this study. The normalized uniaxial stress-strain relationship for concrete under compression and tension is illustrated in Fig. 5.

3.2. Contact and constraint conditions

A general contact procedure is selected with a HARD contact property specified in the normal direction to define the interaction at the interface between the steel beam and the concrete slab. The PENALTY approach with a friction coefficient of 0.1 is used for the tangential response, which was referenced from the study of Al-Jabri et al. [23]. A sensitivity analysis was done by Dai et al. [24] revealed that using a wide range of friction coefficient values had no impact on the simulation results. A rigid body constraint is used to link the loading surface's nodes to the point where a controlled displacement is applied.

3.3. Solution scheme

Because of the numerical instabilities in the nonlinear analysis during concrete cracking, convergence is always complicated to achieve when using the general static procedure. For this reason, RIKS method is often used to avoid such convergence issues. However, this procedure is not relevant when material damage is included. An alternative consists of using the EXPLICIT procedure to prevent such problems and speed up convergence; this is the selected solution in this study. A quasi-static analysis should be established within the explicit solver to prevent the dynamic effect during the EXPLICIT analysis. This analysis necessitates the application of a smooth loading, which means that the acceleration must only change by a small amount from one increment to the next to apply the load smoothly. If the acceleration is smooth, the velocity and displacement changes would be smooth as well. A reasonable loading rate of 1 mm/min was selected after checking different loading rates on the model, while the initial stable time increment is 10^{-6} s.

Table 1
Geometrical and mechanical characteristics of the investigated specimens (based on test results) [25]

Property	Yield strength (N/mm^2)	Ultimate strength (N/mm^2)	Other properties
Beam web	362	451	
Bottom beam flange	285	380	Steel grade S235
Top beam flange	281	385	
Reinforcement	500	/	14 bars at hogging zone with 2m in length and 6 mm in diameter.
Shear connectors	/	/	h_{sc} = 50mm and D= 12.7 mm; 14 studs with 200mm of spacing in two rows at the sagging zone and 26 studs with 100 mm of spacing in two rows at the hogging zone.
Concrete	37.9	/	E = 27800 MPa

Table 2
Comparison between ultimate loads for FEM and Experiments

Specimen ID [25]	Failure load $Q_u(kN)$		EXP/FE	Mid-span defl. at $Q=80$ kN		EXP/FE
	FE	EXP		FE	EXP	
P03	190	176	0.93	1.74	1.31	0.75
P04	211	179	0.85	1.73	1.35	0.78
P05	179	189	1.06	1.73	1.25	0.72
P06	204	232	1.14	1.73	1.43	0.83
P07	177	175	0.99	1.73	1.44	0.83
P08	189	210	1.11	1.73	1.48	0.86
P09	190	187	0.98	1.73	1.36	0.79
P10	211	231	1.09	1.73	1.25	0.72
		AV	**1.02**		AV	**0.78**

4. Validation of the finite element model

The proposed FE model's validity is examined by comparing the so-obtained numerical results with those determined experimentally by Janss et al. [25]. In this test campaign, ten continuous composite beams were tested under a static control load to study the effect of reinforcement ratio at the internal support section and the effect of concrete strength on the structural behavior. Beams P01 and P02 were tested without reinforcing bars; thus, they are excluded from this study. The details of the investigated beams are shown in Fig. 2 and Table 1. The numerical and experimental results are compared in terms of loading capacity and maximum mid-span deflection.

Table 2 lists the ultimate loads, the mid-span deflections for a specifically applied load (Q = 80 kN), and the ratios between experimental tests and numerical results. Comparing the load versus deflection curves as reported in Fig. 6 demonstrates that finite element results are highly correlated with experimental results. To ensure the accuracy of the Explicit solution, the kinetic energy (KE) should be less than 10% of the internal energy (IE) [18], which is the case here. Thus, the explicit solution can be considered as quasi-static by reducing the dynamic effect even at failure load, as shown in Fig. 7. Finally, the FE model developed herein is capable of accurately predicting the behavior of continuous composite beams. In particular, as reflected in Table 2, the accuracy of the FE analysis in predicting the ultimate load ranges from -15% to 15%, which is assumed to be reasonable.

5. Parametric study

In order to evaluate the effect of the various parameters (i.e., concrete slab width, shear connection degree, and composite joint stiffness) on the effective width, a parametric study is performed as described hereafter. The geometric and material properties of the P03 specimen [25] were adopted as a reference from which the different investigated parameters are varied. A slab width of b_s = 2m is adopted to study the effect of the shear connection degree and the composite

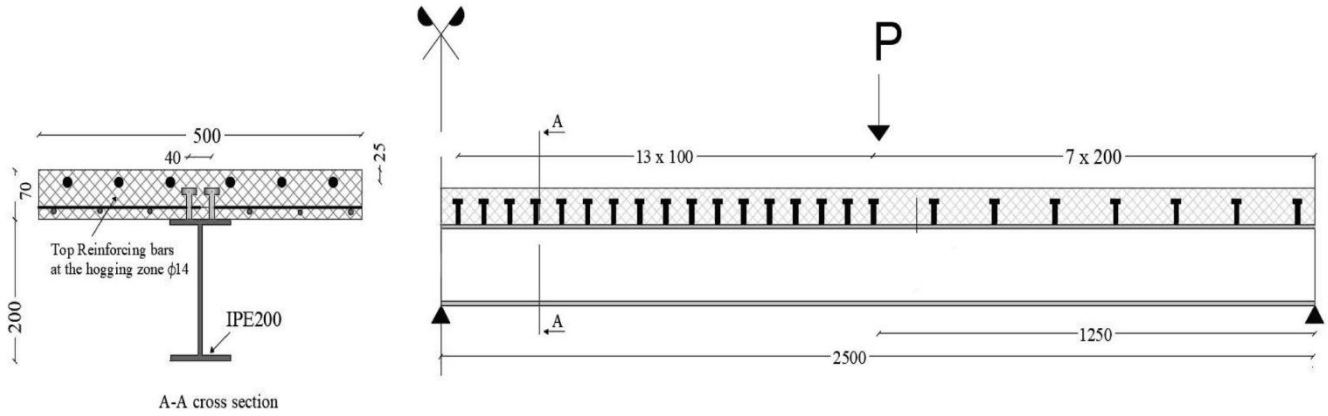

Fig. 2 Geometry of the investigated beam specimen (dimensions in mm)

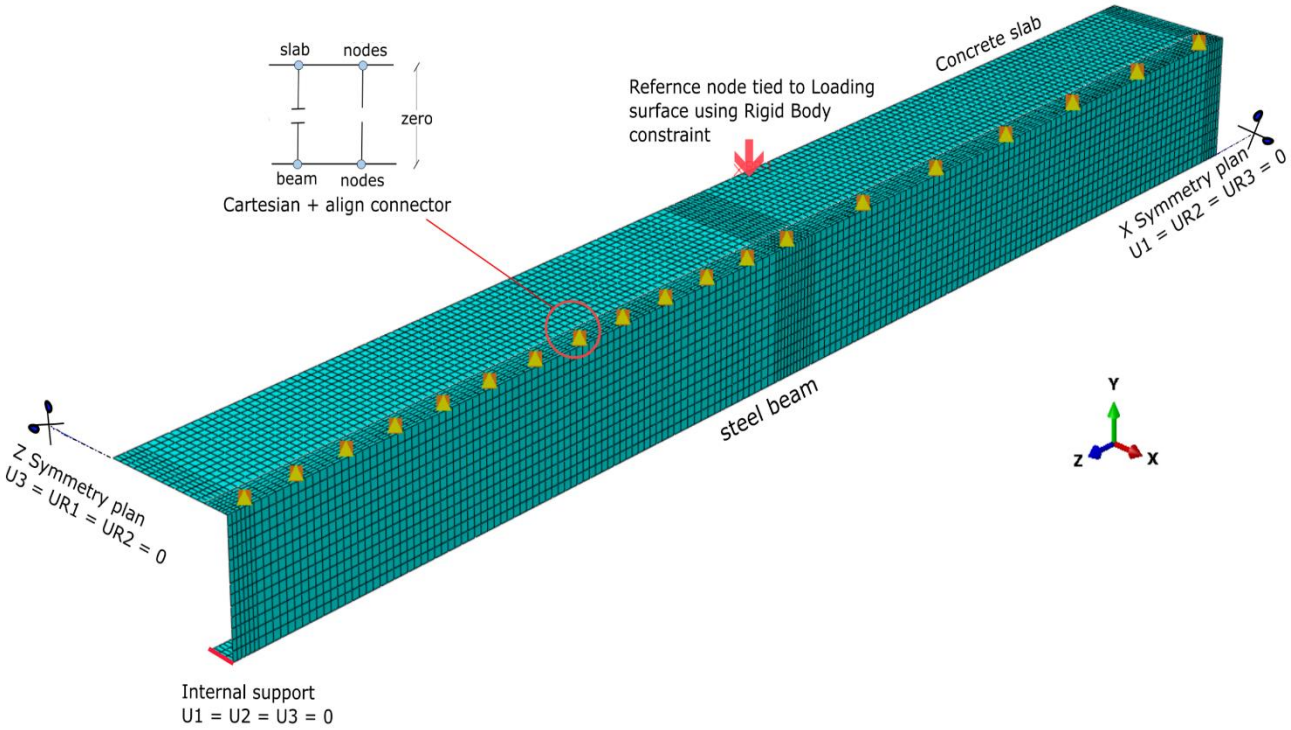

Fig. 3 Finite element mesh and boundary conditions of one-quarter of the composite continuous beam

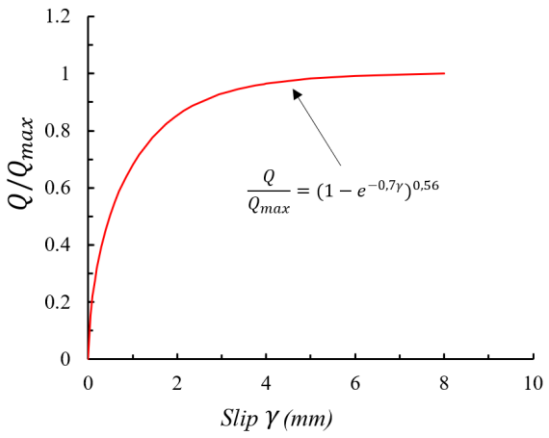

Fig. 4 Nonlinear constitutive law used in the finite element model

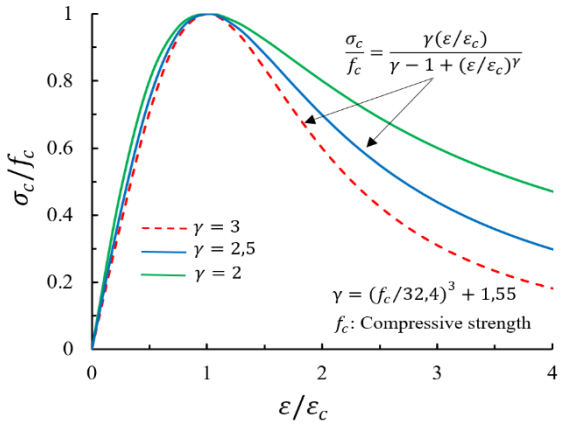

(a) Compression

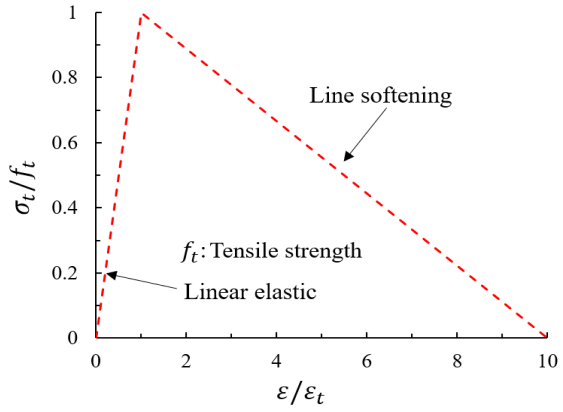

(b) Tension

Fig. 5 Stress-strain relationship of the concrete (Carreira et al. [21])

joint stiffness so that the effective width will be evaluated easily along the beam span. As mentioned previously, the investigated parameters are:

- The effect of the shear connection degree η (see Section 5.1);
- The effect of the concrete slab width b_s (see Section 5.2) and;
- The effect of the initial stiffness $S_{j,ini}$ of a composite joint located at the level of the internal support (see Section 5.3);

The critical sections of the investigated beam are located at the level of the internal support (hogging bending zone) and the loading points (sagging bending zone). Consequently, the effective widths are evaluated for those critical sections for two loading levels: at $Q = Q_e$, i.e., when the structural behavior of the composite beam is still in the elastic domain, and at ultimate load Q_u.

5.1. Effect of shear connection degree

Shear connectors are modeled as explained in Section 3. A full shear connection degree ($\eta = 1$) is adopted in the hogging bending region respecting the recommendation of Eurocode 4 [2], while four shear connection degrees are investigated, as shown in Table 3, for the sagging moment region. Fig. 8 and Fig. 9 highlight the influence of the shear connection degree on the effective width at internal support and mid-span sections. It is demonstrated that the shear connection degree has a limited and negligible influence on the effective width for the investigated composite continuous beams; this confirms the results obtained by Chen et al. [26].

5.2. Effect of slab width

Five beams with different slab widths ranging from 0.5m to 2.5m were simulated, keeping the same reinforcement ratio ($\mu = 2.6$ %) and rebar cross-section ($\phi = 14$mm) as in the tested specimens [24]. Since the shear connection degree does not influence the effective width as demonstrated previously. The node-to-surface tie constraint option available in ABAQUS [18] is used to achieve a full connection degree between the concrete slab and the steel beam.

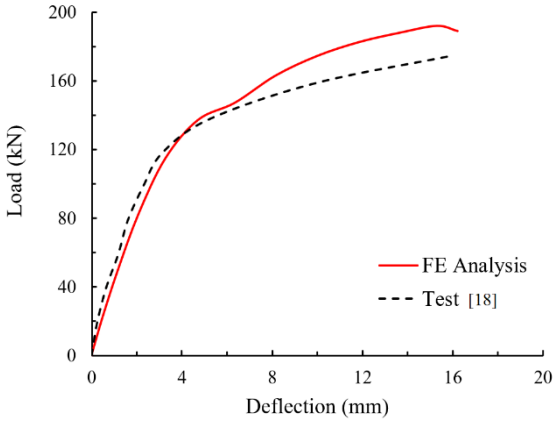

Fig. 6 Comparison between the predicted and measured Mid-span deflection

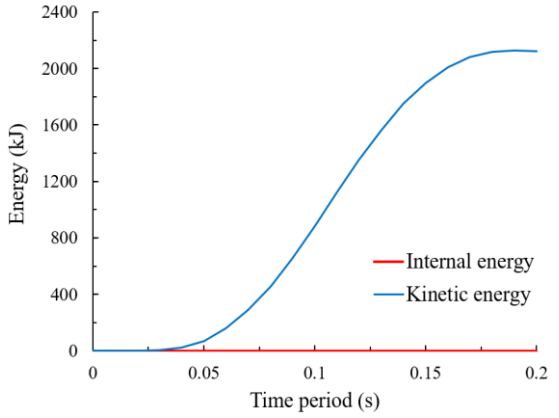

Fig. 7 Comparison between the predicted kinetic and internal energy

Table 3
Details of beams for the shear connections parametric study

Degree of shear connections η	Number of shear connectors	
	Hogging zone	Sagging zone
1	30	20
0.76	26	14
0.60	20	10
0.44	16	6

Therefore, reduced FE model size and convergence time are ensured. Fig. 10 and Fig. 11 compare the predicted effective width and the effective width proposed by the code [2] at midspan and internal support under both loading levels Q_e and Q_u. It is clear from Fig. 10 that the code overestimates the effective width at mid-span for the smallest slab width ($b_s/L \leq 0.3$), while it is underestimated for the higher b_s/L ratios. From Fig. 11, it can be seen that the effective width proposed by the code [2] is consistently underestimated at the internal support compared to the ones proposed by the code [2] and Amadio et al. [5]. Fig. 12 shows a comparison between the predicted effective width and the effective width proposed by some previous researchers and codes in the elastic domain at the midspan section. The computed effective width for the investigated composite continuous beams is smaller than those proposed by Salama et al. [7] and Yuang et al. [1]. In contrast, the predicted effective width at internal support becomes more prominent than the one proposed by Amadio et al. [5] when $b_s/L \geq 0.4$, as shown in Fig. 11.

5.3. Effect of shear connection degree

In order to simulate the presence of a semi-rigid composite joint at the level of the internal support, the beams pan of the previous FE model was reduced by 76 mm at the internal support to place a rectangular bar at the level of the bottom flange, as illustrated in Fig. 13. It is possible to simulate the presence of a joint with different stiffness levels by playing on the mechanical properties of this bar.

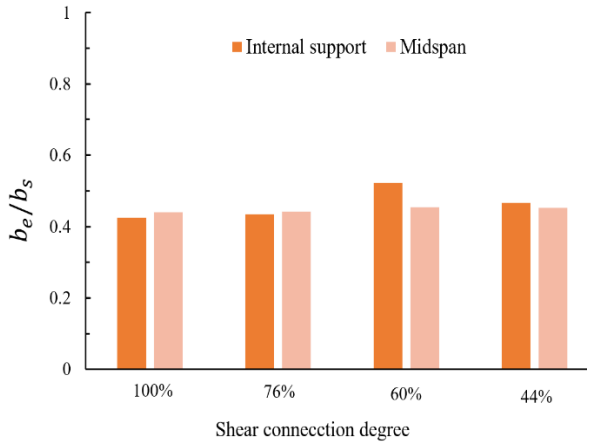

Fig. 8 Effect of the shear connection degree on the effective width at elastic loading level Q_e

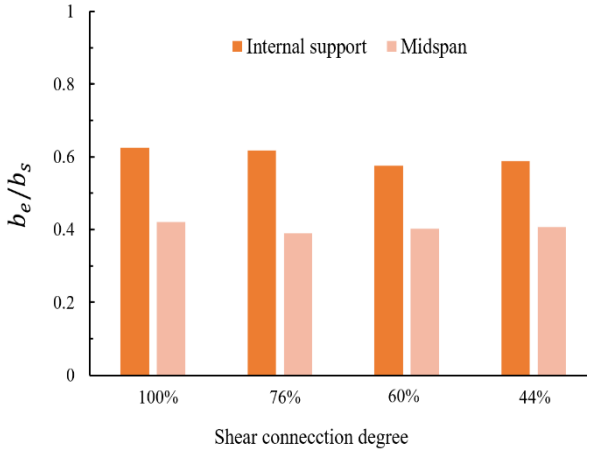

Fig. 9 Effect of the shear connection degree on the effective width at ultimate loading level Q_u

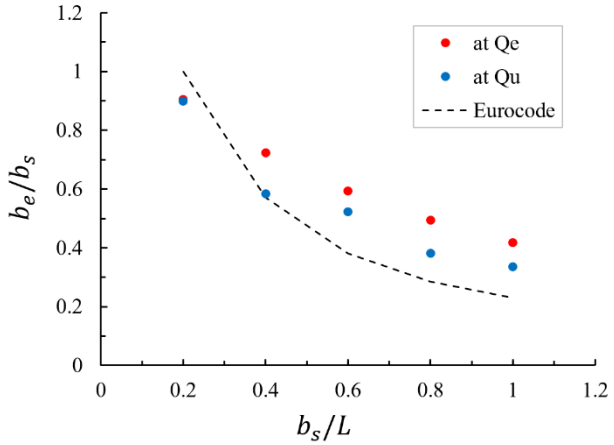

Fig. 10 Comparison between the predicted b_e and b_e proposed by the code [2] at mid-span section

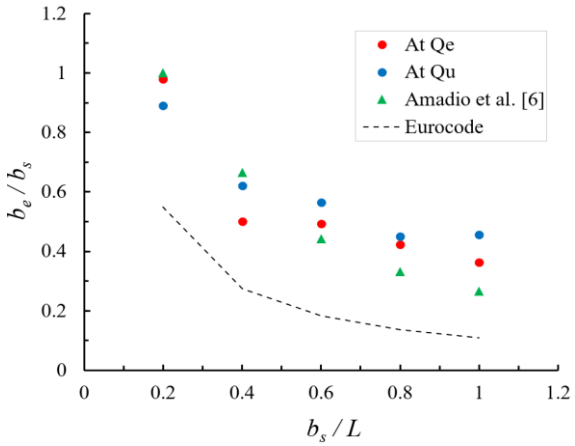

Fig. 11 Comparison between the predicted b_e and b_e proposed by the code [2] at the internal support section

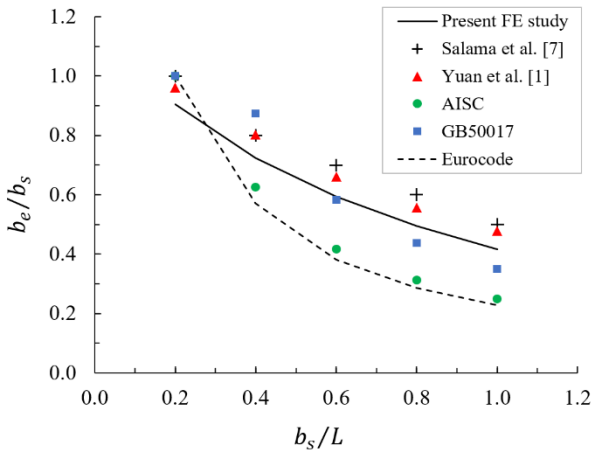

Fig. 12 Comparison between the predicted b_e and b_e calculated using previously proposed formulas at mid-span section

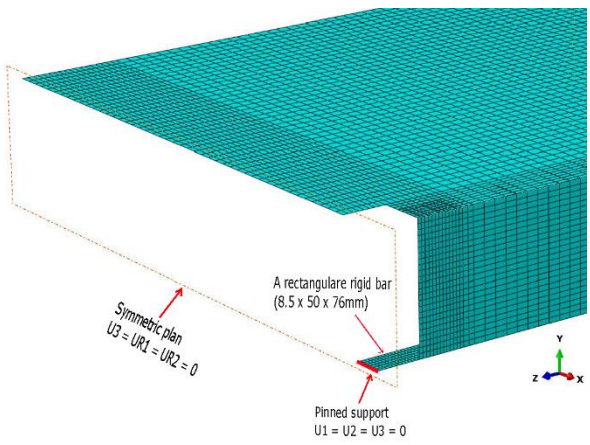

Fig. 13 Details and boundary conditions of the proposed composite joint model

The rectangular bar is assumed to have a perfectly elastic behavior to avoid any failure at its level. In addition, a hole of 76 × 80 mm is created in the concrete slab to simulate the presence of a HEA 160 column passing through the slab. With such modeling, the slab is activated in tension, which means that, in practice, only the reinforcement is activated, while the rectangular bar activates in compression. The rectangular bar and the steel beam's bottom flange were merged to prevent any relative movement between the two surfaces (see Fig. 13). 2 m of width is selected for the concrete slab to perfectly capture the shear lag phenomena. The composite joint model was checked through comparison to the FE model of the continuous beam, assuming a high stiffness for the rectangular bar, i.e., assuming a rigid joint at the level of the internal support. It can be observed from Fig. 15 that the composite joint model predicts almost the same mid-span deflection as the previously adopted FE model, which validates the proposed model. As previously mentioned, the bar stiffness EA/L is calibrated to simulate different composite joint initial stiffness $S_{j,ini}$. The bar's stiffness and the contribution of the reinforcement at the internal support must be considered for computing the composite joint's rotational stiffness. This joint stiffness is calculated according to EC3 [27] and EC4 [2], as follows:

a. Lever arm z between the reinforcement and the rectangular bar (see Fig. 14):

$$z = h_a - 0.5t_{fb} + h_c - a_{cs}$$
$$= 200 - 0.5\times 8.5 + 70 - 25 = 241mm$$

where:

h_a is the nominal height of the steel beam;
t_{fb} is the beam flange thickness;
h_c is the concrete slab thickness;
a_{sc} is the longitudinal reinforcement cover.

b. Stiffness coefficient to be considered for the rebar k_{21} [2]:

$$k_{21} = k_{slip} \times k_{s,r}$$

where:

k_{slip} is the reduction factor to account for possible shear connection slips;
$k_{s,r}$ is the stiffness coefficient for the reinforcement.

In our case, k_{slip} = 1 because a full shear connection degree (η = 1) is adopted in the FE model, and $k_{s,r}$ is equal to:

$$k_{s,r} = \frac{A_{s,r}}{h\frac{(1+\beta)}{2} + K_\beta}$$

where:

$$k_\beta = \beta(4.3\beta^2 - 8.9\beta + 7.2)$$

$A_{s,r}$ is the cross-sectional area of the longitudinal reinforcement in row r within the effective slab width;
h is the depth of the column's steel section;
β is the transformation parameter.

In our case, we have a double-sided beam-to-column joint with equal beam moments on each side ($M_{b1,Ed} = M_{b2,Ed}$). Accordingly, $\beta \to \beta_1$ is equal to 0 according to Eurocode 3 [25].

Finally, the initial stiffness of the simulated joint can be estimated using the following formula:

$$S_{j,ini} = \frac{E_a \times z^2}{\sum(\frac{1}{k_i})} = \frac{210000\times 241?}{\frac{1}{k_{21}} + \frac{1}{k_{bar}}} \quad (3)$$

where:

k_{bar} is the stiffness coefficient of the bar equal to nA/L with $n = E_{bar}/E_a$.

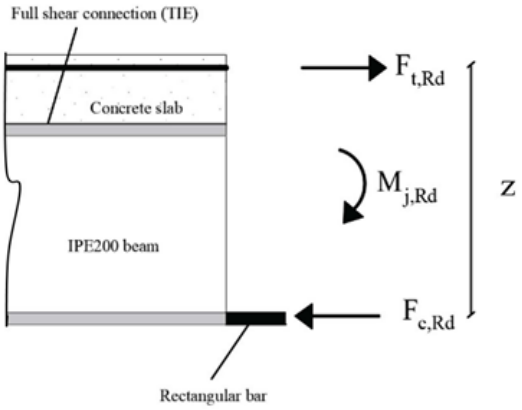

Fig. 14 Internal efforts distribution in the hogging bending moment for the proposed composite joint model

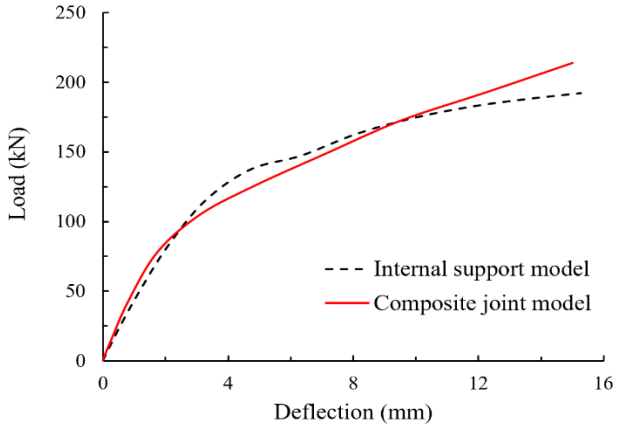

Fig. 15 Effect of the bar stiffness $S_{j,bar}$ on the mid-span deflections and ultimate loads

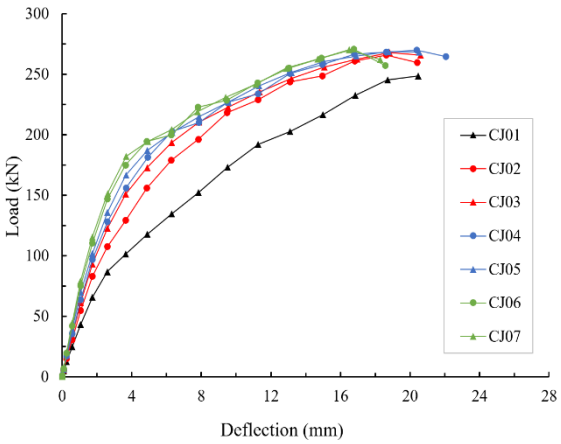

Fig. 16 Mid-span deflection for the proposed composite joint model and the one previously validated in Section 4

Table 4 summarises the considered initial stiffness for the composite joint $S_{j,ini}$ for the investigated beams. Fig. 16 shows the effect of the composite joint stiffness on ultimate load and maximum mid-span deflection. Globally, it can be seen that the beam stiffness decreases as the composite joint stiffness decreases, as expected, while the initial joint stiffness has almost no effect on the ultimate resistance of the composite beam for $S_{j,ini} \geq 65$ MN.m/rad. The predicted deformations and Von Mises stresses distribution for beam CJ07 are presented in Fig. 17 and Fig. 18 as an example. It can be observed from Fig. 20 that at the ultimate loading state, the initial joint stiffness affects the effective width slightly at the joint level (hogging moment zone).

In contrast, in the elastic domain, the effective width increases significantly with the initial stiffness. However, its value decreases slightly with the increase of the initial stiffness shows at mid-span. The reason for such behavior is that the shear lag shrinks with the increase of the initial joint stiffness, and the effective width is becoming smaller, as shown in Fig. 20.

Table 4
Details of beams for the slab width parametric study

Beam ID	Failure load Q_u (kN)	Maximum deflection δ_{max} (mm)	b_e at the joint region (mm)		E_{bar} (GPa)	$S_{j,ini}$ (MN.m/rad)
			at Q_e	at Q_u		
CJ01	248	20	350	579	210	41.60
CJ02	266	19	278	709	840	64.70
CJ03	268	19	393	732	1680	98.30
CJ04	268	20	451	706	2100	114.40
CJ05	270	19	558	690	4200	151.40
CJ06	270	17	627	720	8400	178.80
CJ07	270	16	647	711	21000	191.90

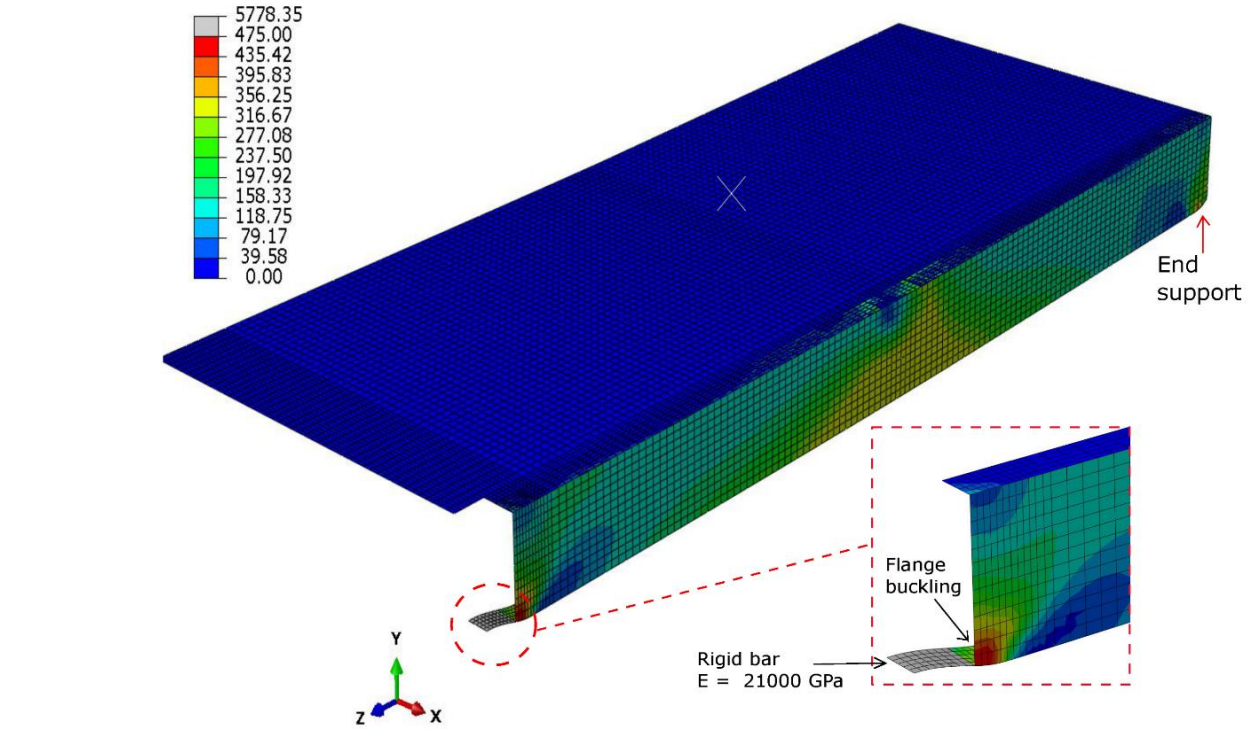

Fig. 17 Predicted stress distribution and deformation for CJ07 specimen at failure load

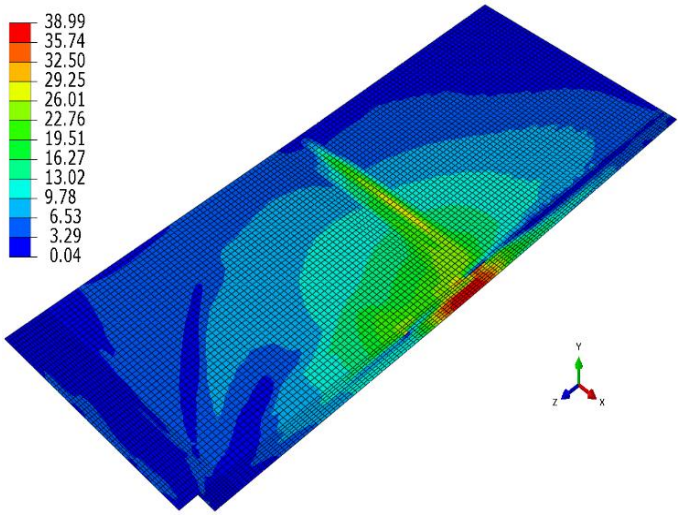

Fig. 18 Von Mises stress's distribution in the concrete slab for CJ07 specimen at failure load

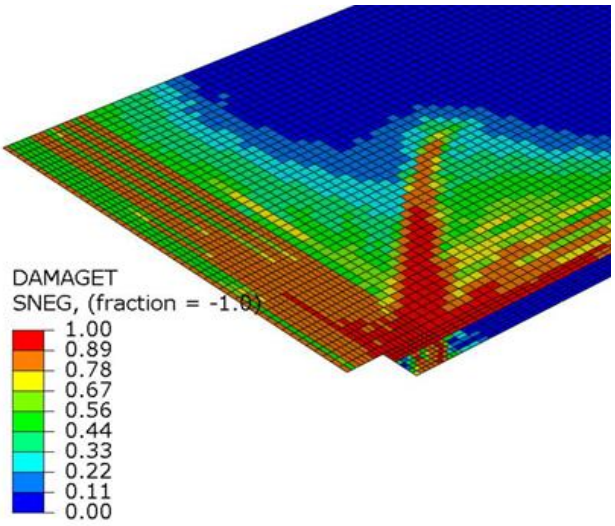

Fig. 19 Predicted concrete tension failure in the composite joint region for at ultimate load

6. Discussion of the obtained results

From the conducted parametric studies, it can be concluded that the main parameters affecting the effective slab width are b_s (or, more precisely, the b_s/L ratio) and $S_{j,ini}$. The effects of these two parameters on the effective width are discussed hereafter.

6.1. Effect of slab width b_s

In Fig. 12, the effective widths proposed by Eurocode [2], AISC [4], and GB50017 [3] for the midspan section are compared with the present FE results and the formulas proposed by Yuan et al. [1] and Salama et al. [7]. The effective width proposed by different codes is not in good agreement with the numerical results. Indeed, the value of b_e is underestimated for $b_s/L \geq 0.4$ using the Eurocode and AISC codes. Using the GB50017 code, b_e is slightly underestimated for $b_s/L \geq 0.6$, and below those ratios, b_e is overestimated. However, the values of b_e found using simplified formulas recommended by Yuan et al. [1] and Salama et al. [7] are overestimated compared to the present FE results. Moreover, the effective width formulas proposed by Amadio et al. [6] and in the Eurocode [2] for the internal support section give approximately the same values as the FE results for $b_s/L \geq 4$ (see Fig. 11). However, those values of b_e are underestimated compared to FE results when the ratio b_s/L is more significant than 0.6 at both loading levels Q_e and Q_u. As shown in Fig. 19, significant cracks are developed in the hogging moment zone at the ultimate limit state for the smallest slab widths $b_s \leq 0.2L$. Based on the obtained results from the parametric study and the regression method, the following simplified formulas has been calibrated to predict the effective width of the continuous composite beams in the elastic domain and at failure load, respectively:

- At joint region:

$$b_e/b_s = -0.36 \times \ln(b_s/L) + 0.32 \quad (4)$$

$$b_e/b_s = -0.278 \times \ln(b_s/L) + 0.42 \quad (5)$$

- At midspan:

$$b_e/b_s = -0.303 \times \ln(b_s/L) + 0.43 \quad (6)$$

$$b_e/b_s = -0.347 \times \ln(b_s/L) + 0.32 \quad (7)$$

6.2. Effect of the joint initial stiffness $S_{j,ini}$

From Fig. 21, it can be seen that the effective width increases significantly with the increase of the initial stiffness $S_{j,ini}$ at $Q \leq Q_e$ loading levels, while it increases slightly at the mid-span section (see Fig. 21). Therefore, its effect has to be taken into account at those levels. Accordingly, new simplified equations are developed to evaluate the effective width at mid-span and joint regions in the elastic domain and failure load. The coefficients of the following equations are determined based on a regression method:

- At joint region:

$$b_e/b_s = 0.0012 \times S_{j,ini} + 0.23 \quad (8)$$

$$b_e/b_s = 0.0002 \times S_{j,ini} + 0.64 \quad (9)$$

- At midspan:

$$b_e/b_s = -0.0004 \times S_{j,ini} + 0.57 \quad (10)$$

$$b_e/b_s = 0.0004 \times S_{j,ini} + 0.33 \quad (11)$$

where the unit of the initial stiffness $S_{j,ini}$ is (MN.m/rad).

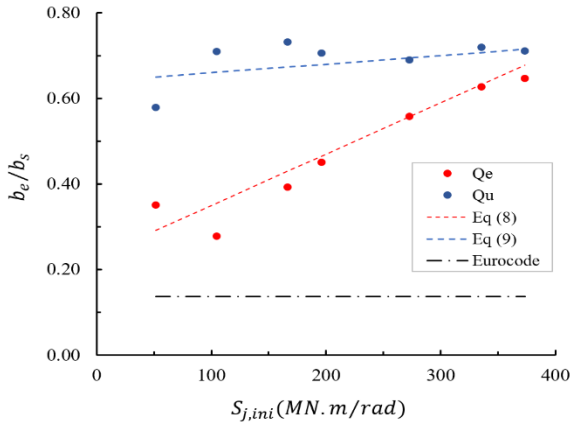

Fig. 20 Comparison of the proposed formulas Eq. (8) and Eq. (9) against the predicted FE results

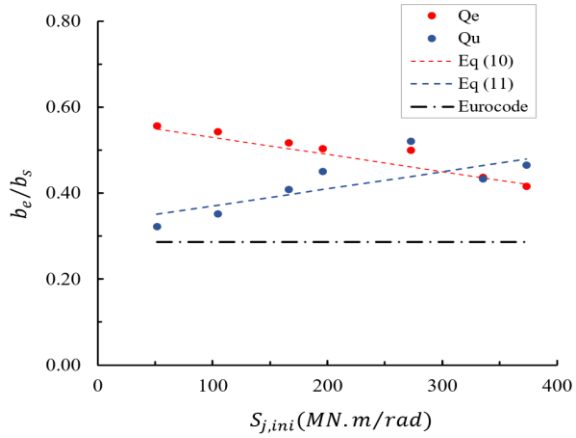

Fig. 21 Comparison of the proposed formulas Eq. (10) and Eq. (11) against the predicted FE results

The so-proposed formulas are promising, and the validation of the formulas to other composite beam configurations can be seen as a perspective to the present work.

7. Conclusions

A reliable FE model has been developed through the conducted investigations for continuous and semi-continuous composite beams. In particular, the validity of the continuous composite beam model was verified and validated by comparing the numerical results to experimental ones. A simplified model was developed to simulate the presence of semi-rigid joints in the composite beam, and the component method was used to determine the associated initial stiffness of the composite joint. With these numerical models, it was possible to accurately predict the load-deflection response of the investigated continuous and semi-continuous composite beams and evaluate the associated effective slab widths along the beams. An extensive parametric study was conducted to identify the influence of some key parameters on the effective widths. As a result, it was demonstrated that the slab width and the joint stiffness significantly influence the effective width, while the effect of the degree of connection is negligible.

Finally, simplified design formulas were proposed to evaluate the effective widths considering the effect of the so-identified key parameters. The effective widths calculated with the proposed formulas predict the effective widths accurately compared to the numerical results. The formulas provided in this paper are based on the experimental findings of a specific set of geometrical and mechanical characteristics presented in Section 4 and Table 1. Further experimental studies are required to explore the applicability of the proposed formulation to other composite beam configurations and better understand the behavior of composite continuous and semi-continuous beams, which constitutes a perspective to the presented work.

Acknowledgment

The authors gratefully acknowledge the support provided by the Urban and Environmental Engineering department at Liege University (Belgium) and the SREML research laboratory at Laghouat University (Algeria). Thanks, are also extended to the DGRSDT Directorate of the Ministry of High Education and Scientific Research of Algeria for providing a scholarship to enable this research work to be conducted.

References

[1] Yuan, H., Deng, H., Yang, Y., Weijian, Y. and Zhenggeng, Z., "Element-based effective width for deflection calculation of steel-concrete composite beams," Journal of Constructional Steel Research, 121, 163-172, 2016. Doi: https://doi.org/10.1016/j.jcsr.2016.02.010

[2] European Committee for Standardization (CEN), Design of composite steel and concrete structures, Part 1-1: General rules for buildings, EN 1994-1-1 Eurocode 4, Brussels, 2004.

[3] GB50017, Code for Design of Steel Structures, Beijing, Ministry of Construction of People's Republic of China, 2003.

[4] AISC, load, and resistance factor design specifications for structural steel buildings, Chicago, American Institute of Steel Construction, 2010.

[5] Amadio, C. and Fragiacomo, M., "Effective width evaluation for steel-concrete composite beams," Journal of Constructional Steel Research, 58(3), 373-388, 2002. Doi: https://doi.org/10.1016/S0143-974X(01)00058-X

[6] Amadio, C., Fedrigo, C., Fragiacomo, M. and Macorini, L., "Experimental evaluation of effective width in steel-concrete composite beams," Journal of Constructional Steel Research, 60(2), 199-220, 2004. Doi: https://doi.org/10.1016/j.jcsr.2003.08.007

[7] Salama, T., and Nassif, H. H., "Effective flange width for composite steel beams," The Journal of Engineering Research [TJER], 7(2), 28, 2011. Doi: https://doi.org/10.24200/tjer.vol8iss1pp28-43

[8] Lasheen, M., Shaat, A. and Khalil, A., "Numerical evaluation for the effective slab width of steel-concrete composite beams," Journal of Constructional Steel Research, 148, 124-137, 2018. Doi: https://doi.org/10.1016/j.jcsr.2018.05.015

[9] Al-Sherrawi, M. H. and Dawood, A. R., "Shear -lag in continuous composite steel-concrete beam," International Research Journal of Advanced Engineering and Science, vol. 4, issue 1, pp. 85-90, 2019.

[10] Transportation Research Board and National Academies of Sciences, Engineering, and Medicine. Effective slab width for composite steel bridge members. Transportation Research Board, 2005. Doi: https://doi.org/10.17226/13853

[11] Nie, J. and Tao, M., "Slab spatial composite effect in composite frame systems. I : Effective width for ultimate loading capacity", Journal of Engineering Structures, 38, 171-184, 2012. Doi: https://doi.org/10.1016/j.engstruct.2011.11.034

[12] Khalaf, M., El-Shihy, A., El-Kasaby, E.-S. and Youssef, A., "Numerical estimation and analysis of effective width of composite beams with ribbed slab," International Journal of Application or Innovation in Engineering and Management 3 (8) 1–15, 2014.

[13] Dezi, L., Gara, F. and Leoni, G., "Effective slab width in prestressed twin-girder composite decks," Journal of Structural Engineering, 132(9), 1358-1370, 2006. Doi: https://doi.org/10.1061/(ASCE)0733-9445(2006)132:9(1358)

[14] Gara, F., Leoni, G., and Dezi, L., "A beam finite element including shear lag effect for the time-dependent analysis of steel-concrete composite decks," Journal of Engineering Structures, 31(8), 1888-1902, 2009. Doi:https://doi.org/10.1016/j.engstruct.2009.03.017

[15] Nicoletti, R. S., Rossi, A., Souza, A. S. C. de and Martins, C. H., "Numerical assessment of effective width in steel-concrete composite box girder bridges," Journal of Advances in Structural Engineering, 24(5), 977-994, 2021. Doi: https://doi.org/10.1177/1369433220971744

[16] Gara, F., Ranzi, G., & Leoni, G., "Partial interaction analysis with shear-lag effects of composite bridges: a finite element implementation for design applications.", Journal of Advanced Steel Construction, 7(1), 1-16, 2011. Doi: https://doi.org/10.18057/IJASC.2011.7.1.1

[17] MathWorks, Inc. MATLAB R2016a. Natick, MA: Math Works, Inc.; 2016.
[18] ABAQUS, ABAQUS Analysis User's Guide, Version 6.14, Dassault Systèmes Corp., Providence, RI (USA), 2014.
[19] Thai, H.-T. and Uy, B., "Finite element modeling of blind bolted composite joints," Journal of Constructional Steel Research, 112, 339-353, 2015.
Doi: https://doi.org/10.1016/j.jcsr.2015.05.011
[20] Aribert , J. and Al Bitar , A., "Optimisation du dimensionnement en connexion partielle de poutres de planchers mixtes réalisés avec un bec en tôle mince nervurée", La revue Construction métallique 26 (4) 3–33, 1989.
[21] Yun, X. and Gardner, L., "Stress-strain curves for hot-rolled steels," Journal of Constructional Steel Research, 133, 36-46, 2017.
Doi: https://doi.org/10.1016/j.jcsr.2017.01.024
[22] Carreira, D. J., and Chu, K. H. "Stress-strain relationship for plain concrete in compression," ACI Journal Proceedings, 82(6), 1985.
Doi: https://doi.org/10.14359/10390
[23] Al-Jabri, K. S., Pillay, P., Waris, M. B. and Pervez, T., "Modeling of composite beam-column flexible endplate joints at elevated temperature," Journal of Composite Structures, 143, 180-188, 2016.
Doi: https://doi.org/10.1016/j.compstruct.2016.01.069
[24] Dai, X. H., Wang, Y. C., and Bailey, C. G., "Numerical modeling of structural fire behavior of restrained steel beam-column assemblies using typical joint types," Journal of Engineering Structures, 32(8), 2337-2351, 2010.
Doi: https://doi.org/10.1016/j.engstruct.2010.04.009
[25] Janss, J. and Jean-Claude, L., Essais de poutres mixtes sur troisappuis, Centre de Recherches Scientifiques et Techniques de l'Industrie des Fabrications Métalliques, Bruxelles, 1973.
[26] Che, S. and Zhang, Z., "Effective width of a concrete slab in steel-concrete composite beams prestressed with external tendons," Journal of Constructional Steel Research 62 (5) 493–500, 2006.
Doi: https://doi.org/10.1016/j.jcsr.2005.08.009
[27] CEN. EN 1993-1-8. Eurocode 3: Design of steel structures, part 1-8: Design of joints, Brussels: CEN; 2005.

Advanced Steel Construction – Vol. 17 No. 4 (2021) 340–348
DOI:10.18057/IJASC.2021.17.4.2

INVESTIGATION OF BEHAVIOR OF INTERIOR STEEL CONNECTIONS WITH OPENINGS IN BEAM WEB AND FLANGE UNDER MONOTONIC LOADING

Dan-Dan Yan [1], Bai-Li Zhou [2], Xin Guo [1], Fang Lai [2], Xi Wei [2], Yi-Peng Xu [3, *], Mehdi Esfandi Sarafraz [4] and Maryam Jahanian [5, *]

[1] *School of Energy and Power Engineering, XiHua University, Chengdu, Sichuan, 610039, China*
[2] *School of Civil and Environmental Engineering, Xihua University, Chengdu, Sichuan, 610039, China*
[3] *School of Mathematical Sciences, Tiangong University, Tianjin, 300387, China*
[4] *Department of Civil Engineering, Islamic Azad University, West Tehran Branch, Tehran, Iran*
[5] *MSc graduate of Structural Engineering, University of Tabriz, Tabriz, Iran*
** (Corresponding author: E-mail: xu.yipeng90@gmail.com; mjahanian454@gmail.com)*

ABSTRACT

Connections are considered to be one of the most prominent components of steel moment frames and have received studious attention in recent years. The core problem of welded connections is premature brittle fracture of weld in the critical beam-to-column connection region. Within the framework of this issue, various approaches have been proposed to solve the mentioned problem. Intentional weakening of the beam web or flange is in line with the purpose of leading the plastic hinge away from the column face, hence, increasing the ductility. The aim of this research is to investigate the behavior of interior connections subjected to monotonic lateral loading in case of presence of openings in beam web or flange. To do so, an ordinary fully welded rigid connection, reduced beam section, reduced web section, and drilled flange connection models are simulated numerically, utilizing finite element software, ANSYS. The results indicate that scrupulous selection of opening sizes are of great importance to fulfill the desired outcome which is avoiding the brittle failure of connections. Furthermore, the use of drilled flange, reduced beam section, or reduced web section connections satisfy the expected performance and it is proposed to use them according to practicability, architectural and economic considerations as well as site conditions. Shear deformation and local buckling is observed in reduced web section connections while in drilled flange connections, stress concentration around the opening is critical.

ARTICLE HISTORY

Received: 21 June 2020
Revised: 31 March 2021
Accepted: 4 April 2021

KEYWORDS

Interior connection;
Monotonic loading;
RWS;
RBS;
DF;
Steel moment frame

1. Introduction

The premature failure of steel structures due to connection damages, induced by various loadings, has received studious attention leading to the development of beam-to-column connection design processes and revision of different codes in recent years. Consequently, enhancing the structural ductility is the issue that still continues to evoke interest among researchers since the regulations emphasize the urge to design ductile systems. Intentional weakening of beam parts, strengthening the connection or utilizing dissipative elements are among commonly discussed approaches of relocating the plastic hinge away from the column face, hence, increasing the structural ductility, which is consonant with the formation of plastic hinge.

Prequalified steel moment connections described in ACI 358 [1] for SMF and IMF systems are categorized into 10 groups, among which reduced beam section (RBS) connection is a type of connection in which intentional weakening of a part of the beam flange is employed to obtain the desirable performance of beam-to-column connections. Consequently, AISC design codes have imposed some regulations on the design principles of RBS connections. However, the other types of connections are within the group in which strengthening the connection is based on added members including end-plates, steel brackets, plates, etc. Many studies have been published on utilizing RBS connections in steel moment frames [2-9]. Yet, according to [10], one of the major drawbacks to adopting the RBS connections are the limited range of beam and column dimensions in tests. Despite the fact that RBS connections are among the robust connections to be employed in steel moment frames, they experience stiffness degradation as well as loss of moment capacity [5,11-15]. Furthermore, stress concentration due to flange cut fabrication in site is a disadvantage for the seismic performance of RBS connections [16]. Based on some researches, designing RBS connections in conformance to AISC code in case of utilizing IPE sections with large dimensions appears to be insufficient, hence, stiffeners must be provided [17].

In terms of web reduction, limited number of codes including [18-20] have deemed attenuating beam web as a means of improving connection behavior, and there exist limited guidelines on steel frames with perforations in beam web. However, various opening shapes except for rectangular and circular ones are not covered in the afore-mentioned codes. In this regard, other opening shapes including elliptical-shaped, hexagon-shaped, etc. have been investigated by [21-26] and other researches.

DF (drilled flange) connections are not covered in design codes such as [1, 10, 27-29]. Accordingly, neither regulations nor design guidance are suggested on DF connections, hence, utilizing DF connections instead of RBS ones are in their early stages. Despite the fact that fabrication of DF connections is easier than RBS ones, they perform slightly weaker [16] or nearly similar to the RBS connections [30]. However, there is still considerable uncertainty regarding the performance of DF connections. In this regard, some of the researches have approved the desired performance of DF connections in which these connections are capable of satisfying [29] AISC 341-16 requirements for rigid connections [31-34]. Hence, DF connections are deemed a sough-after substitute fo r RBS connections.

Many studies have investigated the behavior of connections [35-39]; also, the behavior of prefabricated beam-to-column connections were studied by many researchers [40-42] among which [40] utilized short post-tensioned prestressed strands to prevent on-site aerial tensions. Furthermore, the connection of H-Shaped steel beam to box columns with flange plate connection was scrutinized by [43]. The behaviour of the TS semi-rigid connections were investigated through utilizing both experiments and numerical simulations by [44-45]; etc. The assessment of performance of joints between steel beam and LSWL-C columns was performed numerically and through experimental tests by [46]; among most recent researches conducted on connections, [47] used folded axillary plates, which are located at the outer side of the beam-end flanges, to improve the behavior of fully welded connection.

Various approaches have been put forward to lead the plastic hinge away from the column face through intentionally attenuating a part of the beam, among which, many attempts have been made with the purpose of improving the connection behavior through cutting of the beam flange [12, 15-16, 48-57]. Plumier [58] was the first to introduce trapezoidal beam flange cuts. Much work on the potential cut profiles of RBS connection was carried out by [11, 59-62], yet the radius cut revealed the appropriate seismic performance in comparison with other cut configurations [11,63]. Furthermore, ameliorating the behavior of RBS connections are the topic of many studies in terms of buckling which leads to an early strength degradation [64-66]. The first investigation on double reduced beam section was carried out by [57], in which two adjacent radius cuts was implemented in beam flange named as DRBS, and

concluded that implementing the second cut leads to maximum equivalent plastic strain index reduction as well as delaying the local buckling. Investigating the behavior of RBS connections through numerical or experimental studies in the recent years are conducted by many researchers among which [67-76] can be mentioned. Fanaie et al. [69] pointed to a method in which a mathematical approach in conjunction with principles of structural analysis is employed in order to acquire the drift as well as changes in stiffness of stories in frames with RBS connections. Meng et al. [77] introduced a novel RBS connection with V-shaped reinforcing plate which improved the seismic performance of RBS connections. Moreover, the use of RBS-free and RBS-based systems in moment frames in tall buildings under earthquake excitations were scrutinized by [78]. Sensitivity study on the effect of beam slope angle as well as different design factors, including material or geometry, on the cyclic behavior of RBS connections in terms of initial stiffness, rupture index, plasticity index, moment capacity, yield moment, hysteretic energy dissipation, and strength degradation rate was performed by [79]. Results indicated the significance of the slope angle and beam depth in the response of the RBS connections.

Reduced beam web connections in which an opening is implemented in beam web has been widely investigated by many researchers [22, 24-25, 80-103]. Geol and Itani [104-105] drew the attention of researchers to reducing the beam web as a way of achieving desired performance of moment frames. The possibility of using the connections with reduced beam web was investigated by [88]. In this regard, a more recent evidence reveals that RWS connections are a desirable replacement for RBS connections in terms of story drifts and strength [106]. Furthermore, issues regarding the energy dissipation of RWS connections are addressed by [22, 95]. Detailed examination of influential parameters including opening size, location, etc. was undertaken by many researchers [81, 85-86], leading to the conclusion that scrupulous selection of opening dimension, shape and location is essential in order to obtain the favorable frame behavior. Various shapes of openings in RWS connections is further explored by [21-26]. Also, the capability of RWS models to reach higher story drifts (six percent) was evaluated by [82-83] both in experimental and numerical ways. The behavior of RWS connections via numerical or experimental studies in the recent years are assessed by many researchers among which [107] developed a novel RWS connection with vertical slits; [108] investigated the RWS connection with an elliptic opening in the web; [109] evaluated the cyclic performance of an eight-story welded moment frame with elliptical-shaped RWS and compared it to the conventional RBS connections; Yu and Li [110] evaluated the steel frames with RWS connections and WFP connections using the probabilistic seismic demand analysis and seismic capability analysis; Lin et al. [111] investigated the behavior of RWS in progressive collapse under critical column removal scenario, the results demonstrated the capability of the mentioned connections in terms of rotational capacity; Erfani et al. [112] studied the lateral load carrying behavior of steel moment resisting frames with reduced web beam sections and propounded an algorithm to select appropriate opening size; Bi et al. [113] scrutinized the castellated beam-to-column connections with four regular hexagonal web openings under cyclic loading with and without floor slab, the results indicated the importance of the space between web openings, and depth-to-thickness ratio of the web. Moreover, due to the limitations imposed on beam span-to-depth ratio in different codes which result in the impossibility of the use of short beams in some of the prequalified rigid connections, Hoseinzadeh Asl and Jahanian [114] investigated using web opening located at the mid-span of the deep steel beams in rigid connections in order to lead the plastic hinge away from the column face.

Utilizing drilled flange moment resisting connections is another approach to overcome the problem of weld brittle failure in the beam-to-column connections which is studied by many researchers and is almost in its early stages [17, 31-34, 115-117], among which the optimum algorithm of drilled holes in order to achieve desired performance of structure is proposed by [34, 116-117]; in this regard, initial suggestion of design algorithm for drilled flange connections as well their behavior evaluation under seismic load was performed by [118]. Evaluation of seismic performance of DF connections was reported by [119], leading to the conclusion that DF connections are capable of exhibiting desired behavior. In their 2019 study, [30] used IDA analysis method in order to investigate the seismic performance of special moment resisting frames, the results revealed that DF connections performed similar to RBS connections in case of low-rise buildings, while in high-rise buildings, DF connections demonstrated a more sought-after behavior with 43% higher seismic capacity. Among recent studies, conducted experimentally or numerically, on DF connections, the investigation of rigid connection of drilled beam to CFT columns with external stiffeners is performed by [120]; Vaidian et al. [121] evaluated the effect of different connections on the behavior of steel moment frames including RBS, DF, and DFCV connections, based on the results, DFCV connections (diamond-shaped holes) performed better than the other DF connections; the assessment of the effect of different connections, DF connections included, on the behavior of steel moment frames is performed by [122]; the results obtained in the research performed by [123] showed that clockwise pattern holes drilled in the beam flange are desirable in terms of flexibility, reduction of bending stresses, and transferring the plastic hinge away from the column face. Moreover, the investigation of the arrangement, type, and number of holes in DF connections was assessed by [124] in which it was concluded that the mentioned parameters are of great significance in the ductility, stress concentration, and preventing the brittle failure of the DF connections; [125] investigated different configurations of connections among which CDF c onnection (with combined circular hole and notches) performed better in terms of damage index, and equivalent plastic strain.

It is well-documented that pre-Northridge connections failed to resist the applied loads despite being in conformance with the existing building codes during earthquakes [10]. The afore-mentioned issue piqued interest among researches to utilize two main approaches in order to enhance the structure safety whether through strengthening the connection [96, 126-128] or weakening a part of the beam [48-125]. In terms of reducing a part of the beam, cutting the beam flange or web reduction has been widely evaluated in recent years [22-24, 56, 67-79, 88, 93-99, 127, 129]. Although comparing the behavior of interior connections with voids in beam web or flange has received numerous attention, there exists a significant ambiguity regarding the behavior of frames with web or flange cuts since cutting a part of the beam alters the force transfer from the beam to the column [95, 129] and parameters affecting the strength of the frame such as opening area, shape, use of stiffeners, etc., are of great significance in the behavior, resistance, energy dissipation capacity, and failure mode of the connections[2, 23-25, 114]. Hence, numerous studies have been conducted on steel connections including Reduced Beam Section (RBS)[64-79], Reduced Web Section (RWS) [80-114], Drilled Flange Connection (DFC) [115-125], and many design codes and standards [1, 10, 18-20, 27-29] employed the introduced connections as an engineered connections. Since each connection has advantages and disadvantage, e.g. limited range of beam and column dimensions in tests, stiffness degradation, loss of moment capacity, and stress concentration are among major downsides of RBS connections; limited guidelines and codes, limited shapes of openings, and loss of strength are among drawbacks of RWS connections, while absence of regulations or design guidelines, and in some cases equal or weaker performance of DF connections compared to RBS ones are considered as weaknesses of DF connections, the present study aims to evaluate the effect of different interior connections on the behavior of steel moment frames. It must be noted that connections are classified from different perspectives e.g. from the behavioral, dissipated energy capacity, modes of failure point of view. However, rotational capacity of the connections is among connection features for which there exists no proper way, and accurate estimation of the mentioned features play a significant role in the structural design of different frames and connections. In the present study, an interior connection is utilized to investigate the behavior of the connection in case of presence of openings in beam web or flange, in this regard, models with openings solely implemented in beam web or flange (RBS, RWS, and DF connections) has been investigated under monotonically increasing lateral displacement conditions with varying connection parameters like length and width of openings, and a fully welded rigid connection is simulated as a reference model. Finally, a comparative analysis is made to understand the performance of different connections under imposed monotonic loading in terms of initial stiffness, rotational capacity, resistance, and stress distribution.

2. Modeling

In order to investigate the performance of interior connection subjected to lateral loading, Finite element models are utilized. The numerical models are categorized into four groups, including the interior connections with fully welded rigid connection, RBS connections, interior connections with opening in beam web, and interior connections with voids in beam flange. The beam-to-column connection is deemed as a welded connection due to its vulnerability to brittle failure.

Since the location of plastic hinge formation is an influential parameter in avoiding the brittle failure of column, the spacing between the location of plastic hinge and the column face is proposed to be at least equal to the half of the beam depth [27].

Table 1 presents the properties of A992 steel, used in FE simulation, which is adopted from the coupon tests done by [130]. The weld material is assumed to have the same properties as steel base material. Stress- strain curves of the adopted A992 steel is illustrated in Fig. 1. Material nonlinearities were accounted for using a multilinear kinematic rate independent hardening rule.

This option uses the Besseling model also called the sublayer or overlay model (Zienkiewicz) to characterize the material behavior [131]. In order to predict the yielding of the material, the Von-Mises yield criterion was used in the current paper.

Table 1
Steel properties

Material		Young modulus (GPa)	Yield point Stress (MPa)	Yield point Strain	Ultimate point Stress (MPa)	Ultimate point Strain
A992 Steel	Flange	203	444	0.0042	577	0.1381
	Web	202	409	0.0148	573	0.1555

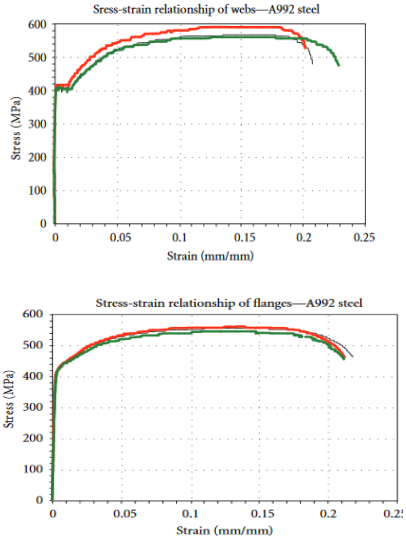

Fig. 1 Stress-strain curves of A992 steel [116]

The software package used to analyze the models was ANSYS; the FE models are comprised of a quadrilateral four-node element with six degrees of freedom per node (three rotations and three translations) which is known as SHELL181 in the ANSYS element library. SHELL181 is suitable for analyzing thin to moderately-thick shell structures [131]. Material plasticity, large deflection, and large strain nonlinearities are of the characteristics of the mentioned element. Furthermore, accurate estimations of displacements and stresses can be provided by shell elements, while according to [132-134], the utilization of the solid elements results in inaccurate prediction of the dissipated energy. Sensitivity mesh analysis was performed in order to optimize the run time, and finer mesh with mesh size 1.5 cm was adopted for critical areas such as connection region and the vicinity of openings while coarser mesh with mesh size 4.5 cm was used for the rest. Geometrical and material nonlinearities were taken into account.

In order to model the interior connection, inflection points are considered at the mid-span as well as mid-height of the column. In this regard, pinned supports is considered at the lower part of the column, besides, roller support condition is applied at the both right and left half-beam ends. The supposed boundary conditions for interior connections are a commonplace assumption which is utilized by many researchers [135-137].

Dimensions of simulated beams and column are deemed constant in all models, in which W36X150 and W14X398 sections are used for beams and column, respectively. The interior joint consists of a 3.65 m column and two beams with half-length of 3.65 m fully welded by fillet-welds to connect the beam and the column, as shown in Fig. 2. The modeled interior connection is extracted from a MRF system which is designed based on the Iranian steel building code and Iranian code "Standard 2800" for seismic resistant design of buildings using the structural analysis software, SAP 2000; in addition; in the afore-mentioned structure, the loading algorithm (the imposed dead load, live load, etc.) is as recommended by design codes (according to Fig. 2). Continuity plates are considered to enhance the column strength as well as transferring the forces from beam to column. Furthermore, doubler plates with thickness of 0.025 m are considered on both sides of panel zone.

In order to investigate the performance of frame, monotonic lateral loading is applied at the tip of the column with steps of 0.002 rad drift ratio. On the other words, the displacement is imposed at the top of the column increasingly until the connection is failed. The loading system is illustrated in Fig. 2. Based on the [29], the capability of the connection to tolerate the inter-story drift ratio of 0.04 rad is required in the seismic-force resisting systems, where the loss of flexural resistance of the connection is not exceeding 0.2 of plastic moment capacity. Consequently, the failure criteria include the weld fracture, local buckling of the beam web, strength loss exceeding 20% of the capacity and plastic strain reaching the ultimate strain of base material.

A parametric study is performed to study the effect of openings on the behavior of interior connections. To do so, an isolated circular opening is considered in RWS models in beam web with 2 influential parameters including the distance of opening from column face and opening diameter. The distance of the opening center from the column face is considered to be 0.87h, 1.3h, and 1.74h. Furthermore, 3 different diameters are considered for opening as well, including 0.5h, 0.65h, and 0.8h in which h is the beam depth. It should be noted that the parameters are taken from the research done by [94]. Similarly, the influential dimensions of DF connections such as L*/D and L/D are considered in accordance with the studies performed by [34, 138], respectively. In the afore-mentioned studies, the parameter L*/D was suggested to be in the range of 3 to 5 and the desired ratio for L/D parameter was taken equal to 2, where L*, L, and D are indicants of the distance between the void and column face, length of opening, and opening diameter, respectively. Accordingly, the L*/D parameter is considered to be 4 in all DF models and L/D is considered to be equal 2 in the HS-40-55-60 model.

Summary and configuration of the studied models are presented in Table 2 and Fig. 3, as well. Also, Fig. 4 indicates the finite element models of different configurations.

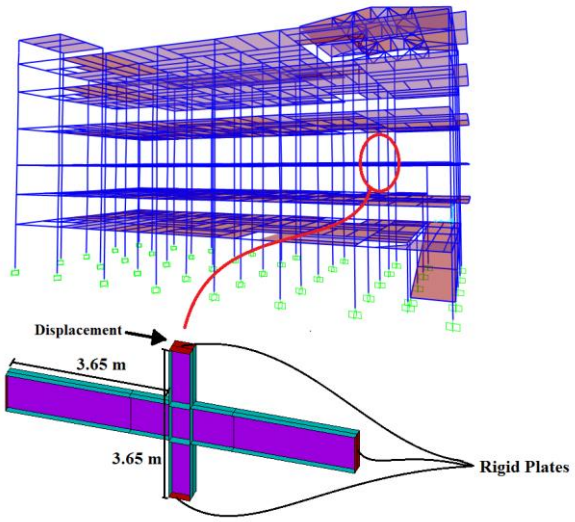

Fig. 2 Location and dimension of studied interior connection

3. Results

Fig. 5 to 7 present the lateral force-story drift curves of studied models. Also, the Von Mises plastic strain distribution of models in 0.04 story drift is illustrated in Fig. 8.

The brittle failure of the beam-to-column connection in ordinary fully welded rigid connection has occurred at 3.6% story drift. However, introduction of appropriate openings in beam web or flange prevents the premature failure of the connection and brings about the plastic hinge initiation in beam web or flange, away from the critical area. Furthermore, according to the results, utilizing the typical RBS connection prevents connection failure and leads to the increased ductility, which is a desirable behavior. The studied RBS connection, designed in accordance with AISC 358-16, fails at 4.2% story drift, as illustrated in Fig. 7, due to steel rupture.

Although RBS connection is capable of fulfilling the expected performance through leading the failure toward the beam which is considered a ductile behavior, it experiences excessive loss of lateral strength as well as initial stiffness. Compared to RBS connections, drilled flange connections are considered a more practical method in terms of beam flange cut. Based on the results, DF category in which openings are implemented in beam flange, models with different width of singular horizontal slot including DF-HS-40, DF-HS-55, and DF-HS-60 experience an early failure due to more than 20% loss of lateral force at early stages of loading. However, no plastic strain was observed in the vicinity of connection. On the other hand, model with 3 different width of horizontal slots, DF-HS-40-55-60, performs better than the

models with similar width of singular horizontal slot, as the story drift of 0.04 rad is reached without connection failure. Based on the Von Mises plastic strain distribution illustrated in Fig. 8, the initiation of plastic hinge has occurred at the opening edge, and the model is perfectly capable of leading the plastic hinge away from the column face.

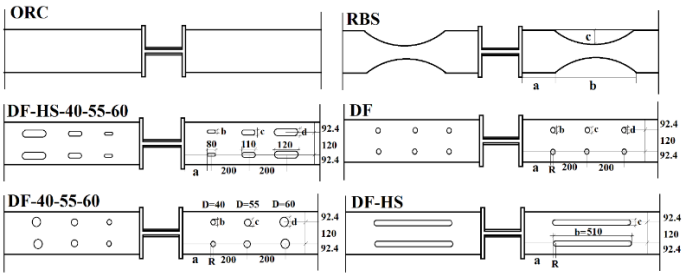

Fig. 3 Configuration of studied models

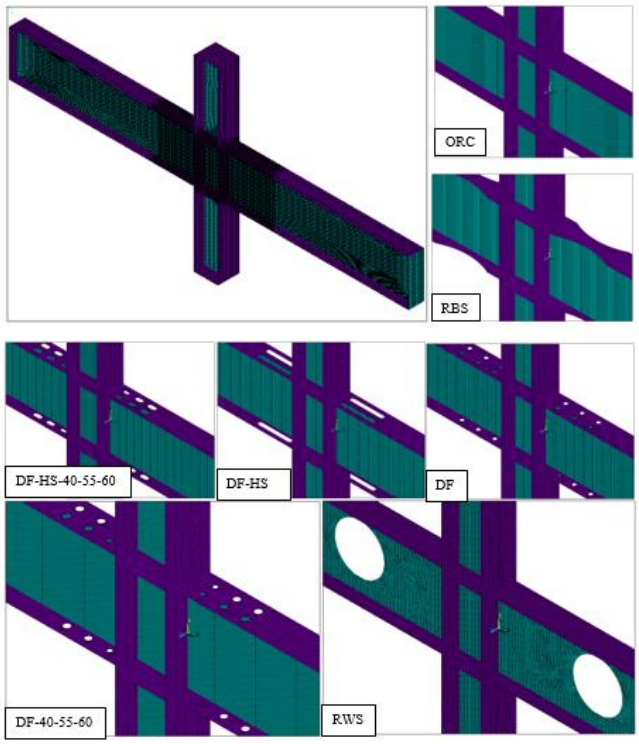

Fig. 4 FE models of different configurations

The initial stiffness of models with 3 circular openings, drilled in 2 rows at beam flange, is higher than the models with singular horizontal opening. The highest initial stiffness and lateral force belongs to the DF-40-40-40 model, in which the connection has experienced weld failure in 0.04 rad story drift. Furthermore, based on the Von Mises plastic strain distribution, the model has failed to move the developed strain away from the connection region. On the other hand, increasing the opening radii leads to the decreased Von-Mises Plastic strain at connection area. However, DF-55-55-55 and DF-60-60-60 models are incapable of reaching 0.04 rad story drift due to steel rupture in opening edges. Use of different opening diameters as indicated in Fig. 5 and Fig. 8 results in a sought-after behavior of interior connection, in which the openings are capable of transmitting the plastic hinge towards the beam length without experiencing beam-to-column connection failure. The lateral force-story drift curve of this model is almost similar to the DF-55-55-55 model with the difference that the DF-40-55-60 model can sustain story drift of 0.044 rad up to its failure. It must be noted that the maximum lateral force of DF-40-55-60 is 7% less than the model DF-40-40-40 which has the highest maximum lateral force amongst the models with opening in beam flange. Yet, DF-40-55-60 has exhibited higher story drift, hence, higher ductility. Furthermore, in terms of initial stiffness, max lateral force, ductility, and the failure drift, interior connections with circular openings consisting of 3 various diameters perform better than the interior connections with 3 horizontal slots having different opening width. Overall, based on the results, model DF-40-55-60 reveals the desired performance amongst the other models, this finding supports previous research into this area by [34].

Also, according to the results, RWS category with singular large opening in beam web is capable of transferring the plastic hinge toward the beam mid-span, provided that the opening radii and the distance between the opening center and column face is selected appropriately. Comparing the developed plastic strain in the beam-to-column critical regions of ORC and RWS models, it is evident that the maximum developed plastic strain as well as highest lateral force has occurred in the model with no opening (ORC). Also, comparing the lateral force-story drift curves of models in terms of the mentioned influential parameters, there was a significant correlation between the ultimate lateral force and the opening radii, indicating that increasing the opening diameter results in the significant decrease of initial stiffness and frame lateral force, as shown in Fig. 6. However, shortening the distance between opening center and the column face causes degradation in lateral force as well as initial stiffness and intensifies the plastic strain in the critical area. Nevertheless, by decreasing the distance of the opening center from the column face, the amount of the lateral force declines slightly. Based on the results, diameters of 0.65h and 0.8h as well as parameter 'a' which is equal to 1.3h and 1.74h can reduce the plastic strain, developed in beam-to-column connection region. Based on the Von Mises plastic strain distribution, appropriate selection of opening size and distance leads to the occurrence of Vierendeel mechanism, hence, increased ductility. The results are in accordance with the [94].

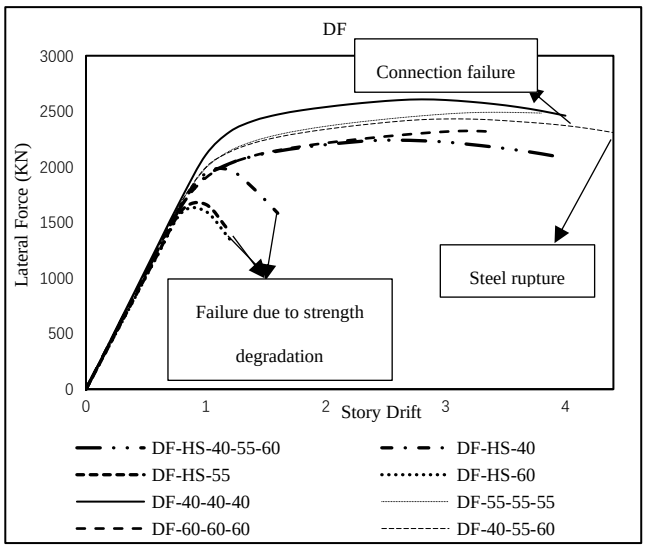

Fig. 5 lateral force-story drift curves of models with opening in beam flange (DF category)

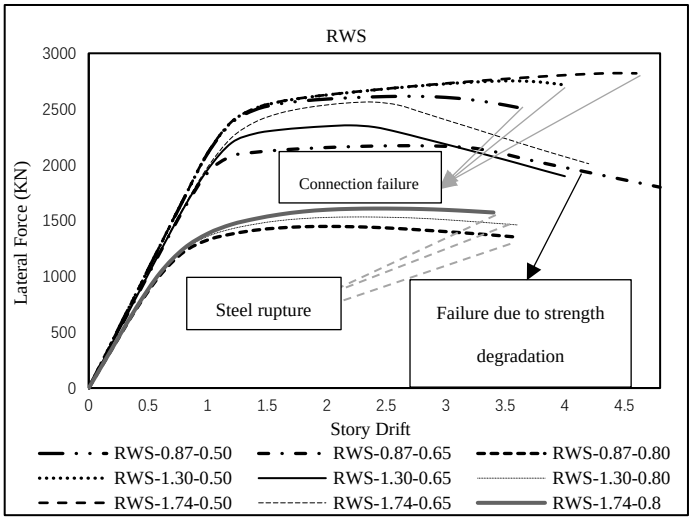

Fig. 6 Lateral forc-story drift curves of models with opening in beam web

4. Discussion

Fig. 7 indicates the lateral force-story drift curves of models in which the story drift of 0.04 rad is reached. Also, the maximum lateral force of interior connections as well as lateral force of frames at 0.04 story drift is presented in Fig. 9 and Fig. 10, respectively. The DF and RWS curves are placed between ORC (reference) and RBS models. Based on the results, the behavior of RWS-1.7-0.5 and RWS-1.3-0.5 models are almost similar to the ORC model, with the difference that RWS-1.7-0.5 and RWS-1.3-0.5 models can withstand story drift up to 4.6% and 4%, respectively. Besides, the degradation of initial stiffness due to introduction of the opening is insignificant in both models and can be neglected. As can be seen in Fig. 8, both models are incapable of transferring the plastic hinge toward the vicinity of the opening, hence, the failure has occurred due to connection fracture. Although initial stiffness of the DF-40-40-40 model is similar to the reference model with a slight difference, the lateral resistance of the model is 12% less than the reference model. This is while, the mentioned model could not satisfy the expected behavior and the failure occurred because of connection fracture. The results show that in case of using DF connections, DF-40-55-60 and DF-HS-40-55-60 models are in accordance with the aim of the connection design in which moving the plastic hinge away from the column face is considered a sough-after behavior. However, DF-40-55-60 performs better than the model with horizontal slots (DF-HS-40-55-60), as the area of the openings in flange is lower than the other model. Furthermore, stress concentration is observed at the edge of openings in flange. Overall, in terms of using DF connections, it is propounded to utilize 2 rows of drilled flange with 3 circular openings in which by shortening the distance of the circular opening from the column face, the diameter of the openings decreases. RWS models including RWS-1.74-0.65, RWS-1.3-0.65, and RWS-0.87-0.65, have experienced local buckling at 2.6, 2.6, and 3.4% drift, consequently, the lateral force-story drift curves of models is projected to decline after occurrence of local buckling. Although shear deformation and Vierendeel mechanism is evident in the mentioned models, according to the Fig. 8, the models are capable of transferring the failure toward the beam, hence, exhibiting desired performance. Furthermore, according to Fig. 9, it is conspicuous that increasing the area of the opening results in decreased lateral load resistance as well as decreased initial stiffness.

As illustrated in Fig. 9, the maximum lateral force of interior connection in RWS-1.74-0.65 is higher than both DF-40-55-60 and DF-HS-40-55-60 models while the maximum area of opening belongs to the mentioned model. In this regard, the lateral force of RWS-1.74-0.65 model at 0.04 story drift is 12% and 0.3% lower than the lateral force of DF-40-55-60 and DF-HS-40-55-60 models at 0.04 story drift. This is because the RWS model has experienced early loss of lateral force which stems from the initiation of local buckling. Accordingly, wise selection of opening sizes in RBS, RWS, and DF connections are of great importance and use of them is dependent on the site condition and implementation considerations as well as design principles.

It must be noted that connections in special moment frames (SMRFs), intermediate moment frames (IMFs), and ordinary moment frames (OMFs) are expected to withstand total rotations of 0.04, 0.03, and 0.02 radian while maintaining 0.03, 0.02, and 0.01 radian plastic rotations, respectively (AISC). The results drawn from the current study is indicant of the fact that RBS, DF-40-55-60, DF-HS-40-55-60, DF-40-40-40, RWS-1.30-0.50, RWS-1.30-0.65, RWS-1.74-0.50, RWS-1.74-0.65, and RWS-0.87-0.65 connections are capable of retaining their strength till story drift angle of 0.04 rad and higher, and are capable of being utilized in the SMRF connections, while ordinary fully welded rigid connections, DF-HS connections, and rest of the studied connections experience early failure due to lateral resistance degradation, steel rupture, or brittle failure at early stages, moreover, from the perspective of initial stiffness, the initial stiffness of DF-HS connections are less than the other studied DF connections, the maximum initial stiffness is for the DF-40-40-40 model, which has the least opening are in flange. Among RWS connections, the highest initial stiffness belongs to the model with minimum opening area.

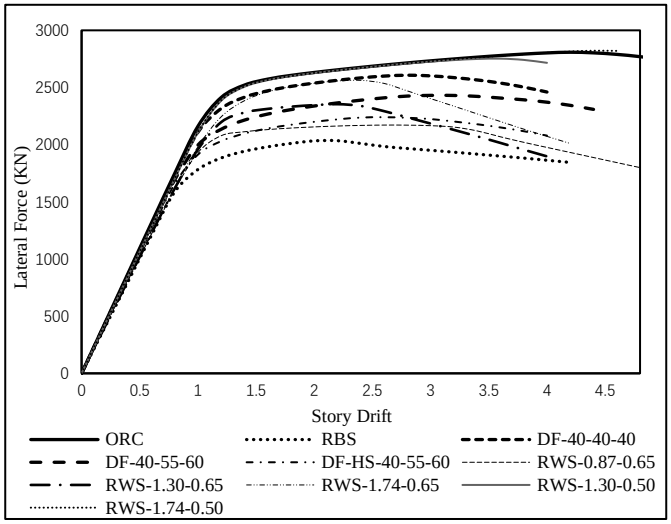

Fig. 7 Comparison of lateral force-story drift curves of DF, RWS, and RBS category with the ORC (reference) model

From the ease of construction point of view, DF connections are considered more practical than RBS ones. the utilization of RWS connections are recommended where there is a need to provide pipelines, or ducts, etc., functionally. However, in case of wise selection of the opening sizes implemented in beam web or flange, DF and RWS connections can be sough-after substitutes for connections in SMRF systems.

Overall, the afore-mentioned connections correspond well with the expected rotational capacity of the SMRFs, OMFs, and IMFs. Nevertheless, few connections are available that have significantly larger rotation capacity as well as capability of leading the plastic hinge away from the column face and are suggested to be used in special moment frames among which DF-40-55-60 connections (DF connection with different opening diameters in flange), RWS connections with diameters of 0.65h and 0.8h, and a parameter of 1.3h, and 1.74 h are suggested to be used in SMRF systems

5. Conclusions

There is a considerable amount of literature on intentionally attenuating a part of the beam whether in beam flange or web to relocate the plastic hinge away from the column face. Thus, this paper questions the behavior of interior connections with openings in beam web or flange subjected to monotonic loading through numerical simulation. The studied models are comprised of an ordinary fully welded rigid connection as a reference model, a model with prevalent RBS cut according to AISC 358-16, models with different configurations of flange cut (DF) as well as the models with singular opening in beam web (RWS). The obtained results are as follows:

The premature failure of the beam-to-column connection in ordinary fully welded rigid connections has led to intentional wakening of the beam as an approach to overcome the mentioned issue. Based on the numerical results, ordinary rigid connection experiences connection failure at 3.6% story drift while the prevalent RBS connection is capable of transferring the plastic hinge toward the beam length, hence, increasing the ductility, which is a sough-after performance. It should be noted that the failure drift of RBS connection due to steel rupture has occurred in 4.2% story drift. In other words, utilizing RBS connections in moment steel frames lead to an increase of 0.6% in story drift, in addition, the location of initiation of plastic hinge instead of column face (in ORC model) is led toward the beam length (reduced are) in RBS connections.

Although RBS connection is capable of fulfilling the expected performance through leading the failure toward the beam which is a ductile behavior, it experiences excessive loss of lateral strength as well as initial stiffness which is calculated to be approximately 27% and 8%, respectively, compared to the ORC model. Compared to RBS connections, drilled flange connections are easier to construct, hence, a more practical method in terms of beam flange cut. Based on the results, utilizing singular horizontal slot with different opening width in beam flange in 2 rows does not lead to the expected outcome and models experience an early failure due to loss of strength and the failure drift is less than 2% story drift due to excessive loss of lateral force which is considered to be 20%. However, model with 3 horizontal slots, having different opening width, results in the desired performance in which the failure from beam-to-column connection region has been transferred towards the beam length, in other words, the model is fully capable of transferring the plastic hinge away from the column face, the failure drift is 4% story drift due to steel rupture around the opening edges.

The initial stiffness and maximum lateral force of circular openings in beam flange is higher than the models with elongated circular opening since the opening area is smaller, e.g. 5% and 32% degradation is observed in stiffness and maximum lateral force of model with elongated circular opening in which the opening diameter is 60 mm compared to the model with circular holes of 60 mm diameter. The same conclusion can be drawn for models with different diameters of openings, since increasing the diameter of drilled holes leads to the decease of both initial stiffness and lateral force in a way that the loss of stiffness and lateral force in the model with opening diameter of 60 mm compared to the model with opening diameter of 40 mm is estimated to be 3% and 6%, approximately. Nevertheless, models with circular openings experience increased Von Mises plastic strain distribution in beam-to-column regions.

However, the use of openings with different diameters brings about an increase in frame ductility as well as transferring the plastic hinge away from the critical region, hence, sough-after substitute for identical opening diameters. In the afore-mentioned model, the failure drift is 4.4% which is the highest experienced drift among models with drilled flange. In addition, the stiffness and lateral force degradation, which is respectively 1.5% and 7%, is negligible compared to the model with 3 drilled holes of 40 mm, yet, the failure in model with 3 different opening diameters is due to steel rupture, while connection fracture is the cause of failure in model with 3 opening having the same diameters.

RWS connections, which consist of circular opening in beam web, fulfill the condition of moving the plastic hinge away from the column face in case of proper selection of opening size and location. Although increasing the opening radii leads to the reduced plastic strain in beam-to-column connection region, it significantly reduces the lateral force and stiffness of the frame. Furthermore, moving the opening away from the column face results in desired performance of the frame in terms of maximum lateral force and initial stiffness, accordingly, it is concluded that the model with opening diameter of 0.8 beam height in which the distance between the column face and opening center is considered to be 0.87 beam height has the lowest values in terms of initial stiffness and lateral force whereas the highest amounts of initial stiffness and lateral force belongs to the model with opening diameter 0.5 times the beam height in which the opening center distance from the column face is considered to be 1.74 times the opening height, the difference of the amount of initial stiffness and lateral force between the mentioned models is respectively considered to be 17% and approximately 50%. Despite the fact that the model with minimum opening radii in conjunction with the maximum opening distance from the column face is expected to have the desired performance in terms of initial stiffness and lateral resistance, the model might be incapable of transferring the plastic hinge away from the column face due to insufficient weakening of beam web. It is concluded that shear deformation and local buckling is observed in RWS connections while in DF connections, stress concentration around the opening is critical.

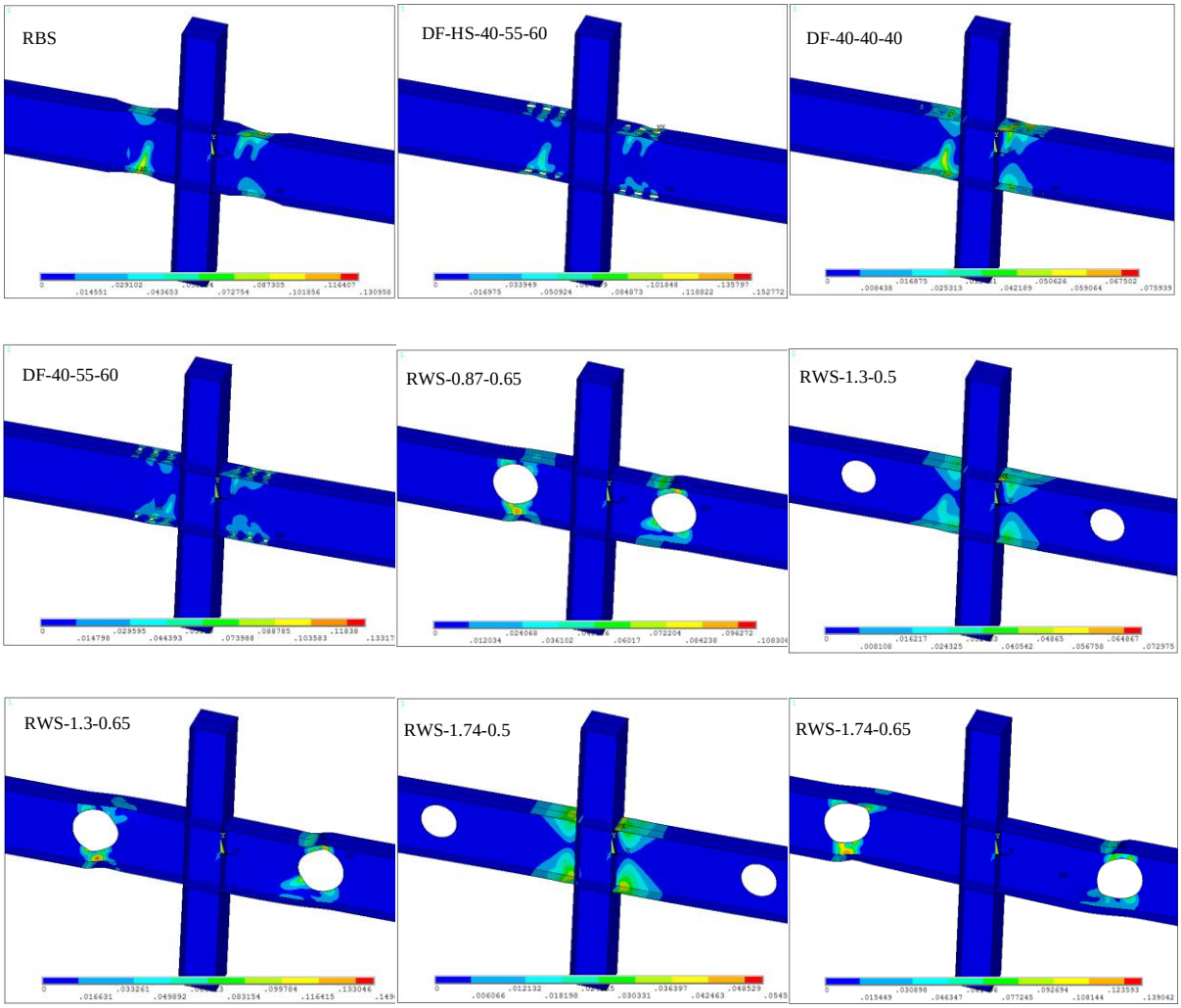

Fig. 8 Von Mises plastic strain distribution of FE models at 0.04 story drift

Table 2
specification of studied models

Category	Model	a (mm)	b (mm)	c (mm)	d (mm)	Description
ORC	ORC	-	-	-	-	Ordinary fully welded rigid connection
RBS	RBS	225	680	75	-	Prevalent reduced beam flange according to AISC 358-16
DF	DF-HS-40-55-60	160	40	55	60	3 horizontal slots with L/D=2 and different opening diameter
	DF-HS-40	160	510	40	-	Single horizontal slot with L=510 mm and D=40 mm
	DF-HS-55	220	510	55	-	Single horizontal slot with L=510 mm and D=55 mm
	DF-HS=60	240	510	60	-	Single horizontal slot with L=510 mm and D=60 mm
	DF-40-40-40	160	40	40	40	3 circular voids with similar diameters of 40 mm
	DF-55-55-55	220	55	55	55	3 circular voids with similar diameters of 55 mm
	DF-60-60-60	240	60	60	60	3 circular voids with similar diameters of 60 mm
	DF-40-55-60	160	40	55	60	3 circular voids with diameters of 40, 55, and 60 mm
RWS	RWS-0.87-0.50	793.	455	-	-	Circular opening at beam web with various a and b parameter
	RWS-0.87-0.65	793.	592	-	-	
	RWS-0.87-0.80	793.	729	-	-	
	RWS-1.30-0.50	1185	455	-	-	
	RWS-1.30-0.65	1185	592	-	-	
	RWS-1.30-0.80	1185	729	-	-	
	RWS-1.74-0.50	1585	455	-	-	
	RWS-1.74-0.65	1585	592	-	-	
	RWS-1.74-0.80	1585	729	-	-	

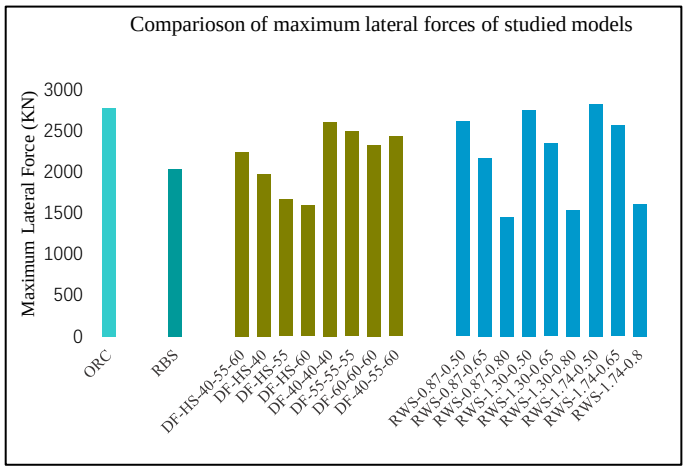

Fig. 9 Comparison of maximum lateral forces of studied models

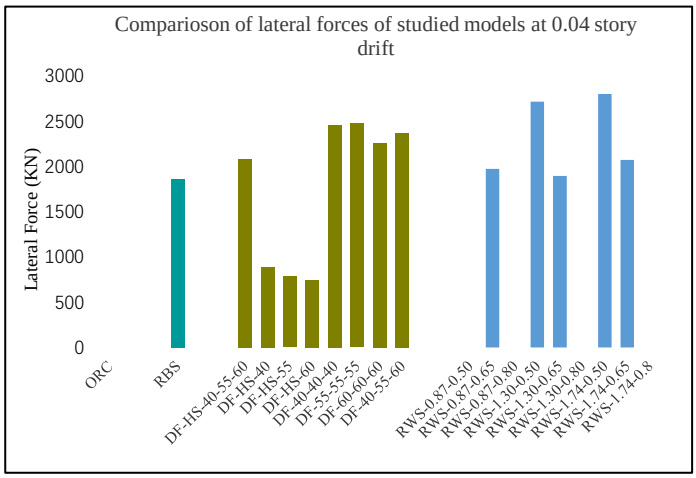

Fig. 10 Comparison of lateral forces of studied models at 0.04 rad story drift

References

[1] AISC 358 (2016), Prequalified Connections for Special and Intermediate Steel Moment Frames for Seismic Applications, American Institute of Steel Construction; Chicago, Illinois, USA.

[2] Ohsaki, M., H. Tagawa, and P. Pan. "Shape optimization of reduced beam section under cyclic loads." Journal of Constructional Steel Research 65, no. 7 (2009): 1511-1519.

[3] Pachoumis, D. T., E. G. Galoussis, C. N. Kalfas, and A. D. Christitsas. "Reduced beam section moment connections subjected to cyclic loading: Experimental analysis and FEM simulation." Engineering Structures 31, no. 1 (2009): 216-223.

[4] Pachoumis, D. T., E. G. Galoussis, C. N. Kalfas, and I. Z. Efthimiou. "Cyclic performance of steel moment-resisting connections with reduced beam sections—experimental analysis and finite element model simulation." Engineering Structures 32, no. 9 (2010): 2683-2692.

[5] Bartley, Tony C., and Janice J. Chambers. "State-of-the-art analysis of frames with reduced beam section connections." In Structures Congress 2008: Crossing Borders, pp. 1-10. 2008.

[6] Shen, Jie-Hua Jay, A. Astaneh-Asl, and D. B. McCallen. "Use of deep columns in special steel moment frames." Steel Tip Rep 24 (2002).

[7] Zhang, Xiaofeng, and James M. Ricles. "Experimental evaluation of reduced beam section connections to deep columns." Journal of Structural Engineering 132, no. 3 (2006a): 346-357.

[8] Zhang, Xiaofeng, and James M. Ricles. "Seismic behavior of reduced beam section moment connections to deep columns." Journal of structural engineering 132, no. 3 (2006b): 358-367.

[9] Chen, Sheng-Jin, and Y. C. Chao. "Effect of composite action on seismic performance of steel moment connections with reduced beam sections." Journal of Constructional Steel Research 57, no. 4 (2001): 417-434.

[10] FEMA-355D. State of the art report on connection performance. Washington (DC): Federal Emergency Management Agency; 2000.

[11] Carter, Charles J., and Nestor R. Iwankiw. "Improved ductility in seismic steel moment frames with dogbone connections." Journal of Constructional Steel Research 1, no. 46 (1998): 448.

[12] Chen, Sheng-Jin, C. H. Yeh, and J. M. Chu. "Ductile steel beam-to-column connections for seismic resistance." Journal of Structural Engineering 122, no. 11 (1996): 1292-1299.

[13] IwankiW, NeStor. "Ultimate strength considerations for seismic design of the reduced beam section (internal plastic hinge)." Engineering Jouranal 1 (1997): quarter.

[14] Chi, Brandon, Chia-Ming Uang, and Albert Chen. "Seismic rehabilitation of pre-Northridge steel moment connections: A case study." Journal of Constructional Steel Research 62, no. 8 (2006): 783-792.

[15] Deylami, A., and A. Moslehi Tabar. "Promotion of cyclic behavior of reduced beam section connections restraining beam web to local buckling." Thin-Walled Structures 73 (2013): 112-120.

[16] Tahamouli Roudsari, M., H. Jamshidi K, and M. Mohebi Zangeneh. "Experimental and numerical investigation of IPE reduced beam sections with diagonal web stiffeners." Journal of Earthquake Engineering 22, no. 4 (2018): 533-552.

[17] TahamouliRoudsari, M., and M. Torkaman. "Experimental and numerical investigations of rigid IPE beam connections with drilled flange and web stiffener." In Structures, vol. 16, pp. 303-316. Elsevier, 2018.

[18] ASCE 23-97. Specifications for Structural Steel Beams with Web Openings. American Society of Civil Engineers 1999 / 30 pp.

[19] Lucas, Warren K., and David Darwin. Steel and composite beams with web openings. University of Kansas Center for Research, Inc., 1990.

[20] Lawson, R. M., and S. J. Hicks. Design of composite beams with large web openings: in accordance with Eurocodes and the UK National Annexes. Steel Construction Institute, 2011.

[21] Hedayat, Amir A., and Murude Celikag. "Post-Northridge connection with modified beam end configuration to enhance strength and ductility." Journal of Constructional Steel Research 65, no. 7 (2009): 1413-1430.

[22] Chung, K. F., T. C. H. Liu, and A. C. H. Ko. "Investigation on Vierendeel mechanism in steel beams with circular web openings." Journal of Constructional Steel Research 57, no. 5 (2001): 467-490.
[23] Liu, T. C. H., and K. F. Chung. "Steel beams with large web openings of various shapes and sizes: finite element investigation." Journal of constructional steel research 59, no. 9 (2003): 1159-1176.
[24] Tsavdaridis, Konstantinos Daniel, and Cedric D'Mello. "Vierendeel bending study of perforated steel beams with various novel web opening shapes through nonlinear finite-element analyses." Journal of Structural Engineering 138, no. 10 (2012a): 1214-1230.
[25] Tsavdaridis, Konstantinos Daniel, and Cedric D'Mello. "Optimisation of novel elliptically-based web opening shapes of perforated steel beams." Journal of Constructional Steel Research 76 (2012b): 39-53.
[26] De'nan, Fatimah, Hazwani Hasan, Duaa Khaled Nassir, Mohd Hanim Osman, and Sariffuddin Saad. "Finite element analysis for torsion behavior of flat web profile beam steel section with opening." Procedia Engineering 125 (2015): 1129-1134.
[27] FEMA-350. Recommended seismic design criteria for new steel moment-frame buildings. Washington (DC): Federal Emergency Management Agency; 2000.
[28] FEMA P-750. Council, B. S. S. (2009). NEHRP recommended seismic provisions for new buildings and other structures, 2009 edition. Federal Emergency Management Agency, Washington, DC.
[29] AISC 341 (2016), Seismic Provisions for Structural Steel Buildings, American Institute of Steel Construction; Chicago, Illinois, USA.
[30] Maleki, Mehdi, Roohollah Ahmady Jazany, and Mohammad Soheil Ghobadi. "Seismic fragility assessment of SMRFs with drilled flange connections using ground motion variability." KSCE Journal of Civil Engineering 23, no. 4 (2019): 1733-1746.
[31] Farrokhi, Hooman, F. Danesh, and Sassan Eshghi. "A modified moment resisting connection for ductile steel frames (Numerical and experimental investigation)." Journal of Constructional Steel Research 65, no. 10-11 (2009): 2040-2049.
[32] Vetr, M., M. Miri, and A. Haddad. "Seismic behavior of a new reduced beam section connection by drilled holes arrangement (RBS_DHA) on the beam flanges through experimental studies." In 15th world conference of earthquake engineering (15WCEE), Lisbon, Portugal. 2012.
[33] Vetr, M., and A. Haddad. "Study of drilled flange connection in moment resisting frames." In Report No. 3732. International Institute of Earthquake Engineering and Seismology Tehran; Iran, 2010.
[34] Atashzaban, Ardavan, Iman Hajirasouliha, Roohollah Ahmady Jazany, and Mohsen Izadinia. "Optimum drilled flange moment resisting connections for seismic regions." Journal of Constructional Steel Research 112 (2015): 325-338.
[35] Bojórquez, E., López-Barraza, A., Reyes-Salazar, A., Ruiz, S. E., Ruiz-García, J., Formisano, A., ... & Bojórquez, J. Improving the structural reliability of steel frames using posttensioned connections. Advances in Civil Engineering, 2019.
[36] Qu, W., Zhao, E., & Zhou, Q. Refined analysis of fatigue crack initiation life of beam-to-column welded connections of steel frame under strong earthquake. Shock and Vibration, (2017).
[37] Faridmehr, I., Tahir, M. M., Lahmer, T., & Osman, M. H. Seismic performance of steel frames with semirigid connections. Journal of Engineering, (2017).
[38] Yan, Shen, Kim JR Rasmussen, Lu-li Jiang, Chen Zhu, and Hao Zhang. "Experimental evaluation of the full-range behaviour of steel beam-to-column connections." *Advanced Steel Construction* 16, no. 1 (2020): 77-84.
[39] da Silva, Luís Simões, Sara Oliveira, Ricardo Costa, and Filippo Gentili. "DESIGN AND ANALYSIS OF STEEL STRUCTURES CONSIDERING THE 3D BEHAVIOUR OF THE JOINTS." *ADVANCED STEEL CONSTRUCTION* 16, no. 2 (2020): 137-145.
[40] Zhang, Yan-xia, Quan-gang Li, Wei-zhen Huang, Kun Jiang, and Yu Sun. "Behavior of prefabricated beam-column connection with short strands in self-centering steel frame." *Advanced Steel Construction* 15, no. 2 (2019): 203-214.
[41] Ding, Chenting, Xuebei Pan, Yu Bai, and Gang Shi. "Prefabricated connection for steel beam and concrete-filled steel tube column." *Journal of Constructional Steel Research* 162 (2019): 105751.
[42] Zhang, Ai-Lin, Guang-Hao Shangguan, Yan-Xia Zhang, Qing-Bo Wang, and Wen-Chao Cai. "Experimental study of resilient prefabricated steel frame with all-bolted beam-to-column connections." *ADVANCED STEEL CONSTRUCTION* 16, no. 3 (2020): 255-271.
[43] Gholami, M., M. Tehranizadeh, and A. Deylami. "Evaluation of welded flange plate connections between steel beams and box columns." *Advanced Steel Construction* 9, no. 1 (2013): 59-76.
[44] Xue, Su-duo, Si-yao Li, Xiong-yan Li, and Chen Yao. "BEHAVIOUR AND MATHEMATICAL MODEL FOR SEMI-RIGID THREADED-SLEEVE CONNECTION." *ADVANCED STEEL CONSTRUCTION* 15, no. 2 (2019): 123-128.
[45] Liu, Hong-bo, Ying-jie Zhang, Lan Wang, and Zhi-hua Chen. "Mechanical performance of welded hollow spherical joints at elevated temperatures." *Advanced Steel Construction* 16, no. 1 (2020): 1-12.
[46] Ma, Rong-Quan, Ping-Yu Zhao, Hui-Yong Ban, Yuan-Qing Wang, Yu-Zheng Zhao, and Cheng-Bo Peng. "BEHAVIOUR OF REINFORCED JOINTS BETWEEN STEEL BEAM AND L-SHAPED WIDE LIMB COMPOSITE COLUMN." *BEHAVIOUR* 17, no. 1 (2021): 66-72.
[47] Meng, Bao, Liang-De Li, Wei-Hui Zhong, Ji-Ping Hao, and Zheng Tan. "ENHANCING COLLAPSE-RESISTANCE OF STEEL FRAME JOINTS BASED ON FOLDED AXILLARY PLATES." *ADVANCED STEEL CONSTRUCTION* 17, no. 1 (2021): 84-94.
[48] Engelhardt, Michael D., Ted Winneberger, Andrew J. Zekany, and Timothy J. Potyraj. "Experimental investigation of dogbone moment connections." (1998).
[49] Plumier, Andre. "The dogbone: back to the future." Engineering Journal-American Institute of Steel Construction 34 (1997): 61-67.
[50] Engelhardt, Michael D., G. Fry, S. Jones, M. Venti, and S. Holliday. "Behavior and design of radius cut reduced beam section connections." Rep. No. SAC/BD-00 17 (2000).
[51] Jones, Scott L., Gary T. Fry, and Michael D. Engelhardt. "Experimental evaluation of cyclically loaded reduced beam section moment connections." Journal of Structural Engineering 128, no. 4 (2002): 441-451.
[52] Zhang, Xiaofeng, James M. Ricles, Le-Wu Lu, and John W. Fisher. "Development of seismic guidelines for deep-column steel moment connections." (2004).
[53] Chen, Cheng-Chih, Chun-Chou Lin, and Chieh-Hsiang Lin. "Ductile moment connections used in steel column-tree moment-resisting frames." Journal of Constructional Steel Research 62, no. 8 (2006): 793-801.
[54] Oh, Sang-Hoon, Young-Ju Kim, and Tae-Sup Moon. "Cyclic performance of existing moment connections in steel retrofitted with a reduced beam section and bottom flange reinforcements." Canadian journal of civil engineering 34, no. 2 (2007): 199-209.
[55] Zhang, Xiaofeng, and James M. Ricles. "Seismic behavior of reduced beam section moment connections to deep columns." Journal of structural engineering 132, no. 3 (2006): 358-367.
[56] Soliman, Amr A., Omar A. Ibrahim, and Abdelaziz M. Ibrahim. "Effect of panel zone strength ratio on reduced beam section steel moment frame connections." Alexandria engineering journal 57, no. 4 (2018): 3523-3533.
[57] Morshedi, Mohamad A., Kiarash M. Dolatshahi, and Shervin Maleki. "Double reduced beam section connection." Journal of Constructional Steel Research 138 (2017): 283-297.
[58] Plumier, Andre. "New idea for safe structures in seismic zones." In IABSE Symposium-Mixed Structures Including New Materials. 1990.
[59] Iwankiw, N. R., and J. Mohammadi. "Elastic in-plane stiffness for a circular cut reduced beam section (RBS)." ENGINEERING JOURNAL-AMERICAN INSTITUTE OF STEEL CONSTRUCTION INC 41, no. 1 (2004): 23-36.
[60] Jin, Jun, and Sherif El-Tawil. "Seismic performance of steel frames with reduced beam section connections." Journal of Constructional Steel Research 61, no. 4 (2005): 453-471.
[61] Chen, Sheng-Jin, and Chin-Te Tu. "Experimental study of jumbo size reduced beam section connections using high-strength steel." Journal of Structural Engineering 130, no. 4 (2004): 582-587.
[62] Tremblay, Robert, and André Filiatrault. "Seismic performance of steel moment resisting frames retrofitted with a locally reduced beam section connection." Canadian Journal of Civil Engineering 24, no. 1 (1997): 78-89.
[63] Engelhardt, Michael D., and Thomas A. Sabol. "Reinforcing of steel moment connections with cover plates: benefits and limitations." Engineering structures 20, no. 4-6 (1998): 510-520.
[64] Yu, Qi-Song Kent, and Chia-Ming Uang. "Effects of near-fault loading and lateral bracing on the behavior of RBS moment connections." Steel and Composite Structures 1, no. 1 (2001): 145-158.
[65] Uang, Chia-Ming, Qi-Song "Kent Yu, Shane Noel, and John Gross. "Cyclic testing of steel moment connections rehabilitated with RBS or welded haunch." Journal of Structural Engineering 126, no. 1 (2000): 57-68.
[66] Lee, Cheol-Ho. "Seismic design of rib-reinforced steel moment connections based on equivalent strut model." Journal of Structural Engineering 128, no. 9 (2002): 1121-1129.
[67] Ghaderi, Mohsen, Mohsen Gerami, and Reza Vahdani. "A comparison of seismic low cycle fatigue and extremely low cycle fatigue on steel moment frames with reduced beam section connection (RBS)." International Journal of Fatigue 119 (2019): 139-149.
[68] Hong, Jong-Kook. "Sloped RBS moment connections at roof floor subjected to cyclic loading: Analytical investigation." International Journal of Steel Structures 19, no. 1 (2019): 329-339.
[69] Fanaie, Nader, Shervin Safaei Faegh, and Fatemeh Partovi. "An improved and innovative formulation for calculating amplified elastic story drift induced by RBS connections in steel moment frames." Journal of Constructional Steel Research 160 (2019): 510-527.
[70] Lee, Cheol-Ho, Jong-Hyun Jung, and Sung-Yong Kim. "Cyclic seismic performance of weak-axis RBS welded steel moment connections." International Journal of Steel Structures 19, no. 5 (2019): 1592-1604.
[71] Sofias, C. E., and D. T. Pachoumis. "Assessment of reduced beam section (RBS) moment connections subjected to cyclic loading." Journal of Constructional Steel Research 171 (2020): 106151.
[72] Di Benedetto, Sabatino, Antonella Bianca Francavilla, Massimo Latour, Giovanni Ferrante Cavallaro, Vincenzo Piluso, and Gianvittorio Rizzano. "Pseudo-dynamic testing of a full-scale two-storey steel building with RBS connections." Engineering Structures 212 (2020): 110494.
[74] Hamed, Arash Akbari, and Mohammad Charkhtab Basim. "Experimental-numerical study on weakened HSS-to-HSS connections using HBS and RBS approaches." In Structures, vol. 28, pp. 1449-1465. Elsevier, 2020.
[74] Parvari, Ali, S. Mehdi Zahrai, S. Mohammad Mirhosseini, and Ehsanollah Zeighami. "Comparing cyclic behaviour of RBS, DFC and proposed rigid connections in a steel moment frame with CFT column." Australian Journal of Civil Engineering (2020): 1-20.
[75] Lee, Sang-Yun, Sam-Young Noh, and Young-Soo Na. "Comparison of Progressive Collapse Resistance of Steel Moment Frame Systems with WUF-B verse RBS Connection Details." Journal of the Architectural Institute of Korea 36, no. 9 (2020): 145-156.
[76] Vajdian, Mehdi, S. Mehdi Zahraei, S. Mohammad Mirhosseini, and Ehsanollah Zeighami. "Investigation of Seismic Performance of (RBS) and Drilled Flange Connection (DFC) Containing rhombus Shaped Hole in Steel Moment Frames." Australian Journal of Civil Engineering 18, no. 2 (2020): 246-262.
[77] Meng, Bao, Weihui Zhong, Jiping Hao, and Xiaoyan Song. "Improving anti-collapse performance of steel frame with RBS connection." Journal of Constructional Steel Research 170 (2020): 106119.
[78] Shariati, Mahdi, Mostafa Ghorbani, Morteza Naghipour, Nasrollah Alinejad, and Ali Toghroli. "The effect of RBS connection on energy absorption in tall buildings with braced tube frame system." Steel and Composite Structures 34, no. 3 (2020): 393-407.
[79] Nia, Majid Mohammadi, and Saber Moradi. "Effects of design factors on the cyclic response of sloped RBS moment connections." Engineering Structures 207 (2020): 110228.
[80] Tippe, S. P., & Kulkarni, P. M. "Finite element analysis of perforated beam–column connections." International Research Journal of Engineering and Technology, (2018): 5(1), 477-481.
[81] Tsavdaridis, Konstantinos Daniel, Christopher Pilbin, and Chun Kit Lau. "FE parametric study of RWS/WUF-B moment connections with elliptically-based beam web openings under monotonic and cyclic loading." International Journal of Steel Structures 17, no. 2 (2017): 677-694.
[82] Shin, Myoungsu, Seung-Pil Kim, Arne Halterman, and Mark Aschheim. "Seismic toughness and failure mechanisms of reduced web-section beams: Phase 1 tests." Engineering Structures 141 (2017a): 198-216.
[83] Shin, Myoungsu, Seung-Pil Kim, Arne Halterman, and Mark Aschheim. "Seismic toughness and failure mechanisms of reduced web-section beams: Phase 2 tests." Engineering Structures 141 (2017b): 607-623.
[94] Najafi, M., and Y. C. Wang. "Behaviour and design of steel members with web openings under combined bending, shear and compression." Journal of Constructional Steel Research 128 (2017): 579-600.
[85] Momenzadeh, Seyedbabak, Mohammad Taghi Kazemi, and Masoud Hoseinzadeh Asl. "Seismic performance of reduced web section moment connections." International Journal of Steel Structures 17, no. 2 (2017): 413-425.
[86] Morkhade, Samadhan G., and Laxmikant M. Gupta. "Experimental investigation for failure analysis of steel beams with web openings." Steel and Composite Structures 23, no. 6 (2017): 647-656.
[87] Kumar, SR Satish, and DV Prasada Rao. "RHS beam-to-column connection with web

opening—experimental study and finite element modelling." Journal of Constructional Steel Research 62, no. 8 (2006): 739-746.
[88] Yang, Qingshan, Bo Li, and Na Yang. "Aseismic behaviors of steel moment resisting frames with opening in beam web." Journal of Constructional Steel Research 65, no. 6 (2009): 1323-1336.
[89] Ju, Young K., Do-Hyun Kim, and Sang-Dae Kim. "Experimental assessment of the shear strength of an asymmetric steel composite beam with web openings." Canadian Journal of Civil Engineering 32, no. 2 (2005): 314-328.
[90] Naimi, Sepanta, Murude Celikag, and Amir A. Hedayat. "Ductility enhancement of post-Northridge connections by multilongitudinal voids in the beam web." The Scientific World Journal 2013 (2013).
[91] Morkhade, Samadhan G., and Laxmikant M. Gupta. "Analysis of steel I-beams with rectangular web openings: experimental and finite element investigation." Engineering Structures and Technologies 7, no. 1 (2015): 13-23.
[92] Morkhade, Samadhan G., and L. M. Gupta. "Ultimate load behaviour of steel beams with web openings." Australian Journal of Structural Engineering 20, no. 2 (2019): 124-133.
[93] Tsavdaridis, Konstantinos Daniel, and Cedric D'Mello. "Web buckling study of the behaviour and strength of perforated steel beams with different novel web opening shapes." Journal of Constructional Steel Research 67, no. 10 (2011): 1605-1620.
[94] Tsavdaridis, Konstantinos Daniel, Faezeh Faghih, and Nikolaos Nikitas. "Assessment of perforated steel beam-to-column connections subjected to cyclic loading." Journal of Earthquake Engineering 18, no. 8 (2014): 1302-1325.
[95] Tsavdaridis, Konstantinos Daniel, and Theodore Papadopoulos. "A FE parametric study of RWS beam-to-column bolted connections with cellular beams." Journal of Constructional Steel Research 116 (2016): 92-113.
[96] Shanmugam, N. E., V. T. Lian, and V. Thevendran. "Finite element modelling of plate girders with web openings." Thin-Walled Structures 40, no. 5 (2002): 443-464.
[97] Kazemi, M. T., and S. Erfani. "Analytical study of special girder moment frames using a mixed shear–flexural link element." Canadian Journal of Civil Engineering 34, no. 9 (2007): 1119-1130.
[98] Kıymaz, Güven, Erdal Coşkun, and Edip Seçkin. "Transverse load carrying capacity of sinusoidally corrugated steel webs with web openings." (2010).
[99] Bayramoglu, Guliz. "Reliability analysis of tested steel I-beams with web openings." Structural Engineering and Mechanics 41, no. 5 (2012): 575-589.
[100] Erfani, Saeed, and Vahid Akrami. "Increasing seismic energy dissipation of steel moment frames using reduced web section (RWS) connection." Journal of Earthquake Engineering 21, no. 7 (2017): 1090-1112.
[101] Erfani, Saeed, Ata Babazadeh Naseri, and Vahid Akrami. "The beneficial effects of beam web opening in seismic behavior of steel moment frames." Steel and Composite Structures 13, no. 1 (2012): 35-46.
[102] Boushehri, Kavoos, Konstantinos Daniel Tsavdaridis, and Gaochuang Cai. "Seismic behaviour of RWS moment connections to deep columns with European sections." Journal of Constructional Steel Research 161 (2019): 416-435.
[103] Goel, Subhash C., and Ahmad M. Itani. "Seismic behavior of open-web truss-moment frames." Journal of Structural Engineering 120, no. 6 (1994): 1763-1780.
[104] Elilarasi, K., S. Kasthuri, and B. Janarthanan. "EFFECT OF CIRCULAR OPENINGS ON WEB CRIPPLING OF UNLIPPED CHANNEL SECTIONS UNDER END-TWO-FLANGE LOAD CASE." *ADVANCED STEEL CONSTRUCTION* 16, no. 4 (2020): 310-320.
[105] Goel, Subhash C., and Ahmad M. Itani. "Seismic-resistant special truss-moment frames." Journal of Structural Engineering 120, no. 6 (1994): 1781-1797.
[106] Naughton, Daniel Tomas, Konstantinos Daniel Tsavdaridis, Chrysanthos Maraveas, and Andreas Nicolaou. "Pushover analysis of steel seismic resistant Frames with reduced Web section and reduced Beam section connections." Frontiers in Built Environment 3 (2017): 59.
[107] Nazaralizadeh, Hamidreza, Hamid Ronagh, Parham Memarzadeh, and Farhad Behnamfar. "Cyclic performance of bolted end-plate RWS connection with vertical-slits." Journal of Constructional Steel Research 173 (2020): 106236.
[108] Davarpanah, Mohammad, Hamid Ronagh, Parham Memarzadeh, and Farhad Behnamfar. "Cyclic behaviour of elliptical-shaped reduced web section connection." In Structures, vol. 24, pp. 955-973. Elsevier, 2020.
[109] Davarpanah, Mohammad, Hamid Ronagh, Parham Memarzadeh, and Farhad Behnamfar. "Cyclic behavior of welded elliptical-shaped RWS moment frame." Journal of Constructional Steel Research 175 (2020): 106319.
[110] Yu, Haoran, and Weibin Li. "Comparison of steel frames with RWS and WFP beam-to-column connections through seismic fragility analysis." Advances in Structural Engineering (2020): 1369433220977284.
[111] Lin, Shentong, Huiyun Qiao, Jinpeng Wang, Jiahao Shi, and Yu Chen. "Anti-collapse performance of steel frames with RWS connections under a column removal scenario." Engineering Structures 227 (2021): 111495.
[112] Erfani, Saeed, Vahid Akrami, and Arash Mohammad-nejad. "Lateral load resisting behavior of steel moment frames with reduced web section (RWS) beams." In Structures, vol. 28, pp. 251-265. Elsevier, 2020.
[113] Bi, Ran, Lianguang Jia, Pengyu Li, and Qinghe Wang. "Multiparameter seismic behavior of castellated beam-to-column connections based on stress migration." In Structures, vol. 29, pp. 1137-1153. Elsevier, 2021.
[114] Asl, Masoud Hoseinzadeh, and Maryam Jahanian. "Behaviour of Steel Deep Beams in Moment Frames with Web Opening Subjected to Lateral Loading." International Journal of Steel Structures 20, no. 5 (2020): 1482-1497.
[115] Fanaie, Nader, and Hossein Sadeghi Moghadam. "Experimental study of rigid connection of drilled beam to CFT column with external stiffeners." Journal of Constructional Steel Research 153 (2019): 209-221.
[116] ALIBAKHSHI, MOHSEN, JAZANY ROOHOLLAH AHMADY, MOHAMMAD SOHEIL GHOBADI, and ABADI MASOMEH SAADAT MAKI. "CONSIDERING THE EFFECT OF HOLES DISTANCES OF BEAM FLANGES ON SEISMIC BEHAVIOR OF DRILLED FLANGE (DF) CONNECTIONS." (2015): 52-66.
[117] Atashzaban, A., M. Izadinia, JAZANY R. AHMADY, and I. HAJIRASOULIHA. "Seismic Performance of Drilled Flange Beam to Column Connections for Ductile Steel Frames." (2016): 53-65.
[118] Jazany, Roohollah Ahmady. "Improved design of drilled flange (DF) moment resisting connection for seismic regions." Bulletin of Earthquake Engineering 16, no. 5 (2018): 1987-2020.
[119] Maleki, M., R. Ahmady Jazany, and M. S. Ghobadi. "Probabilistic seismic assessment of SMFs with drilled flange connections subjected to near-field ground motions." International Journal of Steel Structures 19, no. 1 (2019): 224-240.
[120] Fanaie, Nader, and Hossein Sadeghi Moghadam. "Experimental study of rigid connection of drilled beam to CFT column with external stiffeners." Journal of Constructional Steel Research 153 (2019): 209-221.
[121] Vajdian, Mehdi, S. Mehdi Zahraei, S. Mohammad Mirhosseini, and Ehsanollah Zeighami. "Investigation of Seismic Performance of (RBS) and Drilled Flange Connection (DFC) Containing rhombus Shaped Hole in Steel Moment Frames." Australian Journal of Civil Engineering 18, no. 2 (2020): 246-262.
[122] Vajdian, Mehdi, Ali Parvari, and Mohammad Afzali. "Improvement of Seismic Performance of Beam-column Connection With Replaceable Drilled Attachment Parts." Periodica Polytechnica Civil Engineering 64, no. 4 (2020): 1202-1218.
[123] Vajdian, Mehdi, S. Mehdi Zahrai, S. Mohammad Mirhosseini, and Ehsanollah Zeighami. "Cyclic Behavior of Variously Drilled Flange Beam Connected to Box Column." AUT Journal of Civil Engineering (2020).
[124] Parvari, Ali, Seyed Mehdi Zahrai, S. Mohammad Mirhosseini, and Ehsanollah Zeighami. "Numerical and experimental study on the behavior of drilled flange steel beam to CFT column connections." In Structures, vol. 28, pp. 726-740. Elsevier, 2020.
[125] Heidari, Peyman Shadman, Armin Aziminejad, A. S. Moghadam, and Mohammad Ali Jafari. "Evaluation of drilled flange connections with combined arrangements of holes and notches." Bulletin of Earthquake Engineering 18, no. 14 (2020): 6487-6532.
[126] Ting, L. C., N. E. Shanmugam, and S. L. Lee. "Box-column to I-beam connections with external stiffeners." Journal of Constructional Steel Research 18, no. 3 (1991): 209-226.
[127] Shin, Kyung-Jae, Young-Ju Kim, Young-Suk Oh, and Tae-Sup Moon. "Behavior of welded CFT column to H-beam connections with external stiffeners." Engineering Structures 26, no. 13 (2004): 1877-1887.
[128] Kang, Chang-Hoon, Kyung-Jae Shin, Young-Suk Oh, and Tae-Sup Moon. "Hysteresis behavior of CFT column to H-beam connections with external T-stiffeners and penetrated elements." Engineering structures 23, no. 9 (2001): 1194-1201.
[129] Tsavdaridis, Konstantinos Daniel, and Christopher Pilbin. "Finite element modelling of steel connections with web openings: aseismic design and progressive collapse." In The 7th European Conference on Steel and Composite Structures. Eurosteel 2014, 2014.
[130] Arasaratnam, P., K. S. Sivakumaran, and M. J. Tait. "True stress-true strain models for structural steel elements." ISRN Civil Engineering 2011 (2011).
[131] ANSYS Inc. ANSYS user guide, version 15.0.
[132] Uriz, Patxi. Towards earthquake resistant design of concentrically braced steel structures. University of California, Berkeley, 2005.
[133] Uriz, Patxi, Filip C. Filippou, and Stephen A. Mahin. "Model for cyclic inelastic buckling of steel braces." Journal of structural engineering 134, no. 4 (2008): 619-628.
[134] Santagati, S., D. Bolognini, and R. Nascimbene. "Strain life analysis at low-cycle fatigue on concentrically braced steel structures with RHS shape braces." *Journal of earthquake engineering* 16, no. sup1 (2012): 107-137.
[135] Lee, C. H., & Kim, J. H. (2007). Seismic design of reduced beam section steel moment connections with bolted web attachment. Journal of Constructional Steel Research, 63(4), 522-531.
[136] Zee, Howard L., and Jack P. Moehle. Behavior of interior and exterior flat plate connections subjected to inelastic load reversals. University of California, Earthquake Engineering Research Center, 1984.
[137] Benavent-Climent, A., X. Cahís, and J. M. Vico. "Interior wide beam-column connections in existing RC frames subjected to lateral earthquake loading." Bulletin of Earthquake Engineering 8, no. 2 (2010): 401-420.
[138] Shademan, Pouya, and Roohollah ahmady Jazany. "Study of seismic behavior of Drilled flange connection with slot hole."DOI: 10.22060/CEEJ.2018.14422.5652

Advanced Steel Construction – Vol. 17 No. 4 (2021) 349–355
DOI:10.18057/IJASC.2021.17.4.3

ENERGY DISSIPATING MODES AND DESIGN RECOMMENDATION OF H-SHAPED STEEL BAFFLES SUBJECTED TO BOULDER IMPACT

Lei Zhao [1], Li-Jun Zhang [1], Zhi-Xiang Yu [1, *], Jian-Wei He [2] and Xin Qi [1]

[1] *School of Civil Engineering, Southwest Jiaotong University, Chengdu, China*
[2] *Department of Civil and Environmental Engineering, The Hong Kong Polytechnic University, Hong Kong, China*
** (Corresponding author: E-mail: yzxzrq@swjtu.edu.cn)*

ABSTRACT

Flexible barriers are one of the most effective protective structures, which have been widely used for the mitigation of rockfalls. As the only compression members in a flexible barrier system, steel posts maintain the integrity of the interception structure to keep the function of the system. Due to the random trajectories of rockfalls, steel posts may be impacted by boulders directly. The impact scenario may result in the failure of the post and even the collapse of the system. In this paper, firstly, steel baffles were proposed to be an additional structural countermeasure to avoid the direct impact of posts. Secondly, numerical method was adopted to study the structural behaviour of steel baffles under direct boulder impact. Then, an available published experimental test of H-shaped steel beams under drop weight impact loading by others was back analyzed to calibrate the finite element model. Finally, numerical simulations were carried out to investigate the energy dissipating modes and energy dissipating efficiency of the H-shaped steel baffles. The simulation results show that there are three typical energy dissipating modes of H-shaped baffles subjected to boulder impact, namely flexural, local compression buckling and shear buckling. Local compression buckling is the most efficient energy dissipating mode. The thickness of the web of an H-shaped baffle is suggested to be 4 mm and 6 mm for the rated dissipating energy of 50 kJ and 100 kJ, respectively.

ARTICLE HISTORY

Received: 22 December 2020
Revised: 10 April 2021
Accepted: 15 May 2021

KEYWORDS

Steel baffle;
Flexible barrier;
Boulder impact;
Energy dissipating mode;
Design recommendation;
Numerical simulation

1. Introduction

The function of flexible barriers is similar to that of spider orb webs (Fig. 1a), which is to absorb the kinetic energy of the impact while minimizing structural damage. Benefiting from the weight of material, cost, ease and speed of construction, aesthetics and favourable environmental effect, flexible barriers are the most effective protective structures and have been extensively used for the mitigation of rockfalls [1-6] in hilly regions. In addition to footings, a typical flexible barrier (Fig. 1b) is mainly composed of three parts: 1) an interception structure; 2) a support structure; 3) connection components [7]. The interception structure is usually made up of cable nets or ring nets and bears the direct impact of the rockfall, transmitting the stresses to the connection components. A support structure usually consists of steel posts and maintains the interception structure erected through the connection components. The connection components include support ropes, anchor ropes and shackles, etc. They transmit the impact loads to the footing structure and then to the ground. They also help to maintain the integrity of the interception structure. Energy dissipating device is the most critical component in the system, dissipating around 60%-80% of the total impact energy [8] through friction between components, plastic deformation or their combination [9]. As energy dissipating devices are attached to steel ropes and allowed for a controlled displacement after activation, they are usually classified as a connection component.

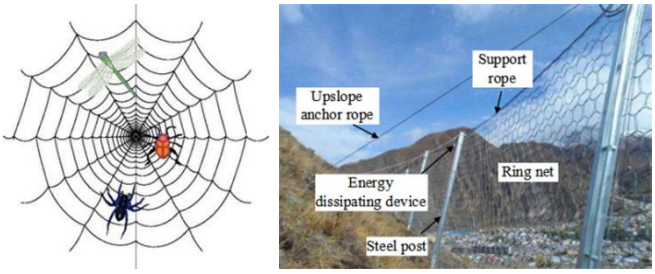

(a) Spider orb web (b) Flexible rockfall barrier

Fig. 1 Typical flexible barrier

As the support structure in a flexible barrier, steel posts ensure the position of the interception structure and the function of the system. From the view of stress characteristics, steel posts are the only compression members in the system, and all the other components are in tension during interception. The stress characteristic of flexible barriers is similar to tensegrity structures, figuratively described as “small islands of compression in a sea of tension” [10]. Due to the random trajectories of rockfalls [11], steel posts may be impacted by boulders directly which may result in the failure of the post and even the collapse of the system [1,12,13]. Field investigations (Fig. 2) also show that the failure of steel posts due to the direct impact of boulders happened occasionally. To solve this problem, it is necessary to improve the impact resistance of steel posts of flexible barrier or reduce the impact energy of the boulder or even avoid the scenario that boulders directly impact on steel posts.

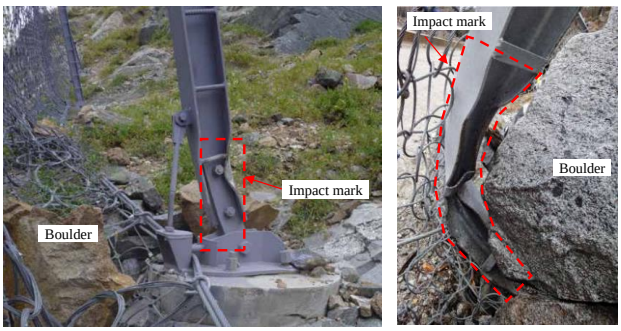

Fig. 2 Steel post directly impacted by boulders [14]

In this paper, firstly, steel baffles, as a straining structure, were proposed to be an additional structural countermeasure installed in front of the steel posts of flexible barriers to protect the steel posts from boulder impact in Section 2, and the principle of the baffles was also discussed in the section. Then, an available published experimental test of H-shaped steel beams under drop weight impact loading by others was back analyzed in Section 3. The test results of contact force and lateral deflection were used to calibrate the finite element model. Finally, numerical simulations were carried out to investigate the energy dissipating modes and energy dissipating efficiency of the H-shaped steel baffles in Section 4.

2. Principle of the baffle

The impact resistance of the steel post can be improved by increasing the section size. However, this measure will significantly increase the weight of the steel post and bring difficulties in field construction. Besides, the enhanced steel post is still the first and only line of defense against the direct

impact of a boulder which is not conducive to improving the reliability of flexible barrier systems.

The concept of multiple lines of defense has been widely accepted and adopted in structural seismic design [15]. Based on this concept, a baffle is proposed to be installed in front of the post to be the first line of defense. Instead of the protected post, the baffle will bear the first direct impact of boulders which could have impacted the post directly. After impacting the baffle, the kinetic energy of the boulder will be reduced significantly, owing to the plastic deformation of the baffle, damping or additional energy dissipating device. By trapping boulders upstream, the impact load can be reduced for the post of a flexible barrier in the downstream. In addition, the trajectory of the boulder will be changed, the boulder will impact the interception structure of the flexible barrier rather than the downstream post. In summary, the principle of the baffle mainly lies in the following two aspects: a) dissipate the impact energy of the boulder; b) change the trajectory of the boulder.

In essence, the baffle is a cantilever post subjected to impact load. Shaped steel is suggested to be used, such as H-shaped steel, circular tube and square tube. Concrete-filled steel tube (CFST) is also a good choice. Therefore, the baffles are light-weight and can be easily transported and constructed on a relatively steep terrain with poor access. The site of the baffle is certainly in front of the post to be protected. The height and the capacity of a baffle mainly depend on the bounce height and the kinetic energy of the boulder, respectively, which can be predicted by the movement analysis of rockfalls. In general, the height of the baffle is smaller than the protected post.

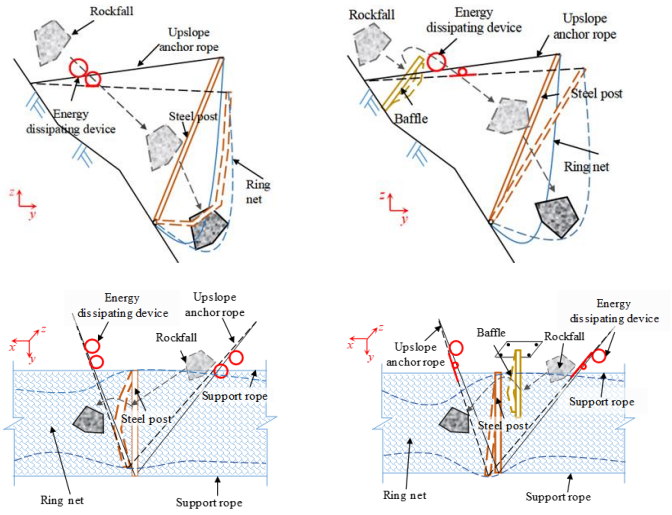

(a)Without baffle (b) With baffle

Fig. 3 Principle of the baffle

3. Validation of the numerical model

A considerable amount of literature has been published on studies of the dynamic behaviour and failure modes of steel members under the transverse impact. In particular, the behaviour of axially restrained beams and axially compressed steel columns has been studied extensively and intensively [16-20]. This is understandable since axially restrained beams and axially compressed steel columns are frequently used as members in buildings and bridges, etc. Obviously, the behaviour of cantilever posts under transverse impact will be different, and the related studies are few. Consequently, there is insufficient data to understand the dynamic behaviour of the baffle subjected to boulder impact.

As there is no available test data of baffles or cantilever steel posts under transverse impact, in this section, a published experimental test of a series of H-shaped steel beams under drop weight impact loading by others will be back analyzed to calibrate the LS-DYNA model.

3.1. Description of the test

The experimental test for calibration was conducted by Zhao et al. [19]. The specimens were with fixed-pinned (FP) end condition. Two square end plates with a thickness of 16mm were welded to each specimen. The length of each specimen was 1.5 m, and the section was $h \times b \times t_w \times t_f$=100×100×6×8 mm. The beam was impacted at the midpoint by a hammer. The hammer is made of GCr 15 steel with 64 HRC hardness and a 30mm×80mm rigid bottom surface. The experimental setup is shown in Fig. 4 as well as the details of steel beams and the LS-DYNA back-analysis model. In the test, the impact forces were monitored and recorded by a dynamic load cell. The details of the H-shaped steel specimens are illustrated in Table 1.

Table 1
Details of H-shaped specimens [19]

Case	Specimen label	m_0 (kg)	H_0 (m)	v_0 (m/s)	E_0 (kJ)
1	H-0.9-FP	89	1.04	4.5	0.9
2	H-2.5-FP	150	1.67	5.7	2.5
3	H-2.9-FP	150	2	6.2	2.9
4	H-3.7-FP	150	2.5	7.0	3.7

Note: m_0 is the weight of the hammer, H_0 is the hammer release height; E_0 is the impact energy before collision; v_0 is the initial impact velocity of the hammer.

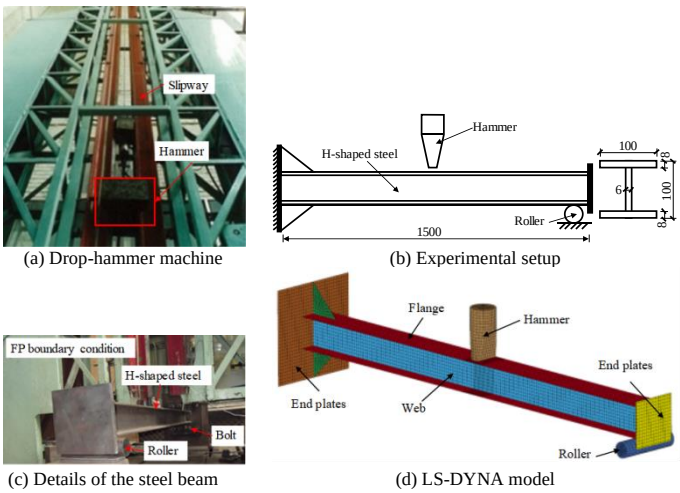

(a) Drop-hammer machine (b) Experimental setup

(c) Details of the steel beam (d) LS-DYNA model

Fig. 4 Experimental setup of Zhao et al. [19]

3.2. Description of LS-DYNA model

Considering the thickness of the H-section is much smaller than the other two dimensions, the default shell element named Belytschko-Lin-Tsay element, which is computationally efficient and stable for explicit calculations, was selected for modelling the beams. A five-stage elastic-plastic model developed by Han et al. [21] was employed to simulate the steel material. The model includes the elastic, elastic-plastic, plastic, hardening and secondary plastic flow stages, as presented in Fig. 5. Referring to the tests conducted by Zhao et al. [19], the following parameters were used: the density was 7850kg/m^3, the modulus of elasticity was 211 GPa, Poisson's ratio was 0.3, yield stress was 291.3 MPa, the tangent modulus was 1.476 GPa and the failure strain was 0.284. Additionally, the Cowper-Symonds model [22] was adopted to scale the yield stress by a strain rate dependent factor, as shown in Eq. (1):

$$\sigma_{yd} = \sigma_{ys}\left[1+\left(\frac{\dot{\varepsilon}}{C}\right)^{\frac{1}{P}}\right] \quad (1)$$

where σ_{yd} and σ_{ys} are the dynamic yield stress of steel under the stress rate and the static yield stress, respectively; C and P are the strain rate parameters with values 40.4s^{-1} and 5 according to the summary of Jones [23], respectively.

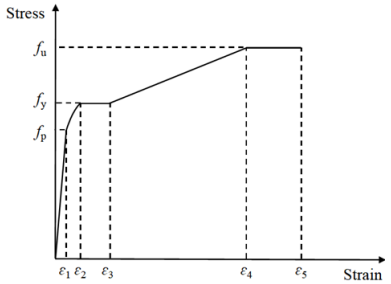

Fig. 5 Five-stage elastic-plastic model

The hammer and the roller were modelled by the default constant stress solid element. As the deformations of the hammer and the roller were very small during the impact process, they were defined as rigid bodies to reduce the computational requirement. The neglect of the deformations only has little influence on the impact results.

The mesh size will affect the computational cost and accuracy. A reasonable mesh size means that the computational accuracy is satisfactory and the computational cost is acceptable. When the mesh is too fine, the computational cost will increase significantly, but the computational accuracy will not be improved noticeably. When the mesh is too rough, the computational cost will decrease, but the accuracy will also be decreased. By trial and error, the mesh size was selected to be 5mm at the impact zone and 10mm at other zones.

An automatic surface-to-surface contact algorithm (Contact_Automatic_Surface_To_Surface in LS-DYNA) [24] was adopted to simulate the contact behaviour between the hammer and the steel beam, as well as the beam and the roller. In the test, the hammer dropped freely from a specified height, but it was positioned above the top flange of the beam with an equivalent initial velocity to reduce the computer time in the model.

3.3. Calibration of LS-DYNA model

Fig. 6 compares the local deformations at the midspan zone. It can be seen that the simulated deformed shapes agree well with the test. The local deformations are mainly concentrated on the midspan and minor buckling in the web occurs. Fig. 7 compares the experimental and numerical impact force-time relationships. The test results and the simulation results, including the peak impact forces (F_{peak}), the plateau impact forces ($F_{plateau}$), and the durations of impact force (T) are presented in Table 2. For Cases 1 to 4, the maximum error of experimental and numerical results is 19.2%, which occurs at the peak impact force in Case 1. It can be seen that both the impact force and the durations all agree very well.

As a conclusion, it may be accepted that the present LS-DYNA model with the associated material behaviour is capable of simulating the behaviour of steel members subjected to impact loading.

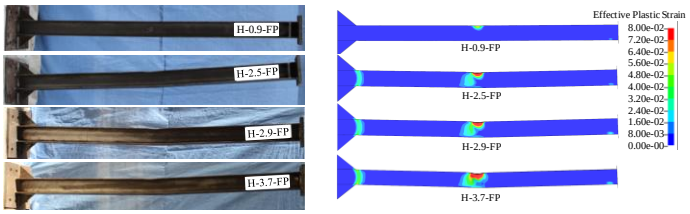

(a) Experimental result (b) Numerical result

Fig. 6 Comparison of the local deformation shape

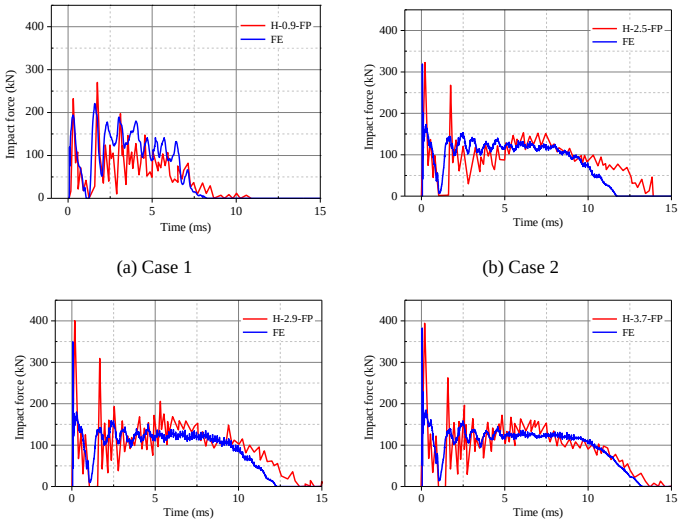

(a) Case 1 (b) Case 2

(c) Case 3 (d) Case 4

Fig. 7 Comparison of the impact force

Table 2
Comparison of the results

Case	Specimen label	F_{peak} (kN)		Error (%)	$F_{plateau}$ (kN)		Error (%)	T(ms)		Error (%)
		Tested	FE		Tested	FE		Tested	FE	
1	H-0.9-FP	239.9	193.7	19.2	122.8	133.5	8.7	10.1	8.26	18.2
2	H-2.5-FP	324.0	318.5	1.7	141.1	125.2	11.3	13.8	11.7	15.2
3	H-2.9-FP	422.5	348.9	17.4	143.4	126.3	11.9	14	12.3	12.1
4	H-3.7-FP	399.2	382.4	4.2	158.9	129.7	18.4	14.3	13.2	7.7

4. Dynamic response

4.1. Modelling properties

H-shaped baffles with a height of 2.0 m were used to reveal the energy dissipating modes of an H-shaped steel baffles subjected to boulder impact. The same LS-DYNA simulation method calibrated in the previous section was used. It should be mentioned that the steel grade was assumed to be Q235 [25] and the yield strength was assumed to be a standard value of 235 MPa. The full-frontal impact was applied to the flanges (Point P in Fig. 8) to cause bending about the major axis (x-x axis) of the baffle, which represents the most typical case for design purposes. The impact point was assumed to be 0.8 m away from the top of the baffle. The bottom of the baffle was fixed end condition. A side-view schematic of the model is shown in Fig. 8.

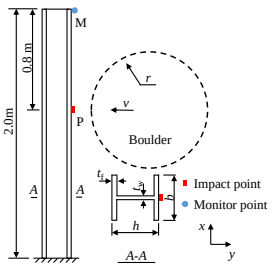

Fig. 8 Side view schematic of the model

4.2. Simulation case

According to the elastic mechanic, the critical stress of a steel plate can be uniformly expressed as Eq. (2):

$$\sigma_{cr} = \chi k \frac{\pi^2 E}{12(1-\nu^2)}\left(\frac{t}{b}\right)^2 \quad (2)$$

where χ is the constraint coefficient, k is the buckling coefficient, E and v are the modulus of elasticity and Poisson's ratio of steel, t and b are the thickness and width of the plate, respectively.

From Eq. (2), it can be seen that either the flange or the web of an H-shaped baffle, the critical stress of which mainly depends on the ratio of thickness and width of the plate. In other words, the energy dissipating mode of a baffle subjected to the impact of a boulder may mainly depend on the flange width-thickness ratio and the web depth-thickness ratio, denoted by γ_f and γ_w, respectively. From this point of view, three typical cases as shown in Table 3 were conducted. In these cases, the depth and width of these cross-sections both were fixed to 300 mm. The thickness of the flange and web were carefully chosen to obtain different combinations of γ_f and γ_w. In these cases, the boulder was 1.2 m in diameter and about 2000 kg in mass. The boulder impacts at point P as shown in Fig. 8 with the initial velocity of 10 m/s. So, the impact energies (E_0) of these cases all were 100 kJ.

Table 3
Typical cases of energy dissipating mode

Case	Cross-section properties			Impact properties		
	Size	γ_f	γ_w	m (kg)	v_0 (m/s)	E_0 (kJ)
Case-1	H300×300×12×12	12.5	23.0	2000	10.0	100
Case-2	H300×300×6×12	12.5	46.0	2000	10.0	100
Case-3	H300×300×6×25	6.0	41.7	2000	10.0	100

4.3. Simulation results

4.3.1. Impact force

The velocity-time histories of these boulders (Fig. 9) show that the boulders rebound with 1.2 m/s, 1.3 m/s and 1.4 m/s in velocity for Case 1 to Case 3 after the impact, which means that all the baffles withstood the frontal impact of the boulder with 100 kJ in kinetic energy successfully. The impacts last about 55 ms, 99 ms and 65 ms for Case 1 to Case 3, respectively.

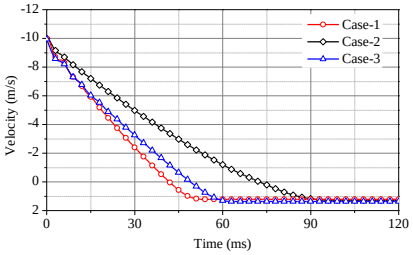

Fig. 9 Velocity-time history of boulder

The impact force-time histories (Fig. 10) of these cases are similar. All of them show the same characteristic of three stages, named peak stage (S_1), stable stage (S_2) and unload stage (S_3), respectively. In the peak stage, the interaction between the boulder and impact area of the baffle increases rapidly due to the transient action of the impact and the big local stiffness of the impact area, resulting in the maximum peak impact force at the first impact. As the mass of the boulder is much bigger than that of the baffle, the velocity of the baffle increases rapidly, but the velocity of the boulder decreases. The interaction between boulder and baffle becomes weaker, resulting in a rapid decrease of the impact force. Then, the velocity of the baffle decreases due to the boundary condition. The interaction increases again, resulting in another peak impact force. After repeated impact and separation several times, the velocities of the boulder and the impacted part of the baffle tend to be consistent gradually. This explains why the impact force fluctuates drastically in this stage. Subsequently, in the stable stage, the impacted part of the baffle and the boulder move at almost the same velocity. The plastic deformation of the baffle develops steadily, and the impact force is relatively stable. In this stage, the impact energy of the boulder is gradually transformed into the plastic strain energy of the baffle. The impact energy is mainly dissipated in this stage. Then, with the decreasing velocity of the boulder and baffle, the impact force starts to decrease until the velocity is close to zero and the unload stage starts. The impact ends when the boulder rebounds and separates from the baffle. The impact force decreases to zero at the moment.

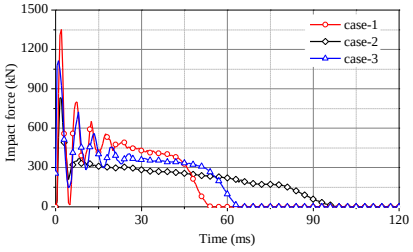

Fig. 10 Impact force-time history

For Case 1 and Case 3, there are several peaks during the first stage. For Case 1, the maximum peak force is 1350 kN at 3.0 ms. The stable stage lasts 21 ms and the stable impact force is about 400 kN. When T=55 ms, the impact force decreases to zero. For Case 2, there is only one significant peak force (F_{peak}) 832 kN when T=2.0 ms during the peak stage. The stable stage lasts about 60 ms, from T=10 ms to T=70 ms. The stable impact force (F_{stable}) is about 250 kN. When T=99 ms, the impact force decreases to zero. For Case 3, the maximum peak force is 1110 kN at 2.0 ms. The stable stage lasts about 25 ms and the stable impact force is about 350 kN. When T=65 ms, the impact force decreases to zero. The maximum impact forces and impact durations of the three cases show that the impact stiffness of Case 2 is the lowest, and that of Case 1 is the highest.

4.3.2. Energy dissipating mode

As shown in Fig. 11, for Case 1, the permanent displacements of the impact point and the monitor point are 181 mm and 290 mm, respectively. The displacement of the monitor point located at the top of the baffle is much larger than that of the impact point. From the development of deformation as shown in Fig.12 (a), the buckling of the compression flange at the bottom occurs firstly when T=11 ms. Then, the buckling of the web in compression at the bottom occurs when T=30 ms. As the impact continues, the plastic deformation of the flange and the web at the bottom gradually increases until the boulder rebounds. The deformation of the baffle impacted by the boulder is mainly concentrated on the compression flange and web at the bottom of the baffle.

For Case 2, the permanent displacements of the impact point and the monitor point (Fig. 7) are 292 mm and 218 mm, respectively. The permanent displacement of the impact point is much larger than that of the monitor point located at the top of the baffle, which means the deformation of the baffle is local. From the development of deformation as shown in Fig. 12(b), the buckling of the web at the impact area occurs soon after the impact happens when T=9.0 ms. As the impact continues, the plastic deformation of the web gradually increases until the boulder rebounds. The deformation of the baffle impacted by the boulder is mainly concentrated on the impact area, derived from the buckling of the web subjected to local compression.

For Case 3, the permanent displacements of the impact point and the monitor point are 204 mm and 206 mm, respectively. The displacements of the two points are practically the same, which means the deformation of the baffle above the impact point is almost the overall translation. From the development of deformation as shown in Fig. 12(c), the web below the impact point demonstrates obvious shear buckling characteristic when T=14.5 ms. As the impact continues, the plastic deformation of the web below the impact point gradually increases until the boulder rebounds. The deformation of the baffle impacted by the boulder is mainly concentrated on the area below the impact point, derived from the shear buckling of the web below the impact point.

From what has been discussed above, the energy dissipating modes can be classified into three major types according to the typical deformation characteristics, namely: a) flexural, b) local compression buckling and c) shear buckling.

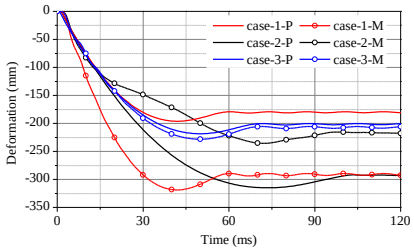

Fig. 11 Displacement-time history

4.3.3. Energy-dissipating characteristic

The internal energies of the flange and the web of each case after the boulder rebounded and separated from the baffle were extracted from the simulations and shown in Fig. 13. The internal energy of the flange and web are denoted as E_f and E_w, respectively. The summation of E_f and E_w is the energy dissipated by the baffle denoted as E_b. For Case 1, E_f, E_w and E_b are 61.8 kJ, 34.1 kJ and 95.9 kJ, respectively. For Case 2, E_f, E_w and E_b are 17.9 kJ, 79.6 kJ and 97.5 kJ, respectively. For Case 3, E_f, E_w and E_b are 17.1 kJ, 80 kJ and 97.1 kJ, respectively. It can be seen that the energies dissipated by the baffles all are slightly less than the impact energy 100 kJ. The main reason lies in the energy dissipated by friction and the kinetic energy of the rebounded boulder. For Case 2 and Case 3, the web of the baffle dissipated almost 80% of the impact energy, which means the web is the major energy dissipation component. For Case 1, the major energy dissipation component is the flange, which dissipated about 60% of the impact energy. The energy-dissipating characteristics are also consistent with the deformation characteristics as shown in Fig. 12. It also shows that both the flange and the web can be the major energy dissipation component of an H-shaped baffle.

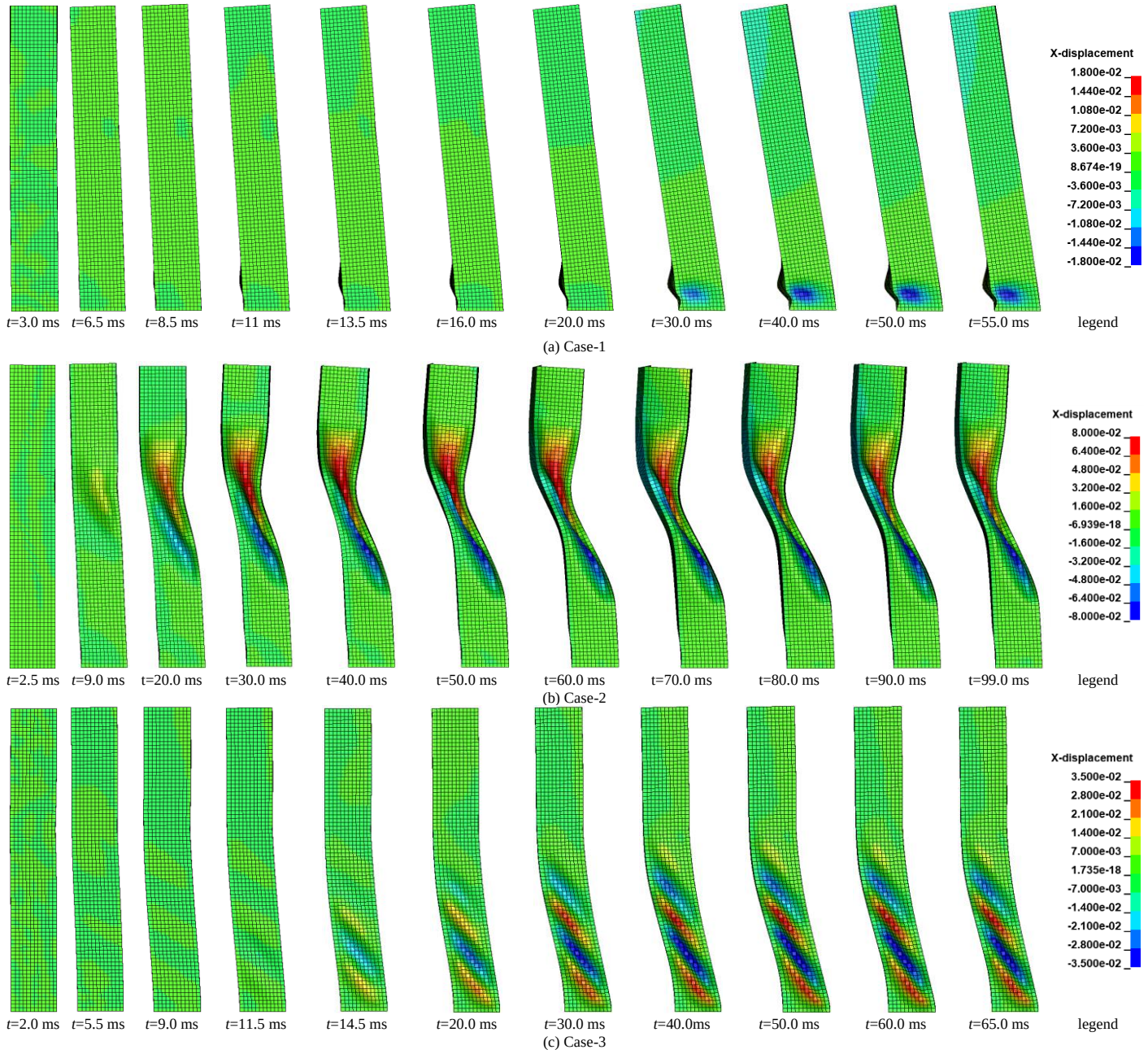

Fig. 12 Deformation development of baffles

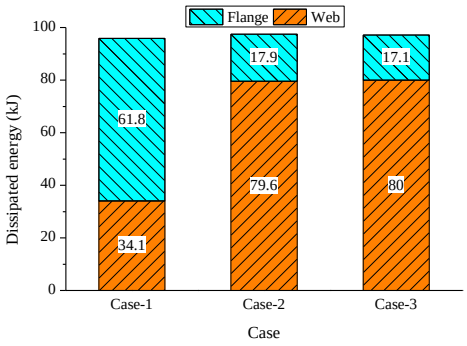

Fig. 13 Energy-dissipating characteristic

4.3.4. Energy dissipating efficiency

The energy dissipated per unit area denoted as λ (J/mm^2) is defined to evaluate the energy dissipating efficiency of a baffle, and λ is calculated by Eq. (3):

$$\lambda = \frac{E_b}{s_b} \tag{3}$$

where s_b is the cross-section area of the baffle (mm^2). λ can also be used to evaluate the energy dissipating efficiency of the flange or the web of an H-shaped baffle when E_b is substituted by E_f or E_w and s_b is substituted by the cross-section area of the flange or the web.

Table 4 shows the energy dissipating efficiency of these baffles, as well as that of the flange and web. It can be seen that, as far as the baffle is concerned, the highest energy dissipating efficiency is Case 2, which is 11. The lowest energy dissipating efficiency is Case 3, which is only 5.9. The former is about twice as much as the latter. It indicates that the energy-dissipating mode represented by Case 2, which is local compression buckling as discussed in Section 4.3.2, is the most efficient. The energy dissipating efficiencies of the flange of these cases all are below 10, and the lowest is only 1.1 in Case 3. But the energy dissipating efficiency of the web is much higher than that of the flange. In Case 2 and Case 3, the energy dissipating efficiencies of the web both are about 50. Even the lowest dissipating efficiency of the web in the three cases is also larger than 10. It indicates that the web and flange of an H-shaped baffle are the effective and ineffective components for energy dissipation, respectively. The web of an H-shaped baffle is recommended to be designed as the major energy dissipation component of an H-shaped baffle.

Table 4
Energy dissipating efficiency

	E_b (J)	E_f (J)	E_w (J)	s_b (mm^2)	s_f (mm^2)	s_w (mm^2)	λ_b (J/mm^2)	λ_f (J/mm^2)	λ_w (J/mm^2)
case-1	9.59×10^4	6.18×10^4	3.41×10^4	1.05×10^4	7.20×10^3	3.31×10^3	9.1	8.6	10.3
case-2	9.75×10^4	1.79×10^4	7.96×10^4	8.86×10^3	7.20×10^3	1.66×10^3	11.0	2.5	48.1
case-3	9.71×10^4	1.71×10^4	8.01×10^4	1.65×10^4	1.50×10^4	1.50×10^3	5.9	1.1	53.3

5. Design recommendation

As discussed above, the energy dissipating modes of an H-shaped baffle subjected to the impact of a boulder can be divided into three types, and local compression buckling is the most efficient. Considering the fact that the mode of energy dissipation is mainly determined by γ_f and γ_w, a total of 34 impact cases divided into 4 groups with different cross-sectional properties (Table 5) were simulated to find out the boundary value in this section. In these cases, the depth and width of the cross-section were both fixed to 300 mm. From Group 1 to Group 4, the thicknesses of the webs were fixed to 4mm, 6mm, 8mm and 10mm, respectively. In each group, the thicknesses of the flanges ranged from 6 mm to 25 mm. The mass of the boulder was fixed to 2000 kg. In order to ensure that the boulders were all stopped by these baffles and the baffles deformed significantly, the initial velocities of the boulders were different in these cases. For these cases named G-1-1 ~ G-1-10 and G-2-1, the impact velocity of the boulder was 7.07 m/s, which means the impact energy was 50 kJ. For these cases in Group 2 and Group 3 except for G-2-1, the impact velocity of the boulder was 10.0 m/s and the impact energy was 100 kJ. For these cases in Group 4, the impact velocity of the boulder was 14.1 m/s and the impact energy was 200 kJ.

The simulated results show that with the increasing of γ_w/γ_f, the energy dissipating mode is transformed from flexural (Type 1) to shear buckling (Type 3) gradually as a whole. But for the baffle with different thicknesses of the webs, the difference of the boundary values of the three energy dissipating modes is significant.

For Group 1, the thickness of the web of these cases was 4 mm, and the energy dissipating modes were all local compression buckling (Type 2) when the γ_w/γ_f ranged from 2.9 to 10.4. Only when the thickness of the flange was increased to 25 mm and the γ_w/γ_f was 10.4, the energy dissipating mode was transformed to Type 3; Type 1 did not appear even when γ_w/γ_f = 2.9. Therefore, for this group, it can be summarized that there are only two energy dissipating modes, Type 2 and Type 3, and the boundary value is 9.4.

For Group 2, the thickness of the web of these cases was 6 mm, and all the three types of energy dissipating modes appeared when γ_w/γ_f ranged from 2.5 to 6.9. The boundary values of γ_w/γ_f between Type 1 and Type 2, Type 2 and Type 3 were 3.7 and 4.2, respectively.

For Group 3, the thickness of the web of these cases was 8 mm, and Type 2 did not occur. The energy dissipating mode was transformed from Type 1 when γ_w/γ_f = 3.6 to Type 3 when γ_w/γ_f = 4.0. Therefore, for this group, the boundary value of these types is between 3.6 and 4.0.

For Group 4, the thickness of the web of these cases was 10 mm, and Type 2 did not occur either. The energy dissipating mode was transformed from Type 1 when γ_w/γ_f = 3.5 to Type 3 when γ_w/γ_f = 3.8. Therefore, for this group, the boundary value of these types is between 3.5 and 3.8.

Therefore, considering the energy dissipating efficiency of a baffle, the thickness of the web, denoted as t_w, is suggested to be 4 mm or 6 mm. For t_w=4 mm, when $\gamma_w/\gamma_f \le 9.4$, it can ensure that the energy dissipating mode is Type 2. For t_w=6 mm, when $3.7 \le \gamma_w/\gamma_f \le 4.2$, it can also ensure that the energy dissipating mode is Type 2.

Table 5
Parametric study

Case		Cross-section properties				Impact properties			Energy dissipating mode
		Size	γ_f	γ_w	γ_w/γ_f	m (kg)	v_0 (m/s)	E_0 (kJ)	
Group 1	G-1-1	H300×300×4×6	25.0	72.0	2.9	2000	7.07	50	Type 2
	G-1-2	H300×300×4×8	18.8	71.0	3.8	2000	7.07	50	Type 2
	G-1-3	H300×300×4×10	15.0	70.0	4.7	2000	7.07	50	Type 2
	G-1-4	H300×300×4×12	12.5	69.0	5.5	2000	7.07	50	Type 2
	G-1-5	H300×300×4×14	10.7	68.0	6.3	2000	7.07	50	Type 2
	G-1-6	H300×300×4×16	9.4	67.0	7.1	2000	7.07	50	Type 2
	G-1-7	H300×300×4×18	8.3	66.0	7.9	2000	7.07	50	Type 2
	G-1-8	H300×300×4×20	7.5	65.0	8.7	2000	7.07	50	Type 2
	G-1-9	H300×300×4×22	6.8	64.0	9.4	2000	7.07	50	Type 2
	G-1-10	H300×300×4×25	6.0	62.5	10.4	2000	7.07	50	Type 3
Group 2	G-2-1	H300×300×6×8	18.8	47.3	2.5	2000	7.07	50	Type 1
	G-2-2	H300×300×6×10	15.0	46.7	3.1	2000	10.0	100	Type 1
	G-2-3	H300×300×6×12	12.5	46.0	3.7	2000	10.0	100	Type 2
	G-2-4	H300×300×6×14	10.7	45.3	4.2	2000	10.0	100	Type 2
	G-2-5	H300×300×6×16	9.4	44.7	4.8	2000	10.0	100	Type 3
	G-2-6	H300×300×6×18	8.3	44.0	5.3	2000	10.0	100	Type 3
	G-2-7	H300×300×6×20	7.5	43.3	5.8	2000	10.0	100	Type 3
	G-2-8	H300×300×6×22	6.8	42.7	6.3	2000	10.0	100	Type 3
	G-2-9	H300×300×6×25	6.0	41.7	6.9	2000	10.0	100	Type 3
Group 3	G-3-1	H300×300×8×10	15.0	35.0	2.3	2000	10.0	100	Type 1
	G-3-2	H300×300×8×12	12.5	34.5	2.8	2000	10.0	100	Type 1
	G-3-3	H300×300×8×14	10.7	34.0	3.2	2000	10.0	100	Type 1
	G-3-4	H300×300×8×16	9.4	33.5	3.6	2000	10.0	100	Type 1
	G-3-5	H300×300×8×18	8.3	33.0	4.0	2000	10.0	100	Type 3
	G-3-6	H300×300×8×20	7.5	32.5	4.3	2000	10.0	100	Type 3

	G-3-7	H300×300×8×22	6.8	32.0	4.7	2000	10.0	100	Type 3
	G-3-8	H300×300×8×25	6.0	31.3	5.2	2000	10.0	100	Type 3
Group 4	G-4-1	H300×300×10×12	12.5	27.6	2.2	2000	14.1	200	Type 1
	G-4-2	H300×300×10×14	10.7	27.2	2.5	2000	14.1	200	Type 1
	G-4-3	H300×300×10×16	9.4	26.8	2.9	2000	14.1	200	Type 1
	G-4-4	H300×300×10×18	8.3	26.4	3.2	2000	14.1	200	Type 1
	G-4-5	H300×300×10×20	7.5	26.0	3.5	2000	14.1	200	Type 1
	G-4-6	H300×300×10×22	6.8	25.6	3.8	2000	14.1	200	Type 3
	G-4-7	H300×300×10×25	6.0	25.0	4.2	2000	14.1	200	Type 3

Note: Type 1 - flexural type, Type 2 - local compression buckling type, Type 3 - shear buckling type.

6. Conclusions

Flexible barriers have been extensively adopted for the mitigation of rockfalls. Steel posts are the important compression members to ensure the integrity of interception structure and the function of the system. Due to the random trajectories of rockfalls, steel posts may be impacted by boulders directly and the impact scenario may result in the failure of the post and even the collapse of the system. In this paper, steel baffles were proposed to install in front of steel posts of flexible barrier systems to protect the posts. Numerical simulations were carried out to investigate the energy-dissipating modes and control method of H-shaped steel baffles subjected to boulder impact. The key findings from this study are summarized as follows:

1. Steel baffles are proposed to be an additional structural countermeasure installed in front of the posts of flexible barriers to protect the posts from boulder impact. The principle of the baffle mainly lies in the following two aspects: a) dissipate the impact energy of the boulder; b) change the trajectory of the boulder.

2. Three typical energy-dissipating modes, i.e., a) flexural, b) local compression buckling and c) shear buckling, are observed based on the numerical simulation results.

3. Energy dissipating efficiency is defined as the energy dissipated per unit area to evaluate the efficiency of a baffle. The local compression buckling mode is the most efficient.

4. With the increasing of ratio γ_w/γ_f, the energy dissipating mode is transformed from Type 1 to Type 3 gradually. However, for the baffle with different thicknesses of the webs, the boundary values of the three energy dissipating modes differ widely. The thickness of the web of an H-shaped baffle is suggested to be 4 mm and 6 mm for the rated dissipating energy of 50 kJ and 100kJ, respectively. For t_w=4 mm or t_w=6 mm, when $\gamma_w/\gamma_f \leq 9.4$ or $3.7 \leq \gamma_w/\gamma_f \leq 4.2$, respectively, the energy dissipating modes of the baffles is ensured to be the local compression buckling (Type 2).

Besides, it should be clarified that the findings from this paper are based on a specific height, width and depth of H-shaped baffles subjected to a specific impact scenario. Further studies on more factors affecting the dynamic response of a baffle are recommended.

Acknowledgements

The authors are grateful for the support provided by the National Key Research and Development Program of China (Grant No. 2018YFC 1505405), the National Natural Science Foundation of China (Grant No. 51678504), the Department of Science and Technology of Sichuan Province (Grant No. 2018JY0029, 2020YJ0263) and the Fundamental Research Funds for the Central Universities (Grant No. 2682020CX62), and Geological Survey Project of CGS (Grant No. DD20190637).

Appendix A

A.1 Notations

m_0	Mass	E	Elasticity modulus
H_0	Release height	v	Poisson ratio
E_0	Impact energy	t	Thickness
v_0	Initial impact velocity	b	Width
σ_{yd}	Dynamic yield stress	γ_f	Flange width-thickness ratio
σ_{ys}	Static yield stress	γ_w	Web height-thickness ratio
C	Dynamic strain rate parameter	F_{stable}	Stable impact force
P	Dynamic strain rate parameter	E_f	Internal energy of flange
F_{peak}	Peak impact force	E_w	Internal energy of web
$F_{plateau}$	Plateau impact force	E_b	Dissipated energy
T	Duration of impact force	λ	Energy dissipated per unit area
χ	Constraint coefficient	s_b	Cross-section area
k	Buckling coefficient		

References

[1] Zhao L., Yu Z.X., Liu Y.P. He J.W. and Zhao S.C., "Numerical simulation of responses of flexible rockfall barriers under impact loading at different positions", Journal of Constructional Steel Research, 167, 2020.
[2] Yu Z.X., Zhao L., Liu Y.P., Zhao S.C., Xu H. and Chan S.L., "Studies on flexible rockfall barriers for failure modes, mechanisms and design strategies: a case study of Western China", Landslides, 16, 347-362, 2019.
[3] Qi X., Yu Z.X., Zhao L., Xu H. and Zhao S.C., "A new numerical modelling approach for flexible rockfall protection barriers based on failure modes", Advanced Steel Construction, 14, 479–495, 2018.
[4] Xu H., Gentilini C., Yu Z.X., Qi X. and Zhao S.C., "An energy allocation-based design approach for flexible rockfall protection barriers", Engineering Structures, 173, 831–852, 2018.
[5] Kwan J.S.H., Chan S.L., Cheuk J.C.Y. and Koo R.C.H., "A case study on an open hillside landslide impacting on a flexible rockfall barrier at Jordan Valley, Hong Kong", Landslides, 11, 1037-1050, 2014.
[6] Gentilini C., Gottardi G., Govoni L., Mentani A. and Ubertini F., "Design of falling rock protection barriers using numerical models", Engineering Structures, 50, 96–106, 2013.
[7] EOTA-European Organization for Technical Assessment. Falling rock protection kits EAD 340059–00-0106 [S]. 2018.
[8] Qi X., Mechanics performance of passive flexible protection structure, Chengdu, Southwest Jiaotong University, 2013. (In Chinese)
[9] Castanon-Jano L., Blanco-Fernandez E., Castro-Fresno D. and Ballester-Muñoz F., "Energy dissipating devices in falling rock protection barriers", Rock Mechanics and Rock Engineering, 50, 603–619, 2017.
[10] Fuller R.B., Tensile-Integrity Structures, US Patent, 3063521, 1962.
[11] Biagi V.D., Marchelli M. and Peila D., "Reliability analysis and partial safety factors approach for rockfall protection structures", Engineering Structures, 213,110553, 2020.
[12] Zhao L., He J.W., Yu Z.X., Liu Y.P. and Chan S.L., "Coupled numerical simulation of a flexible barrier impacted by debris flow with boulders in front", Landslides, 17, 2723-2736, 2020.
[13] Brunet G., Giacchetti G. and Grimod A., "Rockfall barrier behavior under multiple impact events", 64th highway geology symposium, New Hampshire, USA, 9–12 September 2013.
[14] Scarpato D.J., Ingraham P.C., Group R.P., Shevlin T.D. "Deflection as a Positive Attribute", Geostrata May/June,61-66, 2020.
[15] Wang Y., "Lessons learned from the "5.12" Wenchuan Earthquake: evaluation of earthquake performance objectives and the importance of seismic conceptual design principles", Earthquake Engineering and Engineering Vibration, 7, 255–262, 2008.
[16] Shakir A.S., Guan Z.W. and Jones S.W., "Lateral impact response of the concrete filled steel tube columns with and without CFRP strengthening", Engineering Structures, 116, 148-162, 2016.
[17] Pei C. and Wang R., "Parametric Analysis of the Dynamic Response of Hot-Rolled H-Shaped Steel Beam under Lateral Impact Load", Applied Mechanics and Materials, 215–216, 998–1002, 2012.
[18] Al-Thairy H. and Wang Y.C., "A numerical study of the behaviour and failure modes of axially compressed steel columns subjected to transverse impact", International Journal of Impact Engineering, 38, 732-744, 2011.
[19] Zhao H., Wang R, Li Q.M., Wu H., Hou C.C. and An G., "Experimental and numerical investigation on impact and post-impact behaviours of H-shaped steel members", Engineering Structures, 216, 2020.
[20] Bambach M.R., Jama H., Zhao X.L. and Grzebiets R.H., "Hollow and concrete filled steel hollow sections under transverse impact loads", Engineering Structures, 30, 2859-70, 2008.
[21] Han L.H., Yao G.H. and Tao Z. Performance of concrete filled thin-walled steel tubes under pure torsion. Thin-Walled Struct 2007; 45:24-36.
[22] Cowper G.R. and Symonds P.S., Strain-hardening and strain-rate effects in the impact loading of cantilever beams, Brown Univ, Providence Ri, 1957.
[23] Jones N., "Structural impact", Cambridge university press, 2011.
[24] Hallquist J.O., "LS-DYNA theory manual", Livermore Software. Technol. Corp., 2006.
[25] GB 50017-2017. Standard for Design of Steel Structures. Beijing: China Architecture & Building Press; 2017.

Advanced Steel Construction – Vol. 17 No. 4 (2021) 356–365
DOI:10.18057/IJASC.2021.17.4.4

MECHANICAL PRORERTIES OF EXPOSED COLUMN BASE CONNECTIONS FOR L-SHAPED COLUMNS FABRICATED USING CONCRETE-FILLED STEEL TUBES

Jing Su [2], Ting Zhou [1, 2, *], Zhi-Hua Chen [1, 2] and Xiao-Dun Wang [1, 2]

[1] *Key Laboratory of Coast Civil Structure Safety of China Ministry of Education, Tianjin University, Tianjin, China*
[2] *School of Civil Engineering, Tianjin University, Tianjin 300072, China*
[*] *(Corresponding author: E-mail: zhouting1126@126.com)*

ABSTRACT

The response of exposed column base connections for L-shaped column is investigated through finite element analysis (FEA) in this paper which is affected by complex interactions among different components. Three finite element models are constructed to simulate the response of these connections under axial and cyclic horizontal loading, which interrogate a range of variables including anchor rod strength, base plate size and thickness. The results of the simulations provide insights into internal stress distributions which have not been measured directly through experiments. The key findings indicate that thicker base plates tend to shift the stresses to the toe of the base plate, while thinner plates concentrate the stresses under the column flange. Base on the analytical results, a hysteretic model is proposed to describe the cyclic moment-rotation response of exposed column base connections. The core parameters used to define the backbone curve of the hysteretic model are calibrated through configurational details. The comparison between the simulation and the calculated values indicates that the hysteretic model is suitable to characterize the key aspects of the physical response, including pinching, recentering and flag-shaped hysteresis phenomenon. Limitations of the model are outlined.

ARTICLE HISTORY

Received: 9 July 2020
Revised: 15 April 2021
Accepted: 18 April 2021

KEYWORDS

L-shaped columns;
Finite element analysis;
Exposed column base;
Hysteretic model;
Flexural strength

1. Introduction

Column bases are one of the most important components in a real building. Their rotational stiffness and moment resistance affect storey drifts, force distributions and collapse resistance of the whole structure. It is of great importance to design the column bases with sufficient strength, stiffness, as well as energy dissipation capacity. It has been summarized that generally there are three types of column bases in engineering practices, including exposed column bases, embedded column bases and concrete-encased column bases. The exposed type, advancing in fast and easy construction, consists of column, base plate, anchor rods and concrete foundation which bears loads through interactions among various components. The concrete-encased connection can be regarded as an enhanced version of the exposed one, as it is encased by an outer reinforced concrete part on the basis of the base-plate joints. It is not suitable for the large-scale columns with an additional part which could waste much available area. Although the embedded column base inserted into the foundation could achieve higher strength and stiffness compared with the former two, it would increase construction difficulties once the size of the column becomes extremely large that requires very deep embedment.

In recent studies, the concrete-filled special-shaped steel tubular columns (SCFT) have been widely used for its mechanical benefits, such as high strength, superior ductility and high energy-absorption capacity [1]. The width of mono-column is always smaller than the thickness of the wall, allowing SCFST columns to be embedded into the wall, which provides greater flexibility for architectural design. Three types of SCFST columns have been proposed. Chen et al. [2] proposed a kind of composite special-shaped column, including three cross sections: L-shaped, T-shaped and crisscross-shaped, which are fabricated with mono-rectangular columns and shear connectors. The connectors have developed from the early welded lacing bars [2] to single steel plates [3], and then double steel plates [4]. The second type is the multiple-cell special-shaped concrete-filled steel tubular columns, formed by the connection of multiple rectangular steel tubes through vertical welds. The third one is concrete-filled special-shaped steel tubular column. Compared with the other two types, the composite concrete filled steel tube mono-columns improve the confinement effect of the core concrete. In general, an L-shaped column (L-CFST) composed of three small-sized mono-columns and double steel plate connectors can meet universal demands for structures. It has been studied under axial, biaxial and cyclic loads in past 10 years through experiments and finite element model (FEM) analysis [2–8]. The seismic performance of such structural system constructed with SCFT columns and different lateral resistance members has also been investigated [9-10]. Nevertheless, the number of theoretical works and experimental programs specifically devoted to investigating the seismic behaviors of the SCFT column base connections is limited and the knowledge of them is still far from a complete understanding. As mentioned earlier, the encased connection which could achieve the required strength and stiffness in most situations would meet construction difficulties caused by the large-scale section of the L-CFST column. The exposed connection, relatively simple for construction, which has excellent ductility and large deformation capacity shows good potential for applications in such case. Previous studies [11-22] mainly investigate the major axis bending conditions of the H-section or box section steel column bases, while none examines the response of L-CFST column bases. The strength characterization methods presented in prior researches [17-18] are not applicable to such connections because of the inner anchor bolt layouts and special-shaped base plate. These different configurations alter internal stress distributions and affect the deformation form of the connection that could not be measured directly through experiments. Considering the fact that the seismic performance of exposed L-CFST column bases is influenced by many variables, such as the value of axial load, different loading history, embedment depth and layouts of anchor rods, base plate size and thickness, and experimental tests could consume much accurately interrogating all these parameters, finite element simulations are ideal methods for investigating the connection response. Motivated by these issues, this paper established three finite element (FE) models to observe the response of the L-CFST column base connections. The FE models are highly sophisticated, considering large deformation, complicated contact relations and multi-axial constitutive response of materials. Next section provides a brief overview of the exposed column base studies. Previous study [24] is used as the validation bed of the simulation. Based on the analytical results, a simplified method is proposed to calculate the flexural bearing capacity of the base joints. And then a hysteretic model describing the seismic response of the L-CFST exposed connection is developed. Conclusions and limitations are outlined at last.

2. Background

Numerous experimental and analytical works have been conducted on exposed base connections to describe their strength, stiffness and failure modes. Unfortunately, the technical literatures devoted to investigating their cyclic response are not as broad as for the beam-to-column joints. It can be explained that the complicated interactions increase the difficulties in establishing an accurate and universal method to characterize the base connection response. Previous experimental studies [11-12] have sought to evaluate the influence of different parameters on their mechanical properties. These findings contributed to the development of the calculation methods in strength and stiffness. Subsequent

works [13-15] led to a refinement of these methods, but they were not convenient to apply owing to the complicated iterative procedures. Then, new design methods, relying on simplified assumptions, were used in design. These methods assumed that the stress distribution under the base plate contained two categories, namely strain compatibility and strength independence. The calculation results based on these methods showed overall agreement with experimental data. However, such design methods are limited to be generalized considering the indeterminacy of internal forces. To address these issues, Kanvinde et al. [18] examined the physical response and stress distributions of the exposed connections through finite element analysis. Based on the simulation results, the author provided modifications with regard to the plate thickness in strength calculation. And then, a hysteretic model characterizing the connection performance under seismic loading conditions in [21] was proposed.

Looking in literature, prevalent researches [17-21] have devoted to extending the component method mainly applicable for H-section steel column bases. Thus, the derivations are not suitable for L-CFST column base design. Considering the difficulties in measuring them directly through experiments, the finite element simulation method discussed in the following sections is more appropriate to exam the internal force distributions and investigate the connection response.

3. Finite element analysis (FEA) model

As mentioned above, there are complicated interactions at the base plate joints. The model contains highly complex contact relations (between base plates and foundations; between base plates and washers; between nuts and washers; between anchor rods and various hole walls), adding the difficulties in simulating these surface properties. Three FEA models were established to study the seismic behaviors of the exposed L-CFST column bases, shown in Fig. 1. Detailed information of the models is listed in Table1.

3.1. Elements, interactions, and boundary conditions

The models are primarily formed by hexahedral(C3D8R) elements, except for the reinforcements using space truss elements. As the deformation mainly concentrates at the base plate joints, anchor bolts are modeled by solid elements to better observe their deformation capacities.

Table 1
Details of models

Specimen	Column	Anchor bolt	Base plate
	$B \times B \times t$ ($mm \times mm \times mm$)	Diameter (mm)	$B \times B \times t$ ($mm \times mm \times mm$)
ZJ1	150 × 150 × 10	20	650 × 650 × 20
ZJ2	150 × 150 × 10	20	850 × 850 × 40
ZJ3	150 × 150 × 10	36	850 × 850 × 40

The welded connections are simulated as “tie”, with the assumption that the welds are detailed enough to resist fracture. The anchor rods and nuts are modeled as monolithic as well to reduce calculation burden, as indicated in [18]. For the interface between the base plate and foundation, contact is defined as surface-to-surface property. The normal behavior is set as “hard contact” and the tangential behavior is simulated through the “Coulomb friction” model according to CECS-230-2008 [23]. The anchor rods are embedded into the foundation considering their embedment depth is enough to resist adhesive damage. The bond relation between steel and concrete in L-CFST column is simulated using the contact element, as stated in [24].The bottom surface of the foundation is fixed. The column base is subjected to axial and cyclic lateral loads controlled by the drift ratio θ, defined as θ = Δ/H, where Δ is the horizontal displacement and H is the height from the loading point to the foundation surface. The drift ratio θ is taken as ± 0.003 rad, ± 0.006rad, ± 0.012 rad, ± 0.018 rad, ± 0.024 rad, and ± 0.03 rad, increasing gradually with two cycles until the drift ratio is more than 0.1 rad.

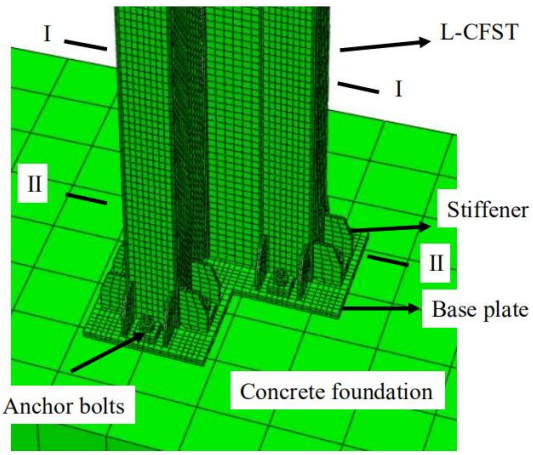

Fig. 1 Overview view of the FEA m

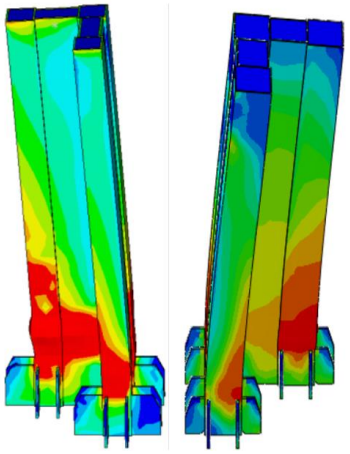

(a) failure mode in [24] (b) failure mode in this study

Fig. 2 Failure mode of the L-CFST column in [24] and in this study respectively.

3.2. Constitutive models for concrete and steel

As stated in Reference [24], the constitutive model of the concrete is described using the incremental theoretical elastic-plastic constitutive model. The steel components are modelled with trilinear curves, while the anchor bolts use the ideal elastoplastic model.

3.3. Validation of the finite element models

The experiments conducted previously in [24] are used as a validation testbed. Table 2 shows the key parameters used in these tests. Referring to Table 2, the experiments provide a rich matrix of column sizes enabling the validation against a comprehensive data set. The failure modes are similar, as shown in Fig. 2, concentrated at the column feet.

Table 2
Details of specimens

Specimen	L(mm)	B × B (mm × mm)	D (mm)	n	t_1 (mm)	t_2 (mm)
SJ1	1500	100 × 100	150	0.4	4	4
SJ3	1500	150 × 150	150	0.4	4	4
SJ4	1500	100 × 100	100	0.4	4	4

L represents the length of the column. B is the width of the steel tube. D is the width of the steel plate. n is the axial compression ratio. t_1 and t_2 is the thickness of the steel tube and steel plate respectively.

The comparisons between the skeleton curves of the FEM analysis and the experiments are shown in Fig. 3. Small differences between the results of tests and simulations are observed. The errors possibly can be caused by some factors: 1) the gap between the concrete and steel tubes in actual working conditions, 2) the damage of concrete is underestimated, 3) the heterogeneity of the materials and initial defects in specimens. Nevertheless, as the predictions generally match with the experiments well, it could be concluded that the FEA models are suitable for further analysis.

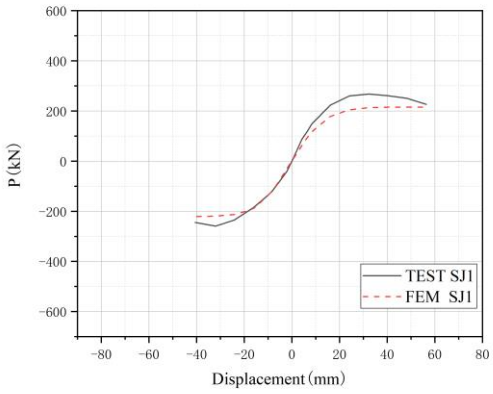

(a) Skeleton curves of SJ-1.

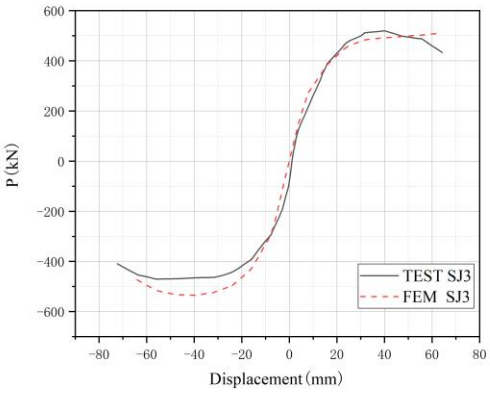

(b) Skeleton curves of SJ-3.

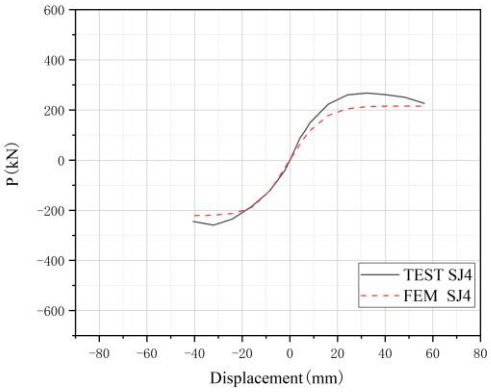

(c) Skeleton curves of SJ-4.

Fig. 3 Comparison between the skeleton curves of the FEM and test.

4. Analytical investigation

Three FE models were constructed and analyzed. Referring to Table 1, variables mainly include the base plate size and thickness, diameter of the anchor rods to investigate the influence of different parameters on seismic performance of the exposed base connections.

4.1. Internal stress distributions

The FE models provide an opportunity to examine internal stress distributions in the base connection. Fig. 4 illustrates the concrete stress distributions in the plane of the moment, assuming that stress within the width of the plate is invariant. It can be seen that the stress mainly concentrates on the flange of the column for ZJ1, while that shifts to the edge of the ribs for ZJ2 and ZJ3, caused by the differences in the plate thickness, as summarized in [18].

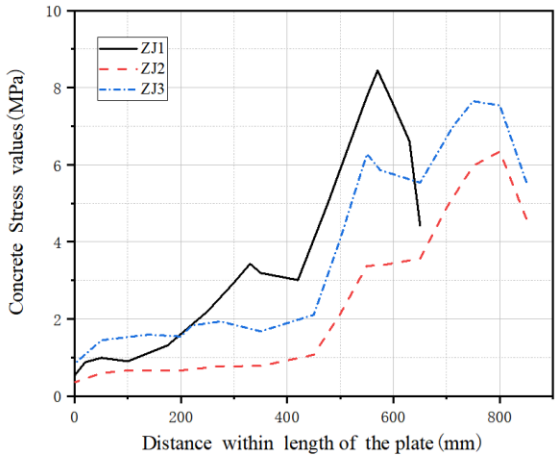

Fig. 4 Stress distribution under the base plate.

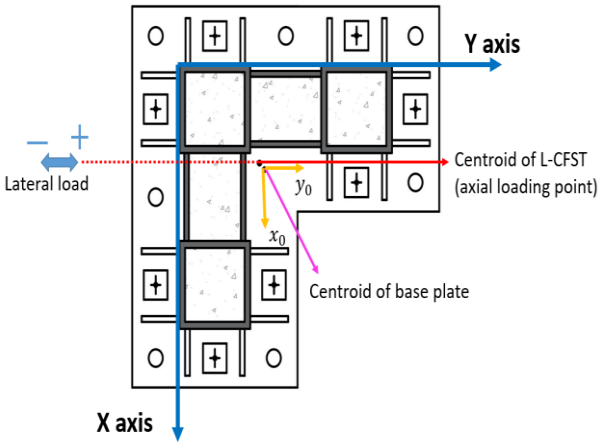

Fig. 5 Definition of the bottom section and loading directions.

4.2. Failure modes and strength

Previous experimental and analytical studies [11-22] have indicated that the exposed connections are prone to fail at the base plate joints, such as plastic elongation of anchor rods, yield of the base plate and spalling of concrete. Table 3 shows the drift ratio θ for each failure mode. The definition of the bottom section is shown in Fig. 5, marking out the positive and negative loading directions. The damage began with the anchor bolts for all three models, indicating that the anchor bolts were weaker than the base plate, such that simply increasing the size of the base plate did not significantly delay the initial yield phenomenon. The anchor bolts of ZJ2 and those of ZJ1 began to yield at the same degree of bending effect, while those of ZJ3 failed later owing to its larger diameter. Then the second-yield event occurred on the base plate. Table 3 shows that the thicker base plate has higher strength and provides more resistance after the anchor bolts yield.

Table 3
Drift ratio of each fracture mode

Specimen	Anchor rods yield (rad)		Base plate yield (rad)	
	Positive direction	Negative direction	Positive direction	Negative direction
ZJ1	0.003	0.003	0.012	0.012
ZJ2	0.003	0.003	0.018	0.018
ZJ3	0.006	0.006	0.024	0.024

As the deformation increased, concrete under the compression side crushed. It could not be observed directly through the simulation but was associated with the negative slope of the curve, indicating the reduction in stiffness and strength. The maximum lateral resistances shown in Fig. 6 were not equal in two directions because of the asymmetric bottom section. One was attributed to that the loading started from the positive direction and the anchor bolts had accumulated plastic deformation when the lateral load reversed. Another reason was caused by the differences of bearing capacities of the L-CFST column in two directions.

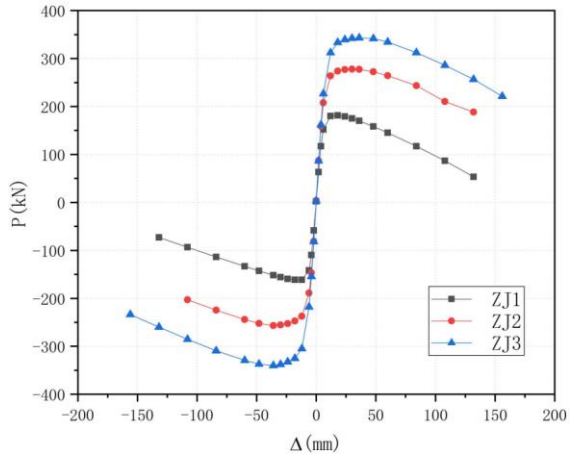

Fig. 6 $P-\Delta$ envelop relation of three models.

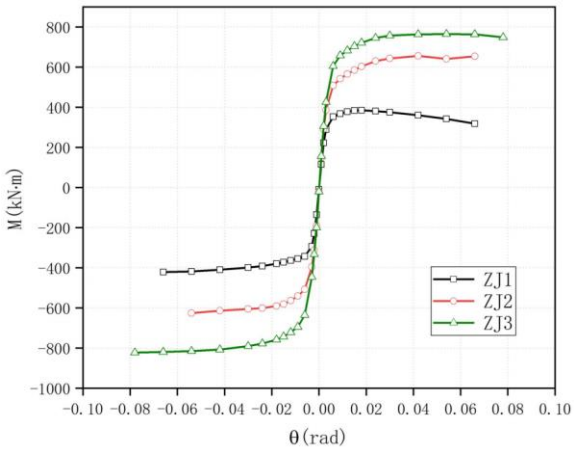

Fig. 7 M-θ envelop relation of three models.

As mentioned above, the degradation in strength and stiffness is caused by two key events. The moments corresponding to these two events are denoted as M_y and M_{max} which are shown in Fig. 7. Despite the limited ranges of parameters investigated in this simulation, it is stated that the base connections have higher strength with enhanced settings.

4.3. Strength calculation

The response of the L-CFST column base connections is the result of nonlinear interactions. Thus, previous approaches [15,18-19] relying on assumed stress distributions under the base plate cannot be applied for this type of connection. The eight-rod configuration and special-shaped base plate increase the degree of static indeterminacy within the connection. The method presented in this section does not characterize the nonlinear interactions in an explicit way but rather devotes to providing a simplified method that can be applied in a practical setting conveniently. During the loading process, the bottom section was subjected to bidirectional bending effect caused by the eccentricity between the centroid of the column section and that of the base plate. The moment of the bottom section can be decided by Eq. (1), and Eq. (2):

$$M_x=P\times H+N\times(y-y_0) \tag{1}$$

$$M_y=N\times(x-x_0) \tag{2}$$

Where P is the horizontal load along y-axis; N is the axial load at the top of the column; x, y are the displacement of the loading point along x-axis and y-axis respectively; x_0,y_0 are the coordinates of the centroid of bottom section respectively.

The calculated flexural strength of the column bases, as well as the simulated results are shown in Fig. 8. The agreement between two values demonstrates that the method provides sufficient accuracy, especially in the early loading phase, and the maximum error is less than 10%. According to the regulations in [23] the anchor rods in compression side are not involved in the strength calculation. As shown in Fig. 9, the strain compatibility method proposed in [28] is utilized.

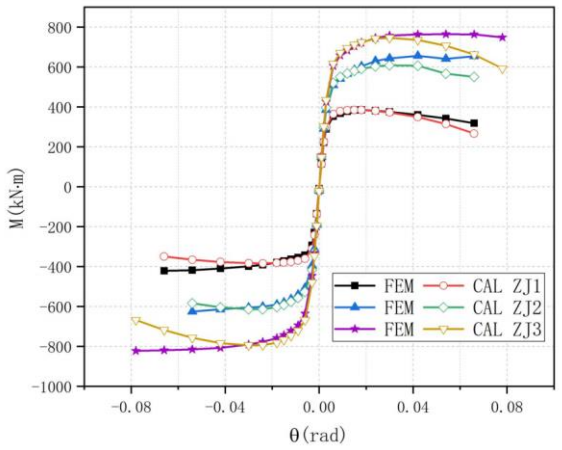

Fig. 8 Comparison between simulations and calculations

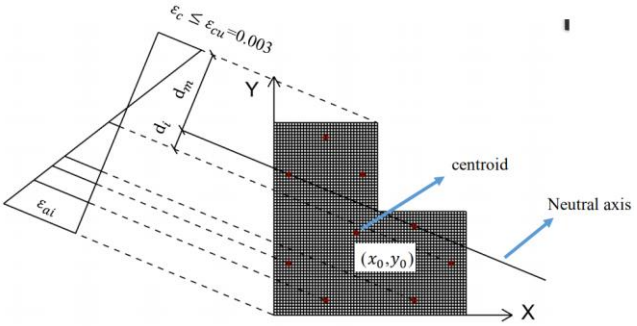

Fig. 9 Strength model for the bottom section.

Following assumptions are used to predict the flexural strength. (1) Linear stain distribution for the bottom section, (2) The extreme strain of concrete in compression side attains 3000 $\mu\varepsilon$, (3) The extreme strain of anchor bolts in tension side is equal to 10000 $\mu\varepsilon$, (3) The tensile strength of concrete is neglected, (4) The constitutive model of anchor bolts follows the ideal elastic–plastic model, (5) The concrete compression stress-strain relation is defined referring to [27], as outlined in the following equations:

$$\sigma_c=\begin{cases} f_c\left[\frac{2\varepsilon}{\varepsilon_0}-\left(\frac{\varepsilon}{\varepsilon_0}\right)^n\right], & \varepsilon<\varepsilon_0 \\ f_c, & \varepsilon_0\le\varepsilon\le\varepsilon_{cu} \end{cases} \tag{3}$$

$$n=2-\frac{1}{60}\left(f_{cu,k}-50\right) \tag{4}$$

$$\varepsilon_0=0.002+0.5\left(f_{cu,k}-50\right)\times10^{-5} \tag{5}$$

$$\varepsilon_{cu}=0.003-0.5\left(f_{cu,k}-50\right)\times10^{-5} \tag{6}$$

$n\le2$, if the calculation value is greater than 2, then n=2.

Where σ_c is the compressive stress of concrete, f_c is the axial compressive strength of concrete, ε_0 is the compressive strain of concrete corresponding to the compressive strength f_c, ε_{cu} is the extreme strain of concrete, $f_{cu,k}$

is the concrete cubic compressive strength, n is a coefficient.

Specific calculation procedures are shown in Fig. 10, as indicated in following steps:

(1) Divide the bottom area into several small rectangular units in which the base plate is located. The coordinates of each small concrete unit and anchor bolts are defined as (x_{ci},y_{ci}) , (x_{si},y_{si}) respectively.

(2) A neutral axis is preliminarily assumed, such that the strain of anchor bolts and each small rectangular unit can be decided according to Eq. (7):

$$\varepsilon_i=\varepsilon_{cu}\frac{d_i}{d_m} \tag{7}$$

Where d_i is the distance from the centroid of each unit to the neutral axis, d_m is distance from the edge of the concrete unit in compression side to the neutral axis.

(3) The stress can be obtained using previous stress-strain relation and following equilibrium equations are established:

$$N\leq\sum_{i=1}^{n_c}A_{ci}\sigma_{ci}+\sum_{j=1}^{n_s}A_{sj}\sigma_{sj} \tag{8}$$

$$M_x\leq\sum_{i=1}^{n_c}A_{ci}\sigma_{ci}(y_{ci}-y_0)+\sum_{j=1}^{n_s}A_{sj}\sigma_{sj}\left(y_{sj}-y_0\right) \tag{9}$$

$$M_y\leq\sum_{i=1}^{n_c}A_{ci}\sigma_{ci}(x_{ci}-x_0)+\sum_{j=1}^{n_s}A_{sj}\sigma_{sj}\left(x_{sj}-x_0\right) \tag{10}$$

Where M_x,M_y are the moment in two directions respectively; n_c is the number of concrete units in compression side; n_s is the number of anchor bolts in tension side; σ_{ci},A_{ci} are the stress and area of the ith concrete unit respectively; σ_{sj},A_{sj} are the stress and area of the ith anchor bolt respectively, (x_0,y_0) are the coordinates of the centroid of bottom surface.

The calculated values are collected in Table 4. It indicates that, on average, the strength calculation method predicts the strength with accuracy, such that the average simulated-to-calculated ratio is 1.02.

Table 4
Comparison between simulations and calculations.

Specimen	M_{FEA}(kN · m)		M_{CAL}(kN · m)		M_{FEA}/M_{CAL}	
	positive	negative	positive	negative	positive	negative
ZJ1	385	379	391	359	0.98	1.05
ZJ2	656	613	712	564	0.92	1.08
ZJ3	764	815	746	764	1.02	1.06
Mean						1.02

4.4. Hysteretic Model for Exposed Column Base Connections

4.4.1. Physical response of the connection

The connection response under cyclic loads is shown in Fig. 11. Each incremental deformation process corresponds to a sudden change in the load-deformation curve. These insets describe half of a cycle and subsequent half-cycle is repeated along similar path. In initial loading stage in Fig. 11(a), the resistance mainly consists of stress in compression side under the plate and axial force at the top of the column, in which the anchor rods do not effect. As the deformation increases, the anchor bolts begin to bear loads. The plate is subjected to bending effect caused by the combination of the stress block under the base plate and tension in anchor rods. The end of this stage is signed by the yield of anchor bolts. After that, multiple components gradually yield, creating sudden changes in the load-deformation curves. The end of the second stage in Fig. 11(b) represents the yield of inner bolts and the failure of base plate is shown in Fig. 11(c) in the third end. With more and more components losing bearing capacities, a strength plateau appears at the end of the fourth stage in Fig. 11(d), illustrating the ultimate strength. The top of the base plate maintains contact with the bottom of nuts in initial unloading stage, as illustrated in Fig. 11(e), while that gradually separates from the nuts because of the plastic deformation of anchor rods, accompanied by a nearly constant moment in Fig. 11(f). Then, the base plate continues to move freely until it contacts the concrete again in Fig. 11(g).

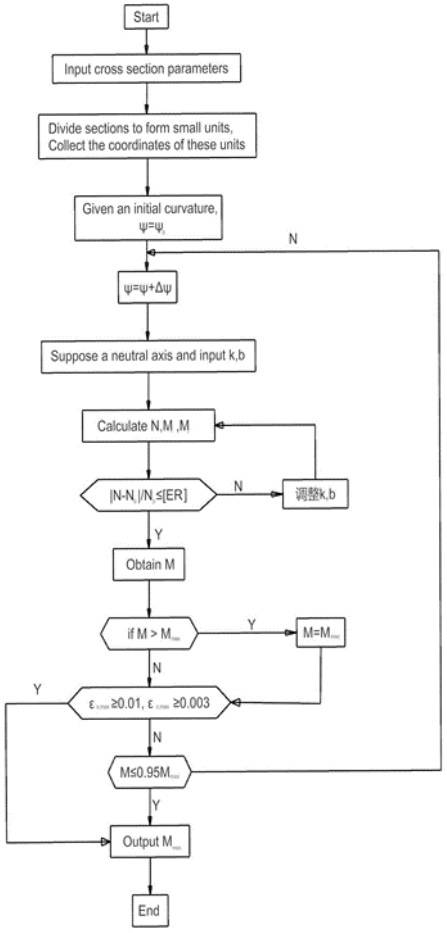

Fig. 10 Flowchart illustrating the proposed method.

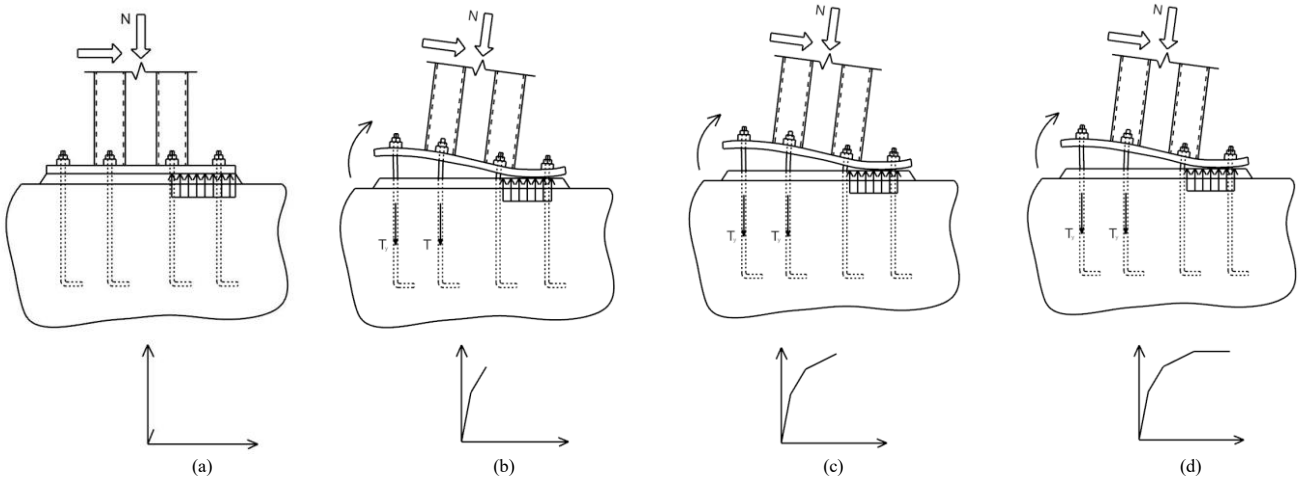

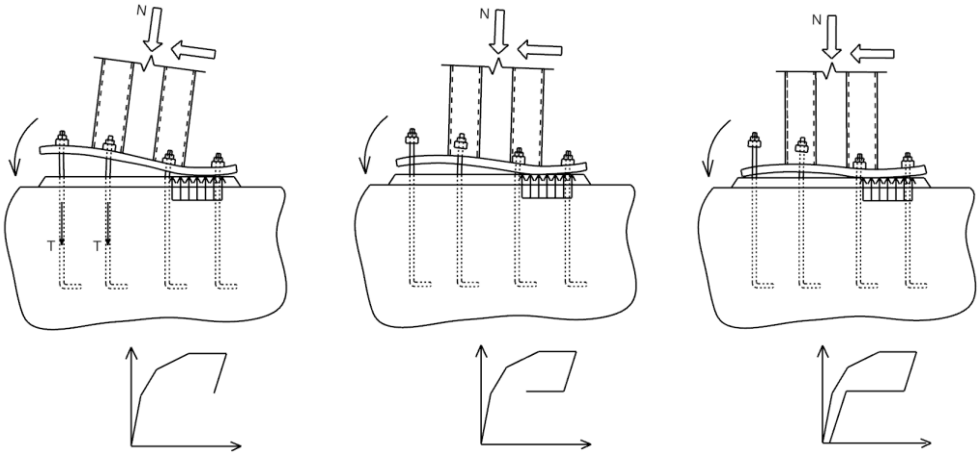

(e) (f) (g)

Fig. 11 Connection response and associated load deformation curves.

4.4.2. Parameters Defining the Backbone Curve

The method presented in this section does not characterize the nonlinear interactions explicitly but rather provides a straightforward method that may be applied conveniently in a practical setting. Referring to Fig. 11, the applied moment may be resisted through the bearing stress block under the plate and tension forces in anchor rods. The failure started from the outer anchor rods to the inner rows. Each yield event corresponds to a change in the corresponding moment-rotation curves that are divided into several linear segments.

For example, the backbone curves of ZJ1 in the positive loading direction consist of five branches. Referring to Fig. 12, the initial elastic Phase I is defined by two parameters including the resistance moment M_1 and associated rotation θ_1. The second branch describes the second-yield event appearing in the end of Phase II. Two additional parameters define this branch, namely θ_2 and M_2. The end of the third branch decided by M_3 and θ_3 means that the yield of the third inner bolt. The strain of concrete in compression side attains 3000 $\mu\varepsilon$ before the fourth anchor bolt yields at the end of Phase VI. In Phase V, the backbone curve is described by a horizontal line representing ultimate strength plateau. The manner describing the backbone curve in the negative loading direction resembles similar laws. Each yield event corresponds to a turning point in the curves defined by M_i and θ_i.

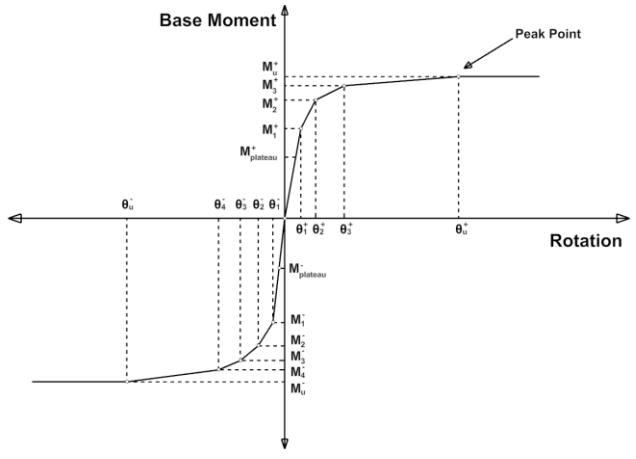

Fig. 12 Parameters defining the backbone curve.

Fig. 13 illustrates the vertical displacement of the base plate under cyclic loading. It can be seen that the part between the anchor bolts approximately satisfy the linear strain assumption. As the deformations of the rods are constrained by the base plate, the linear strain assumption can be extrapolated to the bottom section. Detailed process includes following steps:

(1) Moment of the bottom section.

First it could assume the outermost anchor bolt reached yield and its strain could be obtained using Eq. (11). The strain of other units is decided through the strain compatibility method shown in Fig. 10. In each step, one selected bolt is viewed to be yielding and the strain of concrete units should be proportional to that of the selected yield bolt. Equilibrium equations of the bottom section are outlined in Eq. (8), Eq. (9) and Eq. (10). The key parameter M_i of the backbone curve is equal to M_x in Eq. (8).

$$\varepsilon_{sy}=\frac{\sigma_y}{E_s} \tag{11}$$

$$\varepsilon_{si}=\varepsilon_{sy}\frac{d_{si}}{d_y} \tag{12}$$

$$\varepsilon_{ci}=\varepsilon_{sy}\frac{d_{ci}}{d_y} \tag{13}$$

Where ε_{sy} , σ_y are the yield strain and stress of the anchor bolt respectively, E_s is the elastic modulus of steel, ε_{si} is the strain of the bolts in tension side except for the selected yield bolt, ε_{ci} is the strain of each concrete unit in compression side, d_{si} is the distance from the centroid line of each anchor rod to the neutral axis, d_y is the distance from the centroid line of the selected yield bolt to the neutral axis, d_{ci} is the distance from the centroid of each concrete unit to the neutral axis.

(2) Calculation of the rotation.

The top drift consists of two parts, including the deformation of the L-CFST column and the base plate. The defined parameter θ_i is decided by following equations:

$$\Delta_{bolt}=\frac{\sigma_y l_b}{E_s} \tag{14}$$

$$\theta_{base}=\frac{\Delta_{bolt}}{(d_t+d_c)} \tag{15}$$

$$\theta_{column}=\frac{M_i H}{3EI_{eff}} \tag{16}$$

$$\theta_i=\theta_{base}+\theta_{column} \tag{17}$$

Where l_b is the length of the anchor bolt, Δ_{bolt} is the elongation of the anchor bolt, θ_{base} is the rotation of the bottom section, d_t is the distance from the centroid line of the selected yield anchor bolt to the neutral axis, d_c is the distance from the center line of the anchor rod in compression side to the neutral axis within the region that satisfies the linear strain assumption, θ_{column} is the rotation caused by the deformation of the L-CFST column, EI_{eff} is the flexural stiffness of the composite section according to [26].

The peak point of the backbone curve is defined by M_{max} and θ_u based on the proposed strength model and Eq. (18):

$$\theta_u=\mu\theta_y \tag{18}$$

Where μ is the ductility ratio obtained from simulations; θ_y is the yield rotation of the exposed connection.

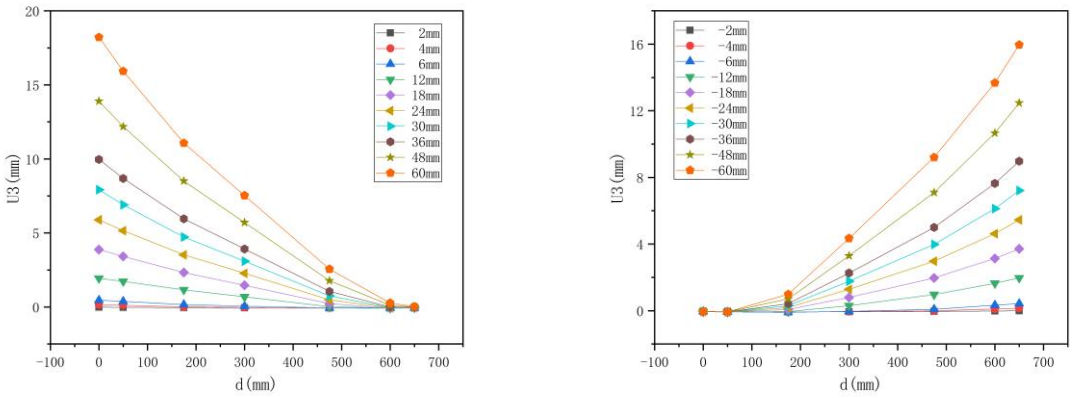

(a) under the positive loading condition (b) under the negative loading condition

Fig. 13 Vertical displacement of the base plate along the edge.

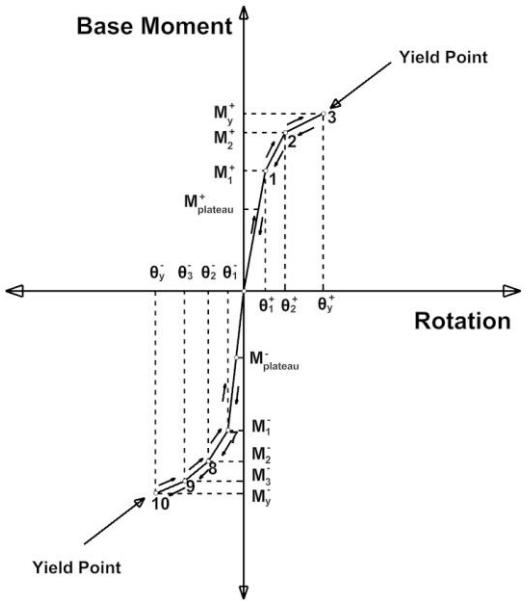

(a) $M<M_y$

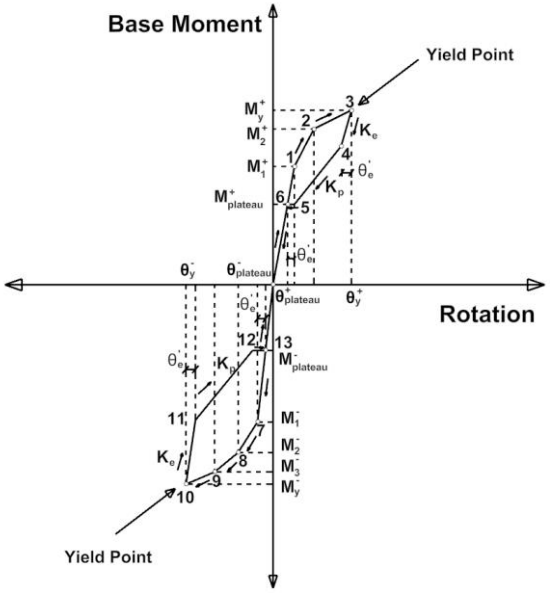

(b) $M_y<M<M_u$ (initial unloading process)

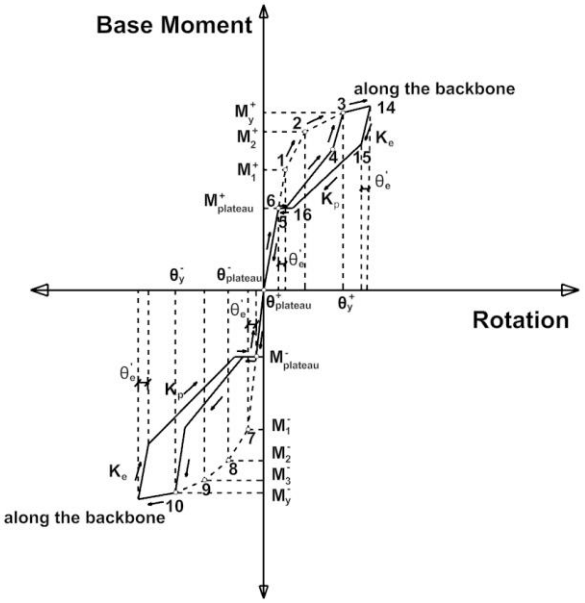

(c) $M_y<M<M_u$

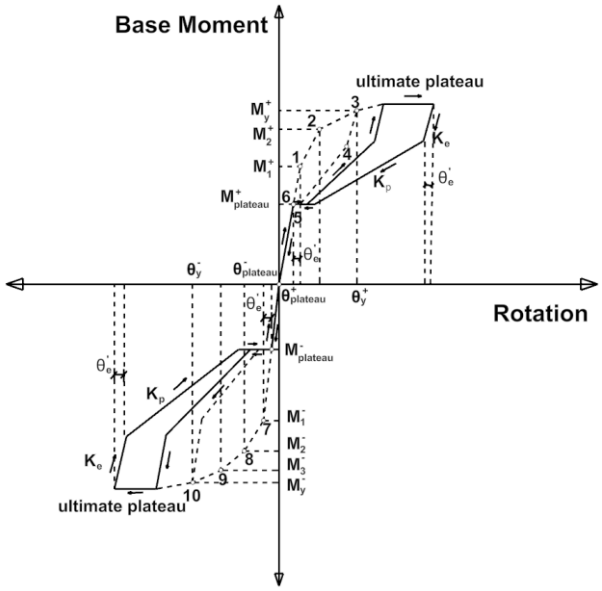

(d) $M>M_u$

Fig. 14 Proposed hysteretic model.

4.4.3. Rules and Parameters Defining Hysteretic Response

Fig. 14 illustrates the rules defining the hysteretic response of the exposed connections. Fig. 14(a) shows the initial phase before the yield point. Marker 1 represents the end of Phase I in which the outermost anchor bolt begins to yield. Marker 2 reflects the second-yield event of the inner anchor bolt at the end of phase II. The yield moment of the connection under the positive loading conditions is defined as Marker 3 at the end of Phase III. Unlike the traditional exposed type, connections in this study have inner bolts, such that single yield event cannot represent the yield of the whole. After the former three stages, there is a significant decline in stiffness of the connection. Thus, it is reasonable to regard Marker 3 as the yield point in the positive loading direction. In the same way, Marker 10 in the negative loading condition is defined as the yield point when the fourth anchor bolt begins to yield.

Observing the curves in Fig. 14, the unloading process can be divided into four stages. Stage 1 is the initial elastic unloading process. Stiffness of the first stage, namely K_e , is equal to the average of phases that the yield point has not occurred. The rotation $\theta_e^{'}$ in this stage is decided by following equations:

$$K_I=\frac{M_1}{\theta_1} \tag{19}$$

$$K_{II}=\frac{M_2-M_1}{\theta_2-\theta_1} \tag{20}$$

$$K_{III}=\frac{M_3-M_2}{\theta_3-\theta_2} \tag{21}$$

$$K_e=1/3((K_I+K_{II}+K_{III}) \tag{22}$$

$$\theta_{plateau}=\frac{M_{plateau}}{K_I} \tag{23}$$

$$\theta_e^{'}=\theta_1-\theta_{plateau} \tag{24}$$

Where K_I is the initial stiffness of Phase I; K_{II} is the secant stiffness of Phase II; K_{III} is the secant stiffness of Phase III, K_e is the elastic unloading stiffness of Stage 1; $\theta_{plateau}$ is the rotation corresponds to the intermediate plateau; $M_{plateau}$ is the moment discussed earlier when the anchor bolt has not developed tension force; $\theta_e^{'}$ is the recoverable rotation in the first unloading stage.

Marker 4 is the end point of this stage decided by K_e and $\theta_e^{'}$. Referring to previous discussions, the pinching phenomenon is caused by cumulated plastic deformation in anchor rods, reflected in Stage 2. The unloading path terminates at Marker 5 containing two parameters $M_{plateau}$ and K_p:

$$M_{plateau}=N\times e \tag{25}$$

$$K_p=\frac{(M_t-M_{plateau})}{(\theta_t-\theta_{plateau})} \tag{26}$$

Where e is the distance from the axial force to the resultant stress line in compression side; K_p is the unloading stiffness of the second unloading stage.

From the simulations with regard to stress distributions under the base plate, the definition of e in Eq. (25) is shown in Fig. 15. Owing to the special shape of the base plate, the stress profiles in two directions are different, which are closer to rectangular in the positive direction and triangular in the negative direction. The width of the stress block is equal to the distance from the outermost anchor bolt to the edge of the base plate in the positive loading direction, while that of the negative direction is equal to the distance from the edge of the L-CFST column to the edge of the base plate.

After Maker 5, the moment maintains a constant value called $M_{plateau}$ which corresponds to the free motion of the base plate caused by the separation between the base plate and nuts. The moment in this stage is resisted by the combined effects of the stress block under the base plate and the applied axial load. Marker 6 is the end of this stage. In the fourth unloading stage, the path retraces previous loading path. Further loading and unloading path in the negative direction follows the similar laws described previously from Marker 7 to Marker 13.

Fig. 14(b) shows one full scale of loading and unloading process when the moment first reaches the yield point. Subsequent reloading process in the positive direction follows previous unloading path from Marker 6 to Marker 3 and continues along the backbone curve as illustrated in Fig. 14(c). With reference to Fig. 14(d), the model maintains the maximum moment after the connection reaches the limit state with the assumption of no deterioration phenomenon existing within the loading and unloading process.

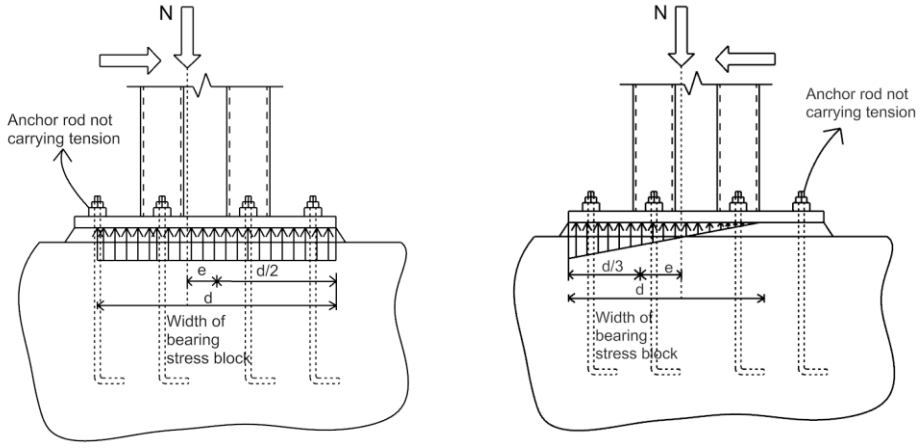

(a) in the positive loading condition (b) in the negative loading condition

Fig. 15 Illustration of stress distributions used for calculation as Eq. (25).

4.4.4. Discussion of the results

Fig. 16 shows the comparison between simulations and calculations using the proposed hysteretic model. It can be seen that the overall response of the connection is well simulated, such that the model may be suitable to characterize the base connection response for which experimental data is not available. The core parameters are determined independently according to configurational details, such that the model is convenient to be generalized into different connection details.

However, there are several inaccurate aspects in the proposed model. First, the simplified hysteretic model does not consider the deterioration from cycle to cycle, such as the strength decline, stiffness degradation and the intermediate plateau decrease, which may be caused by concrete spalling, base plate yield or other damage phenomenon. Second, the unloading path cannot agree well with the simulated results accurately, mainly associated with the methods that are used to determine the parameters of the hysteretic model. Third, the ultimate strength is underestimated, which may be explained by the underestimation of the compressive strength of concrete.

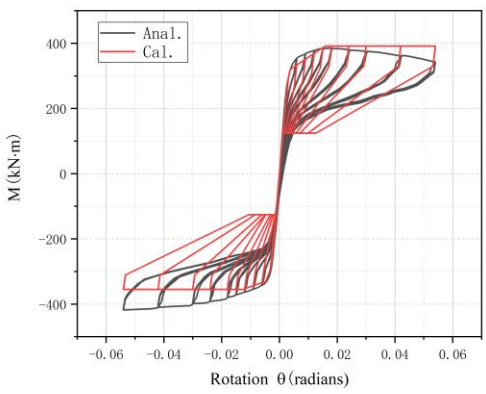

(a) comparison of Model 1

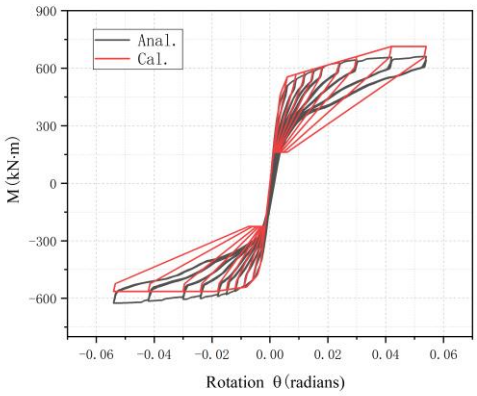

(b) comparison of Model 2

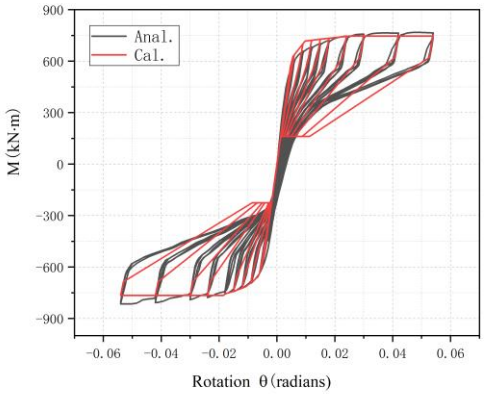

(c) comparison of Model 3

Fig. 16 Comparison between simulations and calculations.

5. Summary and Conclusions

The exposed column base connections, investigated in this paper is different from the traditional one owing to its special-shaped base plate and the eight-rod anchor bolt layouts, improving the difficulties in describing the mechanic properties of this connection. Current design methods in [23] are mainly applicable to steel column bases. Thus, they are limited to be used in the calculation of L-CFST column base connections. Moreover, these methods are verified only on the basis of overall agreement with test data, while stress distributions and behavioral modes affected by many parameters have not been examined. In additional, there is no explicit design method for such connections in practical settings. To address these issues, the paper established three FE models to simulate the seismic behaviors of the exposed L-CFST column base connections which were verified against previous study [24]. The paper aims to use the simulated results of these connections to investigate the force distributions within the connection and develop an appropriate model for describing their seismic performance. The key finding is that the stress distribution is related to the thickness of the base plate, not simply using the rectangular block in previous assumptions, which can be attributed to the differences in their stiffness. Regardless of the limited parameters investigated in this study, it can be found that the flexural resistance for these connections is improved with enhanced settings.

In this paper, the column base, subjected to cyclic lateral loads, moves in both directions during loading process which leads to a biaxial bending effect on the base plate. Based on the analytical results, a strength calculation method was proposed. The model assumed that the strain distribution under the plate was linear combining features of the "plastic stress distribution method" utilized in [28]. Compared with the simulations, the method could provide reasonable predictions for flexural strength of the connection. And then, the method was extrapolated to define the backbone curve of the hysteretic model, formed by several linear segments. The core parameters that have the most dominant effect on the hysteretic response can be obtained directly from configurational details, even if no experiment data is available for calibration.

Although the paper has proposed some specific suggestions for the connection design and its inelastic response, it is important to realize the limitations of this study. First, the FE simulation is still fairly limited in terms of the number of parameters studied. Thus, the derivations may not be reliable to connections that are significantly dissimilar to the models in this study. Second, the flexural evaluating method developed in this paper has several limitations that must be considered in its application. For example, the strain distribution assumed to be linear under the base plate is a lack of experimental validation. The current hysteretic model has several limitations, such as its inaccuracy to capture the unloading branch; its inability to incorporate the degradation phenomenon and its ignorance of the discontinuity of the intermediate plateau. Third, the column base models are subjected to a non-proportional loading history, such that the lateral force increases with constant axial load. It cannot represent the seismic loading scenarios. Current hysteretic model represents an appropriate balance between simplicity and accuracy that can be modified by incorporating more parameters. However, it would increase the complexity of the model and limit its generalization.

Acknowledgements

This research was sponsored by the National Key R&D Program of China（2019YFD1101005）.

References

[1] Han, L.H., Li, W. and Bjorhovde, R., "Developments and advanced applications of concrete-filled steel tubular (CFST) structures: Members", Journal of Constructional Steel Research, 2014, 100, pp. 211–228.

[2] Chen, Z.H., "New-type special-shaped column by steel structure and composite structure", Steel Construction, 2006, 21(2), pp. 27-29(in Chinese).

[3] Xu, M.Y., Zhou, T., Chen, Z.H., Li, Y.B. L. and Bisby, L., "Experimental study of slender L-CFST columns connected by steel linking plates", Journal of Constructional Steel Research, 2016, 127, pp. 231–24.

[4] Zhang, W., Chen, Z.H. and Xiong, Q.Q., "Performance of L-shaped columns comprising concrete-filled steel tubes under axial compression", Journal of Constructional Steel Research, 2018, 145, pp. 573–590.

[5] Rong, B., Chen, Z.H., Apostolos, F. and Yang, N., "Axial compression behavior and analytical method of L-shaped column composed of concrete-filled square steel tubes", Transactions of Tianjin University, 2012, 18(3), pp. 180–187. 18 (3) (2012) 180–187.

[6] Chen, Z.H., Rong, B., Apostolos, F., "Axial compression stability of a crisscross section column composed of concrete-filled square steel tubes", Journal of Mechanics of Materials and Structures, 2009, (10), pp. 1787–1799.

[7] Zhou, T., Chen, Z.H. and Liu, H.B., "Seismic behavior of special shaped column composed of concrete filled steel tubes", Journal of Constructional Steel Research, 2012, 75, pp. 131–

141.
[8] Chen, Z.H., Zhou, T., and Wang, X.D., “Application of special shaped column composed of concrete-filled steel tubes”, Advanced Materials Research, 2011, 163-167, pp. 196–199.
[9] Zhou, T., Jia, Y.M. and Xu, M.Y., “Experimental study on the seismic performance of L-shaped column composed of concrete-filled steel tubes frame structures”, Journal of Constructional Steel Research, 2015, 114, pp. 77–88.
[10] Chen, Z.H., Zhao, B.Z., Li, B., Yu, J.H., Yan, X.Y., Wang, D.N. and Zhou, T., “Pushover analysis of special-shaped concrete filled rectangular steel tubular frame-brace system, Industrial Construction, 2017, 47(6), pp. 152–157(in Chinese).
[11] Picard, A. and Beaulieu, D., “Behavior of a simple column base connection”, Canadian Journal of Civil Engineering, 1985, 12(1), pp. 126–136.
[12] Thambiratnam, D.P. and Paramasivam, P., “Base plates under axial loads and moments”, Journal of Structural Engineering, 1986, 112(5), pp. 1166–1181.
[13] Ermopoulos, J. and Stamatopoulos, G., “Mathematical modeling of column base plate connections”, Journal of Constructional Steel Research, 1996, 36, pp. 79–100.
[14] Ermopoulos, J. and Stamatopoulos, G., “Analytical modeling of column base plates under cyclic loading”, Journal of Constructional Steel Research, 1996, 40(3), pp. 225–238.
[15] Jaspart, J.P. and Vandegans, D., “Application of the Component Method to Column Bases”, Journal of Constructional Steel Research, 1998, 48(2-3), pp. 89–106.
[16] Stamatopoulos, G.N. and Ermopoulos, J.Ch., “Experimental and analytical investigation of steel column bases”, Journal of Constructional Steel Research, 2011, 67(9), pp. 1341–1357.
[17] Kanvinde, A.M., Grilli, D.A. and Zareian, F., “Rotational stiffness of exposed column base connections: Experiments and Analytical Models”, Journal of Structural Engineering, 2012, 138(5), pp. 549–560.
[18] Kanvinde, A.M., Jordan, S.J. and Cooke, R.J., “Exposed column baseplate connections in moment frames—Simulations and behavioral insights”, Journal of Structural Engineering, 2013, 84, pp. 82–93.
[19] Kanvinde, A.M., Higgins, P., Cooke, R.J., Perez, J. and Higgins, J., “Column Base Connections for Hollow Steel Sections: Seismic Performance and Strength Models”, Journal of Structural Engineering, 2015, 141(7), pp. 04014171.
[20] Latour, M., Piluso, V. and Rizzano, G., “Rotational behavior of column base plate connections: Experimental analysis and modelling”, Engineering Structures, 2014, 68, pp. 14-23.
[21] Rodas, P.T., Zareian, F. and Kanvinde, A., “Hysteretic Model for Exposed Column–Base Connections”, Journal of Structural Engineering, 2016, 142(12), pp. 04016137.
[22] Latour, M. and Rizzano, G., “Mechanical modelling of exposed column base plate joints under cyclic loads”, Journal of Constructional Steel Research, 2019, 162, pp. 105726.
[23] CECS-230-2008，Specification for Design of Steel-concrete Mixed Structure of Tall Buildings, China Association for Engineering Construction standardization, 2008 (in Chinese).
[24] Xiong, Q.Q., Chen, Z.H., Kang, J.F., Zhou, T. and Zhang, W., “Experimental and finite element study on seismic performance of the L-CFST-D columns”, Journal of Constructional Steel Research, 2017, 137, pp. 119–134.
[25] Zareian, F., and Kanvinde, A., “Effect of Column Base Flexibility on the Seismic Response and Safety of Steel Moment Resisting Frames”, Earthquake Spectra, 2013, 29(4), pp. 1537–1559.
[26] ANSI/AISC 360-05, Specification for Structural Steel Buildings, American Institute of Steel Construction, 2005.
[27] GB 50010-2010, Code for design of concrete structures, China Association for Engineering Construction Standardization, 2010(in Chinese).
[28] Xu, W., Han, L.H. and Li, W., “Seismic performance of concrete-encased column base for hexagonal concrete-filled steel tube: experimental study”, Journal of Constructional Steel Research, 2016, 121, pp. 352–369.

Advanced Steel Construction – Vol. 17 No. 4 (2021) 366–375
DOI:10.18057/IJASC.2021.17.4.5

EXPERIMENTAL BEHAVIOR AND DESIGN OF RECTANGULAR CONCRETE-FILLED TUBULAR BUCKLING-RESTRAINED BRACES

Yan-Chao Yue [1], Yong-Tao Bai [2, *], Yan Wang [1], Xiao-Fei Ma [3], Yu-Hang Wang [2] and Xiao-Hua Li [2]

[1] *Department of Civil Engineering, Xi'an Jiaotong University, Xi'an 710049, China*
[2] *School of Civil Engineering, Chongqing University, Chongqing 400045, China*
[3] *China Railway First Survey and Design Institute Group Co., Ltd., Xi'an 710043, China*
** (Corresponding author: E-mail: bai.yongtao@cqu.edu.cn)*

ABSTRACT

This paper proposes a new design method for concrete-filled tubular buckling-restrained braces (CFT-BRBs) by incorporating the confinement effect on pre-buckling rigidity. A series of experiments are performed to investigate the effects of concrete strength and sectional dimension on the initial stiffness, ultimate strength, and energy dissipation behaviors. Experimental results indicate that the confined concrete plays an important role in the energy dissipating capacity of CFT-BRBs. On the other hand, the sectional dimensions of the steel tube and core are influential factors governing the ultimate failure modes of CFT-BRBs. The findings in study provide technical supports to optimize the design methods for ductile seismic performance of CFT-BRBs in low-rise and high-rise steel buildings.

ARTICLE HISTORY

Received: 25 January 2021
Revised: 27 May 2021
Accepted: 28 May 2021

KEYWORDS

Buckling-restrained braces;
Concrete-filled steel tube;
Buckling mechanism;
Cumulative plastic deformation;
Energy dissipation;
Performance-based design

1. Introduction

Buckling Restrained Braces (BRBs) as structural control dampers with stable performance and good energy dissipation effect, have been widely used in building engineering practice across the world. The earliest idea on BRBs can be traced back to the 1960s in the case of steel braces enclosed by the reinforced concrete shear wall [1, 2, 3]. Afterwards, the prototypical BRBs were developed by the Tokyo Tech and Nippon Steel in 1988 [4-9]. The initial design for a BRB typically includes a core steel element and an external restraining system. The core steel element, which is the energy-dissipating element, generally consists of a thin-plate section, cross-section, or H-section. The external restraining component such as hollow or concrete-filled steel tubes, restrains the inner core from losing its overall stability to ensure its strength capacity. Between the core steel member and the external restraining system, an un-bonded material is set so that the core steel and external restraining system can be fully isolated and maintain a certain gap. This treatment not only provides deformation space for the expansion of the core section caused by the Poisson effect, also eliminates the adverse effects caused by friction.

In recent years, several scholars around the world have carried out in-depth and comprehensive research on buckling restrained braces from the aspects of structure configurations, material properties, engineering applications, and mechanical properties. In terms of structural configuration, Zhu et al. [10] developed a core-separated BRB, called corrugated-web connected buckling-restrained brace (CWC-BRB), which has much larger flexural stiffness and load-carrying capacity compared to ordinary single-cored steel BRBs [10, 11]. Wang et al. [12] proposed a brace with partial buckling restraint, called the partially buckling-restrained brace (PBRB), which is designed for quick damage evaluation of BRBs after earthquake without disassembling the restraining members. Xie et al. [13] proposed a sandwiched BRB that eliminated the use of unbonded materials, where the core plate could be replaced independently of the restraining members after a large earthquake. Tsai et al. [14] proposed double-tube BRBs that adopt double tee to gusset plate connections, which can reduce the length of the connection. From the point of view of material properties, Hu et al. [15] reviewed the SMA-alloy buckling-restrained braces due to the advantages of aluminum and its alloys that include being lightweight, corrosion resistance and economic and environmental benefits. Wang et al. [16] studied the effects of different un-bonded materials on the mechanical properties of buckling restrained braces. The application and seismic response of BRBs in structures or frames are also investigated using experimental examinations or numerical simulations by many researchers [17, 18, 19].

From the mechanical properties of braces, suitable buckling restrained braces must satisfy the following conditions [20]:

- They should have a good hysteretic curve to ensure that braces do not suffer from overall instability under tension and compression cyclic loads, and the restrained element must have sufficient flexural stiffness and strength. Many researchers have conducted in-depth studies about the overall instability of BRBs and proposed many formulas for design purposes [21, 22, 23].
- The steel core element should not suffer from local instability under the designed axial force and deformation. [20, 24-32].
- The connection joints should have sufficient stiffness to ensure that the braces do not suffer from overall instability under the designed axial force and deformation [33].

However, in the previous studies on the mechanical properties of braces, restraining effects of filled concrete on core steel are neglected or given an approximate reduction factor, without considering the influence of the strength and stiffness of concrete on the overall stability. Compared to the all-steel buckling restrained braces, the concrete pairs in the filled buckling restrained braces are different from those in the all-steel buckling restrained braces. The energy dissipation capacity plays an important role in the hysteretic behavior of buckling restrained braces. The question of how to reasonably consider the effect of concrete on the mechanical properties of buckling restrained braces to reduce the size of restrained members with economical and reasonable filled buckling restrained braces provides invaluable theoretical and engineering values. For those purposes, several groups of specimens are designed to study the influence of concrete strength and section dimensions on the mechanical performance of BRB.

2. Evaluation of failure criteria of concrete-filled tubular BRBs

2.1. Overall buckling of CFT-BRBs

The mechanism of BRB's overall stability is shown in Fig. 1. The core plate generally loses its overall stability before yielding when the restraint member cannot provide sufficient stiffness. It is assumed that the tangential friction between the core plate and concrete is zero, the tube and concrete are tangentially non-slippery, the length of the core material and restraint tube is equal, and the restraint tube has no initial defects. The initial defect of core steel thus is:

$$v_0 = 2 \times g \times \sin\left(\frac{\pi x}{l}\right) \tag{1}$$

where v_0 is the initial imperfection, g is the lateral gap between the steel core and outer tube, l is the buckling length of the outer tube, and x is the distance from the specified brace cross-section to the end, respectively. In Eq. (1), the shape of the first-order buckling mode is adopted for the imperfection

deformation, which is correlated with the numerical results of the finite element analysis. It is usually reasonable to define the gap width as twice that of the imperfection amplitude so that the moment and deformation of "one point contact" between the steel core material and concrete infill can be regarded as the initial imperfection.

According to the static equilibrium method, as shown in Fig. 2, the bending moment equilibrium based on the position of the neutral axis of the core section is given in Eq. (2). The inertia moment of the core plate to the neutral axis is extremely small, and the tangent modulus of the steel after yielding is generally only 1% to 2% of the elastic modulus. Therefore, to simplify the model, the bending stiffness of the core plate is ignored.

$$EI\frac{d^2v}{dx^2}+(v+v_0)P_{max}=0 \tag{2}$$

$$EI=E_bI_b+\alpha E_cI_c \tag{3}$$

where P_{max} is the ultimate axial force of core plate; v is the transverse deflection deformation of steel tubes; E is the elasticity modulus; I is the inertial moment; E_b、I_b are the elasticity modulus and inertial moment of steel tubes, respectively; E_c、I_c—elasticity modulus and inertial moment of filled concrete and α is stiffness reduction factor of concrete. For simplicity, by assigning $k^2=P_{max}/EI$ Eq. (2) can be written as:

$$v"+k^2v=-k^2v_0 \tag{4}$$

The general solution of Eq. (4) can be stated as:

$$v=C_1sinkx+C_2coskx \tag{5}$$

Assuming the special solution is:

$$v^*=C_3sin\frac{\pi x}{l} \tag{6}$$

Substitute Eq. (1) into Eq. (4), we get:

$$-\frac{\pi^2}{l^2}\cdot C_3sin\frac{\pi x}{l}+k^2\cdot C_3sin\frac{\pi x}{l}=-k^2\cdot 2gsin\frac{\pi x}{l} \tag{7}$$

Substitute the formula ($P_E=\frac{\pi^2EI}{l^2}$) into Eq. (7), then we can get Eq. (8):

$$-\frac{P_E}{EI}\cdot C_3sin\frac{\pi x}{l}+\frac{P_{max}}{EI}\cdot C_3sin\frac{\pi x}{l}=-\frac{P_{max}}{EI}\cdot 2gsin\frac{\pi x}{l} \tag{8}$$

From the above equation, we can obtain $C_3=\frac{2g}{\frac{P_E}{P_{max}}-1}$, so the general solution of Eq. (2) is:

$$v=C_1sinkx+C_2coskx+\frac{2g}{\frac{P_E}{P_{max}}-1}sin\frac{\pi x}{l} \tag{9}$$

Considering the boundary conditions: (0) =0, (l)=0, we can get C_1sinkx=0,C_2=0. Since $P_{max}<P_E$, so $sinkl\neq 0$, C_1=0. Eq. (9) can be written as:

$$v=\frac{2g}{\frac{P_E}{P_{max}}-1}sin\frac{\pi x}{l} \tag{10}$$

The mid-span bending moment of the BRB is:

$$M_c=\frac{2g\cdot P_{max}}{1-\frac{P_{max}}{P_E}} \tag{11}$$

where M_c is the mid-span bending moment of BRB components. The maximum stress at the edge of the mid-span section of the steel tube is:

$$\sigma_{max}=\frac{M_cH}{2I}=\frac{gHP_{max}}{I(1-\frac{P_{max}}{P_E})} \tag{12}$$

where H is the height of steel tube.
Since the first-order Euler force is $P_E=\frac{EI\pi^2}{l^2}$, Eq. (12) can be written as:

$$\sigma_{max}=\frac{M_cH}{2I}=\frac{E\pi^2gHP_{max}}{P_El^2(1-\frac{P_{max}}{P_E})}=\frac{E\pi^2gH}{l^2(\frac{P_E}{P_{max}}-1)}\le f_y \tag{13}$$

$$\frac{P_E}{P_{max}}\ge 1+\frac{E\pi^2gH}{f_yl^2} \tag{14}$$

$$\frac{P_E}{P_{yp}}\ge \omega\left(1+\frac{E\pi^2gH}{f_yl^2}\right)$$

where f_y is the yield strength of steel tube; P_{yp} is the yield axial force of core plate; ω is the strain hardening coefficient;

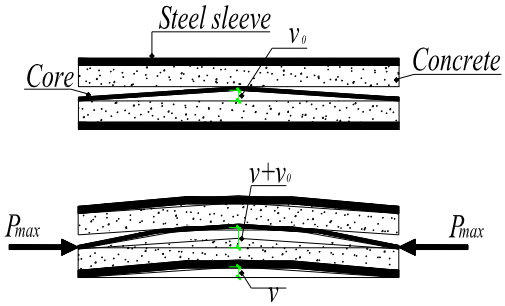

Fig. 1 Schematic diagram of overall stability mechanism of buckling restrained braces

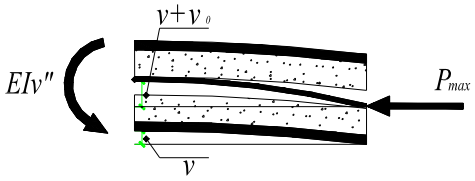

Fig. 2 Schematic diagram of the static equilibrium method

2.2. Local buckling of CFT-BRBs

By satisfying the formula about the constraint ratio limit of tube stiffness, the overall instability of CFT-BRBs can be avoided theoretically. However, this cannot prevent the local buckling of the steel core.

Takeuchi et al. [20, 24, 34] concluded that when the restraint tube can provide sufficient stiffness, the steel core change from first-order buckling to higher-order buckling until the core plate yields. At this moment, the wavenumber does not change and the wavelength decreases. Based on these assumptions, the formula of half-wavelength buckling and the magnitude of local extrusion force is given, and then the local bearing capacity of the restrained member is checked.

Assuming that the wavenumber of the core plate remains unchanged after yielding, with the increase of axial deformation following phenomenon occurs:

- The axial load will be further strengthened due to strain strengthening
- The wavelength of buckling will be further shortened, and
- The local extrusion force will be further increased.

Therefore, for the energy dissipation of the BRB, the ultimate load should be considered as the most disadvantageous condition to check the local bearing capacity.

In Fig. 3 (a), when the core yields, the wavenumber does not increase anymore. Based on the theoretical hypothesis of Takeuchi et al. [20, 24, 34], the inner core segment between adjacent contact points, as shown in Fig. 3 (b), can be regarded as a stress formula conforming to the eigenvalue buckling. Here, the length of the inner core segment between adjacent contact points is defined as the buckling half-wavelength. According to the static equilibrium relation of Fig. 3 (b), the thrust is solved by combining Eqs. (15) and (16):

$$P_b = \frac{2P_{\max}\left(2g + v_p \varepsilon_{\max} t_p\right)}{L_w} \tag{15}$$

where v_p, t_p and ε_{max} are the plastic Poisson's ratio v_p=0.5, the thickness of the core plate, and the maximum tensile strain of the core plate, respectively. L_w is the total wavelength which can be predicted as follows (28, 29, 33):

$$L_w = \pi t_p \sqrt{\frac{E_{tp}}{3 f_{yp}}} \tag{16}$$

where E_{tp} is the tangent modulus of the core plate, and f_{yp} is yield stress of the core plate.

Eq. (15) gives the local bearing demand of restrained members under the ultimate load. To solve the local resistance of constrained members, a simplified model of local resistance of constrained members should be established first as seen in Fig. 4, the plastic hinge design theory is adopted here.

When the thrust of the steel core plate to sleeve exceeds a certain value, the concrete will be fractured along the oblique section and lose its shear resistance. The load will spread to the inner surface of the steel tube. When the local bearing capacity of the steel tube is insufficient, plastic hinges will appear at the boundary of uniform load and the support seat, which is the four-hinged yield mechanism (as shown in Fig. 4 (a)). On the other hand, as for large width of the steel core plate, the steel tube is subjected to uniformly distributed loads creating plastic hinges in the middle of span and support hence forming a three-hinged yield mechanism (Fig. 4(b)). Kishiki [35] and Junxian Zhao et. al [36, 37] pointed out that the failure criterion of resistance should be the edge yield of restrained members. However, the failure criterion of local resistance of buckling restrained braces is different from the edge yield criterion of global instability.

CFT-BRBs can continue to work until irreversible plastic deformation occurs on the sleeve surface. Therefore, the failure criterion of the sleeve plastic hinge forming mechanism is proposed in this paper.

In Fig. 4(a), according to the plastic hinge theory, the ultimate lateral resistance of the steel tube can be given as follows:

$$M_{max} = \frac{qB(B_c + 2at_c)}{24}\left(3 - 3\frac{B_c + 2at_c}{B} + \frac{(B_c + 2at_c)^2}{B^2}\right) \le M_p \tag{17}$$

$$M_p = \frac{Bt^2}{4} f_y \tag{18}$$

$$F_R' = q(B_c + 2at_c) \tag{19}$$

where F_R' is the lateral force resistance of tube; t_c is the concrete thickness between core and tube; a is the transfer coefficient of the oblique section, here a=1; where: M_p is lateral ultimate moment of steel tube; B is the width of steel tube; q is the uniformly distributed load, and t is the thickness of steel tube.

From Eqs. (17), (18), and (19), F_R' can be solved as:

$$F_R' \le \frac{6t^2 f_y}{3 - 3\frac{B_c + 2at_c}{B} + \frac{(B_c + 2at_c)^2}{B^2}} \tag{20}$$

When $B \le B_c + 2t_c$, the failure mode of steel tubes becomes the yield mechanism with three hinges, as in Fig. 4 (b), then:

$$M_{max} = \frac{qB^2}{12} \le M_p \tag{21}$$

$$M_p = \frac{Bt^2}{4} f_y \tag{22}$$

$$F_R' = qB \tag{23}$$

Combining Eqs. (21), (22), and (23), F_R' can be obtained as follows:

$$F_R' \le 3t^2 f_y \tag{24}$$

Once $F_R' < P_b$, the out-of-plane local buckling failure will arise. For a zigzag steel core plate, buckling is more likely to occur in the direction of the weak axis. Note that buckling in the direction of the strong axis is not covered the scope of this section.

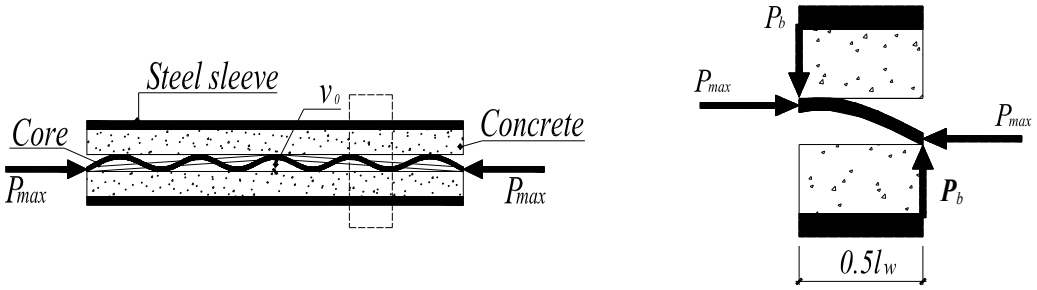

Fig. 3 Schematic diagram of buckling deformation and stress mechanism of core plate

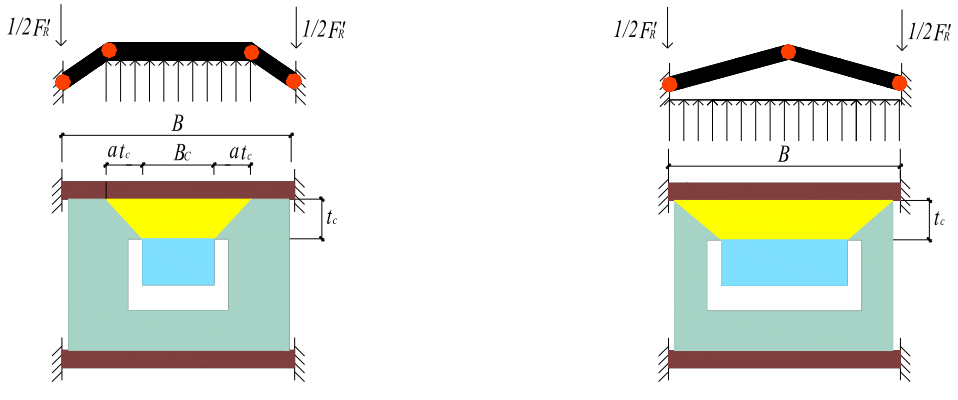

Fig. 4 The local buckling mechanism of BRB (a)with four hinges (b)with three hinges

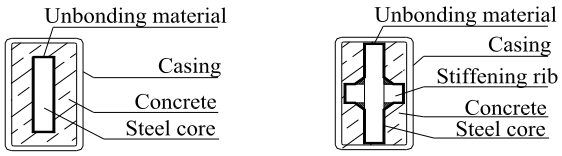

Fig. 5 Cross-section of specimens

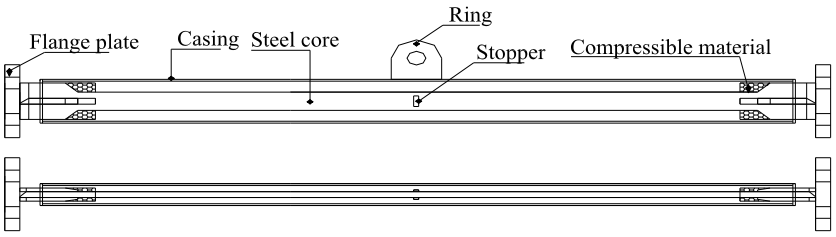

Fig. 6 The side view and top view of specimens

3. Test program

3.1. Test specimen

Eleven specimens with different dimensions and concrete strengths were designed for the test. All the core steel used is of an I-shape steel plate and wrapped with non-bonding material. It is composed of a yielding segment and steel core projections with ribs. The sleeve is made of a rectangular steel tube. The concrete material is filled between the core steel and the sleeve. The cross-section of the specimens is shown in Fig. 5. The side view and top view are shown in Fig. 6.

In this test, two core sections are examined. These core sections are 80 mm x 16 mm and 50 mm x 16 mm, respectively with two strength grades of Q235B and Q345B. The length of the core is 1400 mm. A section steel pipe is used for the tube to eliminate the effect of welding on sleeve performance. The length, width, height of the tube are 1500 mm, 120 mm, and 60 mm, respectively, and the strength grade is Q235, with the only difference in its thickness. The concrete grades filled between the steel core and tube are H20, H40, and H60, respectively. The thickness of the un-bonded material is 1.5 mm. The eleven specimens are named as 80×16-2.75-H40-235, where 80×16 is the cross-section of the steel core, 2.75 is the thickness of steel tube, H40 denotes the concrete strength grade and 235 represents the strength grade of the steel core.

The material properties of the steel used in the test are shown in table 1. Similarly, table 2 shows the material parameters of concrete. All material parameters in table 1 and table2 are the arithmetic mean of measured values of several test pieces.

Table 1
The material properties of the steel tube

Material	Thickness t(mm)	Yield strength (MPa)	Ultimate strength (MPa)	elasticity modulus (MPa)	Ductility ratio (%)	Yielding strain (%)
Q345B	16	396.06	524.89	191386.30	36.28	0.1988
Q235B	16	260.91	417.04	230811.40	24.44	0.1356

Table 2
The material properties of filled concrete

Filled concrete	Flexural strength（Mpa）	Compressive strength（Mpa）
H20	6.85	32.34
H40	12.74	57.70
H60	14.80	71.00

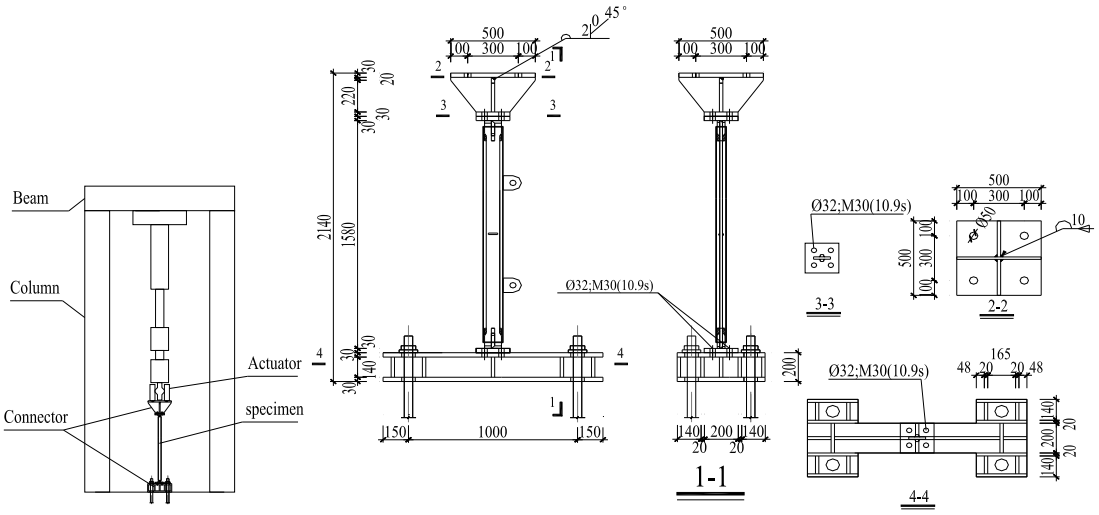

(a) Schematic diagram of BRB installation (b) Front view and side view of connectors

Fig. 7 Installation of BRB specimen

3.2. Loading program and measurements

According to the seismic provisions about the quasi-static test in Chinese code (JGJ/T 101-2015), horizontal low cyclical loading was applied to the top side of specimens after a constant vertical load was applied. The level of the vertical load was determined as specified in GB 50011 (2010).

The data recorded in the experiment is the axial displacements of the specimens and the output forces of the actuator. The type of strain gauge used is the BX120-5AA metal strain gauge, and the type of displacement meter used is YHD100 displacement meter. The data of strain gauge and displacement meter are collected by a dynamic and static testing system.

To accurately obtain the axial displacement of the specimen, two pull-line displacement meters are arranged symmetrically at the connection plates and the energy dissipation section of the specimen to eliminate the influence of the bending deformation. The final displacement is averaged by the data of the symmetrical displacement gauges. Since the displacement gauge arranged at the connection plate is fixed at the specimen, it can be considered that the measured displacement does not contain the errors of bolt slip, rigid displacement, and elastic deformation of the fixed support. The positions of six displacement gauges are shown in Fig. 8.

The specimens were vertically mounted on the Material Test System (MTS) in the Civil Structure Laboratory of Shanghai Normal University. A hydraulic actuator, with a loading capacity of 1500kN and a displacement capacity of 100 mm, was used for the displacement-controlled cyclic loading. Loading is divided into two steps, the first step is preloading which is used to check the reliability of all the test devices, and the second step is formal loading with a loading speed of 0.1 mm/s.

The appendix of Recommended Provisions for Buckling-Restrained Braced Frames compiled by SEAOC (Structural Engineers Association Of California) and AISC(American Institute of Steel Construction) in the United States gives a detailed description of the repeated loading requirements in support tests.

American seismic code AISC (2010) gives a detailed description of the performance test method of BRBs. Based on the test methods in AISC [38] and Zhao [33]. The loading pattern in this experiment is as follows:

All the specimens are loaded with the same quasi-static loading pattern which was divided into three stages as shown in Fig. 9.

- The nominal strain amplitude ε is the axial deformation of the specimen divided by the whole length of the specimen which is 1580 mm.
- The first stage of loading pattern was a series of variable strain amplitude (VSA) loadings with stepwise strain amplitudes Δε (1/1000, 1/500, 1/300, 1/200, every strain amplitude was loaded by three cycles).
- In the second stage, the constant strain amplitude (CSA) loading with a strain amplitude of 1/150 was applied by 30 cycles.
- If the specimens were not damaged after the second stage, in the last stage, a series of VSA loading with strain amplitudes Δε (1/100, 1/75, l/60, 1/50, 1/40, 1/35, 1/30, 1/25, every strain amplitude was loaded by three cycles) until the failure of the specimens.

The loading procedures terminated when one of the following conditions occurs:

- The specimen is fractured
- The out-of-plane displacement of the specimen is too large (displacement recorded by displacement meters D2 and D3 is greater than 50 mm)
- The bearing capacity of the specimen decreases to 85% of the maximum bearing capacity during the third cyclic loading of the last stage deformation.

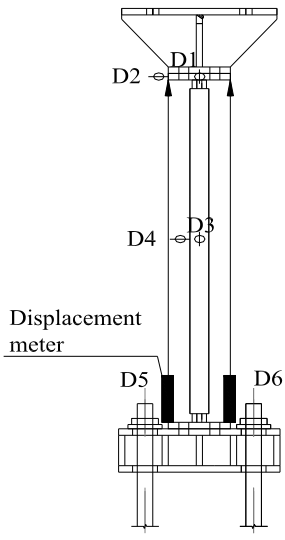

Fig. 8 Arrangement of displacement gages

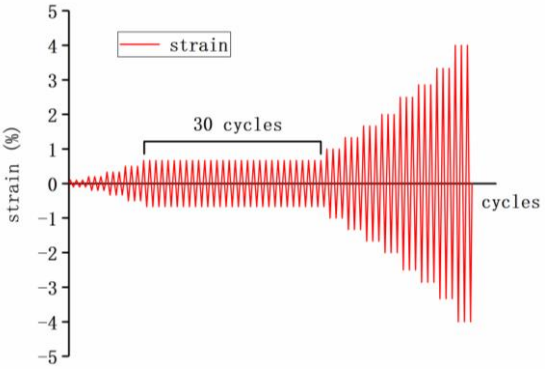

Fig. 9 The loading protocols of the test

4. Test results

4.1. Hysteretic curves

Hysteresis curves of the eleven specimens, which can be divided into two groups, are shown in Fig. 10. Figs. 10 (a), (b), (c), (h), and (i) show that hysteresis curves are full during the early loading, and then the slope of the curves abruptly change and the bearing capacity suddenly decreases, indicating that overall buckling has occurred. The hysteresis curves of the other specimens show that the specimens have local buckling during loading, and the bearing capacity and energy consumption capacity of the specimens have decreased. Among them, Figs. 10 (j) and (k) can not accurately describe the hysteretic performance of the specimens but can reflect the local buckling of the specimens during the loading process.

4.2. Skeleton curves

Skeleton curve refers to the envelope formed by the connection of the peak points of force and displacement in each cycle. That is, the line connecting the corresponding points of the maximum tension and compression displacement of each cycle on the hysteresis curve. The skeleton curves of the specimens are shown in Fig. 11.

Fig. 11 (a1) shows the skeleton curves of CFT-BRBs with different tube thicknesses. It can be seen that the change of tube thickness has no significant effect on the initial stiffness of BRB when other parameters remain unchanged. When the loading displacement continues to increase, the differences become larger. It is shown in Fig. 11 (a1) that when the displacement is 10 mm, both specimens reach the ultimate load, but the specimen with thicker tube exits later. This indicates that the bearing capacity of the two specimens has not reached the maximum, and is limited by the early failure of the restrained members. The stiffness of the curves in Fig. 11 (a2) changes suddenly at about 200 KN because the local buckling of the restrained members occurs at this point.

The limit values of specimens with thinner tubes in Figs. 11 (a2), 11 (a3) and (a4) are slightly smaller than those with thicker tubes. This is because the thinner tube leads to the weak restraint capacity of the restrained members and failures in advance. It shows that the tubular thickness does not change the initial stiffness of the specimen, but affects the post-yield stiffness and load-carrying capacity of the specimen. The stiffness degradation rates and load-carrying capacity degradation rates of specimens with thinner tubes will be faster.

Fig. 11(b) shows the skeleton curves of BRB with different widths of steel cores. It can be seen from Fig.11(b) that under the same restraint conditions, specimens with large core section buckle and fail earlier than the specimen with a smaller core section. The specimen with smaller core sections are more likely to suffer local buckling failure and have a larger stiffness degradation rate.

Fig. 11(c) shows the skeleton curves of CFT-BRBs with different strength of steel core. It can be seen from Fig.1(c) that the stiffness and ultimate load of specimens with smaller core strength are smaller than those with larger core strength. Fig. 11 (d) presents the effect of concrete strength on the hysteretic behavior of BRB. The slopes of the two skeleton curves are basically the same, but the ultimate bearing capacity of 80×16-2.2-H60-235 is greater. Further combining with the test phenomenon, it is shown that the strength of the concrete affects the ultimate bearing capacity of the BRB, but does not affect its stiffness and failure mode.

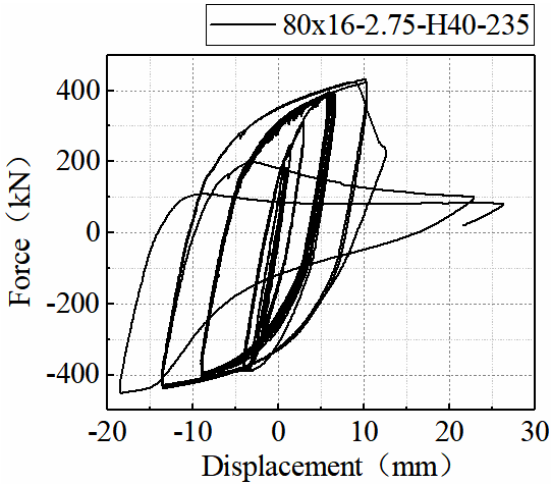
80x16-2.75-H40-235
Force（kN）
Displacement（mm）

(a)

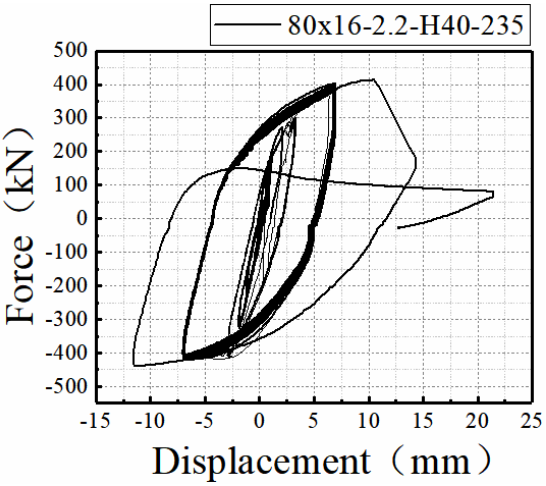
80x16-2.2-H40-235
Force（kN）
Displacement（mm）

(b)

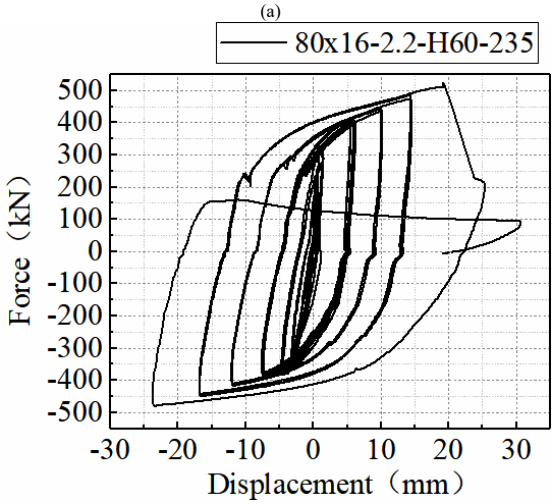
80x16-2.2-H60-235
Force（kN）
Displacement（mm）

(c)

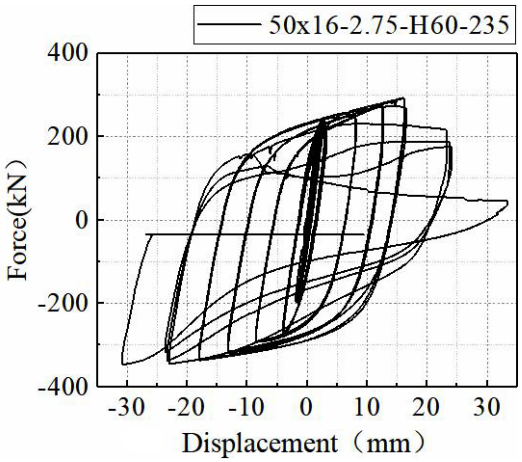
50x16-2.75-H60-235
Force(kN)
Displacement（mm）

(d)

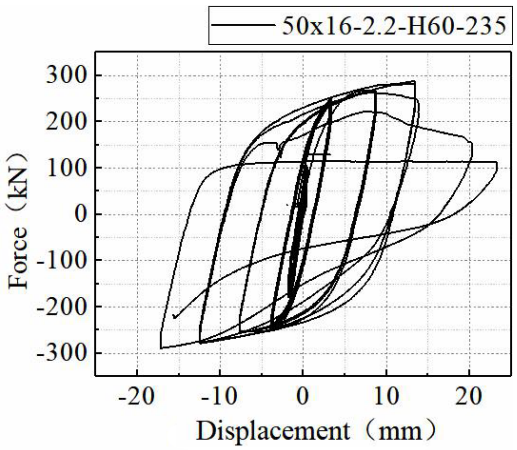
50x16-2.2-H60-235
Force（kN）
Displacement（mm）

(e)

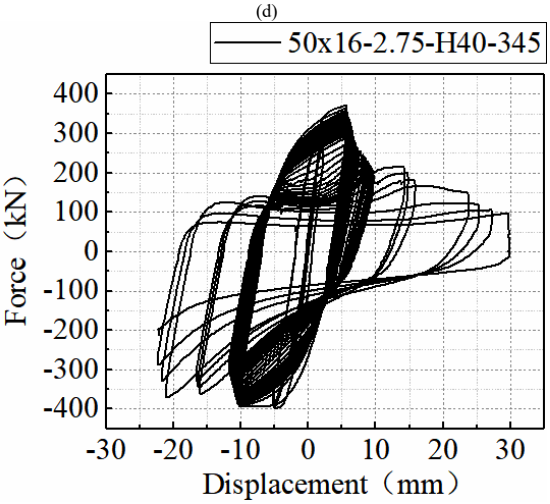
50x16-2.75-H40-345
Force（kN）
Displacement（mm）

(f)

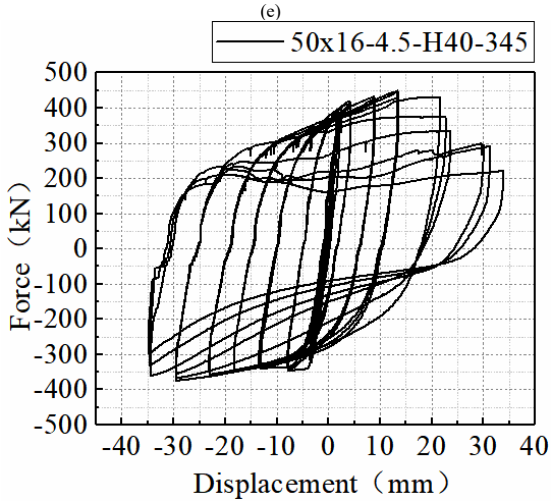
50x16-4.5-H40-345
Force（kN）
Displacement（mm）

(g)

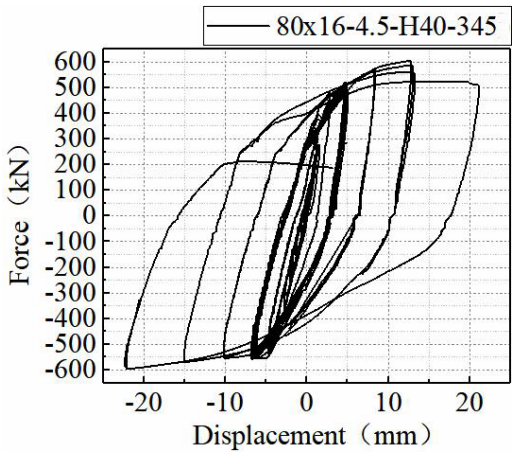
80x16-4.5-H40-345
Force（kN）
Displacement（mm）

(h)

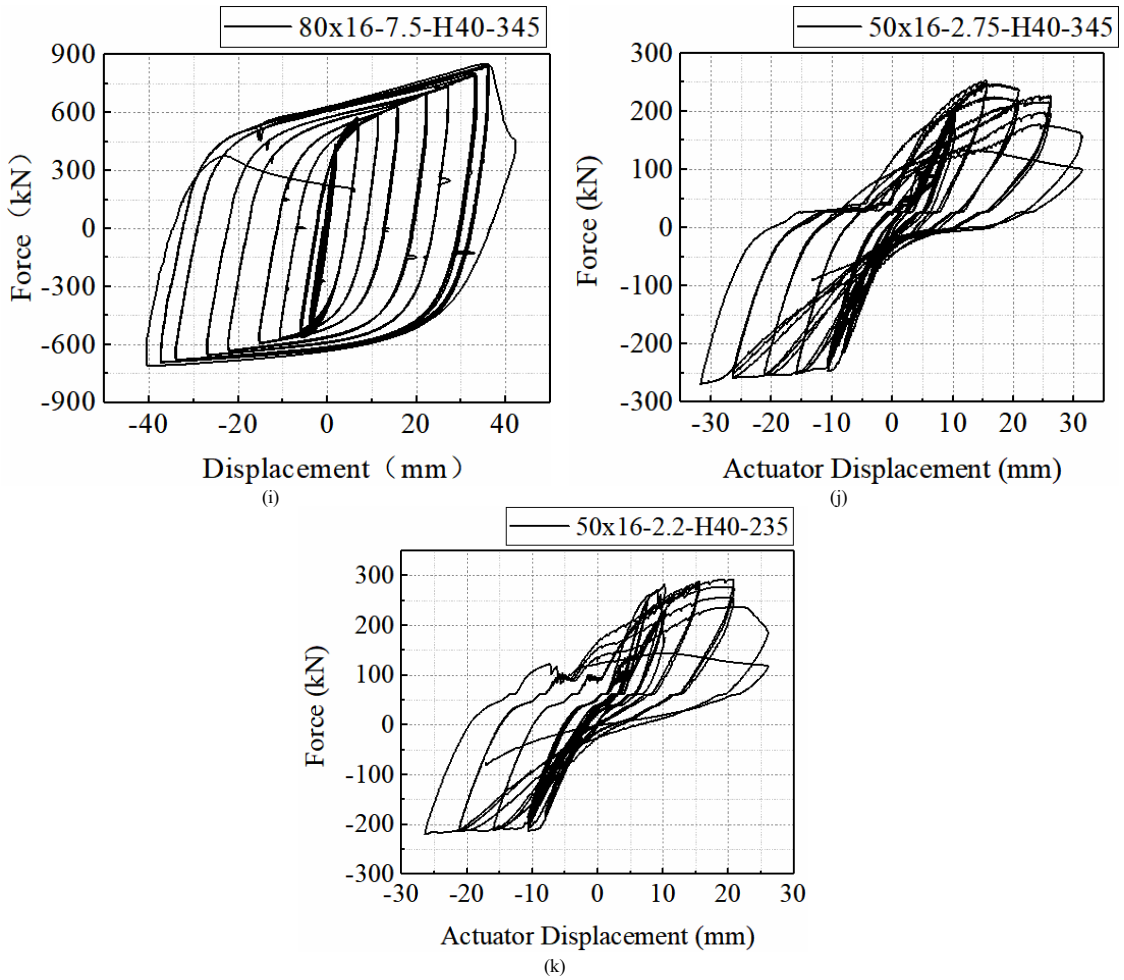

Fig. 10 Hysteretic curves of specimens

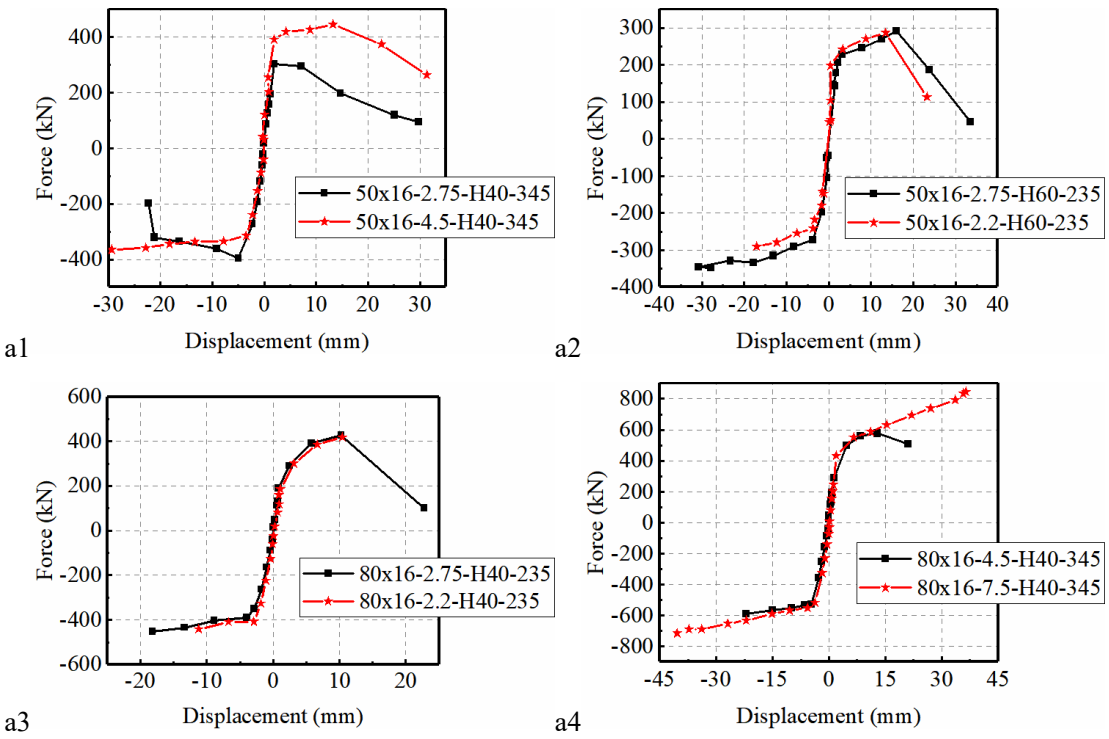

(a) Skeleton evenlop curves with various tubular thicknesses

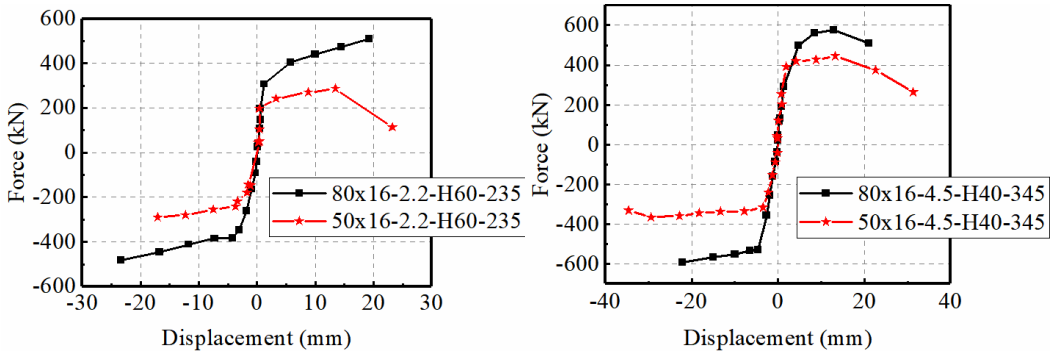

(b) Skeleton curves with various sectional dimensions

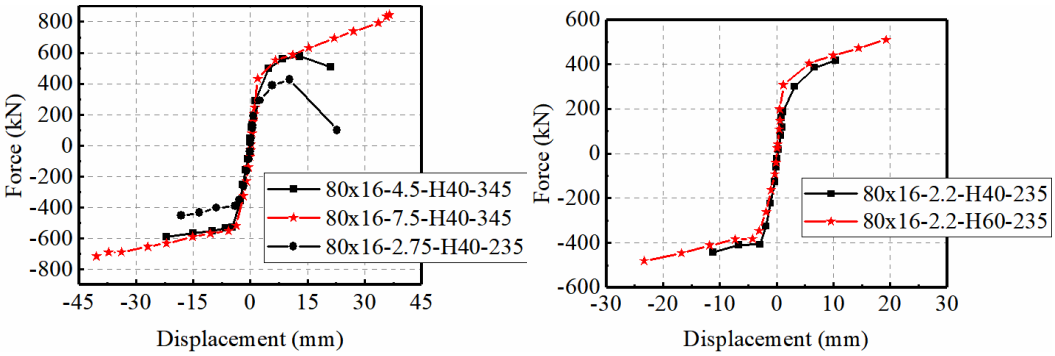

(c) Influences of steel core (d) Influences of concrete infill

Fig. 11 Comparisons on skeleton curves with various parameters

4.3. Failure modes

Based on experimental results, failure modes of the BRB specimens could be divided into three categories, A1, A2, and B. The three failure modes are shown in Fig. 12. The failure mode Type A can be identified as the overall buckling of the specimen. The overall buckling failure type can be divided into two cases: A1 and A2. The first case A1 is the overall buckling without the appearance of local buckling. During the test, the specimen yield first and then the overall buckling happens when the compressive strains were continuously applied. The failure of specimens 80×16-2.75-H40-235, 80×16-2.2-H40-235, and 80×16-2.2-H60-235 can be classified as type A1.

The other case A2 is the overall buckling initiated by local buckling. During the test, the specimen yield first and then the local buckling happens when the compressive strains were continuously applied, finally the compression force dropped significantly and the overall buckling occurs. The failure of specimens 80×16-4.5-H40-345, 80×16-7.5-H40-345 can be classified as type A2.

In contrast, Type B can be identified as the local buckling of the specimen when the tube is spalling and ruptured and concrete is crushed, without the occurrence of overall buckling during the test. The failure of specimens 50×16-2.75-H60-235, 50×16-2.75-H40-235, 50×16-2.2-H40-235, 50×16-2.2-H60-235, 50×16-2.2-H20-235, 50×16-2.75-H40-345, and 50×16-4.5-H40-345 can be classified as type B. Table 3 shows the yield deformation of the core plates and the displacement of the specimens when buckling occurred.

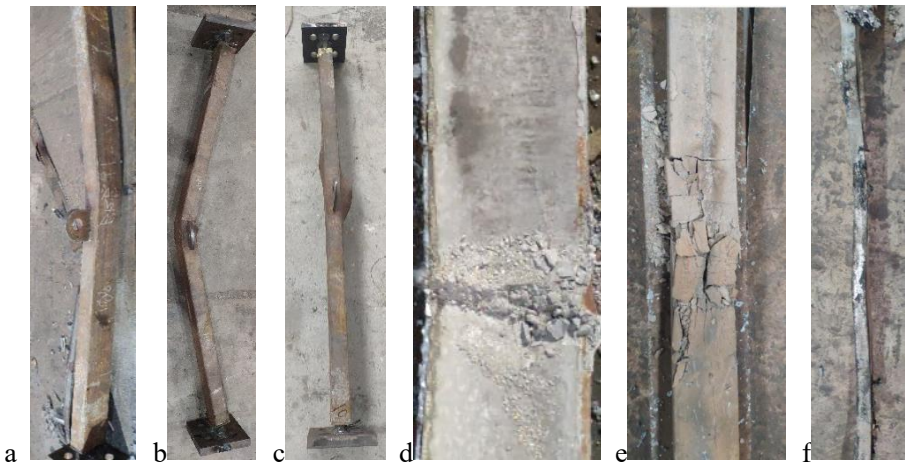

Fig. 12 (a) failure type A2 (80×16-4.5-H40-345, overall buckling initiated by local buckling)

(b) failure type A1 (80×16-2.75-H40-235, overall buckling)

(c) failure type B (50×16-2.75-H40-345, local buckling in mid-span)

(d) Concrete crushing. (specimen 80×16-2.75-H40-235, overall buckling)

(e) Concrete crushing. (specimen 50×16-2.75-H40-345, local buckling)

(f) high mode buckling of steel core. (specimen 50×16-2.75-H60-235, local buckling)

Table 3
Testing results

Specimen name	Behavior during the test	Failure mode
80×16-2.75-H40-235	The specimen yielded when the displacement was 21.07mm, and overall buckling happened at a displacement of 31.6mm.	A1
80×16-2.2-H40-235	The specimen yielded when the displacement was 21.07mm, and overall buckling happened when the displacement was 31.6mm.	A1
80×16-2.2-H60-235	The specimen yielded when the displacement was 21.07mm, and overall buckling happened when the displacement was 39.5mm.	A1
50×16-2.75-H60-235	There were some noises heard when the displacement was 10.53mm, and the specimen broke at the weld of the joint when the displacement was 15.8mm.	B
50×16-2.2-H40-235	There were some noises when the displacement was 10.53mm, and local buckling happened at the weld of the joint when the displacement was 15.8mm.	B
50×16-2.2-H60-235	The specimen yielded when the displacement was 21.07mm, and local buckling happened in the mid-span when the displacement was 26.33mm. Overall buckling happened when the displacement was 39.5mm	B
50×16-2.2-H20-235	The specimen yielded when the displacement was 21.07mm, and local buckling happened in the upper part when the displacement was 26.33mm. The tube was spalling and ruptured in the upper part at a displacement of 39.5mm.	B
50×16-2.75-H40-345	The specimen yielded when the displacement was 21.07mm, and local buckling happened in the lower part when the displacement was 26.33mm. The compressive force suddenly reduced to 221.5kN. The concrete in the lower part was crushed and fractured.	B
80×16-4.5-H40-345	The specimen yielded when the displacement was 15.8mm, and local buckling happened in the lower part when the displacement was 21.07mm. The tube was spalling and ruptured in the upper part when the displacement was 31.6mm.	A2
50×16-4.5-H40-345	The specimen yielded when the displacement was 21.06mm, and local buckling occurred mid-span in the 24th cycle. The compressive force started to reduce when the displacement was 26.33mm. The steel core fractured when the displacement was 39.5mm.	B
80×16-7.5-H40-345	The specimen yielded when the displacement was 21.06mm, and local buckling happened when the displacement was 21.07mm at the first cycle, and overall buckling happened during the second cycle.	A2

Table 4
Parameters for evaluating the performance of specimens

Specimen	σ_{max}/f_y	F'_R/P_b	L_w (mm)	Axial strain	Ductility factor	CPD	Failure mode
80×16-2.75-H40-235	1.05	0.20	169	1.54%	13.6	226	A1
80×16-2.2-H40-235	2.42	0.14	175	0.94%	8.3	110	A1
80×16-2.2-H60-235	3.63	0.11	174	1.86%	16.4	235	A1
50×16-2.75-H60-235	0.61	0.16	172	2.58%	22.8	548	B
50×16-2.2-H40-235	0.60	0.16	172	1.73%	15.3	204	B
50×16-2.2-H60-235	0.58	0.17	181	1.66%	14.7	299	B
50×16-2.2-H20-235	0.42	0.19	172	1.63%	14.4	354	B
50×16-2.75-H40-345	0.68	0.15	128	2.13%	10.3	170	B
80×16-4.5-H40-345	0.84	0.28	128	1.80%	8.7	94	A2
50×16-4.5-H40-345	0.39	0.34	127	2.47%	11.9	245	B
80×16-7.5-H40-345	0.75	0.54	126	3.05%	14.7	448	A2

* σ_{max}, F'_R, P_b, L_w, CPD are maximum stress at the edge of the mid-span section of the steel tube, lateral force resistance of tube, local bearing capacity of restrained members under ultimate load, wavelength, and cumulative plastic deformation respectively.

6. Conclusions

This paper experimentally investigates the cyclic behavior of concrete-filled BRB components subjected to uni-axial loading history. The effects of concrete strength and sectional dimension on the initial stiffness, ultimate strength, failure modes and energy dissipation behaviors are evaluated by quasi-static test results of eleven concrete-filled BRB component specimens. The following conclusions can be drawn:

- The grade of concrete strength has a positive contribution to the energy dissipation behavior of CFT-BRBs. It has a positive influence on the ultimate load of BRB. The BRB filled with H60 concrete had a much higher CPD value than the BRB filled with H40 concrete.
- The grade of concrete strength cannot affect the final failure mode of CFT-BRBs. After the cyclic load, the concrete is crushed before the buckling of the BRB, so the contribution of concrete to the rigidity of the buckling restraining mechanism is suggested to be ignored from the conservative point of view.
- The cross-section dimensions of the core plate and concrete, which are important factors affecting the local buckling mechanism of steel tube, have a great influence on the failure mode of BRB. Compared with the three-hinged yield model, the four-hinged yield model is more likely to have local buckling.
- The failure mode of BRB is related to its overall stability and local stability. If the overall stability is insufficient ($\sigma_{max} > f_y$), the overall buckling failure will occur without local buckling failure. If the overall stability is satisfied ($\sigma_{max} \leqslant f_y$), the failure mode should be determined according to the level of its overall and local stability.

References

[1] Sukenobu T, Katsuhiro K. (1960).” Experimental Study on Aseismic Walls of Steel Framed Reinforced Concrete Structures.” *Transactions of the Architectural Institute of Japan*, 66, 497-500. (In Japanese).

[2] Yoshino T, Kano Y, et al. (1971). “Experimental Study on Shear Wall with Braces (Part 2).” *Summaries of Technical Papers of Annual Meeting, Architectural Institute of Japan*, Japanese, 11,403-404. (In Japanese).

[3] Wakabayashi M, Nakamura T, et al. (1973). “Experimental study on the Elasto-Plastic behaviour of braces enclosed by precast concrete panels under horizontal cyclic loading (part 1 and part 2).” *Summaries of Technical Papers of Annual Meeting, Architectural Institute of Japan*, Japanese, 10,1041-1044. (In Japanese).

[4] Kimura K, Yoshizaki K, Takeda T. (1976). “Tests on Braces encased by Mortar In-filled steel tubes.” *Summaries of Technical Papers of Annual Meeting, Architectural Institute of Japan*, Japanese, 1041-1042. (In Japanese).

[5] Takahashi, S, Mochizuki N. (1979). “Experimental Study on Buckling of Unbonded Braces under Axial Compressive Force (Part 1 and Part 2).” *Summaries of Technical Papers of Annual Meeting, Architectural Institute of Japan*, Japanese, 9, 1623-1626. (In Japanese).

[6] Takahashi, S, Mochizuki N. (1980). “Experimental Study on Buckling of Unbonded Braces under Axial Compressive Force (Part 3).” *Summaries of Technical Papers of Annual Meeting, Architectural Institute of Japan*, Japanese, 9, 1913-1914. (In Japanese).

[7] Fujimoto M. Wada A, Saeki E, et al. (1988). “A Study on the unbonded brace encased in buckling-restraining concrete and steel tube.” *Journal of structural and Construction engineering*, 34B, 249-258. (In Japanese).

[8] Fujimoto M. Wada A, Saeki E, et al. (1988). “A study on brace enclosed in Buckling-Restraining mortar and steel tube (part1).” *Summaries of Technical Papers of Annual Meeting, Architectural Institute of Japan*, Japanese, 10, 1339-1340. (In Japanese).

[9] Fujimoto M. Wada A, Saeki E, et al. (1988). “A study on brace enclosed in Buckling-Restraining mortar and steel tube (part2).” *Summaries of Technical Papers of Annual Meeting, Architectural Institute of Japan*, Japanese, 10, 1341-1342. (In Japanese).

[10] Bo-Li Zhu, Yan-Lin Guo, Peng Zhou et al. (2017). “Numerical and experimental studies of corrugated-web-connected buckling-restrained braces.” *Engineering Structures*, 134,107-124;

[11] Bo-Li Zhu. (2018). “Theoretical and Experimental Study on Core-separated Buckling Restrained Braces with Two External Restrainers Connected by Flat Webs and Corrugated Webs.” Thesis (PhD). Xi’an Jiaotong University.

[12] Chun-Lin Wang, Quan Chen, Bin Zeng, Shaoping Meng. (2017). “A novel brace with partial

buckling restraint: An experimental and numerical investigation." *Engineering Structures*, 150, 190-202.
[13] Xie, L., Wu, J., Shi, J., Zhu, Y. (2020) "Influence of the core-restrained clearance on the mechanical performance of sandwich buckling-restrained braces." *Advanced Steel Construction*, 16(1), 37-46.
[14] TS AI K eh-Chyuan H WANG Yean-chih, WEN G Chung-shing. (2005). "Seismic Performance and Applications of Double-Tube Buckling Restrained Braces." *Progress in Steel Building Structures*, 7(3).
[15] Hu, J. (2013) "Design motivation, mechanical modeling and nonlinear analysis of composite PR moment frames with smart SMA connection systems." *Advanced Steel Construction*, 9(4), 334-349.
[16] Quan Chen, Chun-Lin Wang, Shaoping Meng and Bin Zeng (2015). Effect of the unbonding materials on the mechanic behavior of all-steel buckling-restrained braces, *Engineering Structures 111 (2016) 478–493.*
[17] R. Sabelli, S. Mahin, CcHANG. (2003). Seismic demand on steel braced frame buildings with buckling-restrained braces, *Engineering Structures*, 25, 655-666
[18] L. Di Saeno, A.s.Elnashai. (2009). "Bracing systems for seismic retrofitting of steel frames." *Journal of Constructional Steel Research*, 65, 452-465.
[19] Dipti R. Sahoo, Shih-Ho Chao. (2010). "Performance-based plastic design method for buckling-restrained braced frames." *Engineering Structures*, 32, 2950-2958.
[20] T. Takeuchi, J.F. Hajjar, R.Matsui, K.Nishimoto, I.D.Aiken. (2012)." Effect of local buckling core plate restraint in buckling restrained braces". *Engineering Structures*, 44, 304-311
[21] Atsushi Watanabe, Yasuoshi Hitomi, Eiichiro Saeki, Fujimoto M. (1988). "Properties of brace encased in buckling-restraining concrete and steel tube." *Proceedings of Ninth World Conference on Earthquake Engineering*, Tokyo-Kyoyo 2-9 August 1988, Japan, 4, 719-724
[22] Mamoru Iwata and Masatoshi Murai. (2006). "Buckling-restrained brace using steel mortar planks; performance evaluation as a hysteretic damper." *Earthquake Engineering and Structural Dynamics*, 35, 1807-1826.
[23] N. Hoveidae, B. Rafezy. (2012). "Overall buckling behavior of all-steel buckling restrained braces." *Journal of Constructional Steel Research*, 79, 151-158.
[24] Ryota Matsui, Toru Takeuchi, Jerome, F. Hajjar, Kohji Nishimoto, and Ian Aiken. (2009). "Local buckling restraint condition for core plates in buckling restrained braces." *The 14th World Conference on Earthquake Engineering*, Beijing 12-17 October 2008, Journal of Constructional Steel Research. 66. 139-149.
[25] Francesco Genna and Piero Gelfi (2012). "Analysis of the Lateral Thrust in Bolted Steel Buckling-Restrained Braces. I: Experimental and numerical results." *Engineering Structures*, 138 (10):1231-1243.
[26] Francesco Genna and Piero Gelfi. (2012). "Analysis of the Lateral Thrust in Bolted Steel Buckling-Restrained Braces. II: Engineering Analytical Estimates." *Engineering Structures*, 138 (10), 1244-1254.
[27] An-Chien Wu, Pao-chun Lin and Keh chyuan Tsai. (2014). "High-mode buckling responses of buckling-restrained brace core plates." *Earthquake Engineering & Structural Dynamics*, 43, 375-393
[28] Nader Hoveidae and behzad Rafezy. (2015). "Local buckling behavior of core plate in all-steel buckling restrained braces." *International Journal of Steel Structures*, 2, 249-260.
[29] Giovanni Metelli,Guido Bregoli, Francesco Genna, (2016). "Experimental study on the lateral thrust generated by core buckling in bolted-BRBs." *Journal of Constructional Steel Research*, 122, 409-420.
[30] Talebi, E., Tahir, M., Zahmatkesh, F., Kueh, A., Said, A. (2016) "Fire resistance of a damaged building employing buckling restrained braced system." *Advanced Steel* Construction, 14(1), 1-21.
[31] Pao-Chun Lin, Keh-chyuan Tsai, Chieh-an Chang et al. (2016). "Seismic design and testing of buckling-restrained braces with a thin profile." *Earthquake Engineering & Structural Dynamics*, 45, 339-358.
[32] Wu, A., Tsai, K., Lin, T., Tsai, C., Wang, K. (2020) "Seismic responses of RC braced frames with buckling restrained braced connected to corbels." *Advanced Steel Construction*, 16(1), 85-93.
[33] Junxian Zhao, Bin Wu, Jinping Ou. (2013). "Global stability design method of buckling-restrained braces considering end bending moment transfer: Discussion on pinned connections with collars." *Engineering Structures*, 49,947–962.
[34] Toru Takeuchi. (2018). "Buckling-restrained brace: History, design and applications. 9th international conference on behavior of steel structures in seismic areas Christchurch." New Zealand 14-16 February 2018.
[35] Shoichi Kishiki , Daisuke Uehara , Satoshi Yamada , Kazuaki Suzuki , Eiichiro Saeki and Wada Akir. (2005). "Behavior of beam splices with energy dissipating elements at the bottom flange." *Journal of Structural & Construction Engineering*, 70 (597), 135-143.
[36] Junxian Zhao, Bin Wu, Jinping Ou, (2009). "The working mechanism and stability design method of anti-buckling support." *Engineering Structures*, 49, 947–962.
[37] Junxian Zhao, Bin Wu. (2009) "Working mechanism and stability design methods of buckling-restrained braces". *Earthquake Engineering and Engineering Dynamics*, 29(03), 131-139. (In Chinese)
[38] American Institute of Steel Construction. (2010). *AISC 341-10*, "Seismic provisions for structural steel buildings." Chicago, American.
[39] Pao-Chun lin, Keh chyuan Tsai, Kung juin wang et al. (2012). "Seismic design and hybrid tests of a full-scale three story buckling restrained braced frame using welded end connections and thin profile." *Earthquake Engineering and Structural Dynamics*, 41, 1001-1020.
[40] An-Chien Wu, Pao-chun Lin and Keh chyuan Tsai. (2014). "High-mode buckling responses of buckling-restrained brace core plates." *Earthquake Engineering & Structural Dynamics*, 43, 375-393
[39] Junxian Zhao, Bin Wu, Jinping Ou, (2009). "The working mechanism and stability design method of anti-buckling support." *Engineering Structures*, 49, 947–962.
[41] Junxian Zhao, Bin Wu. (2009) "Working mechanism and stability design methods of buckling-restrained braces. " *Earthquake Engineering and Engineering Dynamics*, 29(03), 131-139. (in Chinese)

Advanced Steel Construction – Vol. 17 No. 4 (2021) 376–384
DOI:10.18057/IJASC.2021.17.4.6

NUMERICAL AND THEORETICAL STUDIES ON DOUBLE STEEL PLATE COMPOSITE WALLS UNDER COMPRESSION AT LOW TEMPERATURES

Zhe Wang [1], Jia-Bao Yan [1, 2, *] and Xue-Mei Liu [3]

[1] *School of civil engineering, Tianjin University, Tianjin 300350, China*
[2] *Key Laboratory of Coast Civil Structure Safety of Ministry of Education, Tianjin University, Tianjin 300350, China*
[3] *Department of Infrastructure Engineering, The University of Melbourne, Parkville, VIC 3010, Australia*
** (Corresponding author: E-mail: ceeyanj@163.com)*

ABSTRACT

Double steel plate composite walls (DSCWs) with several unique types of connectors have been implemented to protect offshore oil exploration platforms from concentric forces caused by ice in the Arctic region. This paper investigates the compressive performance of DSCWs with interlocked J-hooks and overlapped headed studs at low temperatures ranging from 20 ℃ to -80 ℃ with nonlinear finite element models (FEMs). The intricate geometric size of the concrete, multiple interactions of the concrete with the connectors, and material nonlinearities of the concrete have been thoroughly simulated. The reasonable consistency between the results of the monotonic tests and finite element analysis (FEA) on nine DSCWs with interlocked J-hooks and seven DSCWs with overlapped headed studs indicates that the FEMs can effectively predict the compressive performance of the DSCWs at low temperatures. On the basis of the validated FEMs, the effects of the horizontal and vertical spacing of the connectors on the compressive performance of the DSCWs are studied. Finally, theoretical models of the load-displacement curves are developed to reveal the compressive response of DSCWs at low temperatures with different types of connectors, taking into account the restraining effect of steel plates on the inner concrete and the local buckling of steel plates. Compared with previous tests and FEA, the developed theoretical models have reasonable consistency for the load-displacement curves of DSCWs at low temperatures.

ARTICLE HISTORY

Received: 27 June 2020
Revised: 31 January 2021
Accepted: 6 February 2021

KEYWORDS

Double steel plate composite wall;
Low temperature;
Arctic protective structure;
Compressive performance;
Nonlinear finite element model;
Theoretical models

1. Introduction

Recently, the Arctic region has attracted strong interest from researchers because of its potential oil and gas resources [1]. The lowest temperature is approximately -70 ℃ in the Arctic, introducing great challenges to infrastructure. Meanwhile, due to global warming, the rapid melting of ice is a matter of serious concern, increasing the concentration of floating ice in the Arctic. These ice sheets continuously impact oil and gas platforms. Under such fatigue impacts, the service life of such platforms is greatly reduced. Thus, it is necessary to propose a novel protective structure that can be applied to oil and gas platforms. Marshall et al. [2] and Yan et al. [3] developed a DSCW as a protective structure for Arctic offshore platforms, as demonstrated in Fig. 1. A DSCW consists of a sandwiched concrete core with two outer steel plates, which are integrally connected with mechanical shear connectors at the steel-concrete interface. Different types of connectors have been developed and employed in steel-concrete composite walls, e.g., J-hooks and headed studs. The DSCW exhibits superior properties compared to those of conventional reinforced concrete structures, e.g., reduced formwork, increased construction efficiency and high performance under static, seismic, blast and impact loads [4-6].

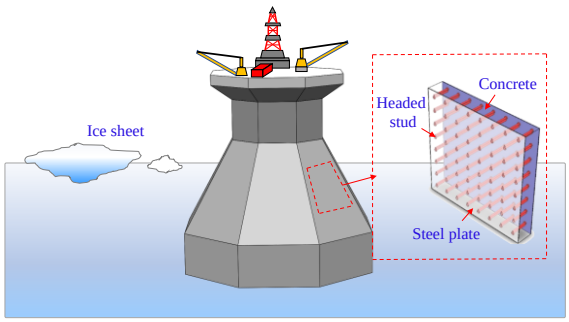

Fig. 1 Application of the DSCW in Arctic offshore platforms [9]

The compressive performance of DSCWs at low temperatures has been experimentally studied in Refs. [7-9]. However, these experimental studies proved to be costly and time consuming, and these tests have limitations in that the influences of the vertical and horizontal spacing of the connectors on the compressive performance of DSCWs at low temperatures have not been thoroughly researched. To overcome these limitations, finite element analysis (FEA) is an alternative way to study the compressive performance of DSCWs.

Several scholars have investigated the push-out behaviour of headed studs by FEM with only a few studs to obtain their shear strength [10–13]. However, for DSCWs with many studies, those models will experience nonconvergence problems [13-14]. Shanmugam et al. [15] proposed a simplified FEM of an SCS sandwich panel, in which the shear-slip behaviour of a head stud at the steel-concrete interface was simulated by a nonlinear spring. Yan et al. [16-17] simplified the interlocked J-hook and overlapped headed stud in the FEM of double steel plate composite structures to two cylindrical studs connected by a nonlinear spring element at its geometric centre. The reliability of the FEM was validated through the test results. Yan et al. [18] developed FEM that simplified the circle headed stud into square to predict the load-transferring mechanism and failure modes of the SCS sandwich plate. Qi et al. [19] investigated the tensile force and bending moment demands on headed studs in the design of DSCWs by FE method. The compressive local buckling behaviour of the steel plate in DSCWs was simulated by Li and Hu [20]. However, the concrete constitutive equation was simplified into a linear elasticity model and could not simulate the ultimate compressive bearing capacity of DSCWs. Fan et al. [21] established FEA modes on large-scale double steel plate composite structures, considering the details of connectors and local buckling of the steel plate. Vecchio and McQuade [22] treated the concrete and steel plate as one material, incorporated into the established 2D FE models of DSCWs. Although the peak loads predicted by the FEA were close to those of the test results, the FE models overestimated the lateral stiffness of the DSCW and failed to observe the local buckling of the steel plate.

Choi and Han [23] proposed calculation models for the initial stiffness and ductility coefficient of DSCWs. Based on Euler's formula, Zhang and Yang et al. [24-25] derived the calculation model of the compressive bearing capacity of steel plates considering the local buckling of the steel plate. Liang and Uy [26] developed two effective width formulas to calculate the maximum compressive capacity of short concrete-filled steel box columns, in which the length coefficient K was considered to be 0.7 by assuming that the boundary condition of the steel faceplate was a semi-fixed support. Yan et al. [27] recommended theoretical models to obtain the ultimate compressive bearing capacity of sandwiched concrete in DSCWs, which took into account the constraints of the steel plate working with overlapped headed studs on the sandwiched concrete. Yan et al. [28-29] proposed novel EC connectors incorporated into the DSCSWs and developed theoretical models to predict the ultimate compressive bearing capacity.

Based on recent studies, previous FE models and theoretical analysis have mainly focused on the compressive behaviours of DSCWs at ambient temperatures, and the theoretical model of the load-displacement curve of DSCWs at low temperatures has not been thoroughly studied. Thus, it is necessary to develop FE models and theoretical models to predict the

compressive performance of DSCWs at low temperatures.

This paper develops FE models to study the compressive performance of DSCWs with J-hooks and headed studs at low temperatures. In these models, the connectors working in pairs are simulated by two cylindrical studs connected through a nonlinear spring element. The reasonable agreement of the ultimate compressive bearing capacity, load-displacement curves and failure modes between the results of the proposed FE analysis and several experimental investigations proves the accuracy of the FEM. With the affirmed FEM, parametric studies are accomplished to study the influence of the vertical and horizontal spacing of the connectors on the compressive performance of the DSCWs. Finally, on the basis of compressive tests and the FEA, theoretical models of load-displacement curves at low temperatures have been proposed to reveal the loading process.

2. Axial compression tests on double steel plate composite walls [7-9]

2.1. Description of the specimens and materials

The geometry of the DSCWs involved in the test program is shown in Fig. 2, and they are composed of nine DSCWs with J-hooks and seven with headed studs. All specimens are composed of two external steel plates, studs (J-hooks or headed studs), sandwiched concrete, loading/end plates, and stiffeners.

Grade Q235 steel plates were used for all of the specimens, and the strength grade of the sandwiched concrete was C30, C40 and C50. J-hook connectors fabricated by grade HPB300 reinforcements were used for WJ1-WJ9. Meanwhile, headed studs with a diameter of 10 mm were used for WH1-WH7. More details of each specimen and the material properties are given in Table 1.

2.2. Experimental setup

A 1500-ton universal testing machine, as illustrated in Fig. 3, was used for the compression tests of DSCWs at low temperatures. Monotonic axial loading applied to the DSCWs was controlled by the displacement at a rate of 0.05 mm/min during the tests.

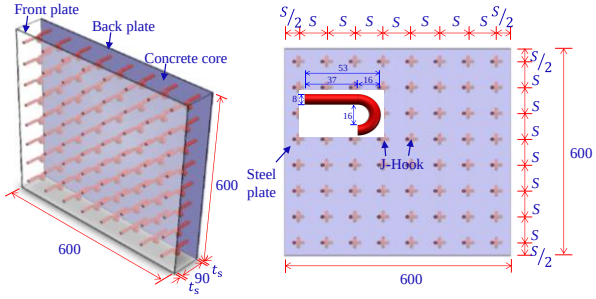

(a) Details of the DSCWs with J-hooks (WJ1-WJ9)

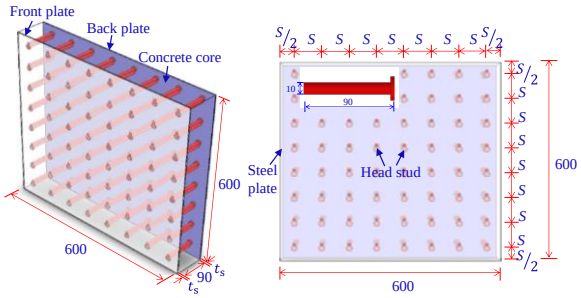

(b) Details of the DSCWs with headed studs (WH1-WH7)

Fig. 2 Details of the DSCWs (unit: mm) [7]

Table 1
Details of the double steel plate composite walls

Item	T (°C)	t_s (mm)	f_{yT} (MPa)	E_{sT} (GPa)	S (mm)	S/t_s	σ_{uT} (MPa)	E_{shT} (GPa)	f_{cT} (MPa)	E_{cT} (GPa)
	(1)	(2)	(3)	(4)	(5)	(5)/(2)	(7)	(4)	(8)	(9)
WJ1	20	2.8	334	201	75	26.8	330	199	43.9	28.4
WJ2	-30	2.8	361	210	75	26.8	347	200	61.7	32.2
WJ3	-60	2.8	378	216	75	26.8	353	204	75.6	33.1
WJ4	-60	4.6	396	224	75	16.2	353	204	75.6	33.1
WJ5	-60	5.9	401	226	75	12.6	353	204	75.6	33.1
WJ6	-60	2.8	378	216	150	53.6	353	204	75.6	33.1
WJ7	-60	2.8	378	216	75	26.8	353	204	48.2	32.8
WJ8	-60	2.8	378	216	75	26.8	353	204	79.3	33.6
WJ9	-80	2.8	391	222	75	26.8	360	206	87.0	34.6
WH1	20	2.8	334	201	75	26.8	494	198	43.9	28.4
WH2	-30	2.8	361	210	75	26.8	522	198	61.7	32.2
WH3	-60	2.8	378	216	75	26.8	555	205	75.6	33.1
WH4	-60	4.6	396	224	75	16.2	555	205	75.6	33.1
WH5	-60	5.9	401	226	75	12.6	555	205	75.6	33.1
WH6	-60	2.8	378	216	150	53.6	555	205	75.6	33.1
WH7	-80	2.8	391	222	75	26.8	593	204	87.0	34.6

T denotes the temperature; t_s denotes the thickness of the steel plate; f_{yT} and E_{sT} denote the yield strength and elastic modulus of the steel plate at low temperatures, respectively; S denotes the spacing of the connectors; σ_{uT} and E_{shT} denote the ultimate strength and elastic modulus of the connectors at low temperatures, respectively; and f_{cT} and E_{cT} denote the compressive strength and modulus of elasticity of the concrete at low temperatures, respectively.

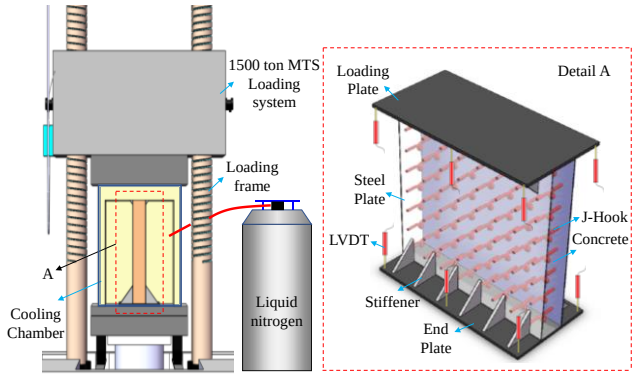

Fig. 3 Test setup of the DSCW

The compressive bearing capacity P_e, vertical displacement Δ_T and strain of the steel plate ε_{sT} must be measured during the test process. The compressive bearing capacity was measured directly by the load cell in the testing machine. Eight linear voltage displacement transducers (LVDTs) were arranged at the corners of the loading/end plates to measure the vertical displacement of the DSCWs. Linear strain gauges were attached to the steel plates between two rows of studs to measure the buckling strain.

3. Numerical analysis of the DSCWs

3.1. General

The compressive performance of the DSCWs is simulated by the general finite element package ABAQUS [30], and the implicit solver is used for the analysis solutions. To improve the accuracy of the FEM, the different components of the DSCW reported in [7,8,9], e.g., sandwiched concrete, steel

plate, loading/end plates and stiffeners, were modelled in detail. The geometric dimensions, mesh, material model, modelling of the connectors, steel-concrete interactions, loading and boundary conditions of the FEM are described in the following sections. It is worth noting that similar FEMs, established according to test parameters reported by Choi and Han [23], are also applied to FEA. More details of the FEMs can be found in Ref. [23,27].

3.2. Geometric dimensions and mesh of the FEM

Fig. 2 and Table 1 present the detailed geometric dimensions of the DSCWs reported in [7,8,9], and the variables of the geometric dimensions include the steel plate thickness and connector space.

The FE model of the DSCW under compression is shown in Fig. 4. All of the components of the DSCW, including the concrete, steel plate, connectors, stiffeners and loading/end plates, are simulated by three-dimensional eight-node solid elements with a reduced integration point (C3D8R). Notably, the mesh size is critical to the accuracy of the FE analysis. A reasonable mesh size not only improves the accuracy of the FEA but also saves computing time. Due to the complex geometry of the FEM, each part is meshed and cut into regularly small pieces until all of the small pieces turn green. Considering the large stress level at the connectors, the mesh sizes of the concrete and steel plate around the connectors are encrypted within a reasonable range to improve the calculation accuracy of those areas. Taking specimen WJ1 as an example, there are 43,520 and 13,312 elements in the sandwiched concrete and steel plate with connectors, respectively.

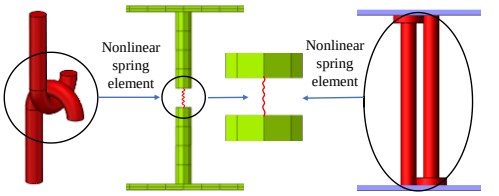

(a) Simulation of the stud connectors by the spring element

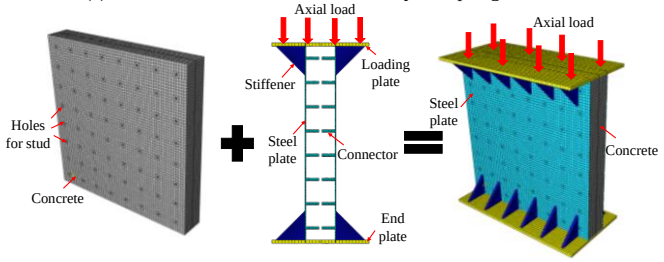

(b) Finite element model

Fig. 4 Finite element model of the DSCWs

3.3. Materials model

3.3.1. Material model for concrete

The concrete damage plasticity (CDP) model was applied to simulate the compressive performance of the sandwiched concrete in the DSCW at low temperatures, which could present two failure modes, namely, compressive crushing and tensile cracking, that may occur in sandwiched concrete during the loading process. To increase the reliability of the FEM, the compressive behaviour and tensile behaviour in the CDP model should be entered precisely.

The compressive constitutive equation of concrete recommended by Xie et al. [31] is used to express the elastic-plastic properties of concrete at low temperatures as given below:

$$\sigma_{cT}=\begin{cases} f_{cT}\left[A\dfrac{\varepsilon_{cT}}{\varepsilon_{0T}}+(3-2A)\left(\dfrac{\varepsilon_{cT}}{\varepsilon_{0T}}\right)^2+(A-2)\left(\dfrac{\varepsilon_{cT}}{\varepsilon_{0T}}\right)^3\right], & 0\le\dfrac{\varepsilon_{cT}}{\varepsilon_{0T}}\le 1 \\ f_{cT}\dfrac{\varepsilon_{cT}}{\varepsilon_{0T}}\left[B\left(\dfrac{\varepsilon_{cT}}{\varepsilon_{0T}}-1\right)^2+\dfrac{\varepsilon_{cT}}{\varepsilon_{0T}}\right]^{-1}, & \dfrac{\varepsilon_{cT}}{\varepsilon_{0T}}>1 \end{cases} \quad (1)$$

where σ_{cT} and ε_{cT} denote the concrete stress and strain under compression at temperature T, respectively, f_{cT} denotes the concrete strength under compression at temperature T, and ε_{0T} denotes the concrete strain under compression corresponding to f_{cT}. The values of constants A and B are shown in Table 2.

Table 2
Coefficients A and B for concrete at different low temperatures

Coefficient	20°C	0°C	-40°C	-80°C
A	2.7	2.7	2.2	1.8
B	0.7	1.3	1.7	2.0

The tensile behaviour of concrete is represented in this FEM by the fracture energy model, in which the parameter can be obtained as follows [33]:

$$G_f=G_{f0}\left(\frac{f_{ck}}{10}\right)^{0.7} \quad (2)$$

where G_f denotes the fracture energy of concrete, Nmm/mm^2, and f_{ck} denotes the concrete cylinder strength under compression, MPa. According to the results of the material tests, G_f= 0.090 Nmm/mm^2 was adopted in this FEM to describe the tensile behaviour.

Other plasticity parameters in the CDP model referring to the ABAQUS user manual [32], such as the dilation angle, eccentricity, f_{b0}/f_{c0}, K and viscosity parameter, are 26°, 0.1, 1.16, 0.667 and 0.0001, respectively.

3.3.2. Material model for the steel plate and connectors

Fig. 5 shows the elastic-plastic isotropic model employed to predict the material properties of the steel plate and connectors in the DSCW at low temperatures. There are two parts in this bi-linear material model, namely, the elastic part and plastic part. The elastic part is linear up to the yield strength for the steel plate and connectors, in which Young's modulus E_{sT} and Poisson's ratio υ need to be entered. Meanwhile, the plastic part is also linear up to the ultimate strength, in which the yield strength f_{yT}, ultimate strength f_{suT} and the corresponding strain ε_{suT} should be precisely defined. The parameters mentioned above are all obtained through tests, as given in Table 1.

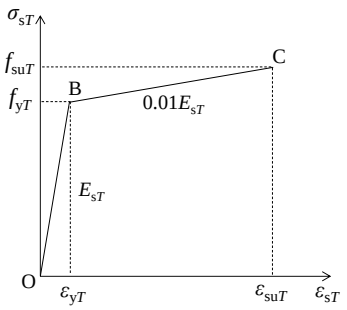

Fig. 5 Stress-strain curve of the steel used in the FEM

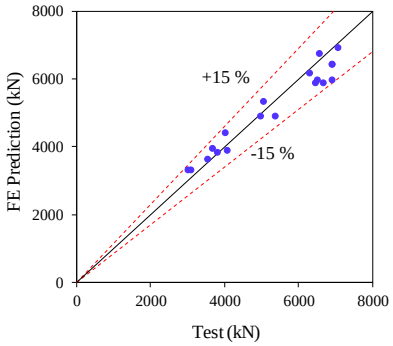

(a) Comparisons between the FE predictions and test results

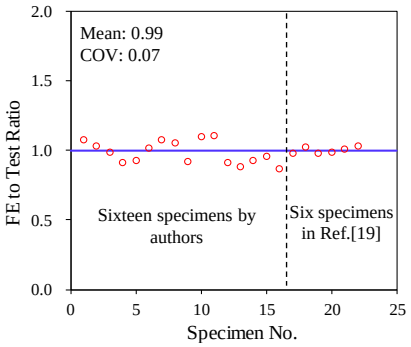

(b) Scatter of the FE-to-test ratios for P_{uT}

Fig. 6 Comparisons of the FE predictions of the ultimate bearing capacity with the test values

3.4. Modelling of the connectors

The interlocked J-hooks and overlapped headed studs in the DSCW must be simulated reasonably because the connectors, effectively maintaining the composite action of the steel plate and concrete, not only transfer the shear force at the contact between the steel plate and concrete but also prevent the premature local buckling of the steel plate. However, it is difficult to simulate the full geometry of the connectors due to the intricate geometry of the connectors themselves and the connector holes reserved in concrete, introducing great challenges to partitioning and producing the mesh while also causing nonconvergence of the FEM with the increasing number of elements. To solve the problems mentioned above, the geometry of the connectors is simplified into two cylinders with the same diameter as the connectors in the tests. One side of the cylinder merges with the steel plate into one part, and the other side of the two cylinders is connected by a three-dimensional spring element with nonlinear properties [16], as demonstrated in Fig. 4(a). The spring stiffness of 24,000 N/mm obtained from pull-out tests [16,34] needs to be properly defined. This simplified method for interlocked J-hooks or overlapped headed studs in steel-concrete composite structures is proven to be reasonable.

3.5. Steel-concrete interactions, loading and boundary conditions

This FEM adopted general contacts at all the surface pairs to simplify the model and save computing time. The contact properties of the tangential behaviour with a friction coefficient of 0.4 [35] and normal behaviour with a "hard" contact have been defined. Tie constraints were used among the steel plates, stiffeners and loading/end plates. A displacement load was applied axially at a reference point coupled to the loading plate, as shown in Fig. 4(b), and the end plate was restrained to move against all degrees of freedom.

Table 3
Comparisons of the ultimate compressive bearing capacity of the DSCWs

Item	P_e (kN)	P_f (kN)	P_t (kN)	P_f/P_e	P_t/P_e
	(1)	(2)	(3)	(2)/(1)	(3)/(1)
	Tests by	Authors			
WJ1	3062	3311	3510	1.08	1.15
WJ2	3532	3638	3782	1.03	1.07
WJ3	4968	4908	5338	0.99	1.07
WJ4	6442	5874	6403	0.91	0.99
WJ5	6897	6424	7074	0.93	1.03
WJ6	3783	3847	4456	1.02	1.18
WJ7	3654	3950	3831	1.08	1.05
WJ8	5046	5325	5540	1.06	1.10
WJ9	6508	5984	5999	0.92	0.92
WH1	3001	3310	3510	1.10	1.17
WH2	3991	4428	4540	1.11	1.14
WH3	5360	4908	5338	0.92	1.00
WH4	6658	5873	6403	0.88	0.96
WH5	6890	6424	7074	0.93	1.03
WH6	4062	3883	4456	0.96	1.10
WH7	6891	5976	5999	0.87	0.87
	Tests in	Ref. [23]			
SS400-S	6282	6175	6417	0.98	1.02
SM490-S	6562	6749	7074	1.03	1.08
SS400-M	7051	6934	7707	0.98	1.09
SM490-M	8069	7946	7707	0.98	0.96
SS400-L	8956	9032	9990	1.01	1.12
SM490-L	8850	9156	9990	1.03	1.13
Mean				0.99	1.05
Cov				0.07	0.08

P_e and P_t denote the experimental and theoretical ultimate compressive bearing capacity, respectively; P_f is the predicted ultimate compressive bearing capacity by the FEM.

3.6. Validations and discussions

The previous 16 compression tests on DSCWs reported in [7,8,9] and 6 tests reported in [23,27] were used to validate the ultimate compressive bearing capacity, load-displacement curves and failure modes of the developed FEM.

3.6.1. Ultimate compressive bearing capacity

Table 3 and Fig. 6 compare the predicted ultimate compressive bearing capacity by the FEA with the experimental values of the 16 DSCWs reported by the authors and 6 specimens reported by Choi and Han. It can be shown that the FE results achieve close agreement with the test results in terms of the ultimate compressive bearing capacity of the DSCW. The errors of the FE predicted values are within ±15%, and the average ratio of P_f/P_e is 0.99 with a coefficient of variation (COV) of 0.07.

3.6.2. Load-displacement curves

Fig. 7 compares the numerical load-displacement curves with the experimental curves obtained by the authors. These figures show that the numerical load-displacement curves divided into three stages, namely, the elastic stage, non-elastic stage, and recession stage, reasonably agree with the experimental curves except for the initial stiffness. The reasons for this difference may be as follows: (1) initial imperfections inside the specimens caused by welding the steel plates and connectors, pouring the concrete, and transporting the specimens; (2) non-axial compression due to the non-flatness of the loading/end plates; and (3) errors of the displacement measurement due to the complicated test process under low temperatures.

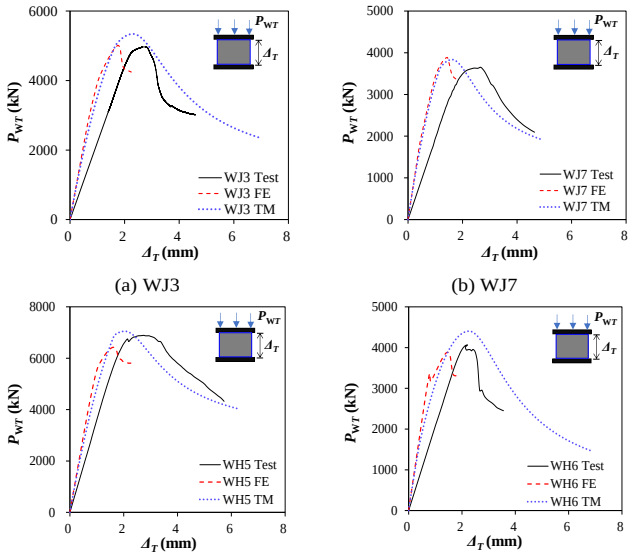

(a) WJ3 (b) WJ7

(c) WH5 (d) WH6

Fig. 7 Validations of the load-displacement curves of the DSCWs by authors

Fig. 8 shows the comparisons of the load-displacement curves between the FE predictions and the experimental curves obtained from the tests in Ref. [23]. If the tests can eliminate the disadvantages mentioned above, the load-displacement curves will be perfectly predicted by the FEA, including the initial stiffness.

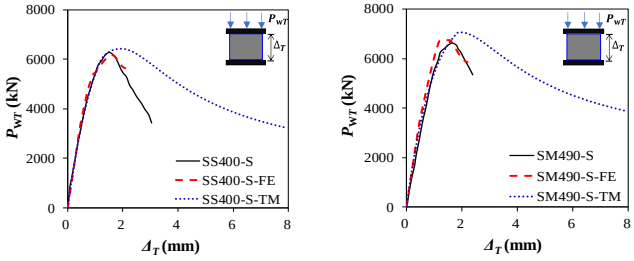

(a) SS400-S (b) SM490-S

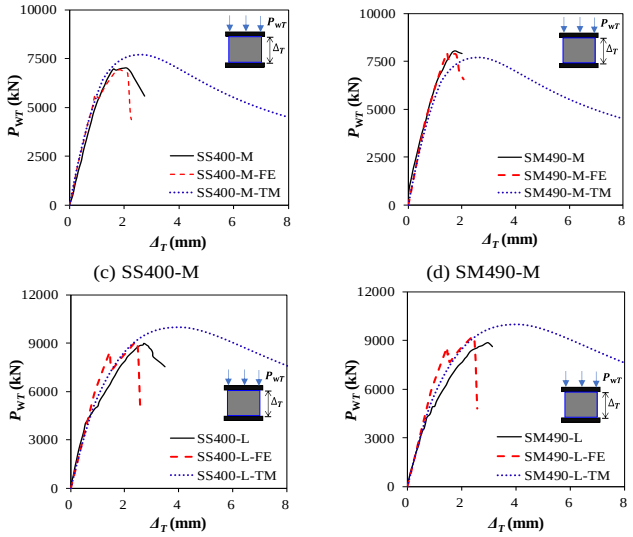

(c) SS400-M (d) SM490-M

(e) SS400-L (f) SM490-L

Fig. 8 Validations of the load-displacement curves in Ref. [23]

3.6.3. Failure modes

Crushing and splitting of the concrete and local buckling of the steel plate occurred in the DSCWs under compression. Fig. 9 presents the failure mode comparisons between those observed from the tests and those predicted from the FEA, in which reasonable agreement was achieved.

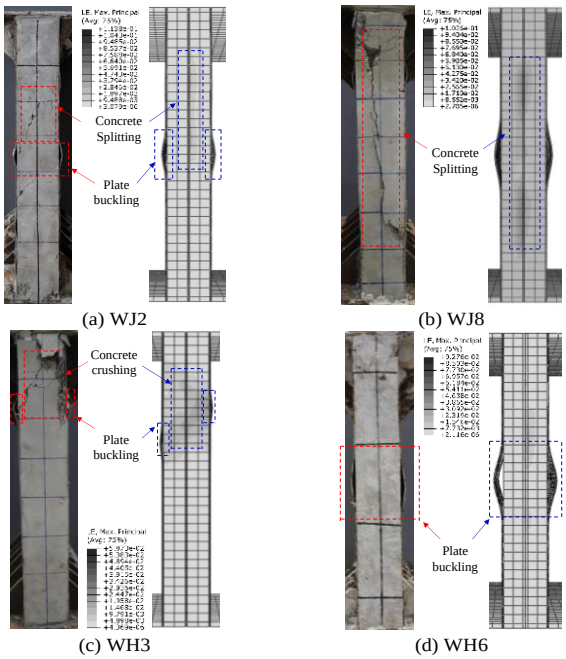

(a) WJ2 (b) WJ8

(c) WH3 (d) WH6

Fig. 9 Validations of the failure modes of the FE modes with those of the experimental results

Through the above validations of the ultimate compressive bearing capacity, load-displacement curves, and failure modes, it can be proven that the FEM established in this study can properly simulate the compression performance of DSCWs.

3.7. Parametric study

Earlier experimental investigations have demonstrated the effects of the steel plate thickness, concrete strength, temperature, connector spacing and connector type on the compression performance of DSCWs. However, the influence of the vertical spacing (S_V) and horizontal spacing (S_H) of the connectors on the compression performance of DSCWs has not been fully investigated due to time and economic limitations. Thus, the FEM proposed in this paper can be used to conduct a parametric study, and only half of the DSCW is built to improve the efficiency of the FEA. The material properties of the models used for parametric analysis are the same as those of WJ3.

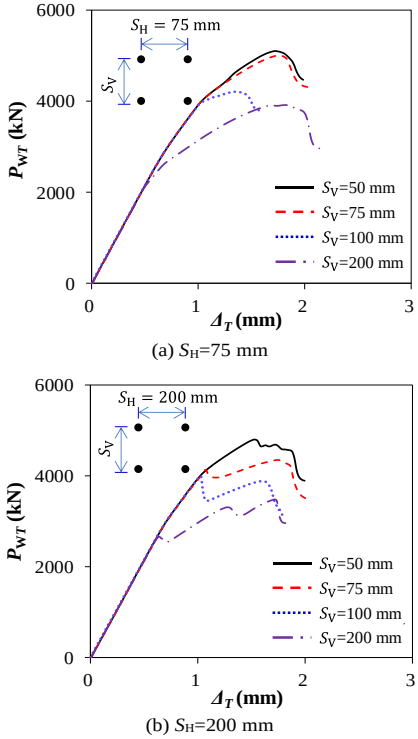

(a) S_H=75 mm

(b) S_H=200 mm

Fig. 10 Influence of the vertical spacing of connectors on the P_{WT}-Δ_T curve

3.7.1. Influence of the vertical spacing of the connectors

Fig. 10 demonstrates the impact of the vertical spacing of the connectors on the compressive performance of the DSCWs when the horizontal spacing is 75 mm and 200 mm. The steel plate and concrete are co-deformed at the initial loading stage with few interactions, causing the initial stiffness of the DSCWs, which is provided by the steel plate and concrete, to have a marginal influence with the increasing S_V value.

Fig. 11 presents the influence of the vertical spacing of the connectors on the area of local buckling of the steel plate when the DSCW reaches P_{uT}. The area of local buckling of the steel plate, mainly observed between the horizontal rows of the connectors, rises with increasing values of S_V. The larger the vertical spacing of the connectors is, the less the vertical constraint of the steel plate, which ultimately increases the area of local buckling of the steel plate.

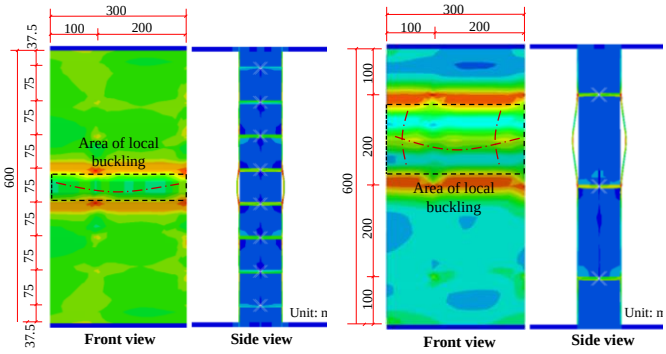

(a) S_V=75 mm, S_H=200 mm (b) S_V=200 mm, S_H=200 mm

Fig. 11 Influence of the vertical spacing of connectors on the area of local buckling of the steel plate

Fig. 12 illustrates the effect of the vertical spacing of the connectors on P_{uT} and *DI*. With increasing S_V values from 50 to 75, 100 and 200 mm, the P_{uT} (or *DI*) of the DSCW decreased by 2% (or 10%), 17% (or 12%) and 23% (or 19%), respectively, when the horizontal spacing of the connectors S_H was 75 mm, as shown in Fig. 12(a). Meanwhile, the P_{uT} (or *DI*) of the DSCW with a S_H of 200 mm declined by 9% (or 13%), 17% (or 15%) and 27% (or 16%), respectively, as shown in Fig. 12(b). As the S_V value increases, the slenderness ratio (S_V/t_s) of the steel plate increases from 16.7 to 25, 33.3 and 66.7. The higher slenderness ratio substantially decreased the buckling resistance of the steel plate under compression and accelerated the premature local buckling of the steel plate, adversely affecting the ductility of the DSCW.

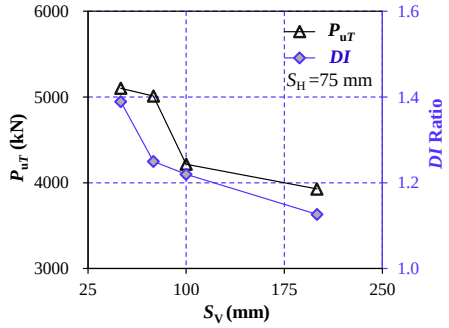

(a) S_H=75 mm

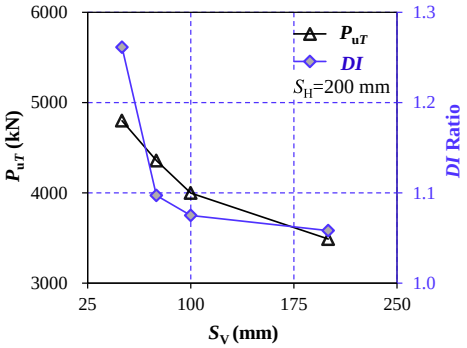

(b) S_H=200 mm

Fig. 12 Influence of the vertical spacing of connectors on P_{uT} and DI

3.7.2. Influence of the horizontal spacing of the connectors

Fig. 13 indicates the effect of the horizontal spacing of the connectors on the compressive performance of the DSCWs. The value of S_H has little effect on the initial stiffness of the DSCW because of the co-deformation of the steel plate and concrete at the initial load with few interactions.

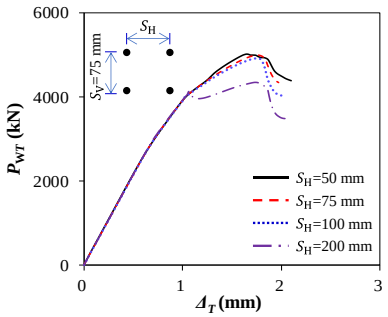

(a) S_V=75 mm

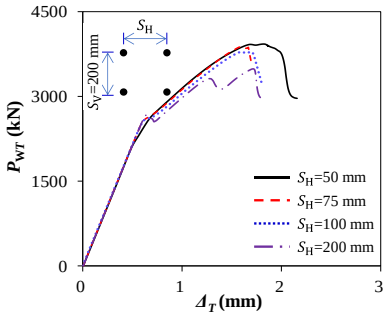

(b) S_V=200 mm

Fig. 13 Influence of the horizontal spacing of connectors on the P_{WT}-Δ_T curve

Fig. 14 depicts the effect of the horizontal spacing of the connectors on the area of local buckling of the steel plate when the DSCW reaches P_{uT}. As the value of S_H changes from 75 mm to 200 mm, the area of local buckling increases slightly. Since the local buckling of the steel plate mainly appears between the horizontal rows of the connectors, the changes in S_H rarely affect the area of local buckling of the steel plate. However, the insufficient horizontal constraint caused by the increased value of S_H causes the local buckling of the steel plate to expand towards the adjacent row of connectors, which results in a slight increase in the area of local buckling of the steel plate.

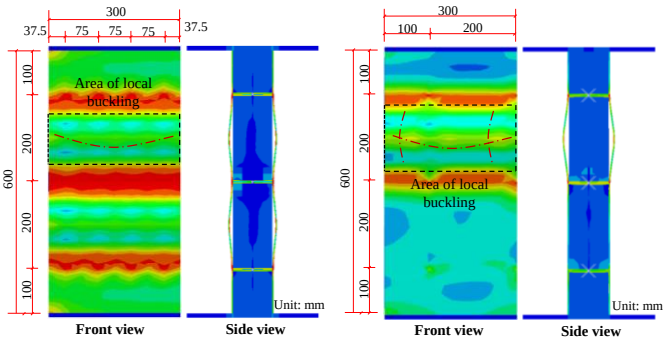

(a) S_V=200 mm, S_H=75 mm (b) S_V=200 mm, S_H=200 mm

Fig. 14 Influence of the horizontal spacing of connectors on the area of local buckling of the steel plate

Fig. 15 demonstrates the influence of S_H on P_{uT} and DI. Increasing the value of S_H from 50 to 75, 100 and 200 mm decreases P_{uT} (or DI) by 1% (or 13%), 2% (or 21%) and 13% (or 24%), respectively, when S_V is 75 mm, as shown in Fig. 15(a). Meanwhile, the value of P_{uT} (or DI) of the DSCW with a S_V of 200 mm decreases by 1% (or 4%), 3% (or 5%) and 11% (or 6%), respectively, as shown in Fig. 15(b). The increased S_H value with insufficient horizontal constraint on the steel plate and concrete accelerates the failure of the DSCW, which directly leads to the decreases in the P_{uT} and DI. However, it is worth noting that when the S_H value is less than 100 mm, S_H has a greater influence on DI than on P_{uT}. In contrast, when S_H is greater than 100 mm, S_H has a greater influence on P_{uT} than on DI. Thus, there must be a critical value for S_H, which is worthy of further research in the future.

4. Theoretical analysis of the compressive performance of the DSCW

4.1. Theoretical model

The load-displacement curves obtained by the experimental studies indicate that the DSCW undergoes a total of three stages from loading to destruction. However, the previous theoretical models only predict the ultimate compressive bearing capacity of the DSCW without describing the loading process, which cannot reveal the failure mechanism of the composite structures. Thus, this study aims to incorporate the loading process in the theoretical model, namely, proposing a theoretical model for the load-displacement curve of the DSCW.

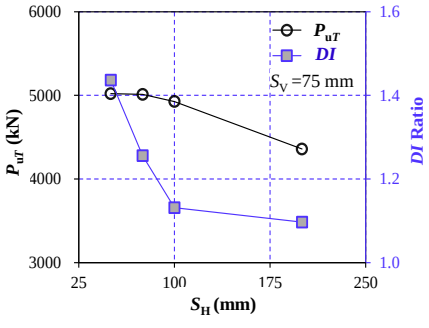

(a) S_V=75 mm

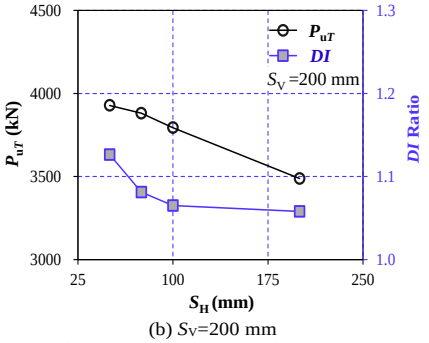

(b) S_V=200 mm

Fig. 15 Influence of the horizontal spacing of connectors on the P_{uT} and DI

The theoretical model presented in this study takes into account the following assumptions:

(1) The compressive bearing capacity of the DSCW, P_{WT}, is composed of the compressive bearing capacity of the sandwiched concrete, P_{cT}, and the compressive bearing capacity of the steel plates, P_{sT}:

$$P_{wT} = P_{cT} + P_{sT} \tag{3}$$

(2) The sandwiched concrete and steel plates in the DSCW are co-deformed under compression, and the strains of the steel plate and concrete can be expressed as follows:

$$\varepsilon_{cT} = \varepsilon_{sT} = \Delta_T / H \tag{4}$$

where ε_{cT} and ε_{sT} denote the strain of the concrete and steel plate; Δ_T denotes the vertical displacement of the DSCW; and H denotes the height of the DSCW.

4.1.1. Theoretical model of the sandwiched concrete

The sandwiched concrete is compressed biaxially under the constraint of the steel plate, which substantially improves the compressive bearing capacity of the concrete. Therefore, a strength improvement coefficient, α, is introduced into the theoretical model of concrete as follows:

$$P_{cT} = \alpha \sigma_{cT} A_c \tag{5}$$

where σ_{cT} denotes the concrete stress under compression, which can adopt the constitutive equation proposed by Xie et al. [31], as shown in Eq. (1); A_c denotes the concrete cross-sectional area, $A_c = W * t_c$; and W and t_c are the width and thickness of the concrete, respectively. The strength improvement coefficient, α, can be expressed as follows:

$$\alpha = \frac{\sigma_{ccT}}{f_{cT}} \tag{6}$$

where σ_{ccT} denotes the compressive strength of concrete under biaxial compression and f_{cT} denotes the concrete strength under uniaxial compression.

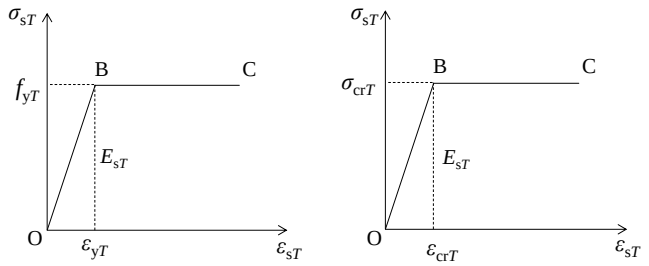

(a) $S/t_s \le \eta$ (b) $S/t_s > \eta$

Fig. 16 The constitutive equation of the steel plate

The formulas recommended by Yan et al. [27] are used to calculate σ_{ccT} as given below:

$$\sigma_{ccT} = \frac{\lambda + \sqrt{\lambda^2 - 4\left(1-\alpha_s^2\right)\left\{\sigma_h^2 - \left[\left(1-\alpha_s\right) f_{cT} + \alpha_s \sigma_h\right]^2\right\}}}{2\left(1-\alpha_s^2\right)} \tag{7}$$

$$\lambda = \left(1 + 2\alpha_s^2\right)\sigma_h + 2\left(1-\alpha_s\right)\alpha_s f_{cT} \tag{8}$$

$$\sigma_h = \frac{T_H}{S_H S_V} \tag{9}$$

$$T_H = \begin{cases} T_s = A_{sd}\sigma_{uT} / \gamma_{M2} \\ T_{pl} = \begin{cases} \left(0.9 f_{ckT} e_h d + 0.116 \sigma_{yT} d^2\right) / \gamma_c, & \text{for J-hook} \\ 8 A_{brg} f_{cT} A_N / \gamma_c, & \text{for Headed stud} \end{cases} \\ T_{CB} = 0.333\sqrt{f_{cT}} A_N / \gamma_c \\ T_{ps} = \pi d t_s \left(f_{ysT} / \sqrt{3}\right) / \gamma_{M0} \end{cases} \tag{10}$$

where α_s denotes the coefficient of shear yielding and is herein adopted as 0.19; σ_h represents the constrained stress contributed by the steel plate; T_H represents the resistance of the connectors under tensile forces; A_{sd} represents the cross-sectional area of the connectors; σ_{uT} represents the ultimate tensile strength of the connectors; A_{brg} represents the tensile area of the connectors; d represents the diameter of the connectors; e_h is the anchoring length of the J-hook; A_N represents the projection area of the concrete cone; t_s represents the thickness of the steel plate; and γ_{M2}, γ_c and γ_{M0} are partial factors and are herein equal to 1.0 for prediction purposes.

4.1.2. Theoretical model of the steel plate

The compressive bearing capacity of the steel plate can be obtained by the following:

$$P_{sT} = 2\sigma_{sT} A_s \tag{11}$$

where σ_{sT} denotes the steel plate stress under compression; A_s denotes the steel plate cross-sectional area, $A_s = W * t_s$; and W and t_s are the width and thickness of the steel plate, respectively. Two failure modes of the steel plate determined by the spacing-to-thickness ratio (S_V/t_s) are observed in the DSCW [7], namely, buckling failure and yield failure. When S_V/t_s is less than the critical value, η, the steel plate undergoes yield failure where the steel plate yields and then buckles with the constitutive equation given in Fig. 16(a). In contrast, when S_V/t_s is greater than the critical value, η, the steel plate undergoes buckling failure where the steel plate buckles and then yields with the constitutive equation shown in Fig. 16(b). Therefore, the steel plate compressive stress can be determined as follows:

$$\sigma_{sT} = \begin{cases} \begin{cases} E_{sT}\varepsilon_{sT}, & 0 \le \varepsilon_{sT} \le \varepsilon_{yT} \\ f_{yT}, & \varepsilon_{yT} \le \varepsilon_{sT} \le \varepsilon_{0T} \\ f_{yT}, & \varepsilon_{0T} \le \varepsilon_{sT} \end{cases}, \ \frac{S_V}{t_s} \le \eta \\ \begin{cases} E_{sT}\varepsilon_{sT}, & 0 \le \varepsilon_{sT} \le \varepsilon_{crT} \\ \sigma_{crT}, & \varepsilon_{crT} \le \varepsilon_{sT} \le \varepsilon_{0T} \\ \sigma_{crT}, & \varepsilon_{0T} \le \varepsilon_{sT} \end{cases}, \ \frac{S_V}{t_s} > \eta \end{cases} \tag{12}$$

where σ_{sT} and ε_{sT} denote the compressive stress and strain of the steel plate; σ_{crT} and ε_{crT} denote the buckling stress and strain of the steel plate; E_{sT} is the steel plate elastic modulus; f_{yT} and ε_{yT} represent the steel plate yield stress and strain; ε_{0T} is the peak strain of the concrete under compression; and η denotes the critical value of S_V/t_s.

The local buckling of the steel plate between the horizontal rows of connectors is observed according to the test results. Thus, the steel plate is simplified as a slender rod with the support points contributed by the connectors, as given in Fig. 17. Combined with the Euler formula [4,20], σ_{crT} can be expressed as follows:

$$\sigma_{crT} = \frac{\pi^2 E_{sT}}{12K^2\left(S_V/t_s\right)^2} \tag{13}$$

$$\varepsilon_{crT} = \frac{\pi^2}{12K^2\left(S_V/t_s\right)^2} \tag{14}$$

$$\eta = \sqrt{\frac{\pi^2 E_{sT}}{12K^2 f_{yT}}} \tag{15}$$

where K denotes the effective length coefficient for local buckling and is herein equal to 0.825 according to the regression analysis by Yan [7].

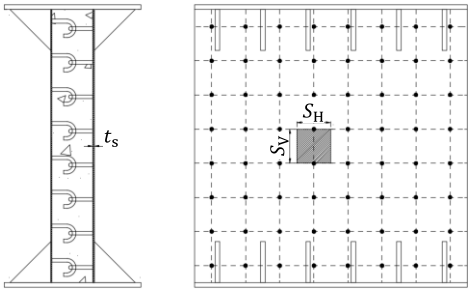

Fig. 17 Analysis model of local buckling

4.2. Validations

Twenty-two compression tests on DSCWs [7,8,9,23] have been analysed to validate the theoretical model proposed in this study. The validations comprise the ultimate compressive bearing capacity and load-displacement curves.

The experimental ultimate compressive bearing capacity of the DSCWs is compared with the predicted values by theoretical analysis, as shown in Table 3 and Fig. 18. The errors of the theoretical model predicted values are within ±15%. The average ratio of P_t/P_e is 1.05, and the coefficient of variation (COV) is 0.08.

Fig. 7 compares the experimental load-displacement curves reported by the authors with those obtained from the numerical and theoretical studies. The results indicate that the degree of agreement of the load-displacement curves between the theoretical model and FEM is better than that between the theoretical model and tests. Meanwhile, the elastic stiffness of the load-displacement curves predicted by the theoretical model is greater than that in the experimental load-displacement curves. This discrepancy may be attributed to the initial imperfections, welding quality, residual stress, accidental eccentricities, and non-uniform axial loading. Fig. 8 shows the validations of the load-displacement curves reported by Choi and Han [23]. The load-displacement curves predicted by the theoretical analysis are in good agreement with the results from the tests and FEA.

All of the validations prove that the developed theoretical model can be used to predict the loading process of the DSCWs under compression. However, according to the Chinese code GB5011-2010 [35], the concrete grade in shear wall cannot exceed C60 to prevent brittle failure. Meanwhile, to improve utilization of steel plate, the steel plate should yield before the concrete crushed, namely $\varepsilon_{yT}=f_{yT}/E_{sT}\leq\varepsilon_{oT}$. The peak strain ($\varepsilon_{oT}$) of normal weight concrete (C20~C60) is about 0.002 and the elastic modulus (E_{sT}) of steel plate is about 200 GPa. Thus, the yield strength (f_{yT}) of steel plate should not exceed 400 MPa. In addition, these formulae were only developed based on limited data, and only applicable to DSCWs with an aspect ratio of 1 within temperature interval of [20℃, -80℃].

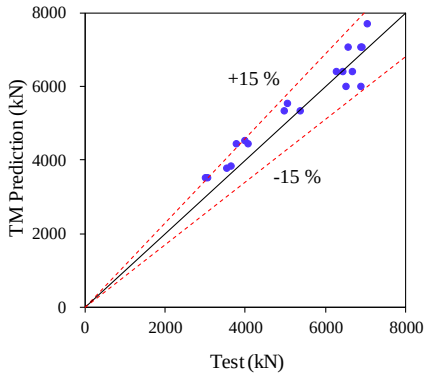

(a) Comparisons between the TM prediction and test results

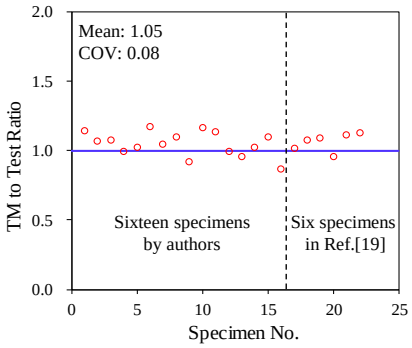

(b) Scatter of the TM to test ratios for P_{uT}

Fig. 18 Comparisons of the TM predictions of the ultimate bearing capacity with the test values

4.3. Steps for predicting the load-displacement curves of the DSCWs

Step I: Use Eqs. (6)-(10) to determine the strength improvement coefficient of the sandwiched concrete provided by the steel plates and connectors;

Step II: Using Eqs. (1) and (5) to determine the load-strain curve of sandwiched concrete;

Step III: Use Eqs. (12)-(15) to determine the stress-strain curve of the steel plate which consider local buckling. Use Eq. (11) to determine the load-strain curve of the steel plate;

Step IV: Use Eqs. (3)-(4) to determine the load-displacement curve of the DSCW from loading to destruction.

5. Conclusions

This paper develops an FEM and a theoretical model to predict the compression performance of DSCWs with interlocked J-hooks and overlapped headed studs at low temperatures.

The validation results for the ultimate compressive bearing capacity, load-displacement curves, and failure modes of the DSCWs obtained from the experimental investigation and FEA prove that the FEM established in this study can reasonably predict the compression performance of DSCWs at low temperatures. On the basis of the validated FEM, the influence of the vertical and horizontal spacing of the connectors on the compressive performance of the DSCWs is studied. Both the vertical and horizontal spacing of the connectors have a minimal effect on the initial stiffness of the DSCWs. However, increasing vertical and horizontal spacing substantially decreases the ultimate compressive bearing capacity and ductility of the DSCWs.

Based on the experimental and numerical investigation, the theoretical model of the load-displacement curve is developed, considering the constraint of the steel plates on the sandwiched concrete and the local buckling of the steel plate. By comparing the load-displacement curves predicted by the theoretical model with the curves obtained from the tests, it can be shown that the predicted curves are also divided into three stages, namely, the elastic stage, non-elastic stage and recession stage, which indicates that the proposed theoretical model can reasonably predict the loading process of the DSCWs at low temperatures.

Acknowledgment

The authors would like to acknowledge the research grant 52178494 received from National Natural Science Foundation of China for the works reported herein. The authors gratefully express their gratitude for the financial supports.

References

[1] Gautier, D.L., Bird, K.J., Charpentier, R.R., Grantz, A., Houseknecht, D.H., Klett, T.R., et al. “Assessment of undiscovered oil and gas in the Arctic”, Science, 324, 1175-1179, 2009. https://doi.org/10.1126/science.1169467.

[2] Marshall, P.W., Sohel, K.M.A., Liew, J.Y.R., Yan, J.B., Palmer, A., Choo, Y.S., “Development of SCS sandwich composite shell for arctic caissons”, Offshore Technology Conference, paper no. 23818, Houston, Texas, USA, 2012. http://dx.doi.org/10.4043/23818-MS.

[3] Yan, J.B., Liu, X.M., Liew, J.Y.R., Qian, X.D., Zhang, M.H., “Steel-concrete-steel sandwich system in Arctic offshore structures: materials, experiments, and design”, Materials and Design, 91, 111-121,2016. https://doi.org/10.1016/j.matdes.2015.11.084.

[4] Sohel, K.M.A. and Liew, J.Y.R., “Behavior of steel–concrete–steel sandwich slabs subject to impact load”, Journal of Constructional Steel Research, 100, 163-175, 2014. https://doi.org/10.1016/j.jcsr.2014.04.018.

[5] Yan, J.B., Liew, J.Y.R., Zhang, M.H., Sohel, K.M., “Experimental and analytical study on ultimate strength behaviour of steel-concrete-steel sandwich composite beam structures”, Materials and Structures, 48(5), 1523-1544, 2015. https://doi.org/10.1617/s11527-014-0252-4.

[6] Dai, X.X. and Liew, J.Y.R., “Fatigue performance of light-weight steel-concrete-steel sandwich systems”, Journal of Constructional Steel Research, 66(2), 256-276, 2010. https://doi.org/10.1016/j.jcsr.2009.07.009.

[7] Yan, J.B., Wang, Z., Luo, Y.B., Wang, T., “Compressive behaviours of novel SCS sandwich composite walls with normal weight concrete”, Thin-Walled Structures, 141, 119-132, 2019. https://doi.org/10.1016/j.tws.2019.01.051.

[8] Yan, J.B., Wang, Z. and Wang, T., “Compressive behaviours of steel-concrete-steel sandwich walls with J-hook at low temperatures”, Construction and Building Materials, 207, 108-121, 2019. https://doi.org/10.1016/j.conbuildmat.2019.02.116.

[9] Yan, J.B., Wang, Z. and Xie, J., “Compressive behaviours of double skin composite walls at low temperatures relevant to the arctic environment”, Thin-Walled Structures, 140, 294-303, 2019. https://doi.org/10.1016/j.tws.2019.03.047.

[10] Mirza, O. and Uy, B., “Effects of the combination of axial and shear loading on the behaviour of headed stud steel anchors”, Engineering. Structures, 32(1), 93-105, 2010. https://doi.org/10.1016/j.engstruct.2009.08.019.

[11] Guezouli, S. and Lachal, A., “Numerical analysis of frictional contact effects in push-out tests”, Engineering. Structures, 40, 39-50, 2012. https://doi.org/10.1016/j.engstruct.2012.02.025.

[12] Qureshi, J., Lam, D. and Ye, J.Q., “Effect of shear connector spacing and layout on the shear connector capacity in composite beams”, Journal of Constructional Steel Research, 67, 706-719, 2011. https://doi.org/10.1016/j.jcsr.2010.11.009.

[13] Pavlovic, M., Markovic, Z., Veljkovic, M., Budevac, D., “Bolted shear connectors vs. headed studs behaviour in push-out tests”, Journal of Constructional Steel Research, 88, 134-149, 2013. https://doi.org/10.1016/j.jcsr.2013.05.003.

[14] Nguyen, H.T. and Kim, S.E., “Finite element modelling of push-out tests for large stud shear connectors”, Journal of Constructional Steel Research, 65(10–11), 1909-1920, 2009. https://doi.org/10.1016/j.jcsr.2009.06.010.

[15] Shanmugam, N.E., Kumar, G. and Thevendran, V., “Finite element modeling of double skin composite slabs”, Finite Elements in Analysis and Design, 38(7), 579-599, 2002. https://doi.org/10.1016/S0168-874X(01)00093-2.

[16] Yan, J.B., “Finite element analysis on ultimate strength behaviour of steel-concrete-steel

sandwich composite beam structures", Materials and Structures, 48(6), 1645-1667, 2015. https://doi.org/10.1617/s11527-014-0261-3.
[17] Yan, J.B., Liew, J.Y.R., Zhang, M.H., "Shear-tension interaction strength of J-hook connectors in steel-concrete-steel sandwich structure", Advanced Steel Construction, 11(1), 72-93, 2015.
[18] Yan, J.B., Wang, Z., Wang, X., "Behaviour of steel-concrete-steel sandwich plate under different ice-contact pressure", Advanced Steel Construction, 15(1), 116-122, 2019. https://doi.org/10.18057/IJASC.2019.15.1.15.
[19] Qi, Y., Gu, Q., Sun, G.H., Zhao, B.C., Wang, H.F., "Tensile force and bending moment demands on headed stud for the design of composite steel plate shear wall", Advanced Steel Construction, 15(4), 338-348, 2019. https://doi.org/10.18057/IJASC.2019.15.4.5.
[20] Li, Y. and Hu, H.S., "Finite element analysis of local buckling behaviour of steel plates in concrete-filled double steel plate composite shear walls", Journal of Building Structures, 38, 112-117, 2017.
[21] Fan, J.S., Zhu, Y.Y., Cui B., Huang, L.J., Spencer, B.F., "Experimental and numerical investigations on large-scale concrete-filled double-steel-plate composite structures", Engineering Structures, 231, 2021. https://doi.org/10.1016/j.engstruct.2020.111749.
[22] Vecchio, F.J. and McQuade, I, "Towards improved modeling of steel-concrete composite wall elements", Nuclear Engineering and Design, 241(8), 2629-2642, 2011. https://doi.org/10.1016/j.nucengdes.2011.04.006
[23] Choi, B.J. and Han, H.S., "An experiment on compressive profile of the unstiffened steel plate-concrete structures under compression loading", Steel and Composite Structures, 9(6), 519-534, 2009. https://doi.org/10.12989/scs.2009.9.6.519.
[24] Zhang, K., Varma, A.H., Malushte, S.R., Gallocher, S., "Effect of shear connectors on local buckling and composite action in steel concrete composite walls", Nuclear Engineering and Design, 269(4), 231-239, 2014. https://doi.org/10.1016/j.nucengdes.2013.08.035.
[25] Yang, Y., Liu, J.B. and Fan, J.S., "Buckling behavior of double-skin composite walls: An experimental and modeling study", Journal of Constructional Steel Research, 121, 126-135, 2016. https://doi.org/10.1016/j.jcsr.2016.01.019.
[26] Liang, Q.Q. and Uy, B., "Theoretical study on the post-local buckling of steel plates in concrete-filled box columns", Computers and Structures, 75(5), 479-490, 2000. https://doi.org/10.1016/S0045-7949(99)00104-2.
[27] Yan, J.B., Wang, X.T. and Wang, T., "Compressive behavior of normal weight concrete confined by the steel face plates in SCS sandwich wall", Construction and Building Materials, 171, 437-454, 2018. https://doi.org/10.1016/j.conbuildmat.2018.03.143.
[28] Yan, J.B., Chen, A.Z., Wang, T., "Compressive behaviours of steel- UHPC-steel sandwich composite walls using novel EC connectors", Journal of Constructional Steel Research, 173, 2020. https://doi.org/10.1016/j.jcsr.2020.106244.
[29] Yan, J.B., Chen, A.Z., Wang, T., "Axial compressive behaviours of steel-concrete-steel sandwich composite walls with novel enhanced C-channels", Structures, 28, 407-423, 2020. https://doi.org/10.1016/j.istruc.2020.08.070.
[30] ABAQUS standard user's manual, version 6.14, Providence, RI(USA): Dassault Systems Corp, 2012.
[31] Xie, J., Li, X. and Wu, H., "Experimental studies on the axial-compression performance of concrete at cryogenic temperatures", Construction and Building Materials, 72, 380-388, 2014. https://doi.org/10.1016/j.conbuildmat.2014.09.033.
[32] Hibbitt, H.D., Karlson, B.I. and Sorensen, E.P., "ABAQUS/standard user's manual. Version 6.9", Hibbitt, Karlsson, & Sorensen, Inc, 2009.
[33] CEB-FIP, CEB-FIP model code 1990, Trowbridge, Wiltshire, UK: Comite´ Euro-International Du Be ´ton, Redwood Books, 1993.
[34] Yan, J.B., Xiong, M.X., Qian, X.D., Liew, J.Y.R., "Numerical and parametric study of curved steel-concrete-steel sandwich composite beams under concentrated loading", Materials and Structures, 49, 3981-4001, 2016. https://doi.org/10.1617/s11527-015-0768-2.
[35] Yan, J.B., "Ultimate strength behavior of steel-concrete-steel sandwich composite beams and shells", PhD thesis, National University of Singapore, Singapore, 2012.
[36] BS EN 1994-1, "Eurocode 4: Design of Composite Steel and Concrete Structures: Part 1.1 General Rules and Rules for Buildings", British Standards Institution, London, 1999.
[37] AISC, ANSI/AISC 360-10, "Specification for Structural Steel Buildings", American Institute of Steel Construction, Chicago, II, 2010.
[38] GB5011-2010, "Code for seismic design of buildings", Beijing, China Standards Press, 2010.

Advanced Steel Construction – Vol. 17 No. 4 (2021) 385–393
DOI:10.18057/IJASC.2021.17.4.7

NUMERICAL INVESTIGATION ON CYCLIC BEHAVIOR OF RING-BEAM CONNECTION TO GANGUE CONCRETE FILLED STEEL TUBULAR COLUMNS

Chen Fang [1], Guo-Chang Li [2] and Lei Zhang [3, 4, *]

[1] *Midwest Roadside Safety Facility, University of Nebraska-Lincoln, Lincoln, Nebraska 68583, USA*
[2] *Professor, Shenyang Jianzhu University, Shenyang, Liaoning110168, China*
[3] *Lecturer, School of Civil Engineering and Architecture, Jiangsu University of Science and Technology, Zhenjiang, Jiangsu 212100, China*
[4] *Postdoctor, Institute of Geotechnical Engineering, Nanjing Tech University, Nanjing, Jiangsu 211816, China*
** (Corresponding author: E-mail: lei.zhang@just.edu.cn)*

ABSTRACT

As a promising composite structure, gangue concrete filled steel tubular (GCFST) column exhibites favarable characteristics including high strength and economic efficiency. This paper conducted numerical investiagations on structural behavior of a ring-beam connection to GCFST column with concrete beam under cyclic loading. Furthermore, finite element models of column-beam connections were developed using ABAQUS and validated against full-scale experimental tests to identify accuracy of selected modeling approaches. Using these validated models, stress distribution of each component was examined to study the force-transferring mechanism among the components and failure modes of the ring-beam connection. Research study indicated that the ring-beam connection showed a reasonable force-transferring mechanism under cyclic loading and the remarkable earthquake-resistant performance with high capacity and acceptable ductility. Finally, parametric studies were performed to assess the influences of beam-to-column stiffness ratio,steel ratio, axial load level, and concrete compressive strength on connection cyclic behaviors. Parametric studies provided some suggestions and references for the application of the ring-beam connection in various engineering projects.

ARTICLE HISTORY

Received: 10 July 2020
Revised: 26 April 2021
Accepted: 1 May 2021

KEYWORDS

Column-beam connection;
Gangue concrete filled steel tube;
Cyclic behavior;
Finite element modeling;
Ring beam

1. Introduction

Concrete-filled steel tubular (CFST) structure has been widely utilized as structural elements in the large-span bridges and high-rise building due to its high strength and stiffness [1]. A new gangue concrete filled steel tubular (GCFST) members is developed by replacing regular concrete with gangue concrete filled in steel tube [2]. Research studies indicate that the GCFST column with a ductile behavior provides high performance under various loading conditions. Compared to normal CFST column, the GCFST column demonstrates several merits [3, 4]: (i) The low density of the gangue concrete results in the reduction of weight (at least 20%) for reinforced concrete (RC) building compared to the normal concrete [5]; (ii) The gangue concrete has better lateral deformation characteristic than the regular concrete to effectively increase tube confinement effect and improve the load bearing capacity of GCFST member [6]; (iii) The use of gangue concrete in the engineering projects is a beneficial method that reduces the environmental pollution and achieves the favorable economic and social benefits [7].

During an earthquake event, the column-beam connection is a critical component that provides a large strength to the entire building and ensures building serviceability. The column-beam connection is designed to have a large strength that allows the forces to transfer into the column with the formation of a plastic hinge in the RC frame beam. In this manner, beams could fail prior to column, which avoids the occurrence of progressive collapse in the building due to cascade effect initiated the failure of low-level columns. Consequently, the stability and safety of a RC building depend on the behavior of column-beam connection under an earthquake event. Experimental and numerical research studies have been completed to investigate the behavior of column-beam connection to the CFST column. Han and Li [8] experimentally examined dynamic behavior of connection between circular CFST column and steel beams under reversed cyclic loading. Pucinotti et al. [9] developed a welded column-beam connection for the CFST column and experimentally investigated its seismic performance. Results demonstrated the acceptable performance for the seismic design requirements. Chen et al. [10] conducted experimental and numerical studies on dynamic response of a through-beam connection between CFST column and RC beam when subjected to cyclic loads. Parametric studies were performed to evaluate effects of reinforcement ratio between the ring beam and frame beam and axial load at the column top on the connection performance. Li et al. [3] developed a rebar-penetrated connection to GCFST column and conducted experimental test and finite element analysis to examine the connection seismic performance. Ding et al. [11] performed experimental and numerical investigations on earthquake-resistance behavior of a non-through-core connection between RC beams and CFST column in terms of strain, ductility, and stiffness degradation. Limited studies have been published that investigated the cyclic-loaded response of the connection to GCFST column. Research studies on the connection to the GCFST column would provide useful design information for its potential application in engineering projects.

This paper conducted numerical investigations that evaluated the performance of a ring-beam connection between GCFST column and RC beam under cyclic loading. This ring-beam connection consisted of four primary components including the GCFST column, frame beams, ring beam and shear ring welded in steel tube. Fig. 1 shows diagram of typical ring-beam connection to the GCFST column. Detailed finite element models of the ring-beam connections were developed using ABAQUS. Numerical results were validated against tested results to evalute the accuracy of the developed model. The connection response to cyclic load was then examined to analyze the stress distribution and failure mode in each component of the ring-beam connection. Finally, extensive parametric studies were conducted to assess effects of critical parameters on cyclic loaded connection behavior. These studied parameters included the axial load level, steel ratio, concrete compressive strength, ring beam width, column slenderness ratio, and column-beam stiffness ratio.

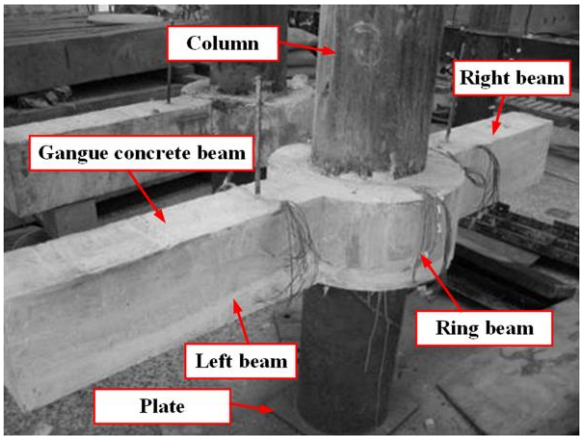

Fig. 1 Ring-beam connection to GCFST column

2. Finite element modeling

2.1. Material model

To reasonably represent concrete stiffness deterioration, ABAQUS's concrete plastic damage model was utilzed to simulate the dynamic response of

the concrete [12]. Given the steel tube confinement effect, the constitutive model for the light-aggregate concrete filled in tube developed by Fu et al. [13] was used to represent the behavior of core concrete in the compression zone. The light-aggregate concrete constitutive developed by Zhang et al. [14] was utilized to simulate the concrete response under dynamic loading for the unconfined gangue concrete in the compression zone, as shown in Fig. 2. These concrete constitutive models demonstrated their abilities to reasonably represent the experimental results and ensure computation convergency. The gangue concrete in the tension zone was modeled using the energy fracture criterion considering the concrete softening characteristics [15]. The concrete fracture energy (G_f) is formulated in the Eq. (1).

$$G_f = a\left(\frac{f_c'}{10}\right)^{0.7} \times 10^{-3} \tag{1}$$

where a = 1.25d_{max}+10 (unit: mm); d_{max} is the maximum size of the concrete aggregate; and f_c' is the compressive strength of the concrete. The concrete accumulative damage was modeled using a damage variable (d_c) with a fracture energy-crack displacement curve as shown in Eq. (2).

$$d_c = 1 - \frac{\sigma_c + n_c\sigma_{cu}}{E_c\left(\frac{n_c\sigma_{cu}}{E_c} + \varepsilon_c\right)} \tag{2}$$

where σ_c is compressive stress; σ_{cu} is ultimate compressive strain; E_c is concrete elastic stiffness; ε_c is compressive strain; and n_c is a constant coefficient under compression and is larger than 0. According to previous research studies [8] and computation trials, n_c was taken to1 for unconfined gangue concrete in the RC beam and 2 for the steel tube confined gangue concrete under compression. The default of compressive stiffness recovery factor (w_c=1) was defined in numerical simulation.

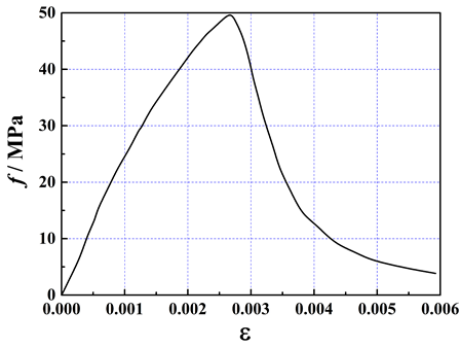

Fig. 2 Constitutive model of confined gangue concrete

A steel hysteretic constitutive model was employed to simualte the cyclic-loading response of steel tube [16]. ABAQUS's kinematic hardening model which involves a von Mises yield surface and consideres an associate plastic flow rule for the steel properties [17] was also utilized for the steel to consider the Bauschinger effects on the connection cyclic behaviors [18]. Based on research studies and computation trails, the reinforcement response to cyclic load was modeled using a double-linear constitutive model that considers bearing capacity deterioration (USTEEL02) developed by Tsinghua University [19]. This model (USTEEL02) has demonstrated its ability to reasonably replicate the experimental results for RC structures and accurately simulated the slip bond between reinforcing bar and its surrounding concrete.

2.2. Mesh and Element

The concrete and rigid plate were modeled using 8-node, reduced-integration, solid element and the mapping self-customized mesh technique in ABAQUS. The steel tube was simulated using 4-node, reduced-integration, shell element and considering Simpson's rule through the cross-section of shell element. Reinforcement embedded in the gangue concrete was modeled using two-node truss element. The embedded region model in ABAQUS was used to couple the reinforcement into its surrounding concrete. Fig. 3 shows the developed numerical model of the ring-beam connection. The accuracy and efficiency of developed numerical model always depends on the mesh density for each component. In order to achieve a balance between the accurate result and computation speed, the mesh size in the central portions of the connection was refined, with the increased mesh size for the remaining portions. The mesh sizes in the steel tube and core gangue concrete was identical to improve computation convergency.

2.3. Contact and boundary conditions

For GCFST column, the interaction between steel tube and confined gangue concrete consists of interfacial contact and slip bond. The interfacial contact in the normal direction was modeled using a hard contact model to fully transfer the tube-concrete contact stress. For the slip bond in the tangential direction, the penalty-based friction contact model was selected using a Mohr-Coulomb friction formulation [20], with a friction coefficient of 0.6 [15]. In order to transfer uniformly the normal force at the column top and reduce effects of boundary conditions, both plates at the column top and bottom were simulated as the elastic plates with large stiffness. The end plate elastic modulus was 1×10^{12} MPa , and the Poisson's ratio was 0.0001. The contact between steel tube and end plates was modeled using a solid-to-shell coupling model, and a hard contact was used to represent the core concrete - end plate contact. In the experimental test, the hinged boundary condition was assumed at the top and the bottom of the GCFST column. In the numerical model, the column bottom was constrained using UR1=UR3=0 and U1=U2=U3=0, with a hinged boundary condition at the top. The cyclic load in a form of a displacement was placed at both ends of frame beams, as shown in Fig. 4, in which P_y is the estimated bearing capacity at yielding of the ring-beam connection. During numerical simulation, a constant axial load (N_0) was applied at the column top.

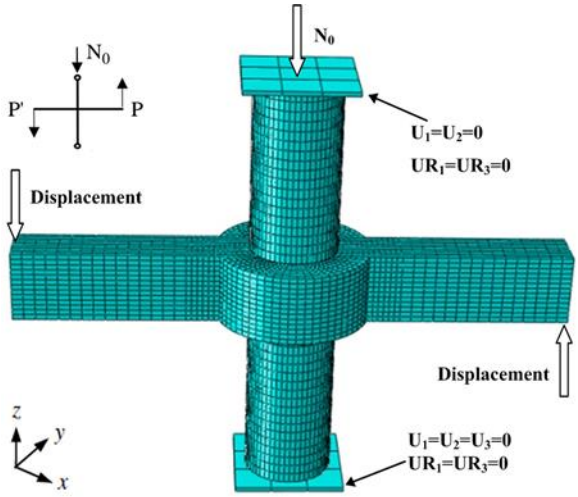

(a) Connection model (ube and concrete)

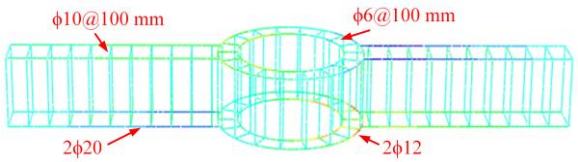

(b) Reinforcement details

Fig. 3 Ring-beam connection numerical model

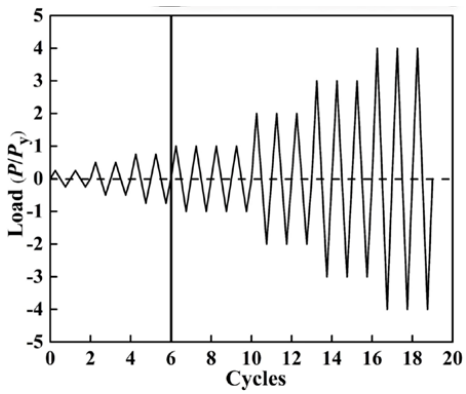

Fig. 4 Cyclic loading

2.4. Validation studies

Table 1
Dimensions of tested and modeled specimens

Specimen	L (m)	$D\times t$ (mm)	b_0 (m)	α	λ	l (m)	k	$f'_{c,b}$ (MPa)	$f'_{c,c}$ (MPa)	n
JH-E-B	1.5	325×6	0.12	0.078	36	1	0.853	30	30	0.6
JH-E-Z	1.5	325×6	0.12	0.078	36	2	0.853	30	30	0.6
JH-A-B	1.5	325×6	0.12	0.078	36	1	0.853	30	30	0.6
JH-A-Z	1.5	325×6	0.12	0.078	36	2	0.853	30	30	0.6

Experimental studies were completed on two specimens with an interior connection having two frame beams (JH-E-Z) and an exterior connection having one frame beam (JH-E-B) subjected to a constant axial load at the column top and cyclic loads at the beam ends. Numerical models corresponding to these specimens were developed and validated by the comprisons between simulated and tested results. In the test, the column was designed as a circular gangue concrete filled steel tubular column with a diameter of 325 mm. All beams having the cross-sectional dimensions of 180×250 mm were reinforced by 2ϕ20 longitudinal bars and ϕ10 hoops spaced at 100 mm. The vertical height of the column was 1500 mm. The ring beam had a cross-sectional dimension of 120×250 mm and 2ϕ12 longitudinal bars, with ϕ6 hoops spaced at 100 mm. The axial load ratio of 0.6 was designed at the column top during testing. Two numerical models that corresponded to the tested specimens were developed using ABAQUS, with interior connection referred to as JH-A-Z and exterior connection as JH-A-B.

Table 1 lists geomitries and properties of tested and modeled specimens. In the table, L is the column height; D is the column diameter; t is the tube thickness; b_0 is the width of ring beam; l is the beam length; α is the steel ratio (A_{SC}/A_{CC}, where A_{SC} and A_{CC} are the cross-sectional areas of GCFST column and core concrete, respectively); λ is the slenderness ratio of column, defined as $4l_c/D$, where l_c is the calculated column height; k is the beam-to-column bending stiffness ratio, which is calculated as the ratio of beam stiffness to column stiffness; $f'_{c,b}$ is the unconfined concrete compressive strength for the frame beam; $f'_{c,c}$ is the confined concrete compressive strength for the GCFST column; n is the axial load ratio, defined as N_0/N_u, where N_0 is the axial load applied at the column top, and N_u is the plastic axial capacity of the GCFST column calculated by CECS28-2012 [21].

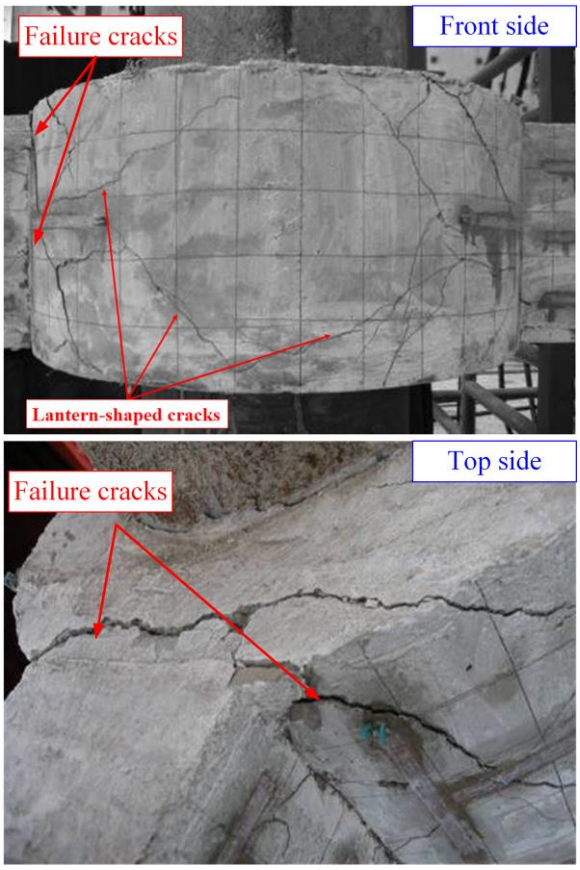

(a) Experimental test

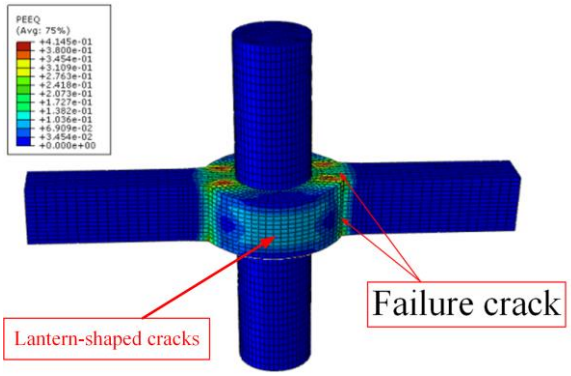

(b) Numerical simulation

Fig. 5 Comparison of simulated and experimental failure mode

2.4.1. Failure modes

Fig. 5 shows a comparison of simulated and tested failure mode. The failure mode of the ring-beam connection obtained in numerical simulation matched well with those in experimental tests, with concrete cracking formed at the ends of frame beam near the region of the ring beam. The ring-beam connection to the GCFST column failed due to the significant cracks in the region between ring beam and frame beam for both modeled and tested results. The lantern-shaped cracks were shown in the side of ring beam for numerical model, which agreed well with the experimental observations. For the ring-beam connection, the GCFST column remained intact in both numerical simulation and experimental test. These observations indicated the adequate strength and stiffness of the ring-beam connection to resist seismic loads, which satisfies the design philosophy in the seismic code for buildings that “strong column and week beam, strong connection and week members” [22].

2.4.2. Load-displacement curve and skeleton curve

Fig. 6 illustrates a comparison of simulated and experimental load (P) - displacement (Δ) curves for exterior and interior connections, where P represents the load imposed at frame beam ends, and Δ represents vertical displacement at the frame beam ends. As shown in Fig. 6, the simulated curves matched acceptably with the experimental curves, with the similar strength degradation and stiffness reduction during the process of loading. However, the simulated curves were fuller than the experimental curves, with the pinching observations formed in the experimental curves. The difference in curve shape would be caused by the deficiency of selected concrete constitutive model in modeling the significant reinforcement-concrete bond slip behavior. Few research studies have been conducted to develop and evaluate the gangue concrete constitutive model under different loading condictions. As a result, a perfect concrete model was not located in the open literature.

Fig. 7 compares simulated and experimental skeleton curves for the interior and exterior ring-beam connections. Table 1 summarizes tested and simulated characteristic loads for each connection. As shown in Fig. 7 and Table 2, the simulated skeleton curves achieved an acceptable agreement with the experimental results with a slightly lower peak. The difference of the peak value between the numerical simulation and experimental tests was approximately 10%. As indicated in relevant research studies [11, 23, 24], the difference between simulated and tested results up to 20% was acceptable for a complex FE model. This difference was attributed to the deficiency of concrete constitutive model and the Tie model selected to represent welding for each steel component. Overall, the developed model reasonably represented the failure mode of ring-beam connection under seismic loading and acceptably predicted the strength and stiffness degradation.

Table 2
Comparison of character loads and displacements

Model	P_0 (kN)	Δy (mm)	P_y (kN)	Δ_{max} (mm)	P_{max} (kN)	P_u (mm)
JH-E-B	11	1.9	21	6.23	39	32.7
JH-A-B	12.10	1.83	19.02	5.93	44.15	37.52
JH-E-Z	13	2.1	24	6.37	49	42.6
JH-A-Z	12.45	2.02	23.38	5.95	47.72	40.56

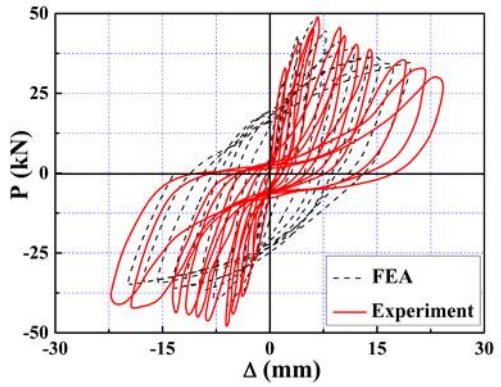

(a) Interior connection

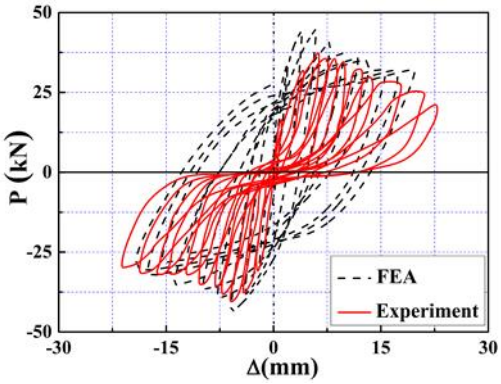

(b) Exterior connection

Fig. 6 Comparison of tested and simulated load-displacement curves

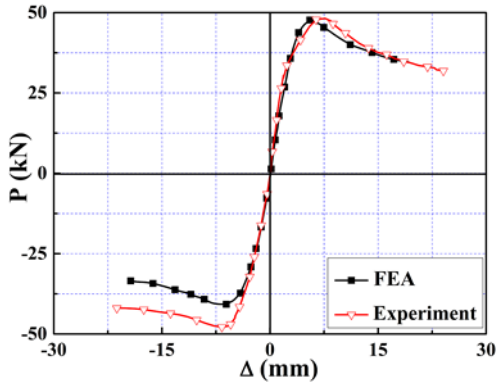

(a) Interior connection

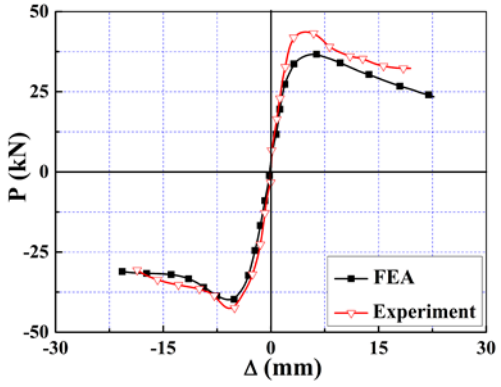

(b) Exterior connection

Fig. 7 Tested and simulated load-displacement skeleton curves

3. Predicted behavior of ring-beam connection

Fig. 8 shows the load-dipslacement curves of the ring-beam connection to CFST column when subjected to cyclic load. In this figure, four representative points were defined to analyze the connection behavior at different phases. Point A indicates the appearance of first crack in the frame beam, with the bearing capacity defined as P_0. Point B represents the yielding of ring beam connection, and the corresponding connection bearing capacity was defined as P_y. As the load reaches the peak value, the ultimate bearing capacity of the ring-beam connection (P_{max}) is obtained in the curve, referenced as to Point C. Point D represents the load at connection failure (P_u) when the load reduced to 85% of P_{max}. The behavior of each component in the ring beam connection was analyzed in the following sections.

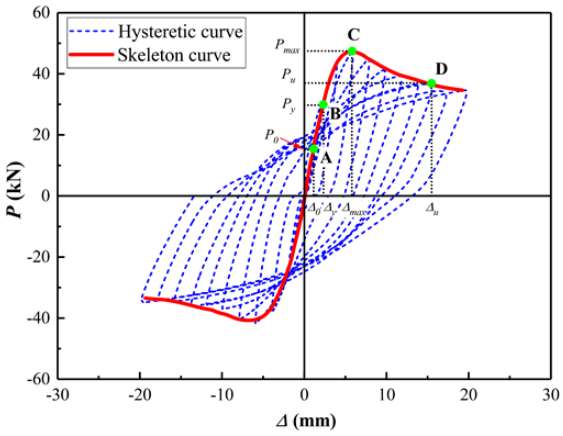

Fig. 8 Typical *P-Δ* curve for a connection to GCFST column

3.1. GCFST column

The GCFST column was subjected to bending moments created from the cyclic load at the ends of frame beams and an axial load at the column top. Fig. 9 depicts the stress of confined gangue concrete (S33, in MPa) in the GCFST column at each point, in which the stress is the concrete compressive stress along the normal direction. The compression region developed along the column height and the compressive stress increased with the increased cyclic load at the ends of frame beams, as shown in Fig. 9. Furthermore, the lateral deformation of the core concrete increased as the axial load was applied at the top, resulting in the increase of the steel tube confinement on the core gangue concrete. At point C, the concrete compressive stress reached 24.1 MPa which approximates to $1.18f_c'$. This finding indicated that the steel tube confinement is beneficial to the increased strength of the concrete due to triaxial stress state. The accumulation of damage in the core gangue concrete resuted in the decrease in the concrete compressive stress after the point C,.

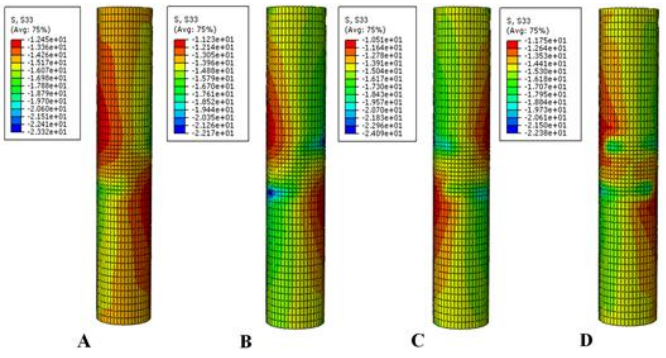

Fig. 9 Compressive stress of core gangue concrete

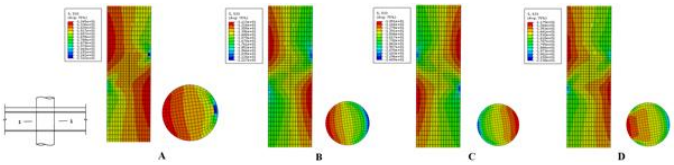

Fig. 10 Compressive stress in the connection zone

Fig. 10 plots cross-sectional stress distribution for the confined concrete in GCFST column at each point. It was observed that the neutral axis of the

confined concrete shifted from the tensile region to the compressive region with the increase in the load. A diagonal compressive strut was developed for the center region of the ring beam connection, identifying that the confined concrete carried the shear stress and moment. The compressive strut extended as the average stress increased with the increased load. The maximum average stress of the compressive strut was obtained at the point C. Then, the compressive strut continued expanding with the decreased average compressive stress due to the accumulated concrete damage after the point C.

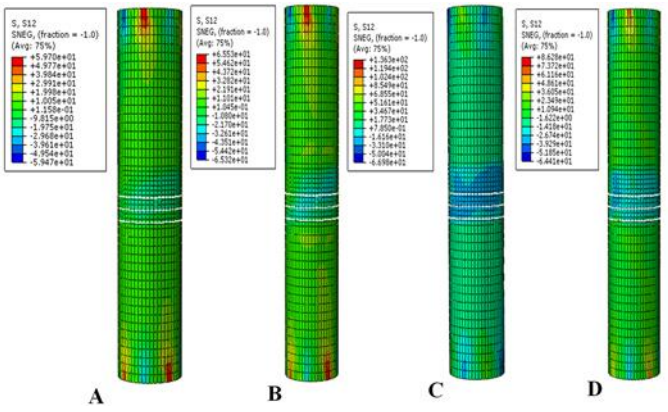

Fig. 11 Shear stress for steel tube

The steel tube shear stress (S12) in the GCFST column at each point is shown in Fig. 11, in which shear stress is used to examine the load-transferring mechanism for the composite connection. Fig. 12 plots the stress of shear ring along the perimeter at the point C. The average stress of the tube increased and the stress zone in the connection region developed with the increase in the cyclic load. A diagonal stress zone was observed in the connection region at the point C, and shear ring stress was lower than the steel yield strength in the elastic state. It can be observed that the shear ring was functioned to transfer the shear stress to the column which was the primary component to sustain the shear stress under cyclic loading.

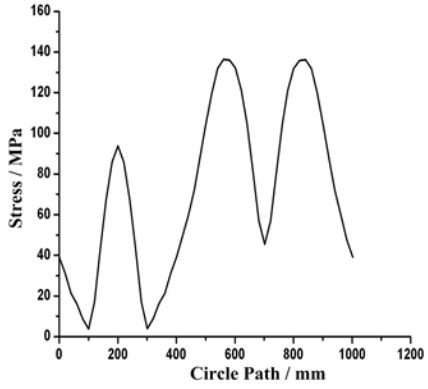

Fig. 12 Shear ring stress along perimeter at point C

3.2. RGC beam

Fig. 13 shows stress distribution (S11, in MPa) in RGC beam at the characteristic points along with the equivalent plastic strain shown in Fig. 14. In Fig. 14, the equivalent plastic strain represents the formation of concrete cracks in the beam. The compressive and tensile stresses were observed at the top and bottom sides of RGC beam close to GCFST column due to bending moment and compression load along the beam length at the point A. The initial crack was formed in the region between the ring beam and the frame beam at this point. As the cyclic load increased, the compression region developed along the beam length, and concrete cracks was shown to propagate along the beam depth. At the point C, the lantern-shape cracks were formed in the side of ring beam with significant concrete cracks observed through the frame beam. At point D, concrete cracks were extended to the ring beam, and this connection failed due to significant concrete cracks in the frame beam.

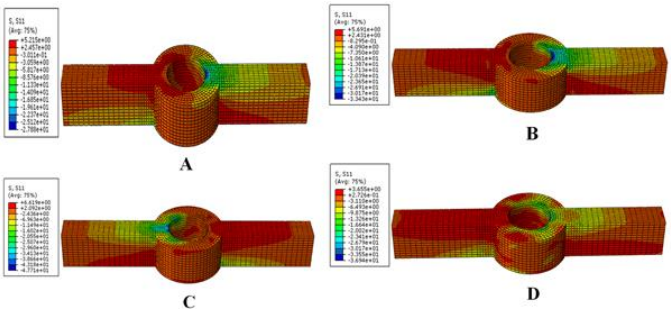

Fig. 13 Stress distribution (S11) in RGC beam

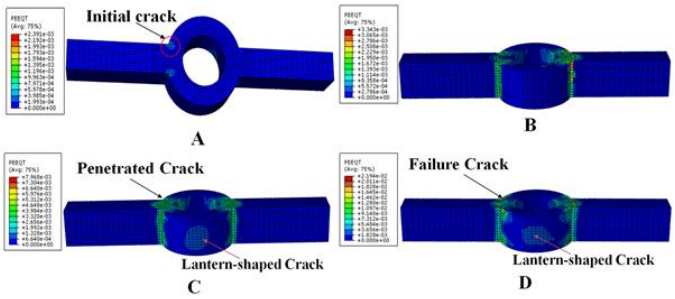

Fig. 14 Equivalent plastic strain distribution in RGC beam

Fig. 15 shows reinforcement stress in the RGC beam at the characteristic points. As shown in Fig. 15, the compressive and tensile stress in reinforcements was formed at the top and bottom sides of the frame RGC beams in the initial phase of loading. The increased cyclic load resulted in the increased stress in the reinforcements. As the cyclic load increased at the point B, the longitudinal reinforcements embedded in the frame beam were yielded with the yielding of circular reinforcements in the ring beam. This observation indicated the yielding of ring-beam connection. At point C, the stress in the longitudinal and circular reinforcements further increased, while was still less than the reinforcement ultimate strength. The hoops in the region between the ring beam and frame beam were yielded during the loading.

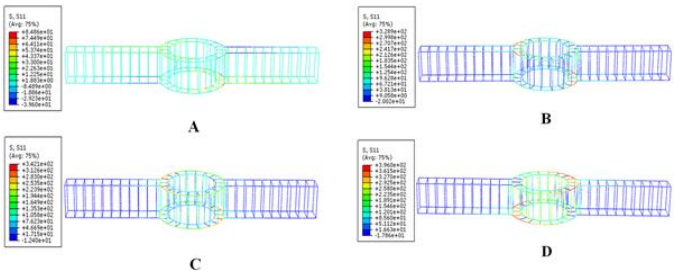

Fig. 15 Stress distribution of reinforcements in RGC beam

Based on the behaviors of structural components in this composite connection, the load transferring mechanism of the ring-beam connection was summarized as: The bending moment was produced on the ring beam and could be simplified as the compression and tension forces at the top and bottom side of the ring beam when the cyclic loads were applied at the ends of the frame beams. The compression force was transferred through the ring beam and sustained by the GCFST column, while the tension force was resisted by the circular reinforcement and hoop in the ring beam. In addition, shear forces formed in the frame beams were transferred to the GCFST column through three primary components, (i) shear ring welded in the tube was used to transfer shear forces through interaction forces between shear ring and steel tube; (ii) adhesive force between ring beam and steel tube also played an essential role in the shear transferring mechanism; and (iii) a diagonal strut was developed around the connection region to produce the significant friction force due to the extrusion of ring beam on the GCFST column.

4. Parametric studies

Parametric studies were performed that examined the influences of several

design parameters on dynamic response of the ring beam connection when subjected to cyclic loads. The studied parameters include: (1) Material parameters: concrete compressive strength and steel yield strength; (2) Geometric parameters: steel ratio, GCFST column slenderness ratio, beam-to-column stiffness ratio, and width of ring beam; (3) Load parameters: axial load magnitude at the column top.

Effects of the studied parameters were evaluated by examining bending moment (M) to rotation (θ) relationship of the beam and the initial stiffness of the connection. In this section, the skeleton curves for the bending moment to rotation relation were used to clearly examine the initial stiffness and the ultimate bearing capacity of the ring-beam connection. The initial stiffness of the ring-beam connection is determined as the secant stiffness corresponding to the $0.2M_{uj}$ according to the research studies [25] for CFST member as shown in Eq. (3).

$$K_i = \frac{0.2M_{uj}}{\theta_{0.2}} \tag{3}$$

where K_i is the ring-beam connection initial stiffness; M_{uj} represents the ultimate beading moment; and $\theta_{0.2}$ is the rotation that corresponds to $0.2M_{uj}$. Fig. 16 illustrates the M - θ curves and resulting skeleton curves in the parametric studies for ring beam connection.

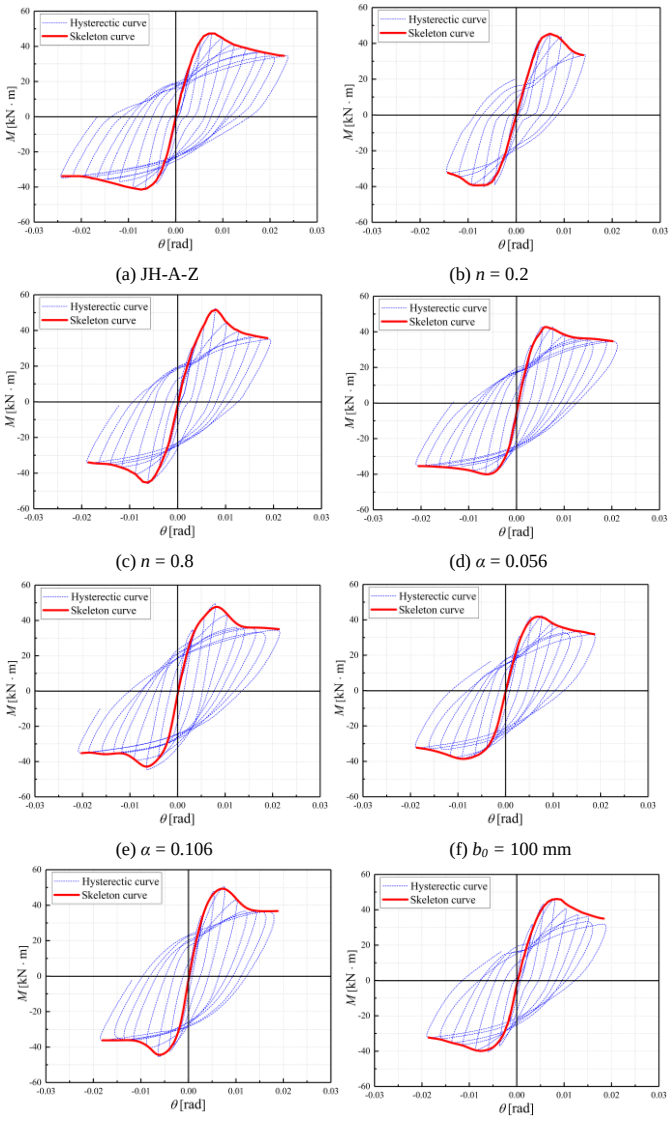

(a) JH-A-Z (b) n = 0.2

(c) n = 0.8 (d) α = 0.056

(e) α = 0.106 (f) b_0 = 100 mm

(g) b_0 = 140 mm (h) $f'_{c,c}$ = 20 MPa

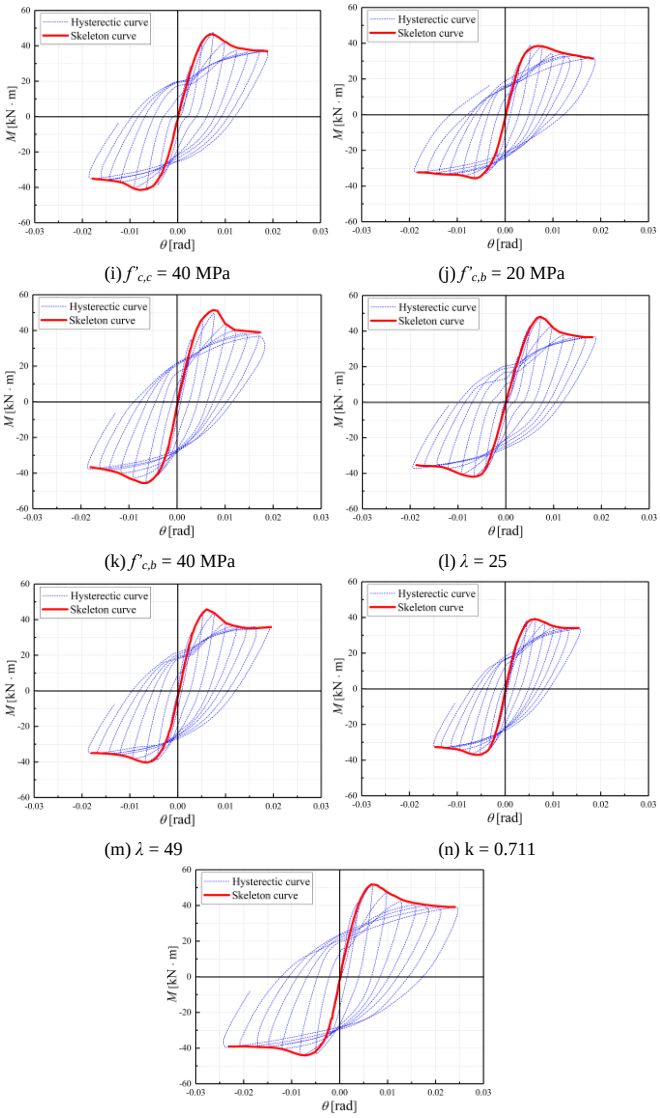

(i) $f'_{c,c}$ = 40 MPa (j) $f'_{c,b}$ = 20 MPa

(k) $f'_{c,b}$ = 40 MPa (l) λ = 25

(m) λ = 49 (n) k = 0.711

(p) k = 1.066

Fig. 16 M-θ curves in parametric studies for ring beam connection

4.1. Axial load ratio (n)

In this section, three axial load ratios, including 0.2, 0.6, and 0.8, were considered to apply the axial load at the column top. Fig. 17 illustrates influences of axial load ratio on the M-θ curves, with Fig. 18 on the connection initial stiffness. The axial load ratio affected the ring-beam connection flexural capacity, as shown in Fig.s 17 and 18. The increased axial load magnitude at the column top resulted in the increased flexural bearing capacity of the ring beam connection. The moment increased linearly with the rotation at the initial phase of loading. As the the axial load ratio increased, the ring-beam connection initial stiffness increased in an approximately linear relation. The connection stiffness at the hardening phase increased with the increased axial load ratio, and the connection would be failed earlier at a higher axial load. The increased axial load magnitude at the column top beneficially improved the column bending moment capacity and enhanced the ring-beam connection flexural capacity.

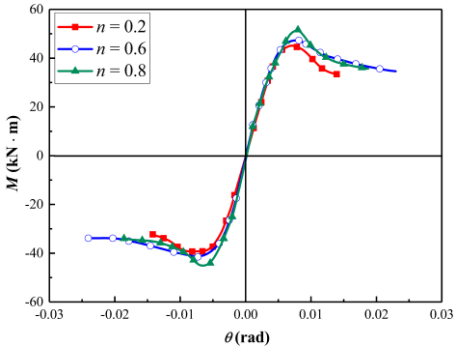

Fig. 17 Effects of n on M-θ curve

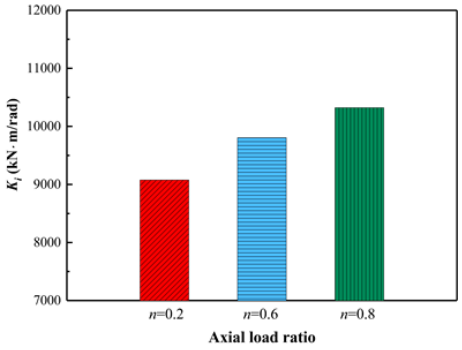

Fig. 18 Effects of *n* on initial stiffness

4.2. GCFST column steel ratio (α)

The steel ratio was varied by the change of steel tube thickness in this study. Three tube thicknesses were selected as 5 mm, 6 mm, and 7 mm. Fig. 19 illustrates effects of steel ratio on the *M-θ* relation, with Fig. 20 shown effects of steel ratio on the connection initial stiffness. The stiffness and flexural capacity of the ring-beam connection increased with the increased steel ratio of the GCFST column. The maximum flexural capacity was improved by 20% when the steel ratio increased from 0.056 to 0.078, while the flexural capacity increased by 5% with the increase in the steel ratio from 0.078 to 0.106. Similarly, the initial stiffness of the connection increased by approximately 25% as the steel ratio increased from 0.056 to 0.106. After the ultimate flexural capacity, the decrease of the flexural bearing capacity is aggravated with the increase of steel ratio. The increase in the connection flexural capacity was not as prominent as that observed from 0.056 to 0.078 in terms of ultimate flexural capacity and initial stiffness when the steel ratio increased from 0.106 to 0.078,. A limit to the connection capacity improvement exists as the column steel ratio increaes. Overall, the steel ratio of GCFST column significantly influenced the bearing capacity of the ring beam connection.

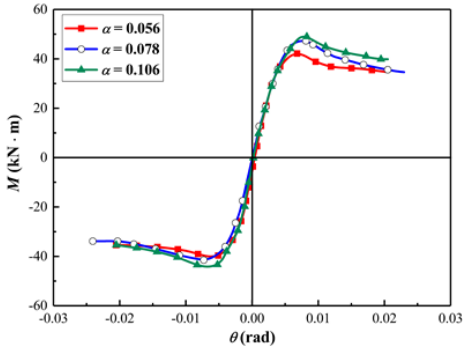

Fig. 19 Effects of *α* on *M-θ* curve

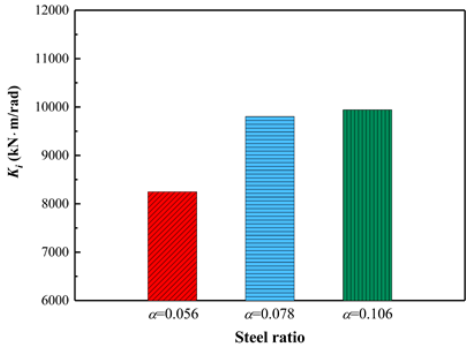

Fig. 20 Effects of *α* on initial stiffness

4.3. Ring beam width (b_0)

The ring beam width is expected to influence the ability of the ring beam to transfer shear force and bending moment to the GCFST column. Three widths (140 mm, 120 mm, and 100 mm) were used to investigate its effect on connection behavior. Fig. 21 illustrates effects of ring beam width on the *M-θ* relation, with Fig. 22 shown effects of ring beam width on the connection initial stiffness. As shown in Fig. 21, the ring-beam connection flexural capacity was enhanced with an increase in ring beam width. The ultimate flexural bearing capacity for b_0 = 140 mm was 18% and 5% higher than those for the connection with b_0 = 100 mm and 120 mm, respectively. It was observed from Fig. 22 that, the influence of ring beam width on the initial stiffness of the connection was insignificant with a similar value of 10000 kN·m·rad^{-1} obtained for three connections. Increasing ring beam width was beneficial to the connection capacity to sustain and transfer the bending moments produced from the cyclic load at the frame beams.

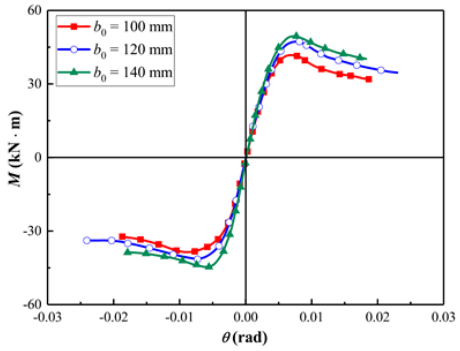

Fig. 21 Effects of b_0 on *M-θ* curve

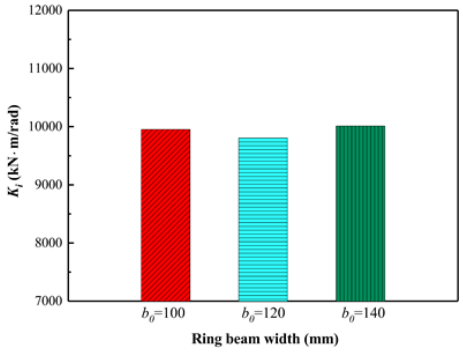

Fig. 22 Effects of b_0 on initial stiffness

4.4. Confined concrete compressive strength ($f'_{c,c}$)

Three compressive strengths of cofined concrete, involving 20 MPa, 30 MPa, and 40 MPa, were selected to analyze its effects on the connection behavior. Fig. 23 illustrates effects of concrete compressive strength in GCFST column on the *M-θ* relation, with Fig. 24 shown on the connection initial stiffness. As shown in Figs. 23 and 24, the confined concrete compressive strength in GCFST column had an insignificant influence on the initial stiffness and flexural capacity of the ring-beam connection. This finding was attributed to the design principle used for the ring-beam connection in this study that "strong column and weak beam" and the intact column during the loading.

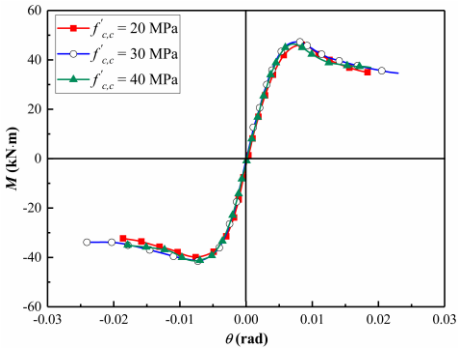

Fig. 23 Effects of $f'_{c,c}$ on *M-θ* curve

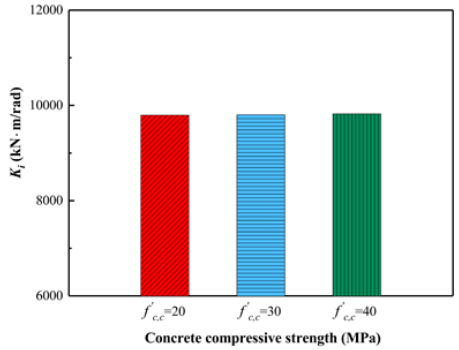

Fig. 24 Effects of $f'_{c,c}$ on initial stiffness

4.5. Concrete compressive strength in frame beam ($f'_{c,b}$)

Similarly, effects of concrete compressive strength in the frame beam were examined in this section. The concrete strength included 20 MPa, 30 MPa, and 40 MPa. Fig. 25 illustrates effects of concrete compressive strength in frame beam on the M-θ relation, with Fig. 26 shown on the connection initial stiffness. It was observed that, the increased concrete compressive strength in the frame beam resulted in the increased the ring-beam connection flexural capacity. The maximum flexural capacity of the ring-beam connection for $f'_{c,b}$ = 40 MPa was 1.1 and 1.4 times larger than those for the connection for $f'_{c,b}$ = 30 MPa and 20 MPa, respectively. At the initial loading phase, the concrete compressive strength in frame beam had an insignificant effect on the behavior of the ring-beam connection with similar initial stiffness of 10000 kN·m·rad^{-1} obtained for three studied connections due to the elastic behavior exhibited in the connections. Therefore, an increase in the concrete compressive strength in the frame beam was advantageous to the ring-beam connection flexural capacity to resist rotation, which improves connection behavior after the occurrence of cracks.

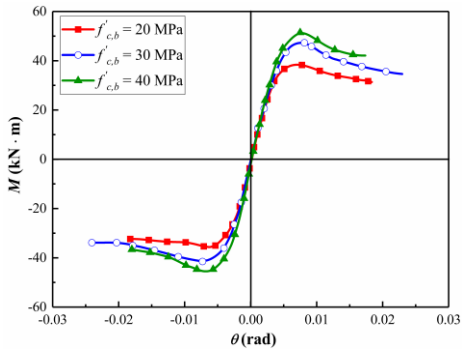

Fig. 25 Effects of $f'_{c,b}$ on *M-θ* curve

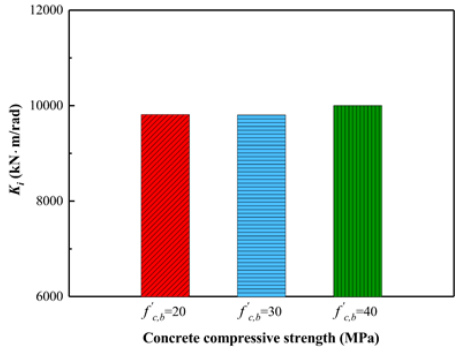

Fig. 26 Effect of $f'_{c,b}$ on initial stiffness

4.6. GCFST column slenderness ratio (λ)

GCFST column slenderness ratio is expected to change the deformation pattern of the connection. In this study, the GCFST column slenderness ratio was varied with the change of column height. The studied column height included 1000 mm, 1500 mm, and 2000 mm, which produced the column slenderness ratios of 25, 36, and 49. Fig. 27 illustrates effects of GCFST column slenderness ratio on the M-θ relation, with Fig. 28 shown on the connection initial stiffness. The effect of the GCFST column slenderness ratio on the flexural capacity and initial stiffness of the ring-beam connection was insignificant with almost identical ultimate flexural capacity and initial stiffness, as shown in Figs. 27 and 28. In the design principle for the connection, the strength of the GCFST column should be higher than the frame beam strength, and the column failure was avoided in this study. Therefore, the slenderness of the GCFST column insignificantly influenced the behavior of the ring beam connection.

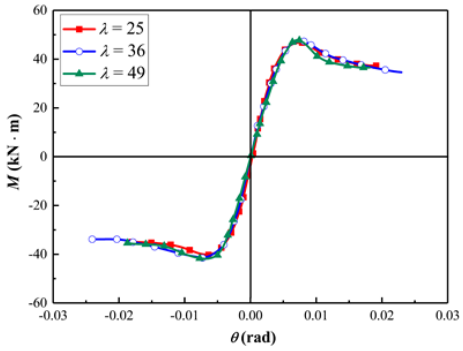

Fig. 27 Effects of λ on *M-θ* curve

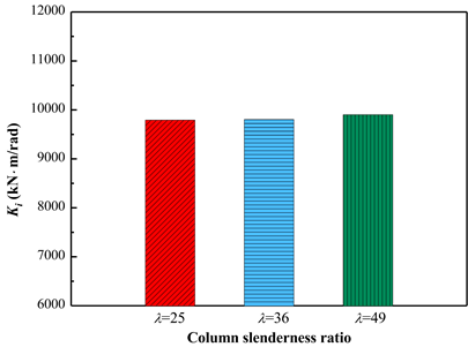

Fig. 28 Effects of λ on initial stiffness

4.7. Beam-to-column stiffness ratio (k)

The beam-to-column stiffness ratio is expected to affect the development and location of plastic hinge in the RGC frame beam. The beam-to-column stiffness ratio was changed by varying the length of frame beam in this study,. Three beam lengths of 800 mm, 1000 mm, and 1200 mm were selected. Fig. 29 illustrates effects of column-beam stiffness ratio on the M-θ relation, with Fig. 30 shown on the connection initial stiffness. As shown in Fig. 29 and Fig. 30, the flexural capacity of the ring beam connection was enhanced as the beam-to-column stiffness ratio increased. The ultimate flexural capacity increased by about 33% with the increase of the beam-to-column stiffness ratio from 0.711 to 0.853, while the connection capacity increased by approximately 5% as *k* increased from 0.853 to 1.066. The ring-beam connection stiffness was significantly improved with the increased beam-to-column stiffness ratio. Connection initial stiffness for *k* = 1.066 was 38% higher than that for the connection with *k* = 0.711. This finding was also attributed to the design principle for the ring-beam connection in this study that “strong column and weak beam”.

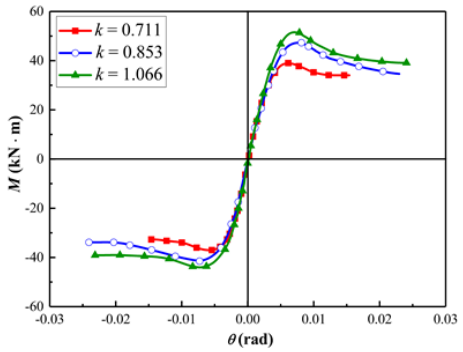

Fig. 29 Effects of *k* on *M-θ* curve

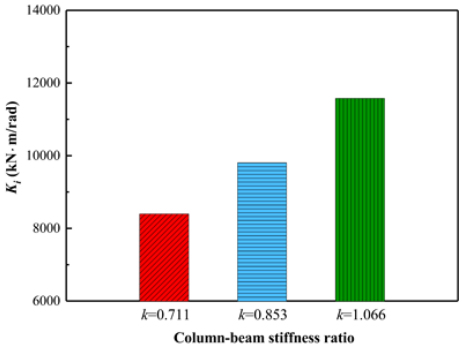

Fig. 30 Effects of *k* on initial stiffness

5. Conclusions

This paper numerically examined cyclic loaded dynamic response of a ring-beam connection between GCFST column and RGC beams. Detailed 3D, nonlinear, numerical models were developed using ABAQUS. Two specimens including an exterior connection and an interior connection were used to validate the feasibility of developed connection model with the experimental results. The behavior of the ring beam connection was examined to identify the force transferring mechanism and failure modes when subjected to the cyclic loads at frame beam ends. Extensive parametric studies were performed to assess the effects of critical design parameters on the connection behavior. The following conclusions were drawn in this paper:

(1) Finite element models were acceptably validated against the full-scale tests. Validation study demonstrated the ability of the developed model to reasonably predict failure modes and cyclic-loaded behaviors of the ring-beam connection.

(2) Failure of the ring-beam connection was due to significant concrete cracking in the frame beam connected to the ring beam with no obvious damage occurred in the GCFST column. This observation satisfied the seismic design principle selected for the ring beam connection, and the design principle requires “strong column and weak beam” in the design code.

(3) Stress distribution analysis indicated that, when cyclic loads were imposed in the frame beam ends, bending moment was transferred by the ring beam and sustained by the GCFST column, while shear forces was transferred through the shear ring and resisted by the GCFST column and adhesive force between ring beam and tube. The cyclic load resulted in the development of a diagonal compressive strut in the region of ring-beam connection.

(4) Parametric studies indicated that GCFST column steel ratio, axial load ratio, beam-to-column stiffness ratio, and concrete compressive strength of the frame beam significantly influenced the initial stiffness and flexural capacity of the ring-beam connection under cyclic loading. Due to seismic design principle, the confined concrete compressive strength and GCFST column slenderness ratio had insignificant effects on the performance and dynamic response of the ring-beam connection.

Acknowledge

This project was supported by Natural Science Foundation of Jiangsu Province (BK20200996), Technology Program of Ministry of Housing and Urban-Rural Development (2011-k3-23), Liaoning Talents Program (LR2011014), University innovation team of Liaoning Province (LT2014012), and China Postdoctoral Science Foundation (2020M681566).

References

[1] Zhao X.L., Han L.H., Lu H. Concrete-Filled Tubular Members and Connections, Spon Press New York, 2010.
[2] Li G.C., Fang C., Zhao X., An Y., Liu Y. "Cyclic Behavior of Rebar-Penetrated Connection between Gangue Concrete Filled Steel Tubular Column and Reinforced Gangue Concrete Beam", Advanced Steel Construction, 115, 54-72, 2015
[3] Li G.C., Fang C., An Y.W., Zhao X. "Seismic Behavior of Rebar-Penetrated Joint between GCFST Column and RGC Beam", Steel and Composite Structures, 19, 547-67, 2015
[4] Xiao J.Z., Li W.G., Fan Y.H., Huang X. "An Overview of Study on Recycled Aggregate Concrete in China (1996–2011)", Construction and Building Materials, 31, 364-83, 2012
[5] Guo J.M. Experimental Research on Performances of Concrete with Coal Gangue. 2011 International Conference on Materials for Renewable Energy&Environment2011. p. 1988-91.
[6] Li G.C. "Strength and Lateral Deformation Coefficient of Gangue Concrete Restrained by Steel Tube", Harbin Jianzhu Daxue Xuebao/Journal of the Harbin University of Civil Engineering and Architecture, 35, 20-3, 2002
[7] Nelson A.J., Rakau O., Dörrenberg P. "Green Buildings: A Niche Becomes Mainstream", Deutsche Bank Research, 2010
[8] Li W., Han L.-H. "Seismic performance of CFST column to steel beam joints with RC slab: Analysis", Journal of Constructional Steel Research, 67, 127-39, 2011
[9] Pucinotti R., Bursi O., Demonceau J.F. "Post-Earthquake Fire and Seismic Performance of Welded Steel-Concrete Composite Beam-to-Column Joints", Journal of constructional steel research, 67, 1358-75, 2011
[10] Chen Q.J., Cai J., Bradford M.A., Liu X.P., Zuo Z.L. "Seismic Behaviour of a Through-Beam Connection between Concrete-Filled Steel Tubular Columns and Reinforced Concrete Beams", Engineering Structures, 80, 24-39, 2014
[11] Ding F.X., Yin G.A., Wang L.P., Hu D., Chen G.Q. "Seismic performance of a non-through-core concrete between concrete-filled steel tubular columns and reinforced concrete beams", Thin-Walled Structures, 110, 14-26, 2017
[12] Yu T., Teng J., Wong Y., Dong S. "Finite Element Modeling of Confined Concrete-II: Plastic-Damage Model", Engineering Structures, 32, 680-91, 2010
[13] Fu Z.Q., Ji B.H., Lv L., Zhou W.J. "Behavior of Lightweight Aggregate Concrete Filled Steel Tubular Slender Columns under Axial Compression", Advanced Steel Construction, 7, 144-56, 2011
[14] Zhang J.W., Cao S.Y. "Research on the Stress-Strain Curves of Structural Lightweight Aggregate Concrete", Building Science, 24, 83-5, 2009
[15] Sorenson H.K. "ABAQUS Version 6.10: Theory Manual, Users’ Manual, Verification Manual and Example Problems Manual", Hibbitt, Karlson, Sorenson Inc USA, 2011
[16] Oehlers D.J., Bradford M.A. Composite Steel and Concrete Structures: Fundamental Behaviour: Fundamental Behaviour, Elsevier, 2013.
[17] Boger R.K. Non-monotonic Strain Hardening and Its Constitutive Representation: The Ohio State University, 2006.
[18] Yoshida F., Uemori T. "A Model of Large-Strain Cyclic Plasticity Describing the Bauschinger Effect and Workhardening Stagnation", International Journal of Plasticity, 18, 661-86, 2002
[19] Lu X.Z., Ye L.P., Miu Z.W. Static-Plastic Analysis on Seismic Performance of Structures. Beijing: China, Building Industry Press, 2009.
[20] Zhang Y.F., Zhao J.H., Yuan W.F. "Study on Compressive Bearing Capacity of Concrete-Filled Square Steel Tube Column Reinforced by Circular Steel Tube Inside", Journal of Civil Engineering and Management, 19, 787-95, 2013
[21] CECS28-2012. Technical Specification for Concrete-Filled Steel Tubular Structures. Beijing, China2013.
[22] GB50011-2010. Code for Seismic Design of Buildings. Beijing: China Architecture &Building Press, 2010.
[23] Han L.H., Li W. "Seismic Performance of CFST Column to Steel Beam Joint with RC Slab: Experiments", Journal of Constructional Steel Research, 66, 1374-86, 2010
[24] Transportation Research Board. Procedures for Verification and Validation of Computer Simulations Used for Roadside Safety Applications. Washington, DC, The National Academies Press, 2011.
[25] Han L.H. Concrete-Filled Steel Tubular Structure: Theory and Practice. Science Press, Beijing, 2017.

Advanced Steel Construction – Vol. 17 No. 4 (2021) 394–402
DOI:10.18057/IJASC.2021.17.4.8

REVIEW OF VARIOUS SHEAR CONNECTORS IN COMPOSITE STRUCTURES

Rahul Tarachand Pardeshi [1, *] and Yogesh Deoram Patil [2]

[1] *Research Scholar, Sardar Vallabhbhai National Institute of Technology, Surat, India*
[2] *Associate Professor, Sardar Vallabhbhai National Institute of Technology, Surat, India*
** (Corresponding author: E-mail: rahultpardeshi@gmail.com)*

ABSTRACT

Shear connectors are devices that provide shear connection at the interface of steel girders and reinforced concrete slabs in composite structures to accomplish composite action in a flexure. The seismic response of composite structures can be controlled using properly designed shear connectors. This state-of-the-art review article presents considerable information about the distinct types of shear connectors employed in composite structures. Various types of shear connectors, their uniqueness and characteristics, testing methods and findings obtained during the last decade are reviewed. The literature, efficacy, and applicability of the different categories of shear connectors, for example, headed studs, perfobond ribs, fibre reinforced polymer perfobonds, channels, pipes, Hilti X-HVB, composite dowels, demountable bolted shear connectors, and shear connectors in composite column are thoroughly studied. The conclusions made provide a response to the flow of the use of shear connectors for their behaviours, strength, and stiffness to achieve composite action.

ARTICLE HISTORY

Received: 20 October 2020
Revised: 4 May 2021
Accepted: 5 May 2021

KEYWORDS

Anchors and anchorages;
Composite structures;
Shear connectors;
Push out test;
Concrete steel interface

1. Introduction

Composite structural systems have been used for decades and widely applied to bridges and building structures with a minimum utilisation of materials. The benefits of composite construction such as a rapid construction process, a reduction in vertical floor spaces, an overall decrease in self-weight, and low structure costs may help provide affordable services to a community. A steel beam–concrete slab with shear connectors is a well-known integrated structural element of composite structures (Fig. 1), which present economic feasibility and excellent structural performance. Shear connectors are used to combine two structural elements together at an interfacial stratum to avert the upright parting of a slab from a steel girder and provide a smooth transmission of longitudinal shear forces (Ahn et al.[1]). During an earthquake, horizontal inertial loads in a slab are distributed to a lateral load resisting frame with the provision of shear connectors at the connection face of the concrete deck and steel beam. The accoutrements of shear connectors could eradicate the slip of individual elements caused by horizontal inertia forces and thus the single T-beam mechanism achieved through composite action. Hence, the stiffness and strength of a composite element increase. The Indian standard code (BIS (Bureau of Indian Standards) IS 3935 1966[2]) specified Equation (1) for the shear force (Sh) at an interface plane, and these shear forces must be smoothly transferred through the shear connector in a composite structure.

$$S_h = \frac{V\, m_s}{I} \tag{1}$$

where V is the vertical load, ms represents the static moment, and I denotes the composite cross-section moment of inertia. Therefore, for the smooth transmission of the shear force among the concrete deck and steel girder, shear connectors should have adequate strength and stiffness.

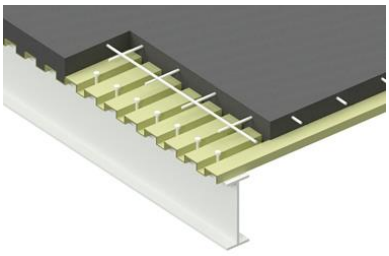

Fig. 1 Typical arrangement of a composite structure employing shear connectors

In this state-of-the-art-review paper, various configuration of shear connectors employed in composite structures in the last one decade and their uniqueness, characteristic, testing methods, and reported findings are reviewed. The efficacy and applicability of different shear connectors such as headed studs, perfobond, channels, pipes, Hilti X-HVB, fibre reinforced polymers (FRPs) connectors, composite dowels, demountable (bolted) connectors, and shear connectors in composite column are thoroughly studied. The use of shear connectors in rapports of their behaviours, stiffness, and strength to achieve composite action is discussed in detail.

2. Various shear connectors in composite structures

2.1. Headed stud shear connectors

Headed studs are the shear connectors commonly adopted in industries (Fig. 2); headed studs provide steel shank resisting longitudinal shear forces and have an anchorage head to prevent the vertical movement of slabs in composite structures (Ollgaard et al.[3]). Generally, to install a headed stud in the prefabricated steel girder beam, special welding equipment are essential. The weld strength should be higher than the stud strength. However, these welds generally face fatigue problems under repeated loadings (Lee et al.[4], Deng et al.[5], Liu et al.[6]). From the last seven decades, many studies have been performed on stud connectors after the invention of headed stud shear connector by Viest[7].

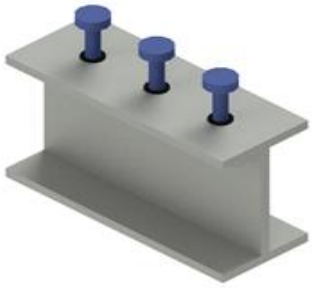

Fig. 2 Headed stud shear connector

Pallarés and Hajjar[8-9] proposed four formulas for the nominal shear strength of headed anchors in the solid slab when a composite beam imperilled the shear force responsible for concrete failure when it was subjected to static and cyclic loadings. Spremic et al.[10] experimentally investigated five different groups of four headed studs through push-out testing specified by Eurocode 4[11] to categorize the stiffness and shear strength performance between the group and standard arrangements. They aimed to minimise the space requirement of the stud in precast concrete slabs to lower than the

Eurocode 4[11] specified requirement of 5 times the stud diameter. Xu and Liu[12] established an analytical model to appraise the shear stiffness of rubber's sleeved headed studs per varying sleeve heights. Xu et al.[13] experimentally tested nine rubber's sleeved headed studs per varying sleeve heights to investigate fatigue performance and observed that with an increase in the rubber's sleeve height, the fatigue strength of the stud decreased. Ding et al. [14] experimentallu investigated the steel stud incased in foamed plastic block of Ethylene-Vinyl Acetate for the slip-released behavior under push out test. Further, the finite element (FE) simulation was performed on shear connector providing Polyvinyl Chloride protective shell layer for improvement in slip behavior of connector. Sjaarda et al.[15] presented a model to envisage the performance of composite beams by using the elastic properties and nonlinear load-slip curves of materials for a shear connector.

Sun et al.[16] explored the performance of the headed stud welded to composite deck accompanied by different steel profile decking receiving cyclic as well as monotonic loadings. The influence of the type, presence, and orientation of decking on the shear capacity of the welded headed stud was acquired experimentally. Mirza and Uy[17] observed the outcomes of headed stud connectors in composite structure with the effect of different strain regimes on concrete profiled steel sheeting and solid slabs using FE analysis, and concluded the significant influence of the strain regimes on strength prediction and load-slip behavior of shear connector in composite structure. Using the FE analysis, Qureshi et al.[18-19] considered the shear influence of central, favourable, and unfavourable positioning of single and double studs in a trough of profiled steel sheeting for experimental investigation. The efficacy of the thickness of profile sheets on the ductility, failure modes, and strength of the headed shear connectors employed in composite beams were determined throught numerical-experimental investigation. Qureshi et al.[18] explored the performance of shear connectors in composite beams under various spacings, stud layouts, and concrete strengths.

Table 1 presents the shear capacity equations of the headed stud connector in solid and profile steel sheeting concrete slabs conforming to international standards (ACI 2008[20], AISC 2005[21], EN 1994-1-1 2004[10], GB50017-2003[22], BSI (Bureau of Indian Standards) IS 3935-1966[2]); the equation developed in earlier historical studies, which led to the development of shear capacity equations for international standards (Viest[7], Slutter and Driscoll[23], Ollgaard et al.[3]); and latest studies (Pallarés and Hajjar[8], Qureshi et al.[19]).

Table 1
Shear-capacity equations of headed stud shear connector

Sr. No.	Reference	Headed stud in	Shear-capacity equations	Equation no.
1	EN 1994-1-1 2004[10]	Solid slab	$P = 0.29\alpha d^2\sqrt{E_c f_c'} \le 0.8 A_s F_u$ Here, $\alpha = 0.2\left(\frac{h}{d}+1\right)\ for\ 3 \le h/d \le 4$ $\alpha = 1\ for\ h/d > 4$	2
2	EN 1994-1-1 2004[10]	Profile deck	$P = 0.29 k_l \alpha d^2\sqrt{E_c f_c'}$ for parallel deck orientation $k_l = 0.6\frac{b_o}{h_h}\left(\frac{h}{h_h}-1\right) \le 1$	3
			$P = 0.29 k_t \alpha d^2\sqrt{E_c f_c'}$ for transverse deck orientation $k_t = \frac{0.7}{\sqrt{n_r}}\frac{b_o}{h_h}\left(\frac{h}{h_h}-1\right) \le k_{t,max}$	4
3	GB50017-2003[22]	Solid slab	$P = 0.43 A_s\sqrt{E_c f_c} \le 0.7 A_s F_u$	5
4	GB50017-2003[22]	Profile deck	$P = 0.43 k_l A_s\sqrt{E_c f_c}$ for parallel deck orientation $k_l = 0.6\frac{b_o}{h_h}\left(\frac{h}{h_h}-1\right) \le 1$	6
			$P = 0.43 k_t A_s\sqrt{E_c f_c}$ for transverse deck orientation $k_t = \frac{0.85}{\sqrt{n_r}}\frac{b_o}{h_h}\left(\frac{h}{h_h}-1\right) \le 1$	7
5	AISC 2005[21]	Solid slab	$P = 0.5 A_s\sqrt{E_c f_c'} \le A_s F_u$	8
6	AISC 2005[21]	Profile deck	$P = 0.5 A_s\sqrt{E_c f_c'} \le R_g R_p A_s F_u$	9
7	ACI 2008[20]	Solid slab	$P_{Rd,S} = 0.65 A_s F_u$	10
			$P_{Rd,C} = k_{cp} k\sqrt{f_c'}(h)^{1.5}$	11
8	IS 3935-1966[2]	Solid slab	$P\ (kg) = 4.8\ \text{h d}\sqrt{f_c}\ For, h/d < 4.2$	12
			$P\ (kg) = 19.6\ d^2\sqrt{f_c}\ For, h/d \ge 4.2$	13
9	Viest[7]	Solid slab	$P = 5.25 d^2 f_c'\sqrt{\frac{4000}{f_c'}}\ when, d < 1$ inch	14
			$P = 5.25 d f_c'\sqrt{\frac{4000}{f_c'}}\ when, d > 1$ inch	15
10	Slutter and Driscoll[23]	Solid slab	$P = \frac{932 d^2\sqrt{f_c'}}{A_s}\ for\ Long\ Studs, h/d > 4.2$	16
			$P = \frac{222 h d\sqrt{f_c'}}{A_s}\ for\ Short\ Studs, h/d < 4.2$	17
11	Ollgaard et al.[3]	Solid slab	$P = 0.5 A_s\sqrt{E_c f_c'} < A_s F_u$	18
12	Pallarés and Hajjar[8]	-	$P_{vc} = 17 A_s {f_c'}^{0.45} E_c^{0.04}$	19
			$P_{vc} = 6.2 A_s {f_c'}^{0.2} E_c^{0.2}$	20
			$P_{vc} = 18 A_s {f_c'}^{0.5} h^{0.2}$	21
			$P_{vc} = 9\lambda {f_c'}^{0.5} d^{1.4} h^{0.6}$	22
13	Qureshi et al.[19]	Profile deck	$P_{U\ S\&D} = \alpha \times P_{F(0.9t_d)} \times (0.38 t_d$	23
			$+ 0.66)$	24
			$P_{CS} = \beta \times P_{F(0.9t_d)} \times (0.25 t_d + 0.78)$	25
			$P_{CD} = \beta \times P_{F(0.9t_d)} \times (0.16 t_d + 0.87)$	

2.2. Perfobond ribs shear connectors

Due to higher fatigue strength and easier installation than those of conventional headed studs, perfobond-ribbed (PBL) shear connectors were christened for composite structures (Leonhardt et al.[24], Oguejiofor and Hosain[25-27]). PBL connectors necessitate the use of perforated rectangular steel plates with circular holes that are more prominent than the diameter of transverse reinforcement and perforating rebars. PBL plates are conventionally welded at the top flange of steel girders.

Vellasco et al.[28] proposed T-rib perfobond shear connectors (Fig. 3a) that were useful in hogging moment areas, corner, and edge column flanges for composite portal frames to transfer forces from rebars. Vianna et al.[29] incorporated one or two rows of two (Fig. 3b) or four holes (Fig. 3c) in the web plate of T-rib perfobond shear connectors. Ahn et al.[1] presented a PBL shear connector suitable for the mixed girder arrangement comprising prestressed reinforced cement concrete (RCC) and steel girders. Shear capacity equations were proposed for single and twin PBL ribs, which accounted for the role of concrete end-bearing effects, the influence of concrete-dowel, and transverse reinforcements in rib holes. Vianna et al.[30] tested T-rib connectors with many variables such as high-grade concrete, connector holes with steel reinforcement, and slab thickness to evaluate the slip capacity, shear resistance, and failure mode. Costa-Neves et al.[31] emphasised the shear connector geometry and introduced double T-perfobond (Fig. 3d) and I-perfobond (Fig. 3e) connectors for composite girders. Their push-out test results revealed that the resistance

enhancement of approximately 150%–300% is achievable due to the flange arrangement of connectors with and without transverse reinforcement in rib holes. Rodrigues and Laím[32] experimentally probed the performance of T-PBL, T shear connectors, and T-block in fire to find the shear resistance capacity, collapse mode, and ductility at ambient and different raised up temperatures.

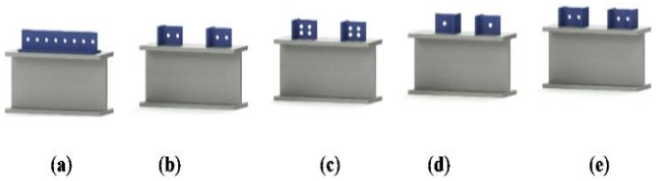

Fig. 3 Perfobond rib shear connectors: (a) T-ribs (Vellasco et al.[28]), (b) two holes in T-rib (Vianna et al.[29]), (c) four holes in two rows T-rib (Vianna et al.[29]), (d) 2T-Perfobond T-rib (Costa-Neves et al.[31]), and (e) I-Perfobond T-rib (Costa-Neves et al.[31])

Kim et al.[33] invented a "Y" shaped PBL shear connector (Fig. 4) and proved its superiority in fatigue and shear resistance through progressive experimental and analytical investigation under the static loading (Kim et al.[33-36]) and cyclic loading (Kim et al.[37-39]). Ramasamy and Govindan[40] studied the effects of triangular holes as perforation on PBL connectors to assess strength capacity through push-out testing. Two types of facing of triangular holes, facing flange TR1 (Fig. 5a) and facing opposite to flange TR2 (Fig. 5b), perfobond plates were discussed to discover the feasibility of resisting the shear capacity and slip. Zheng et al.[41] highlighted the importance of hole geometries in PBL shear connectors for shear capacity evaluation and investigated the performance of circular and long-hole PBL ribs through push-out testing. Fan and Zhou[42] proposed a new PBL connector, perfobond hoop (PBH), comprising PBL with stirrups embedded in the hole for steel–concrete composite arch elements, particularly for bridges. The experimental results showed the better mechanical property and higher shearing capacity of perfobond hoop than PBL connectors. The results of the theoretical and experimental studies of Zhang et al.[43-44] on PBL connectors in groups for the internal force transfer mechanism revealed the uneven distribution of forces in the elastic stage and even plastic deformation. Yu et al.[45] assessed the act of PBL connectors encased in recycled aggregate concrete slabs for strength appraisal of connection.

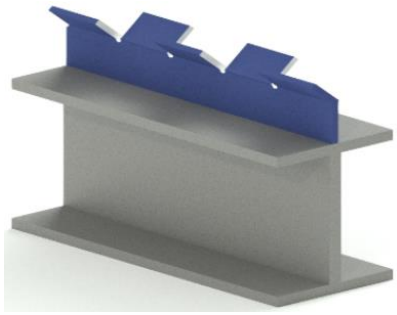

Fig. 4 Y-shaped perfobond rib shear connectors (Kim et al.[33])

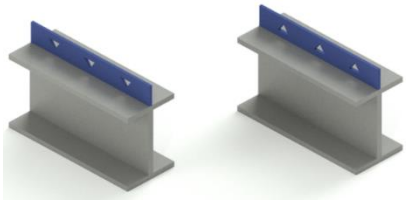

Fig. 5 (a) Triangular-apex fronting the flange and (b) triangular-apex conflicting to flange (Ramasamy and Govindan[40])

Su et al.[46] presented a new push-out testing system while assessing the behaviour of perfobond rib connectors to isolate the effect of friction and specimen size on structural performance by using PBL. Su et al.[47] investigated PBL in a composite girder bridge inlay with transverse rebar and concrete to evaluate the shear resistance capacity. Zhan et al.[48] experimented specific push-out tests (Fig. 6) on PBL and headed stud shear connectors in composite structures to see the stimulus of external pressure on the behaviour of shear connectors. The strength and stiffness of headed studs substantially improved due to the application of external pressure when the friction effect was employed.

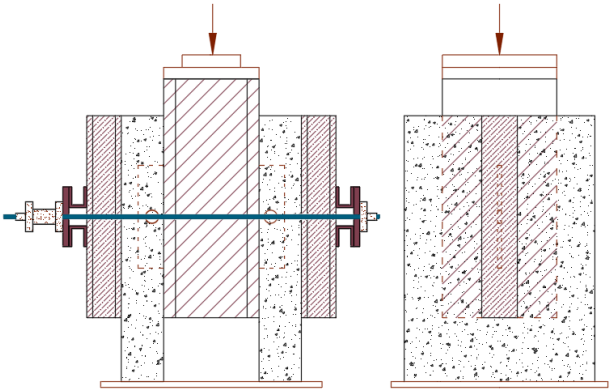

Fig. 6 External pressure on a test block for the push-out test (Zhan et al.[48])

2.3. FRP PBL shear connectors

FRP materials are utilised as shear connector support to enhance the flexural stiffness, obtain excellent corrosion resistance, and increase the capacity of structural strength. Zou et al.[49] used perforated FRP ribs as shear connectors to promote the mutual linking between a pultruded FRP I-girder and concrete slabs. Gwon et al.[50] performed the push-out test on the composite concrete-FRP module with FRP PBL connectors in the one-piece arrangement and introduced an equation to formulate the strength of FRP connectors in shear. Cho et al.[51] reported the importance of the number and diameter of rib holes for FRP PBL connector performance.

Table 2 presents the shear capacity equations developed by various researchers. Parameters responsible for strength predictions are highlighted with mark '✓'. Factors accountable for the PBL strength are: (a) concrete dowel action, (b) perforated rebars, (c) concrete slab end-bearing effects, (d) splitting resistance of concrete slabs, (e) transverse reinforcements, (f) chemical bonds, (g) empirical constants, and (h) other specific factors.

Table 2
Shear-capacity equations of PBL shear connector

Sr. no.	References	Shear-capacity equations	Shear capacity contribution factors								Equation no.
			a	b	c	d	e	f	g	h	
1	Oguejiofor and Hosain[26]	$Q = 0.590A_{cc}\sqrt{f_c'} + 1.233A_{tr}f_y + 2.871nd_h{}^2\sqrt{f_c'}$	✓			✓	✓				26
2	Oguejiofor and Hosain[27]	$Q = 4.5h_p t_p f_c' + 0.91A_{tr}f_y + 3.31nd_h{}^2\sqrt{f_c'}$	✓		✓		✓				27

3	Yoshitaka et al.[52]	Q = 3.38 $d_h{}^2\sqrt{t_p/d_h}\ f_c - 39.0$	✓					✓			28
		with 22.0< $d_h{}^2\sqrt{t_p/d_h}\ f_c$< 194.0	✓	✓				✓			29
		Q = 1.45 $\left[(d_h{}^2 - d_{rh}^2)\ f_c + d_{rh}^2 f_y\right] - 26.1$									
		with 51.0< $(d_h{}^2 - d_{rh}^2)\ f_c + d_{rh}^2 f_y$< 488.0									
4	Al-Darzi et al.[53]	Q_u =255.31+7.62 × $10^{-4} h_p t_p f_c' - 7.59 \times 10^{-10} A_{tr} f_y$ + 2.53 × $10^{-3} A_{cd}\sqrt{f_c'}$	✓		✓		✓		✓		30
5	Ahn et al.[54]	Q = 3.14 $h_p\ t_p\ f_c + 1.21 A_{tr} f_y + 2.98 n d_h{}^2\sqrt{f_c}$ – Single Rib PBL	✓		✓		✓				31
		Q = 2.76 $h_p\ t_p\ f_c + 1.06 A_{tr} f_y + 2.61 n d_h{}^2\sqrt{f_c}$ – Twin Rib PBL	✓		✓		✓				32
6	Zhao and Liu[55] and Deng et al.[56]	Q = 1.38 $(d_h{}^2\text{-}d_{rh}^2)\ f_c + 1.24\ d_{rh}^2\ f_y$	✓	✓							33
7	Verissimo[57]	Q_u =4.04 $\frac{h_{sc}}{b} h_{sc} t_{sc} f_c' + 2.37 n D^2\sqrt{f_c'} + 0.16 A_{cc}\sqrt{f_c'}$ + 31.85 × $10^6 \frac{A_{tr}}{A_{cc}}$	✓		✓	✓	✓				34
9	Medberry and Shahrooz[58]	Q_u =0.747b$h_{ecs}\sqrt{f_c'} + 0.413 b_f C_L + 0.9 A_{tr} f_y$ + 1.66$n\pi \left(\frac{d_h}{2}\right)^2 \sqrt{f_c'}$	✓			✓	✓	✓			35
10	Deng et al.[56]	Q =0.5$A_s\sqrt{E_c f_c'}$ + 1.38 $(d_h{}^2 - d_{rh}^2)\ f_c + 1.24 d_{rh}^2 f_y$	✓	✓					✓		36
11	Gwon et al.[50]	Q_{FRP} =1.84$b_f C_L + 7.346 n\pi\sqrt{f_c'}\left(\frac{d_h}{2}\right)^2 + 0.95 A_{vf} f_r$	✓			✓	✓				37
12	Su et al.[47]	Q_u =$A_{cd}\tau_{cu} + A_{tr}\tau_{sy}$	✓				✓				38
		If, $A_{tr}(\beta' A_{tr}\tau_{su} - \tau_{sy}) \le A_{cd}\tau_{cu}$ Q_u =$\beta' A_{tr}\tau_{su}$									
		If, $A_{tr}(\beta' A_{tr}\tau_{su} - \tau_{sy}) > A_{cd}\tau_{cu}$ Here, $\tau_{cu} = \alpha_c k_s\sqrt{f_c f_t}$					✓				39
13	Zheng et al.[41]	For circular hole PBL, Q_u =1.85[$(A - A_{tr})f_c + A_{tr} f_u$] − 26.1 × 10^3	✓	✓							40
		For long-hole PBL, Q_u = 1.76 $(A - A_{tr})f_c + 1.58 A_{tr} f_y$	✓	✓							41
14	Zou et al.[49]	Shear failure in FRP plate, Q_u =1.1$A_{shear} S_{xy}$ Here, $A_{shear} = (L - 0.7 d_h n) t_p$							✓		42
		Failure in a concrete wedge, Q_u =4.5$h_p t_p f_c'$ + 3.31$n d_h{}^2\sqrt{f_c'} + 0.91 A_{tr} f_y$	✓	✓			✓				43

2.4. Composite dowels as shear connectors

Kopp et al.[59] presented the contextual data of puzzle shaped (PZ) and clothoidal (CL) composite dowels (Fig. 7) for their application as shear connectors in composite beam. The information have been utilised to derive technical rules to prepare the instructions for structural design principles, ultimate limit states, production, and construction. The bidirectional and even distribution of the shear force in composite structure could occur with the symmetric geometry of CL and PZ composite dowels (Seidl et al.[60]). The radius connections of these dowels provide favourable fatigue resistance and relevant strength to fatigue cracks. Hechler et al.[61] reported a fatigue design concept of PZ continuous shear connectors in prefabricated composite beam construction. Dudziński et al.[62] studied the fatigue cracks and fatigue durability of composite dowels through the beam test and FE analysis of the modified CL-shaped composite dowels. Lorenc et al.[63] revealed the behaviour of PZ (PZ 300/100) shear connectors for load-carrying capacity through shear resistance in full-scale push-out tests under static loadings. The influencing parameters such as the dowel size, web thickness, and grade of steel were studied during testing.

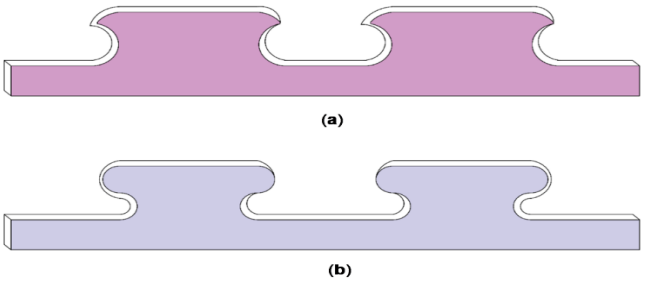

Fig. 7 (a) Clothoidal and (b) puzzle shape composite dowels used as shear connectors (Kopp et al.[59])

2.5. C-shaped angle and channel shear connectors

In general, the low strength of headed studs and complications regarding the provision of transverse rebar in PBL holes lead to the possibility of the development of C-type shear connectors. The two times higher shear strength of channel connectors than that of the headed stud and their better working environment for reinforcement than the working environment of PBL connectors were ascribed to their developed constructability advantages (Shariati et al.[64]). C-shaped connectors are available in two forms: angle and channel profile. Table 3 presents the standard equation used to predict the shear strength of channel connectors and some selective studies contributing in equation development are referenced.

Table 3
Shear-capacity equations of channel connector

Sr. no.	Reference	Shear-capacity equations	Equation no.
1	AISC 2005[21]	$P_c = 0.3(t_f + 0.5t_c)L_c\sqrt{f_c' E_c}$	44
2	NBC (National Research Council) 2005[65]	$P_c = 36.5(t_f + 0.5t_c)L_c\sqrt{f_c'}$	45
3	GB 50017-2003[22]	$P_c = 0.26(t_f + 0.5t_c)L_c\sqrt{f_c' E_c}$	46
4	BIS (Bureau of Indian Standards) IS 3935-1966[2]	$P_c\ (kg) = 10.7\ (h + 0.5t_c)L_c\sqrt{f_c}$	47
5	Soty and Shima[66]	$P_c = \text{kh}L_c\sqrt{f_c'}$ Here, $k = 63\ t_c/h\ + 1.60$	48
6	Pashan and Hosain[67]	$P_c = (336t_c^2 + 5.24L_cH)\sqrt{f_c'}$	49
7	Pashan and Hosain[67]	$P_{cm} = (1.7L_cH\frac{w_d}{h_d} + 275.4t_c^2)\sqrt{f_c'}$	50
8	Baran and Topkaya[68]	$P_c = \frac{2\times L_c\times t_c^2}{H} \times F_u + (f_c' \times 0.25 \times F_1 \times F_2 \times H)$	51
9	Tahmasbi et al.[69]	$P_c = 0.213\ L_c\sqrt{t}\sqrt{f_c'}$	52

Shariati et al.[70] experimentally studied the channel and angle shear (Fig. 8a and 8b) connectors entrenched in high strength concrete (HSC) to compare the performance of shear strength and ductility under static and cyclic push-out loadings. Channel connectors exhibit 6.8%–30.1% and 18.5% higher shear strength when exposed to static and full-reversed fatigue loadings, respectively, than angle connectors do in HSC. The performance of angel connectors was 7.5%–36.4% and 23.6%–49.2% lower for shear strength than that of channel connectors when employed in reinforced normal concrete subjected to monotonic and full-reversed cyclic loadings, respectively (Shariati et al.[71]). By taking the advantages of the properties of ultra-high performance concrete (UHPC) thin plates such as high tensile strength, satisfactory durability, and ultra-high compressive strength, Zhao et al.[72] proposed short steel channel connectors with thin UHPC plates for composite decks. Balasubramanian and Rajaram[73] reported the experimental findings of push-out static loading tests performed on composite structures with angle shear connectors. Deng et al.[5] proposed a unique channel connector type and compared its behaviour with T-rib and angle shear connectors in the experimental push-out test. The test results revealed that the maximum bearing capacity of the channel connector was approximately 92.1% and 47.5% superior than that of T-PBL connectors and angle connectors, respectively, with an adequate energy dissipation capacity. Titoum et al.[74] proposed an I-shaped connector and compared its behavior with the channel connector and confirms the similarity of their behaviors. So, the equation predicting the ultimate strength of channel connector as per Canadian code could significantly be adoptable for I-shape connector. Baran and Topkaya[68] found that the equation presented in Canadian and American specifications for predicting the strength of channel shear connectors was highly conservative as it considers limited parameters. Therefore, considering various lengths, the height of channel connectors, and the outcomes of 15 push-out tests, they invented a equation for determining the shear capacity of channel connectors. Pashan and Hosain[67] developed new equations to estimate the maximum shear capacity of channel connectors employing channel connectors on a composite beam interface with solid and wide-ribbed (ribs parallel to the beam) metal deck concrete slabs. Khorramian et al.[75] experimentally investigated the 112.5° and 135° tilted positions of angle shear connectors with the steel beam and various angle sizes and lengths for strength improvement. Shariati et al.[76] introduced soft computing artificial intelligence techniques and an adaptive neuro-fuzzy inference approach to forecast the behaviour of C-shaped tilt-angle connectors. Their findings open that the slip is a predominant factor and the inclination angle has secondary importance in the shear strength of tilted connectors. Soty and Shima[66] established an experimental beam-type test procedure and concluded that the effect of the shear force direction on shear connectors predominantly influences the strength of angle shear connectors. Shariati et al.[64] introduced V-shaped angle connectors (Fig. 8c) and investigated different parameters such as the height, length, and inclination angle of connectors with a flange of the I-steel beam for uplift resistance, high shear transfer, and ductility under monotonic and cyclic loadings. These results were compared with the C-types angle (Fig. 8b) and channel (Fig. 8a) connectors obtained in the investigation of Shariati et al.[70].

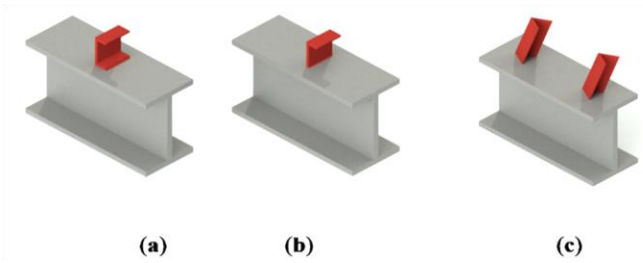

Fig. 8 (a) Channel shear connector, (b) angle shear connector, and (c) inclined V-shaped angle shear connector (Shariati et al. [64], [70])

Hicks et al.[77] evaluated the shear connectors in brides of the Canterbury and West Coast regions, and the Gisborne and Hawke's Bay regions for the New Zealand Heavy Engineering Research Association (HERA). They reported that 72% and 63% of bridges employed welded channels while 18% and 30% of bridges used V-angles as a shear connector in the Canterbury and West Coast regions (see Fig. 9), and the Gisborne and Hawke's Bay regions (see Fig. 10), respectively. In comparison, shear stud and other connectors have been used in 3% and 7% of bridges, respectively. The worked example of the Waipoua river composite bridge in New Zealand has also been specified for new design guidelines.

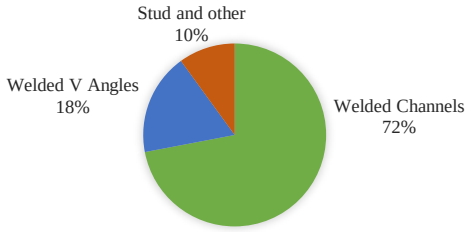

Fig. 9 Different forms of shear connector employed for the Canterbury and West Coast region composite bridges (Hicks et al.[77])

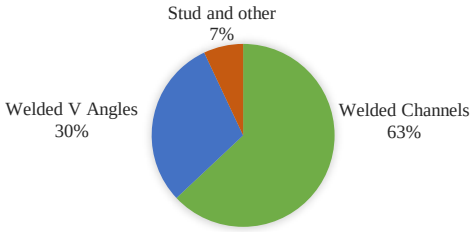

Fig. 10 Different forms of shear connector employed for the Gisborne and Hawke's Bay region composite bridges (Hicks et al.[77])

2.6. Demountable bolted shear connectors

To form steel-concrete composite structures, demountable and bolted connections should be substituted with the frequently employed welded-headed studs. To potentially reuse structural elements including steel beams from composite structures after any destruction, demountable shear connectors are a suitable means for dismantling the structural beam element from the concrete slab. Various novel demountable bolted connectors and corresponding studies are presented here.

Pavlović et al.[78] studied the behaviour of four identical specimens of M16 grade 8.8 high strength single embedded nut bolt shear connectors in the solid slab and headed shear stud connectors by conducting the standard push-out test according to the Eurocode 4[10] specifications. G8.8 high strength single embedded nut-bolt shear connectors achieved 95% higher strength in shear resistance and 50% higher stiffness than the welded headed stud shear connectors did. Dai et al.[79] conducted several experimental static shear tests on solid slabs with demountable shear connectors having different collar sizes manufactured using standard headed stud shear connectors. Demountable connectors were be more ductile than welded connectors with high initial stiffness, but both exhibited a similar ultimate capacity (Dai et al.[80]). Yang et al.[81] proposed a new demountable connector comprising a long bolt, a short bolt, and a coupler and discovered its shear failure performance in composite action from the results of push-out tests. Rehman et al.[82] embarked demountable connectors having the similar shear strength as welded shear studs have on a concrete slab with profiled metal decking. Moreover, they satisfied the Eurocode 4 standard ductility criteria of 6 mm. Using the FE analysis, Patel et al.[83] evaluated the significance of shear connectors in a steel beam with profiled decks slab, and hollow core concrete slab composite structures.

Kozma et al.[84] developed and analysed different bolted demountable shear connection systems for repeated use in solid composite slabs with and without profile steel sheeting. The systems included cylindrical, coupled, and coupled epoxy bolted connections with L-profile (Fig. 11). The failure mode was shear failure but it occurred in a brittle critical manner. Kwon et al.[85] suggested the use of three different post-installed shear connectors as a high-tension friction-grip bolt, a double-nut bolt, and an adhesive anchor to enhance the strength of existing non-composite bridge girders. Sjaarda et al.[86] explored the behaviour of embedded bolt shear connectors by testing large-scale composite beam specimens. Suwaed and Karavasilis[87] proposed an assembly of novel high-strength bolted demountable shear connectors (Fig. 12), called locking nut shear connectors (LNSCs) that comprised special locking nuts to prevent slipping in holes for precast composite bridges.

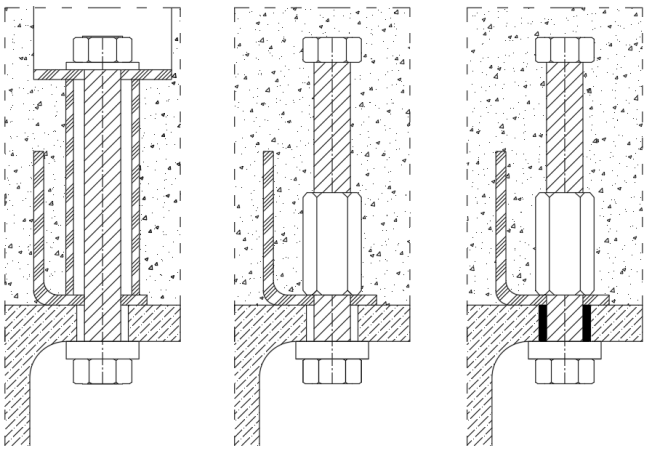

Fig. 11 Bolted demountable shear connections: (a) cylindrical system, (b) coupler system with pretensioned bolt, and (c) coupler system with injection bolts (Kozma et al.[84])

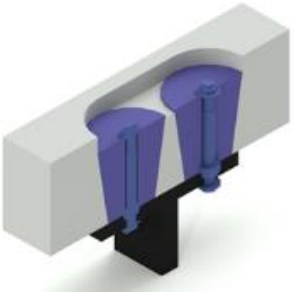

Fig. 12 Cut section of locking nut shear connector (Suwaed and Karavasilis[87])

2.7. Blind bolt shear connectors

To develop highly advantageous and workable demountable shear connection systems that are easy to install, Mirza et al.[88] adopted two removable blind bolts, BB1 and BB2, as a shear connector in a composite structure for slip performance assessment. Pathirana et al.[89] and Henderson et al.[90-91] utilised the same blind bolts to evaluate flexural behaviour and to determine the dynamic behaviour of composite beams by conducting a full-scaled beam test, respectively. Ban et al.[92] reported a long-term effect of static loadings (as a time-dependent behaviour) on composite steel–concrete beams utilising demountable blind bolting shear connections through experimental and FE analyses. Almost all researchers have concluded that the performance of blind bolt shear connectors for strength and stiffness is highly tantamount to that of the welded headed studs; however, the blind bolts presented brittle failure nature.

2.8. Pipe shear connectors

Nasrollahi et al.[93] used pipes as shear connectors having vertical and horizontal positioning in composite steel beams and revealed the economical use of pipes as shear connectors in the moderate shear strength requirement range of 150–350 kN.

2.9. Hilti X-HVB shear connectors

The Hilti X-HVB shear connector is an innovative shear connector that has L-shape and can be fastened with two nails to a beam (Fig. 13). Powder-actuated tools are required to fasten X-HVB to steel beams through two nails. X-HVB shear connectors prevent vertical uplift forces by using the X-HVB head and nails and are designed to resist desired shear forces with suitable ductility (Hilti X-HVB System[94]). Gluhović et al.[95] tested the prefabricated composite deck by conducting push-out tests pursuant to Eurocode 4[10] to assess the shear capacity of X-HVB connectors with powder-actuated fastener X-ENP-21 HVB nails. Their results showed that 26% higher slip to failure and 16% higher ultimate shear resistance to forward orientated shear connectors.

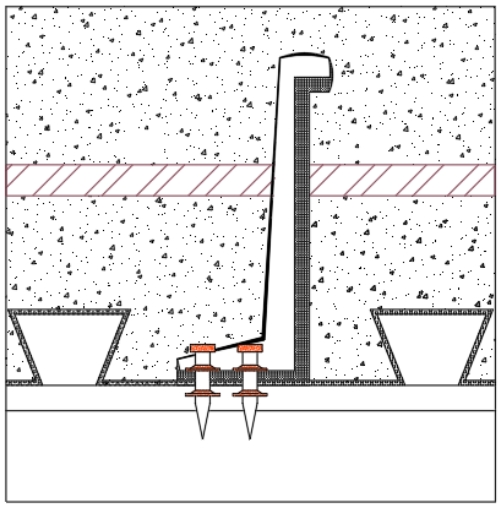

Fig. 13 Hilti X-HVB shear connector (Hilti X-HVB System [94])

2.10. Combination of different shear connectors

The advantages of headed stud shear and PBL connectors together have enabled researchers to improve the shear behaviour of composite structures. Deng et al.[56] developed and tested a combination of headed shear connectors with a single perfobond rib (Fig. 14) by using ten push-out test specimens for evaluating the fracture mode, shear capacity, load-slip behaviour, and ductility. Gu et al.[96] established a combination-type perfobond rib shear connector having a pre-embedded tube, pre-embedded sleeves, and shear pockets in concrete for shear performance assessment.

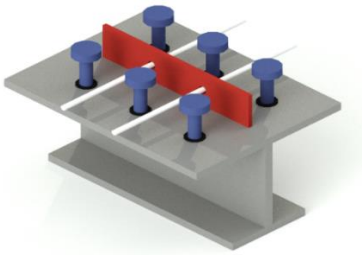

Fig. 14 Combination of headed shear connectors with a single perfobond rib (Deng et al.[56])

2.11. Shear connectors in composite Column

Composite columns are the structural member of composite structure utilizing the properties of structural steel element and concrete together for enriching the structural behavior in compression. The application of shear connectors in a composite column enhances the performance of column and/or beam-column connection in shear resistance, axial strength, and ductility. Eghbali and Mirghaderi[97] utilized a vertical plate called through plate with rigid shear connectors (Fig. 15) in beam-column connection for the composite framed structure to constraint sliding among the steel beam and reinforced concrete column. The ¾ scaled experimental evaluation characterized the composite connection utilizing a through plate with rigid shear connectors as a fully restrained strong panel elastic nature. Whereas, Aguiar et al.[98] utilized Crestbond shear connectors (steel plate with regular cuttings similar to puzzle shape composite dowels used as shear connector shown in Fig. 7 (b)) in concrete filled-steel tube columns at the beam-column interface for shear load transfer.

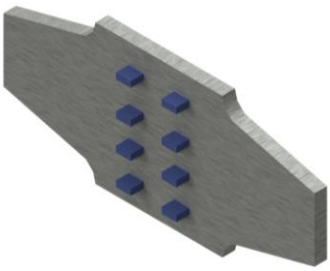

Fig. 15 Through plate with rigid shear connectors (Eghbali and Mirghaderi[97])

Odenbreit et al.[99] developed longitudinal, angled V-shaped and transversal flat shear connector for a steel-concrete composite column to overcome the difficulty of placing and handling the reinforcement associated with utilization of typical headed studs in the composite column. These three connectors were fabricated from conventional reinforcing bars and welded to the steel plates of a composite column under profiled positioning. Quio et al.[100] recommended using the steel plates as a shear connector welded to the square concrete-filled steel tube column. Alenezi et al.[101] used shear connectors for enhancement of compressive strength of cold-formed steel ferro-cement jacketed composite column. Three connectors, namely self-drilling screw, bar angle bolts, and normal bolt shear connectors in composite column-lipped C-channel, were evaluated for load-slip analysis through eight push-out test experiments. Younes et al.[102] employed high strength bolts as a shear connector in concrete-filled thin-walled steel tube short column (Fig. 16) for axial strength improvement. Ductility, buckling, and axial capacity of the composite column due to shear connectors performance were investigated through ten experimentally tested specimens. Whereas, from load-displacement analysis of experimental push-out test, Neto and Sarmanho[103] marked the judgement that bolts application in the composite column as a shear connector exhibits ductile and flexible nature. Tian et al.[104] proposed a shear connector utilizing advantages of engineering cementitious concrete together with perforated steel plate connectors and perforated steel reinforcement for composite column. Eight short columns were tested experimentally under push-out test, and results demonstrated the attribute of ductile failure.

Fig. 16 High strength bolts as a shear connector in concrete-filled thin-walled steel tube short column (Younes et al.[102])

3. Conclusions

Shear connectors are used to join steel girders/beams and RCC decks/slabs together in composite structures for bridges and building. The commonly adopted connectors in industries are welded headed studs, PBL connectors, angle and channel connectors, and demountable bolted connectors. The push-out test is the most commonly adopted typical testing method used to assess the performance of connectors for shear capacity and is performed according to the Eurocode 4 specifications. However, the push-out test omits the information valuable for accounting the interfacial friction, bending, and distribution of forces among connectors. Therefore, researchers have adopted another method called beam test with or without the push-out test for exploring the overall significance of shear connectors in composite structures. The beam test revealed higher yielded values because it accounted for the friction and redistribution of forces among connectors (Ollgaard et al.[3]). In this conclusion section, the adaptability, efficacy, and uniqueness of various shear connectors are discussed.

3.1. Headed stud shear connectors

The welded headed stud shear connectors are surfeited in studies and widely adopted in composite solid concrete slab construction. However, its utilisation in precast composite concrete slabs remains a topic that requires further investigation. The utilisation of rubber sleeves in studs presents potential to overcome the problem associated with fatigue resistance and requires further investigation. Moreover, the application of the headed studs welded through steel profile decks, in which weld flaws could be harmful for ductility and strength and thus lead to additional welding requirements, is a study area. The dominance of the sheet obese and proper positioning of studs in the trough of profile sheeting is a factor contributing to composite shear action.

3.2. PBL shear connectors

PBL connectors are popular in the scientific community due to their superior performance to the performance of headed studs for fatigue and strength contribution in composite structures. Researchers have reported T-rib PBL with various geometrical shapes and hole arrangements and have discovered the shear capacity contribution of concrete dowel performance and the significance of transverse rebar in rib holes.

3.3. FRP PBL shear connectors

FRP-rib connectors are reported to exhibit excellent strength and stiffness in composite action; however, their studies are restricted to a precast one-piece arrangement and in situ situations remain to be performed.

3.4. Composite dowels as shear connectors

CL and PZ dowels are robust shear connectors in composite structures, specifically in pre-fabricated composite bridges. Composite dowels have higher shear strength and functional deformation capacity than headed studs even in high-grade concrete. However, missing standards for the application of composite dowels as shear connectors has led to misunderstanding in structural design principles and production.

3.5. C-shaped angle and channel shear connectors

The shear performance of angel connectors was lower than that of channel connectors when employed in reinforced normal concrete under monotonic and cyclic loadings (Shariati et al.[71]). The function of channel connectors for bearing capacity was supreme than that of T-rib connectors. Due to the better uplift counteraction and ductility fulfilment of V-shaped angle connectors than that of conventional channels and angle connectors, they are recommended to be used for future industrial applications.

3.6. Demountable bolted shear connectors

The drawbacks of using the welded studs in composite construction are overcome by using demountable bolted shear connectors for fatigue performance, dismantling parent elements in rapid non-destructive deconstruction, and employing in precast construction. Providing innovative LNSC facilitates rapid work and minimises construction tolerance problems such as disassembly or replacement and repair of steel and precast elements in bridge structures.

3.7. Different shear connectors

The behaviour of blind-bolted shear connectors for strength as well as stiffness is considerably alike to that of the welded headed stud; however, the blind bolts exhibit a brittle failure nature. Vertical pipes are suitable to be used as shear connectors under moderate shear strength requirements. Hilti X-HVB does not require welding or electric power for installation; thus, it does not infringe spot warm works as welded headed studs, that is, fire watch, and regulations, do.

3.8. Shear connectors in composite column

The utilization of through plate with rigid shear connectors in beam-column connection characterized the performance as a fully restrained strong panel elastic nature. Crestbond shear connectors significantly transfer the shear load at a connection in the concrete-filled steel tube columns. Shear connectors fabricated from conventional reinforcing bars and welded to the steel plates of a composite column under profiled positioning are advantages to overcome the difficulty of placing and handling reinforcement associated with the utilization of typical head studs in composite columns. The high strength bolts as a shear connector enhance the axial strength performance and exhibit ductile and flexible nature in the concrete-filled thin-walled steel tube short column.

Acknowledgement

The authors are indebted for the support they have received by Sardar Vallabhbhai National Institute of Technology, Surat, under the Ministry of Education (MoE), India.

References

[1] Ahn J.H., Kim S.H., and Jeong Y.J., “Shear behaviour of perfobond rib shear connector under static and cyclic loadings”, Magazine of Concrete Research, 60(5), 347–357, 2008. doi:10.1680/macr.2007.00046.

[2] BIS (Bureau of Indian Standards) IS 3935-1966., Code of practice for composite construction, Bureau of Indian Standards, New Delhi, India, 1966.

[3] Ollgaard J.G., Slutter R.G., and Fisher J.W., “Shear strength of stud connectors in lightweight and normal weight concrete”, AISC Engg Jr., 71-10, 1971. https://preserve.lehigh.edu/engr-civil-environmental-fritz-lab-reports/2010.

[4] Lee P.G., Shim C.S., and Chang S.P., “Static and fatigue behavior of large stud shear connectors for steel–concrete composite bridges”, Journal of Constructional Steel Research, 61(9), 1270–1285, 2005. doi:10.1016/j.jcsr.2005.01.007.

[5] Deng W., Xiong Y., Liu D., and Zhang J., “Static and fatigue behavior of shear connectors for a steel-concrete composite girder”, Journal of Constructional Steel Research, 159, 134–146, 2019. doi:10.1016/j.jcsr.2019.04.031.

[6] Liu Y., Zhang Q., Bao Y., and Bu Y., “Static and fatigue push-out tests of short headed shear studs embedded in Engineered Cementitious Composites (ECC)”, Engineering Structures, 182, 29–38, 2019. doi:10.1016/j.engstruct.2018.12.068.

[7] Viest I.M., Investigation of stud shear connectors for composite concrete and steel T-beams, ACI Journal Proceedings, 52(4), 875–892, 1956. doi:10.14359/11655

[8] Pallarés L., and Hajjar J.F., Headed steel stud anchors in composite structures, Part I: Shear, Journal of Constructional Steel Research. 66(2), 198–212, 2010. doi:10.1016/j.jcsr.2009.08.009.

[9] Pallarés L., Jerome F., and Hajjar J.F., “Headed steel stud anchors in composite structures, Part II: Tension and interaction”, Journal of Constructional Steel Research. 66(2), 213-228, 2010. doi.org/10.1016/j.jcsr.2009.08.008.

[10] Spremic M., Markovic Z., Veljkovic M., and Budjevac D., “Push-out experiments of headed shear studs in group arrangements”, Advanced Steel Construction, 9(2), 139–160, 2013. doi:10.18057/IJASC.2013.9.2.4.

[11] EN 1994-1-1 2004., Eurocode 4: Design of composite steel and concrete structures-part 1-1: General rules and rules for buildings, Brussels, Belgium, 2004.

[12] Xu X., and Liu Y., Analytical and numerical study of the shear stiffness of rubber-sleeved stud, Journal of Constructional Steel Research, 123, 68–78, 2016.

[13] Xu X., Zhou X., and Liu Y., “Behavior of rubber-sleeved stud shear connectors under fatigue loading”, Construction and Building Materials, 244, 118386, 2020. doi:10.1016/j.conbuildmat.2020.118386.

[14] Ding Y., Dai X. M., and Yan J. B., “Developments and behaviors of slip-released novel connectors in steel-concrete composite structures”, Advanced Steel Construction, 15(1), 30-36, 2019. doi: 10.18057/ijasc.2019.15.1.5.

[15] Sjaarda M., Walbridge S., and West J.S., “Assessment of shear connection through composite beam modeling”, Transportation Research Record, 2672(41), 177–185, 2018. doi:10.1177/0361198118781685.

[16] Sun Q., Nie X., Denavit M.D., Fan J., and Liu W., “Monotonic and cyclic behavior of headed steel stud anchors welded through profiled steel deck”, Journal of Constructional Steel Research, 157, 121–131, 2019. doi:10.1016/j.jcsr.2019.01.022.

[17] Mirza O., and Uy B., Effects of strain regimes on the behaviour of headed stud shear connectors for composite steel-concrete beams, Advanced Steel Construction, 6(1), 635-661, 2010. doi: 10.18057/ijasc.2010.6.1.8.

[18] Qureshi J., Lam D., and Ye J., “Effect of shear connector spacing and layout on the shear connector capacity in composite beams”, Journal of Constructional Steel Research, 67(4), 706–719, 2011. doi:10.1016/j.jcsr.2010.11.009.

[19] Qureshi J., Lam D., and Ye J., “The influence of profiled sheeting thickness and shear connector’s position on strength and ductility of headed shear connector”, Engineering Structures, 33(5), 1643–1656, 2011. doi:10.1016/j.engstruct.2011.01.035.

[20] ACI (American Concrete Institute) 2008., Committee 318: Building code requirements for structural concrete and commentary, ACI, Farmington Hills, MI, 2008.

[21] AISC 2005., ANSI/AISC 360-05 specification for structural steel buildings, American Institute of Steel Construction, 2005.

[22] GB50017-2003., Code for design of steel structure. China Planning Press, National Standards of People’s Republic of China, Beijing, 2003.

[23] Slutter R.G., and Driscoll G.C., “Research on composite design at Lehigh University”, *In* Proceedings of the AISC National Engineering Conference, 18–24, 1961.

[24] Leonhardt F., Andrä W., Andrä H.P., and Harre W., “Neues, vorteilhaftes Verbundmittel für Stahlverbund-Tragwerke mit hoher Dauerfestigkeit”, Beton- und Stahlbetonbau, 82(12), 325–331, 1987. doi:10.1002/best.198700500.

[25] Oguejiofor E.C., and Hosain M.U., “Behaviour of perfobond rib shear connectors in composite beams: Full-size tests”, Canadian Journal of Civil Engineering, 19(2), 224–235, 1992. doi:10.1139/l92-028.

[26] Oguejiofor E.C., and Hosain M.U., A parametric study of perfobond rib shear connectors, Canadian Journal of Civil Engineering, 21(4), 614–625, 1994. doi:10.1139/l94-063.

[27] Oguejiofor E.C., and Hosain M.U., Numerical analysis of push-out specimens with perfobond rib connectors, Computers & Structures, 62(4), 617–624, 1997. doi:10.1016/S0045-7949(96)00270-2.

[28] Vellasco P.C.G.D.S., de Andrade S.A.L., Ferreira L.T.S., and de Lima L.R.O., “Semi-rigid composite frames with perfobond and T-rib connectors Part 1: Full scale tests”, Journal of Constructional Steel Research, 63(2), 263–279, 2007. doi:10.1016/j.jcsr.2006.04.011.

[29] Vianna J.C., Costa-Neves L.F., Da P.C.G., and de Andrade S.A.L., “Experimental assessment of perfobond and T-perfobond shear connectors’ structural response”, Journal of Constructional Steel Research, 65(2), 408–421, 2009. doi:10.1016/j.jcsr.2008.02.011.

[30] Vianna J.C., de Andrade S.A.L., Vellasco P.C.G.D.S., and Costa-Neves L.F., “Experimental study of perfobond shear connectors in composite construction”, Journal of Constructional Steel Research, 81, 62–75, 2013. doi:10.1016/j.jcsr.2012.11.002.

[31] Costa-Neves L.F., Figueiredo J.P., Vellasco P.C.G.D.S., and da Cruz Vianna J., “Perforated shear connectors on composite girders under monotonic loading: An experimental approach”, Engineering Structures, 56, 721–737, 2013. doi:10.1016/j.engstruct.2013.06.004.

[32] Rodrigues J.P.C., and Laím L., Experimental investigation on the structural response of T, T-block and T-Perfobond shear connectors at elevated temperatures, Engineering Structures, 75, 299–314, 2014. doi:10.1016/j.engstruct.2014.06.016.

[33] Kim S.H., Choi K.T., Park S.J., Park S.M., and Jung C.Y., “Experimental shear resistance evaluation of Y-type perfobond rib shear connector”, Journal of Constructional Steel Research, 82, 1–18, 2013. doi:10.1016/j.jcsr.2012.12.001.

[34] Kim S.H., Choi J., Park S.J., Ahn J.H., and Jung C.Y., “Behavior of composite girder with Y-type perfobond rib shear connectors”, Journal of Constructional Steel Research, 103, 275–289, 2014. doi:10.1016/j.jcsr.2014.09.012.

[35] Kim S.H., Heo W.H., Woo K.S., Jung C.Y., and Park S.J., “End-bearing resistance of Y-type perfobond rib according to rib width-height ratio”, Journal of Constructional Steel Research, 103, 101–116, 2014. doi:10.1016/j.jcsr.2014.08.003.

[36] Kim S.H., Park S.J., Heo W.H., and Jung C.Y., “Shear resistance characteristic and ductility of Y-type perfobond rib shear connector”, Steel and Composite Structures, 18(2), 497–517, 2015. doi:10.12989/scs.2015.18.2.497.

[37] Kim S.H., Kim K.S., Park S., Ahn J.H., and Lee M.K., “Y-type perfobond rib shear connectors subjected to fatigue loading on highway bridges”, Journal of Constructional Steel Research, 122, 445–454, 2016. doi:10.1016/j.jcsr.2016.04.015.

[38] Kim S.H., Kim K.S., Lee D.H., Park J.S., and Han O., “Analysis of the shear behavior of stubby Y-Type perfobond rib shear connectors for a composite frame structure”, Materials, 10(11), 1340, 2017. doi:10.3390/ma10111340.

[39] Kim S.H., Park S., Kim K.S., and Jung C.Y., “Generalized formulation for shear resistance on Y-type perfobond rib shear connectors”, Journal of Constructional Steel Research, 128, 245–260, 2017. doi:10.1016/j.jcsr.2016.08.016.

[40] Ramasamy V., and Govindan B., “Feasibility study on triangular perfobond rib shear connectors in composite slab”, Materials Today: Proceedings, 21(1), 133–136, 2020. doi:10.1016/j.matpr.2019.06.080.

[41] Zheng S., Liu Y., Yoda T., and Lin W., “Parametric study on shear capacity of circular-hole and long-hole perfobond shear connector”, Journal of Constructional Steel Research, 117, 64–80, 2016. doi:10.1016/j.jcsr.2015.09.012.

[42] Fan L., and Zhou Z., New shear connectors based on PBL shear connector for composite arch members, Structural Engineering International, 24(2), 281–284, 2014. doi:10.2749/101686614X13830790993005.

[43] Zhang Q., Jia D., Bao Y., and Cheng Z., “Analytical study on internal force transfer of perfobond rib shear connector group using a nonlinear spring model”, Journal of Bridge Engineering, 22(10), 04017081, 2017. doi: 10.1061/(ASCE)BE.1943-5592.0001123.

[44] Zhang Q., Pei S., Cheng Z., Bao Y., and Li Q., “Theoretical and experimental studies of the internal force transfer mechanism of perfobond rib shear connector group”, Journal of Bridge Engineering, 22(2), 04016112, 2017. doi:10.1061/(ASCE)BE.1943-5592.0000997.

[45] Yu Z., He S., Mosallam A.S., Jiang S., and Feng W., "Experimental and numerical evaluation of perfobond rib shear connectors embedded in recycled aggregate concrete", Advances in Civil Engineering, 3157091, 2020. doi:10.1155/2020/3157091.

[46] Su Q.T., Wang W., Luan H.W., and Yang G.T., "Experimental research on bearing mechanism of perfobond rib shear connectors", Journal of Constructional Steel Research, 95, 22–31, 2014. doi:10.1016/j.jcsr.2013.11.020.

[47] Su Q., Yang G., and Bradford M.A., "Bearing capacity of perfobond rib shear connectors in composite girder bridges", Journal of Bridge Engineering, 21(4), 06015009, 2016. doi:10.1061/(ASCE)BE.1943-5592.0000865.

[48] Zhan Y., Yin C., Liu F., and Song R., "Pushout tests on headed studs and PBL shear connectors considering external pressure", Journal of Bridge Engineering, 25(1), 04019125, 2020. doi: 10.1061/(ASCE)BE.1943-5592.0001506.

[49] Zou X.X., Feng P., and Wang J.Q., "Perforated FRP ribs for shear connecting of FRP-concrete hybrid beams/decks", Composite Structures, 152, 267–276, 2016. doi:10.1016/j.compstruct.2016.05.039.

[50] Gwon S.C., Kim S.H., Yoon S.J., and Choi C.W., "An experimental study on the shear strength of FRP perfobond shear connector", *In* IOP Conference Series: Materials Science and Engineering. IOP Publishing, 12042, 2018.

[51] Cho J.R,. Park S.Y., Cho K., Kim S.T., and Kim B.S., "Pull-out test and discrete spring model of fibre-reinforced polymer perfobond rib shear connector", Canadian Journal of Civil Engineering, 39(12), 1311–1320, 2012. doi:10.1139/cjce-2011-0573.

[52] Yoshitaka U., Tetsuya H., and Kaoru M., "An experimental study on shear characteristics of perfobond strip and its rational strength equations", *In* International Symposium on Connections between Steel and Concrete, RILEM Publications SARL, 1066–1075, 2001.

[53] Al-Darzi S.Y.K., Chen A.R., and Liu Y.Q., "Finite element simulation and parametric studies of perfobond rib connector", American Journal of Applied Sciences, 4(3), 122–127, 2007. doi:10.3844/AJASSP.2007.122.127.

[54] Ahn J.H., Lee C.G., Won J.H., and Kim S.H., "Shear resistance of the perfobond-rib shear connector depending on concrete strength and rib arrangement", Journal of Constructional Steel Research, 66(10), 1295–1307, 2010. doi:10.1016/j.jcsr.2010.04.008.

[55] Zhao C., and Liu Y., Experimental study of shear capacity of perfobond connector, Engineering Mechanics, 29 (12), 349-354, 2012. doi:10.6052/j.issn.1000-4750.2011.09.0604.

[56] Deng W., Gu J., Liu D., Hu J., and Zhang J., "Study of single perfobond rib with head stud shear connectors for a composite structure", Magazine of Concrete Research, 71(17), 1–15, 2019. doi:10.1680/jmacr.18.00051.

[57] Verissimo G.S., Development of a shear connector plate gear for composite structures of steel and concrete and study their behavior, Universidade Federal de Minas Gerais Belo Horizonte [In Portuguese], 2007.

[58] Medberry S.B., and Shahrooz B.M., Perfobond shear connector for composite construction, American Institute of Steel Construction, Engineering Journal, 39(1), 2–12, 2002.

[59] Kopp M., Wolters K., Claben M., Hegger J., Gundel M., Gallwoszus J., Heinemeyer S., and Feldmann M., "Composite dowels as shear connectors for composite beams – Background to the design concept for static loading", Journal of Constructional Steel Research, 147, 488–503, 2018. doi:10.1016/j.jcsr.2018.04.013.

[60] Seidl G., Petzek E., and Bancila R., "Composite dowels in bridges - Efficient solution", Structural Integrity of Welded Structures, 814, 193–206, 2013. doi:10.4028/www.scientific.net/AMR.814.193.

[61] Hechler O., Berthellemy J., Lorenc W., Seidl G., and Viefhues E., "Continuous shear connectors in bridge construction", *In* Composite Construction in Steel and Concrete VI - Proceedings of the 2008 Composite Construction in Steel and Concrete Conference, 78–91, 2011.

[62] Dudziński W., Pękalskip G., Harnatkiewicz P. Kopczyński A., Lorencmkożuch W., and Rowiński S., "Study on fatigue cracks in steel-concrete shear connection with composite dowels", Archives of Civil and Mechanical Engineering, 11(4), 839–858, 2011. doi:10.1016/S1644-9665(12)60081-8.

[63] Lorenc W., Kozuch M., and Rowiński S., "The behaviour of puzzle-shaped composite dowels - Part I: Experimental study", Journal of Constructional Steel Research, 101, 482–499, 2014. doi:10.1016/j.jcsr.2014.05.013.

[64] Shariati M., Ramli Sulong N.H., Shariati A., and Khanouki M.A., "Behavior of V-shaped angle shear connectors: Experimental and parametric study", Materials and Structures, 49(9), 3909–3926, 2016. doi:10.1617/s11527-015-0762-8.

[65] NBC (National Research Council)., National building code of Canada, Associate Committee on the National Building Code, National Research Council, Canada, 2005.

[66] Soty R., and Shima H., Formulation for shear force–relative displacement relationship of L-shape shear connector in steel–concrete composite structures, Engineering Structures, 46, 581–592, 2013. doi:10.1016/j.engstruct.2012.09.003.

[67] Pashan A., and Hosain M.U., New design equations for channel shear connectors in composite beams, Canadian Journal of Civil Engineering, 36(9), 1435–1443, 2009. doi:10.1139/L09-078.

[68] Baran E., and Topkaya C., An experimental study on channel type shear connectors, Journal of Constructional Steel Research, 74, 108–117, 2012. doi:10.1016/j.jcsr.2012.02.015.

[69] Tahmasbi F., Maleki S., Shariati M., Ramli Sulong N.H., and Tahir M.M., "Shear capacity of C-shaped and L-shaped angle shear connectors", Public Library of Science One, 11(8), e0156989, 2016. doi:10.1371/journal.pone.0156989.

[70] Shariati M., Ramli Sulong N.H., Shariati A., and Kueh A.B.H., "Comparative performance of channel and angle shear connectors in high strength concrete composites: An experimental study", Construction and Building Materials, 120, 382–392, 2016. doi:10.1016/j.conbuildmat.2016.05.102.

[71] Shariati M., Ramli Sulong N.H., Suhatril M., Shariati A., Arabnejad Khanouki M.M., and Sinaei H., "Comparison of behaviour between channel and angle shear connectors under monotonic and fully reversed cyclic loading", Construction and Building Materials, 38, 582–593, 2013. doi:10.1016/j.conbuildmat.2012.07.050.

[72] Zhao Q., Du Y., Peng Y., Xu C., and Huang G., "Shear performance of short channel connectors in a steel-UHPC composite deck", International Journal of Steel Structures, 20, 300–310, 2020. doi:10.1007/s13296-019-00289-1.

[73] Balasubramanian R., and Rajaram B., Study on behaviour of angle shear connector in steel-concrete composite structures, International Journal of Steel Structures, 16(3), 807–811, 2016. doi:10.1007/s13296-015-0094-0.

[74] Titoum M., Mazoz A., Benanane A., and Ouinas D., "Experimental study and finite element modelling of push-out tests on a new shear connector of I-shape", Advanced Steel Construction, 12(4), 487-506, 2016. doi: 10.18057/ijasc.2016.12.4.7.

[75] Khorramian K., Maleki S., Shariati M., and Sulong N.H.R., "Behavior of tilted angle shear connectors", Public Library of Science One, 10(12), e0144288, 2015. doi:10.1371/journal.pone.0144288.

[76] Shariati M., Mafipour M.S., Mehrabi P., and Shariati A., "A novel approach to predict shear strength of tilted angle connectors using artificial intelligence techniques", Engineering with Computers, 1-21, 2020. doi:10.1007/s00366-019-00930-x.

[77] Hicks S., Cao J., McKenzie C., Chowdhury M., and Kaufusi R., "Evaluation of shear connectors in composite bridges", NZ Transport Agency report 602, 188, 2016.

[78] Pavlović M., Marković Z., Veljković M., and Budevac D., "Bolted shear connectors vs. headed studs behaviour in push-out tests", Journal of Constructional Steel Research, 88, 134–149, 2013. doi:10.1016/j.jcsr.2013.05.003.

[79] Dai X.H., Lam D., and Saveri E., "Effect of concrete strength and stud collar size to shear capacity of demountable shear connectors", Journal of Structural Engineering, 141(11), 04015025, 2015. doi:10.1061/(ASCE)ST.1943-541X.0001267.

[80] Dai X., Lam D., Sheehan T., Yang J., and Zhou K., "Use of bolted shear connectors in composite construction", *In* 12th International Conference on Advances in Steel-Concrete Composite Structures (ASCCS 2018), València, 475–482, 2018.

[81] Yang F., Liu Y., Jiang Z., and Xin H., "Shear performance of a novel demountable steel-concrete bolted connector under static push-out tests", Engineering Structures, 160, 133–146, 2018. doi:10.1016/j.engstruct.2018.01.005.

[82] Rehman N., Lam D., Dai X., and Ashour A.F., "Experimental study on demountable shear connectors in composite slabs with profiled decking", Journal of Constructional Steel Research, 122, 178–189, 2016. doi:10.1016/j.jcsr.2016.03.021.

[83] Patel V. I., Uy B., Pathirana S. W., Wood S., Singh M. and Trang B. T., "Finite element analysis of demountable steel-concrete composite beams under static loading", Advanced Steel Construction, 14(3), 392-411, 2018. doi: 10.18057/ijasc.2018.14.3.5.

[84] Kozma A., Odenbreit C., Braun M.V., Veljkovic M., and Nijgh M.P., "Push-out tests on demountable shear connectors of steel-concrete composite structures", Structures, 21, 45–54, 2019. doi:10.1016/j.istruc.2019.05.011.

[85] Kwon G., Engelhardt M.D., and Klingner R.E., "Behavior of post-installed shear connectors under static and fatigue loading", Journal of Constructional Steel Research, 66(4), 532–541, 2010. doi:10.1016/j.jcsr.2009.09.012.

[86] Sjaarda M., West J.S., and Walbridge S., "Performance of embedded bolt shear connectors", Structural Engineering International, 30(3), 421–429, 2020. doi:10.1080/10168664.2019.1706435.

[87] Suwaed A.S.H., and Karavasilis T.L., Novel demountable shear connector for accelerated disassembly, repair, or replacement of precast steel-concrete composite bridges, Journal of Bridge Engineering, 22(9), 04017052, 2017. doi:10.1061/(ASCE)BE.1943-5592.0001080.

[88] Mirza O., Uy B., and Patel N., "Behaviour and strength of shear connectors utilising blind bolting", *In* Steel and Composite Structures: Proceedings of the 4th International Conference on Steel and Composite Structures, Sydney, Australia, 791–796, 2010.

[89] Pathirana S.W., Uy B., Mirza O., and Zhu X., "Flexural behaviour of composite steel–concrete beams utilising blind bolt shear connectors", Engineering Structures, 114, 181–194, 2016. doi:10.1016/j.engstruct.2016.01.057.

[90] Henderson I.E.J., Zhu X.Q., Uy B., and Mirza O., "Dynamic behaviour of steel–concrete composite beams with different types of shear connectors Part I: Experimental study", Engineering Structures, 103, 298–307, 2015. doi:10.1016/j.engstruct.2015.08.033.

[91] Henderson I.E.J., Zhu X.Q., Uy B., and Mirza O., "Dynamic behaviour of steel–concrete composite beams with different types of shear connectors Part II: Modelling and comparison", Engineering Structures, 103, 308–317, 2015. doi:10.1016/j.engstruct.2015.08.033.

[92] Ban H., Uy B., Pathiranab S.W., Henderson I., Mirza O., and Zhu X., "Time-dependent behaviour of composite beams with blind bolts under sustained loads", Journal of Constructional Steel Research, 112, 196–207, 2015. doi:10.1016/j.jcsr.2015.05.004.

[93] Nasrollahi S., Maleki S., Shariati M., Marto A., and Khorami M., "Investigation of pipe shear connectors using push out test", Steel and Composite Structures, 27(5), 537–543, 2018. doi:10.12989/scs.2018.27.5.537.

[94] Hilti X-HVB System., Solutions for shear connections, S.E. & O, Germany, 2016.

[95] Gluhović N., Marković Z., Spremić M., and Pavlović M., "Experimental investigation and specific behaviour of X-HVB shear connectors in prefabricated composite decks", CE/Papers, 1(2), 2080–2089, 2017. doi:10.1002/cepa.253.

[96] Gu J.C., Liu D., Deng W.Q., and Zhang J.D., "Experimental study on the shear resistance of a comb-type perfobond rib shear connector", Journal of Constructional Steel Research, 158, 279–289, 2019. doi:10.1016/j.jcsr.2019.03.032.

[97] Eghbali N.B., and Mirghaderi S.R., "Experimental investigation of steel beam to RC column connection via a through-plate", Journal of Constructional Steel Research", 133, 125–140, 2017. doi:10.1016/j.jcsr.2017.02.007.

[98] Aguiar O.P., Caldas R.B., Rodrigues F.C., Fakury R.H., and Veríssimo G. S., "Crestbond shear connectors for load transfer in concrete filled tube columns", Revista IBRACON de Estruturas e Materiais, 11(5), 960-965, 2018. doi:10.1590/s1983-41952018000500004.

[99] Odenbreit C., Chrzanowski M., Obiala R., Bogdan T., and Degée H., "Characterisation of a new flat mechanical shear connection mean for steel-concrete composite columns", Structures, 21, 122-134, 2019. doi:10.1016/j.istruc.2019.03.001.

[100] Qiao Q., Zhang W., Qian Z., Cao W., Liu W., "Experimental study on mechanical behavior of shear connectors of square concrete filled steel tube", Applied Sciences, 7(8), 818, 2017. doi:10.3390/app7080818.

[101] Alenezi K., Tahir M.M., Alhajri T., Badr M.R.K., and Mirza J., "Behavior of shear connectors in composite column of cold-formed steel with lipped C-channel assembled with ferro-cement jacket", Construction and Building Materials, 84, 39-45, 2015. doi:10.1016/j.conbuildmat.2015.03.015.

[102] Younes S.M., Ramadan H.M., Mourad S.A., "Stiffening of short small-size circular composite steel–concrete columns with shear connectors", Journal of Advanced Research, 7(3), 525-538, 2016. doi:10.1016/j.jare.2015.08.001.

[103] Neto J.G.R., and Sarmanho A. M., "Experimental analysis of a mechanical shear connector in concrete filled steel tube column", Revista IBRACON de Estruturas e Materiais, 10(3), 592-625, 2017. doi: 10.1590/s1983-41952017000300004.

[104] Tian L., Liu T., Li T., And Lin H., "Shear resistance of novel perforated shaped steel-engineered cementitious composite (ECC) connectors" Advanced Steel Construction, 16(1), 30-36, 2020. doi:10.18057/ijasc.2020.16.1.4.

Advanced Steel Construction – Vol. 17 No. 4 (2021) 403–411
DOI:10.18057/IJASC.2021.17.4.9

PREDICTION OF ULTRALOW CYCLE FATIGUE DAMAGE OF THIN-WALLED STEEL BRIDGE PIERS

Zhan-Zhan Tang [1, 2], Han-Yang Xue [1], Hong Liu [4] and Wei Zhang [*, 2, 3]

[1] *College of Civil Science and Engineering, Yangzhou University, Yangzhou, Jiangsu 225127, China*
[2] *School of Civil Engineering, Fujian University of Technology, Fuzhou 350118, China*
[3] *Institute of Theoretical and Applied Mechanics of the Czech Academy of Sciences, Prague 190 00, Czech Republic*
[4] *Faculty of Civil Engineering, Department of Structures, VSB-Technical University of Ostrava, L. Podéšté 1875, 708 33 Ostrava, Poruba, Czech Republic*
** (Corresponding author: E-mail: zhangwei621@gmail.com)*

ABSTRACT

Ultralow cycle fatigue (ULCF) failure was first observed on steel bridge piers in the Kobe earthquake, and the ultimate strength and ductility evaluation formulas of thin-walled steel bridge piers were established. In this study, parametric analysis of steel piers was carried out to study the influence of the structural parameters on the ULCF damage evolution. The evolution of the ULCF damage of the base metal, the deposited metal, and the heat-affected zones was studied based on two types of steel piers with hollow box and pipe sections. Then, practical formulas to predict the ULCF damage level of steel piers under cyclic loading were proposed. Finally, the proposed formulas were validated by comparisons with the experimental results. The results show that the heat-affected zone is more vulnerable to ULCF failure than the base metal and the deposited metal. Moreover, the practical formulas to predict the ULCF damage index of the steel piers under cyclic loading were proposed, and the formulas effectively predicted the ULCF crack of the steel piers.

ARTICLE HISTORY

Received: 17 September 2020
Revised: 7 May 2021
Accepted: 7 May 2021

KEYWORDS

Cyclic void growth model;
Damage index;
Structural steel;
Steel bridge piers;
Ultralow cycle fatigue

1. Introduction

For steel structures, the prevention of fracture is always a main concern for engineering design. At present, a great number of steel piers with hollow boxes or pipe sections are still widely used as substructures in highway bridges. During the 1995 Kobe earthquake, in addition to the traditional buckling failure mode, ultralow cycle fatigue (ULCF) failure occurred on steel bridge piers [1-5]. Then, the failure modes and the corresponding thresholds for this type of structure were studied by many researchers. The ultimate strength evaluation formulas of thin-walled steel plates and steel bridge piers, which are usually controlled by their buckling behavior, have been established. Meanwhile, ULCF failure of steel materials and joints can be predicted numerically based on the micromechanics, for example, the cyclic void growth model (CVGM). To date, the applicability of the ultimate strength evaluation formulas and the CVGM has been verified by some experiments. However, without the prediction formulas of ULCF damage, it is not clear in the design stage when the ULCF failure will determine the structural seismic safety.

After the 1995 Kobe earthquake, much research has been conducted on the seismic resistance and ultimate ductility of steel bridge piers. Zheng et al. [4] studied the ductility capacity of thin-walled steel box columns with and without longitudinal stiffeners. A failure strain was employed to define the ductility of steel columns, and the corresponding empirical formulas were developed based on the parametric analysis results. Kono et al. [5] investigated the ultimate deformation formula for steel box columns. The empirical formulas proposed in their study have a rather wide scope of application. Ge et al. [6] and Usami et al. [7] proposed empirical formulas of the ultimate strength for steel bridge piers with rectangular sections, which can consider the influence of the stiffener's slenderness. Based on the elastic-plastic finite deformation analysis, Ge et al. [8] proposed empirical formulas of strength and ductility for steel bridge piers with hollow pipe sections. With the efforts of these researchers, the ultimate strength and ductility, which are controlled by the buckling of steel piers under seismic loading, have been established. Some relevant guidelines can be found in bridge seismic design specifications. For example, Japanese specifications have stipulated the ductility capacity of thin-walled steel bridge piers [9]. Additionally, the limited slenderness ratio, width-to-thickness ratio and radius-thickness ratio for axial compressive or flexural dominant steel members have been provided by the AASHTO specifications [10].

The traditional empirical technique used to predict ULCF failure of structural steels is the Coffin-Manson formula [11-13]. However, the triaxial stress state in the crack initiation site is not considered in the formula, making it more applicable for uniaxial stress conditions. Therefore, the method based on microscopic damage mechanisms has attracted increased attention. In 1969, Rice et al. [14] studied the ductile growth rate of a single spherical void in an infinite ideal elastic-plastic continuum, and the void growth model was first proposed in their study. Through a series of tests and studies, Kanvinde et al. [15-18] proposed the cyclic void growth model to predict crack initiation for structural steels under cyclic loading. In the CVGM, the loading cycles are divided into tensile and compressive types based on the sign of the stress triaxiality for a certain material point. To facilitate the application of the micromechanical model, Liao et al. [19-20] and Yin et al. [21] calibrated the parameters in the CVGM by material tests and scanning electron microscope tests. Li et al. [22] proposed a new CVGM parameter calibration method to extend the scope of its application to a relatively lower-stress triaxiality condition. Moreover, the effect of the damage degradation parameter on the prediction of ULCF failure in steel bridge piers was discussed by them. Zhou et al. [23-24] and Wang et al. [25] conducted ULCF tests of steel joints under cyclic loads. Through the comparison of the prediction and the test results, they reported that the CVGM is a promising approach to predict the ULCF failure of steel structures. Xie et al. [26] studied the seismic damage characteristics of a thin-walled steel arch bridge considering both the strength and the ULCF failure modes. They found that the steel bridge experienced ULCF failure in its arch springing without apparent buckling failure.

During a strong earthquake, no matter which kind of failure mode is encountered for a steel bridge pier, it is fatal for the entire structure [1, 26-27]. The ultimate strength/ductility evaluation formulas of thin-walled steel bridge piers have been established. However, the ULCF damage prediction formulas are not yet available. Thus, the sequential occurrence of different failure modes for a steel bridge pier cannot be easily estimated. The use of the CVGM is a combination of complex FE modeling and void growth calculation. At present, it is not widely used because of the high computational cost and the substantial effort required for FE modeling. Therefore, the ULCF damage prediction formulas are much in need, especially in the design stage.

To establish the ULCF damage prediction formulas of single-column type bridge piers, parametric analysis was carried out in this study. A user subroutine UVARM coded by Fortran was utilized to track the evolution of the ULCF damage during the analysis. Two types of steel piers with hollow boxes or pipe sections were considered. The evolution of the ULCF damage of the base metal, the deposited metal, and the heat-affected zones was studied. The influence of the design parameters, including the diameter-to-thickness ratio, width-to-thickness ratio, slenderness ratio and axial compression ratio, on the evolution of ULCF damage was obtained. Then, practical formulas to predict the extent of ULCF damage of the steel piers under cyclic loading were proposed. Finally, the proposed formulas were validated by comparisons with the experimental results.

2. CVGM for ULCF failure prediction

The crack initiation of ULCF is ductile, and the fracture process depends on microvoid nucleation, dilation, contraction, and coalescence. Based on the void growth theory of Rice et al. [14], Kanvinde et al. [15-18] proposed the CVGM for predicting the ULCF of structural steels. Zhou et al. [23-24] applied the CVGM to investigate the ULCF performance of beam-column joints, thereby validating the effectiveness of the model at the structural level. Considering the different effects of compression and tension, the CVGM index VGI_{cyclic} is defined as:

$$VGI_{\text{cyclic}} = \sum_{\text{tensile-cycles}} \int_{\varepsilon_1}^{\varepsilon_2} \exp\left(|1.5T|\right) \mathrm{d}\varepsilon_{\text{eq}} - \sum_{\text{compressive-cycles}} \int_{\varepsilon_1}^{\varepsilon_2} \exp\left(|1.5T|\right) \mathrm{d}\varepsilon_{\text{eq}} \quad (1)$$

where $\mathrm{d}\varepsilon_{\text{eq}}$ denotes the increment of equivalent plastic strain, ε_1 and ε_2 are the upper and lower plastic strain in the integral, respectively, and T is the stress triaxiality (ratio of the mean stress to the von Mises effective stress).

The critical void growth index of the ULCF fracture is related to that of the monotonic tensile fracture. Based on test data and finite-element analysis, an exponential decay function is selected to express the critical void growth parameter for cyclic loading.

$$VGI_{\text{cyclic}}^{\text{critical}} = \eta \exp\left(-\lambda_{\text{CVGM}} \varepsilon_{\text{eq}}\right) \quad (2)$$

where η is the toughness parameter related to the material property, and it is actually the monotonic counterpart of $VGI_{\text{cyclic}}^{\text{critical}}$, and λ_{CVGM} is a material-dependent damageability coefficient. The cumulative equivalent plastic strain ε_{eq} in the equation is calculated at the beginning of each tensile excursion.

ULCF fracture is thought to occur when VGI_{cyclic} exceeds its critical value $VGI_{\text{cyclic}}^{\text{critical}}$:

$$VGI_{\text{cyclic}} = VGI_{\text{cyclic}}^{\text{critical}} \quad (3)$$

A new damage index D_0 is defined in this study as shown in Eq. (4) to illustrate the ULCF fracture damage evolution process. Thus, D_0=0 indicates no damage, and ductile crack initiation is predicted when D_0 reaches 1.0.

$$D_0 = \frac{\left(VGI_{\text{cyclic}}\right)_{\max}}{VGI_{\text{cyclic}}^{\text{critical}}} \quad (4)$$

3. Structural design and numerical models

3.1. Design parameters

The stability and ductility of thin-walled piers with hollow sections are considered to be influenced by some key parameters [9, 28], such as the slenderness ratio λ, the diameter-to-thickness ratio R_t for a circular pier and the width-to-thickness ratio R_R of the subpanel for a rectangular pier.

$$\begin{cases} \lambda = \dfrac{2h}{r} \cdot \dfrac{1}{\pi} \sqrt{\dfrac{\sigma_y}{E}} \\ R_t = \dfrac{R}{t} \cdot \dfrac{\sigma_y}{E} \sqrt{3\left(1-\mu^2\right)} \\ R_R = \dfrac{B}{t} \sqrt{\dfrac{\sigma_y}{E} \dfrac{12\left(1-\mu^2\right)}{4n^2\pi^2}} \end{cases} \quad (5)$$

In the above equations, h is the height of the column, r is the radius of gyration in the bending direction for the section, σ_y is the yield strength of the steel, E is the Young's modulus, μ is the Poisson's ratio, R is the radius of the circular pier, t is the thickness of the steel plate, B is the flange width of the rectangular pier, and n denotes the number of subpanels into which the plate is divided by the longitudinal stiffeners.

3.2. Loading method and numerical model

Fig. 1 shows a schematic view of single-column type bridge piers with hollow boxes or pipe sections. The cantilever piers are fixed to the ground in their bottom and subjected to a constant axial force N and a cyclic horizontal force H. The variable a is the distance between each diaphragm, D is the depth of the rectangular section, and a' is the transverse spacing between each longitudinal stiffener.

To study the influence of the design parameters on the structural failure mode, 22 circular piers and 24 rectangular piers are designed with different structural parameters for the parametric analysis. For the circular piers, the parameters are set within the following ranges: the radius-to-thickness ratio $0.024 \le R_t \le 0.095$, the slenderness ratio $0.197 \le \lambda \le 0.459$, the axial compression ratio $0.0 \le N/N_y \le 0.3$ (N donates the applied axial load and N_y denotes the yield strength of the entire section) and the diaphragm spacing ratio $0.0 \le \alpha (=a/R) \le 3.0$. For the rectangular piers, the parameters are set within the following ranges: the width-to-thickness ratio $0.270 \le R_R \le 0.524$, the slenderness ratio $0.215 \le \lambda \le 0.573$, the axial compression ratio $0.0 \le N/N_y \le 0.3$ and the diaphragm spacing ratio $0.556 \le \alpha (=a/B) \le 1.222$. Thus, all the parameters herein have ranges wide enough to satisfy the pier design demands [9, 28].

The horizontal cyclic load H applied at the top end of the piers can be equivalent to a forced displacement δ. That is, apart from a constant axial force induced by the weight of the superstructure, the pier is subjected to a horizontal cyclic displacement with increasing amplitudes for every 3 loops, as shown in Fig. 2. The variable δ_y is the horizontal yield displacement corresponding to the yield thrust H_y of the pier.

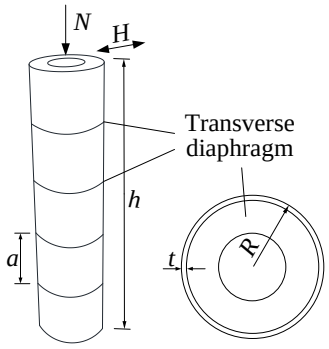

(a) Circular piers

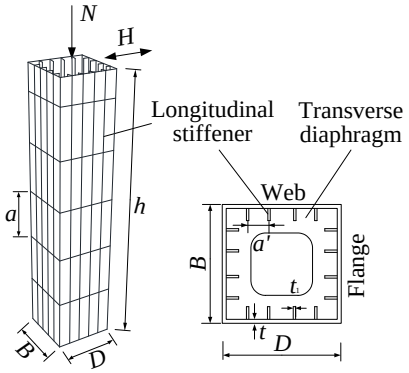

(b) Rectangular piers

Fig. 1 Structural design and loading method of steel piers

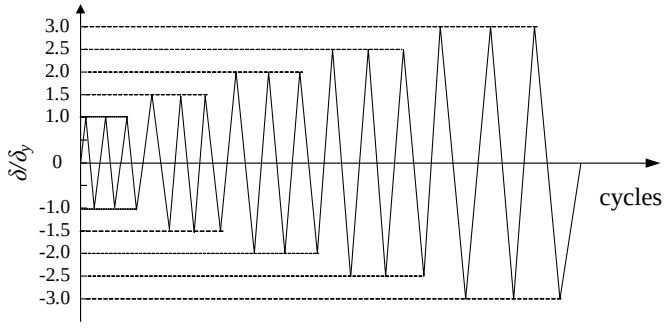

Fig. 2 Cyclic loading method

Numerical models of the steel piers with different structural parameters were constructed using the commercial software ABAQUS. For each steel pier, two individual models were created. To take into account the local deformations of the plate near the base and the local strain in the weld region, a hybrid model with two different types of elements was adopted. Fig. 3 shows the models and the element discretization. The shell elements were used to model the steel plates within a distance of twice the length of the transverse diaphragm spacing L_d near the base. Parts with slight or no seismic damage above the second diaphragm from the base were modeled by the fiber beam elements. Thus, both the computational accuracy and the cost can be considered. The MPC-beam interaction was used as the linkage between the beam and the shell elements.

The deformation history during loading around the edges of the most dangerous region near the base, which contains the heat-affected zone, the deposited metal, and the base metal, can be obtained. Then, a solid element model of the critical region was constructed with the deformation history applied on its edges. The dimensions of the shell and solid elements are less than 0.25 mm, thereby satisfying the characteristic-length requirement of the CVGM. For the hybrid element model, approximately 25,000 elements were used, and the transverse section of the beam element was divided into 145 fibers. For the solid element model, approximately 48,000 elements were used.

Chaboche's combined hardening constitutive model, which can account for the kinematic and isotropic hardening effect of the material, was adopted since the CVGM parameter calibration was conducted with this kind of constitutive law [19-22]. The mechanical properties of the heat-affected zone, the deposited metal, and the base metal are different from each other. Table 1 shows the mechanical parameters of Q345, Chinese steel with a nominal yield strength of 345 MPa, in Chaboche's combined hardening model [22, 29]. The plastic modulus is continuously transformed during the loading, thereby ensuring the smooth transition of the stress-strain curve. The isotropic hardening effect is reflected by changing the yield surface radius σ_0, which is defined as a nonlinear function of the equivalent plastic strain ε_p, as follows.

$$\sigma_0 = \sigma|_0 + Q_\infty\left(1-e^{-b\varepsilon_p}\right) \tag{6}$$

where $\sigma|_0$ is the initial yielding strength, Q_∞ is the maximum hardening value of the yield surface, and b is the ratio of the change in yield strength to the development of plastic strain.

The movement of the yield surface center α is treated as the kinematic hardening effect, where α is determined by a group of back stress α_k.

$$\begin{cases} \alpha = \sum_{i=1}^{N}\alpha_k \\ \alpha_k = \dfrac{C_k}{\gamma_k}\left(1-e^{-\gamma_k\varepsilon_p}\right)+\alpha_{k,1}e^{-\gamma_k\varepsilon_p} \end{cases} \tag{7}$$

where C_k is the initial modulus of the kinematic hardening, and γ_k is the ratio of the kinematic hardening modulus change to the plastic strain.

During the calculation, both the material and the geometric nonlinearities were considered. A user subroutine UVARM was integrated into the FE analysis to track the evolution of the ULCF damage index during the loading. Thus, the damage indices of the entire structure can be seen directly in the visualization module of the software.

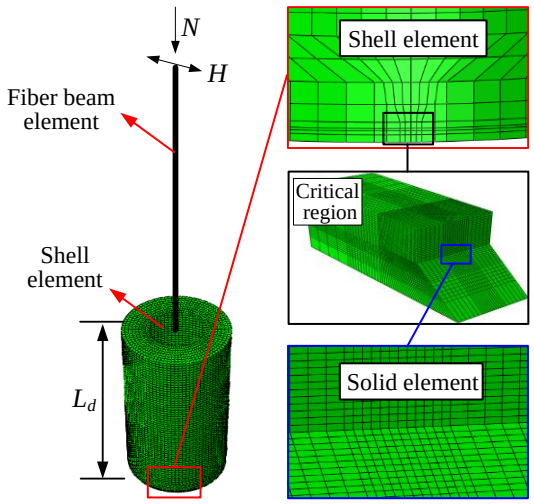

(a) Circular piers

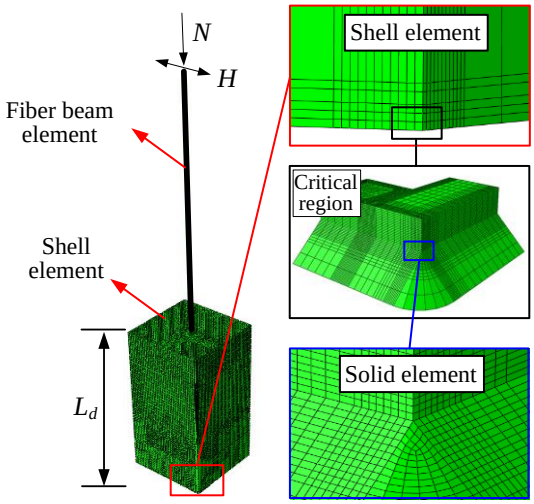

(b) Rectangular piers

Fig. 3 Numerical models and element discretization

Table 1
Material parameters of Q345 steel

Material	$\sigma\|_0$ (MPa)	Q_∞ (MPa)	b	C_1 (MPa)	γ_1	C_2 (MPa)	γ_2	C_3 (MPa)	γ_3	η	λ_{CVGM}
Base metal	354.10	13.2	0.6	44373.7	523.8	9346.6	120.2	946.1	18.7	2.55	0.20
Heat-affected zone	312.57	9.8	0.7	32242.4	199.2	3858.5	43.1	329.2	0.3	2.53	0.33
Deposit metal	428.45	17.4	0.4	12752.3	160.0	1111.2	160.0	630.5	26.0	2.63	0.25

4. ULCF damage evolution under cyclic loading

The horizontal load-displacement curves and the corresponding envelope curves at the top of the steel piers were obtained during the loading. For a thin-walled structure, the ultimate strength and ductility are usually controlled by the buckling behavior. Consequently, some critical states based on the envelope curves were adopted to check the value of the ULCF damage index. Three critical states were selected: the peak point on the envelope curve [9], the point when the horizontal strength on the envelope curve has exceeded the peak value and decreased to 95% of the ultimate strength [4, 7], and the point when the horizontal strength on the envelope curve has exceeded its peak value and decreased to 90% of the ultimate strength [30].

Fig. 4 shows the ULCF damage indices of the circular pier with different design parameters under the three critical buckling states. Similarly, Fig. 5 shows the ULCF damage indices of the rectangular pier. In these figures, H_m is the peak strength on the envelope curve. Thus, $1.00H_m$, $0.95H_m$, and $0.90H_m$ denote the three critical states previously defined, and D_B, D_D, and D_H denote the ULCF damage indices corresponding to the base metal, the deposited metal, and the heat-affected zone at the bottom of the pier, respectively. The ULCF damage indices gradually increase as the horizontal resistance of the piers reaches the peak value and then decreases. If one of the parameters of the axial compression ratio, the radius-to-thickness ratio, and the width-to-thickness ratio is large enough (e.g., N/N_y>0.3, R_t>0.05, or R_R>0.5), the ULCF damage indices are rather small (D<1.0). This indicates that the buckling failure mode plays a dominant role in these circumstances. The heat-affected zone is more vulnerable to ULCF failure than the base metal and the deposited metal since the damage index D_H is usually larger than indices D_B and D_D.

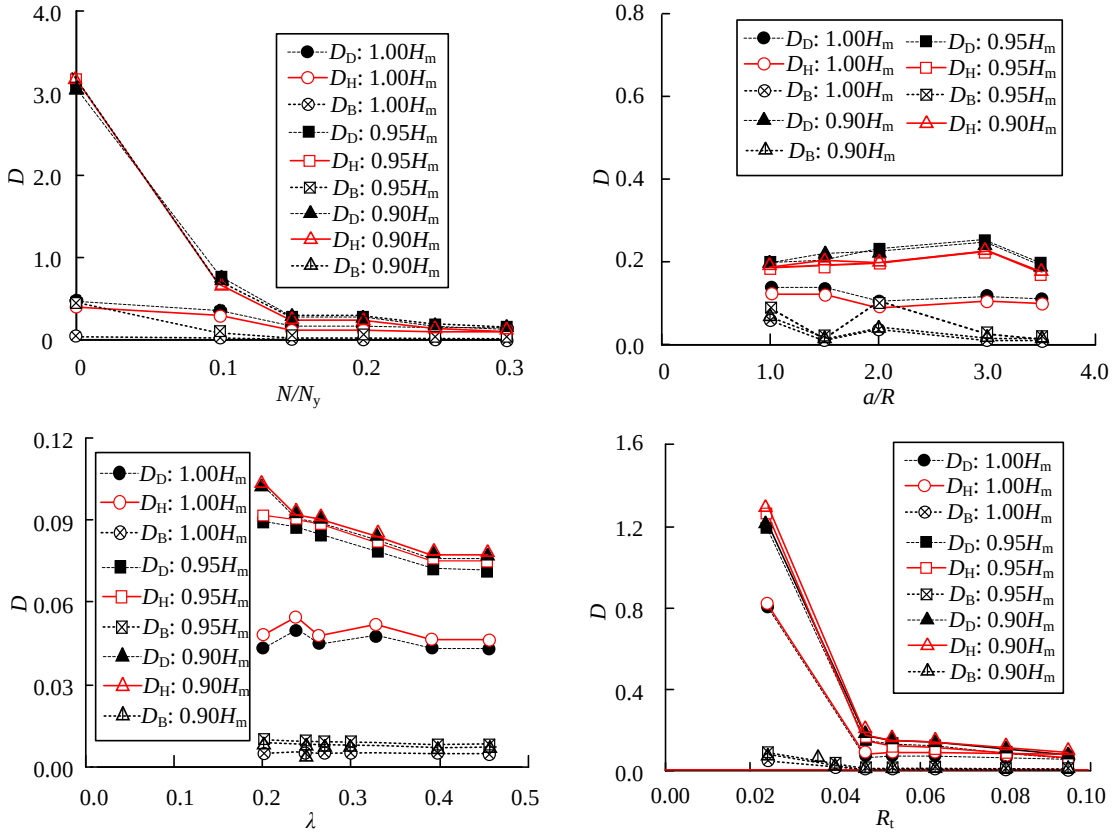

Fig. 4 ULCF damage indices of the circular piers under the critical states

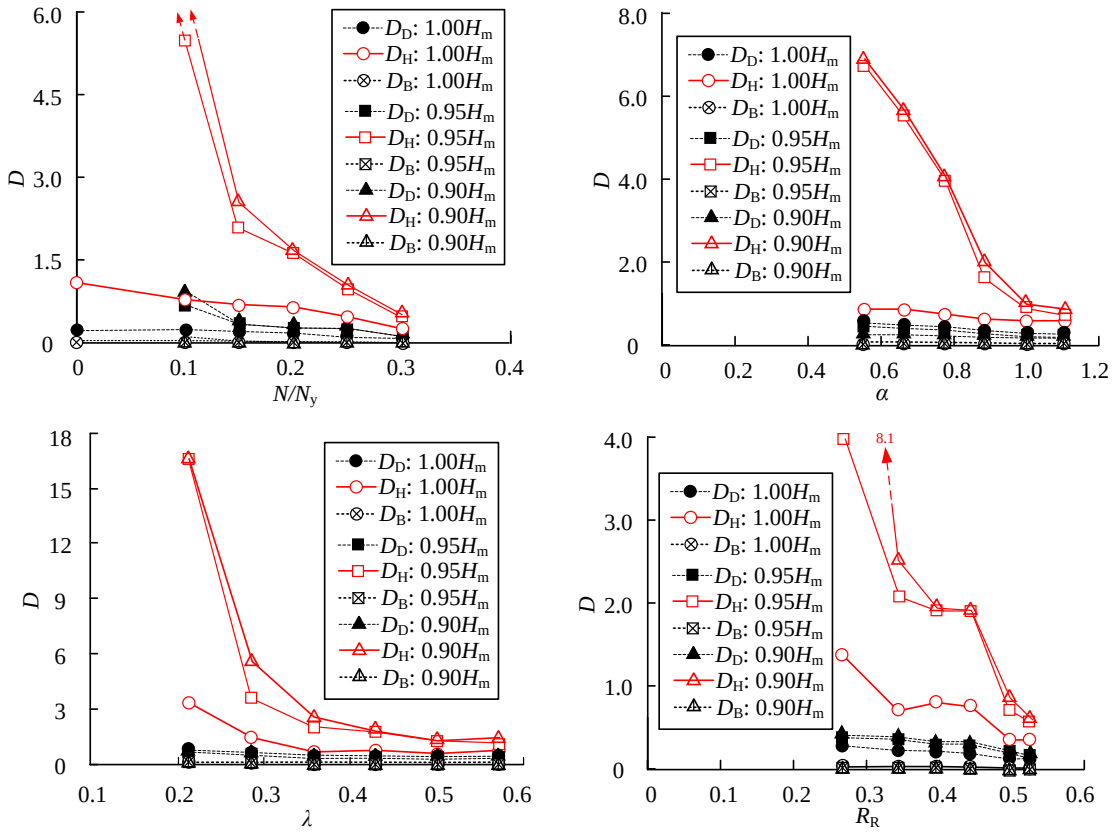

Fig. 5 ULCF damage indices of the rectangular piers under the critical states

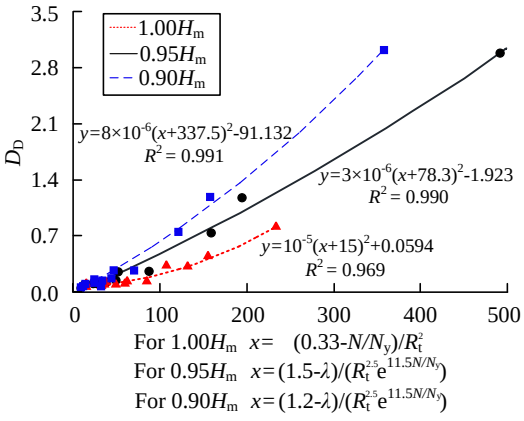

(a) D_D of the circular piers

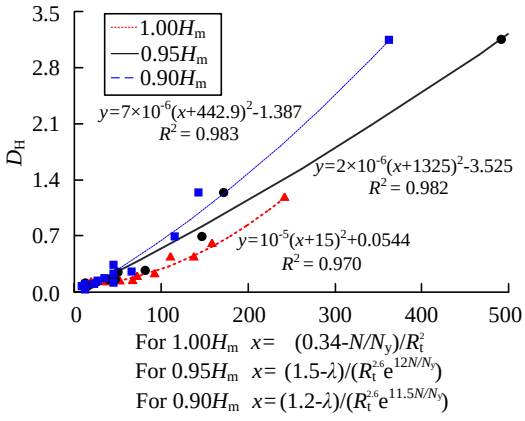

(b) D_H of the circular piers

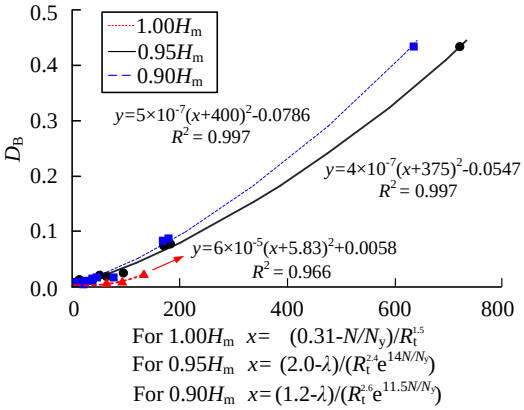

(c) D_B of the circular piers

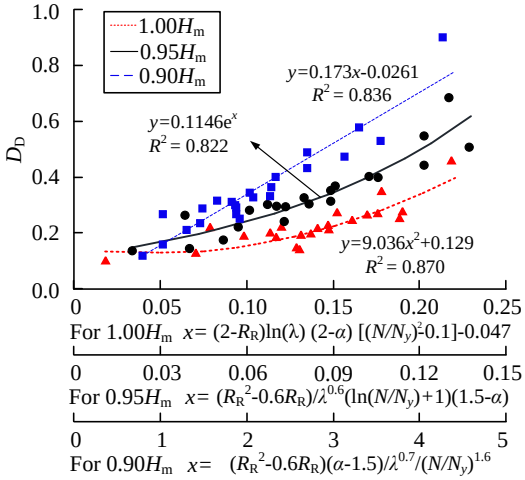

(d) D_D of the rectangular piers

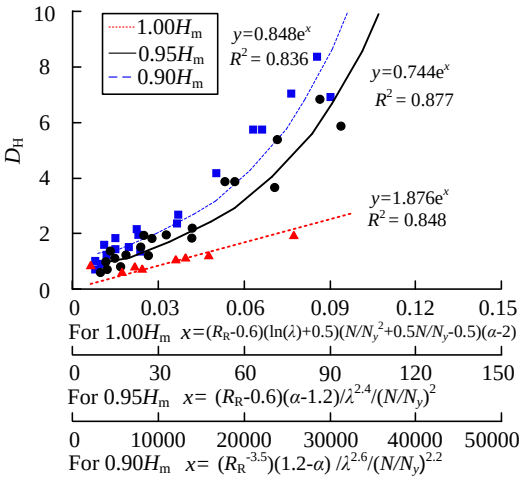

(e) D_H of the rectangular piers

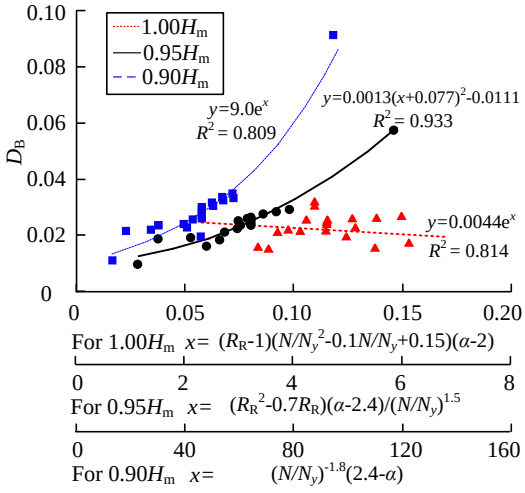

(f) D_B of the rectangular piers

Fig. 6 ULCF damage indices of the pier bottoms under the critical states

Fig. 6 shows the fitting relationship between the ULCF damage indices and the designed structural parameters of the steel bridge piers. Eqs. (8)-(10) are the ULCF damage indices fitting formulas for the circular piers, while Eqs. (11)-(13) are the fitting formulas for the rectangular piers. For most cases, the satisfactory accuracy of regression analysis can be achieved since the determination coefficients, R^2, of the estimations are all above 0.8. Moreover, for the piers with circular sections, if the radius-to-thickness ratio is rather small (e.g., R_t<0.03), the ULCF failure may occur at the heat-affected zone near the base when the horizontal strength on the envelope curve just exceeds its peak value. For the piers with rectangular sections, the order of the failure modes is more complicated. When the width-to-thickness ratio of the flange plate, the slenderness ratio, and the diaphragm spacing ratio are all small enough (e.g., R_R<0.3, λ<0.3 and α<0.8), ULCF failure occurs at the heat-affected zone before the horizontal ultimate strength state.

$$\begin{cases} D_D = 1\times10^{-5}\cdot\left(\dfrac{0.33-N/N_y}{R_t^{2}}+15\right)^2+0.0594 \\ D_H = 1\times10^{-5}\cdot\left(\dfrac{0.34-N/N_y}{R_t^{2}}+15\right)^2+0.0544 \\ D_B = 6\times10^{-5}\cdot\left(\dfrac{0.31-N/N_y}{R_t^{1.5}}-5.833\right)^2+0.00586 \end{cases} \quad \text{for circular section at } 1.00H_{\max} \text{ state} \tag{8}$$

$$\begin{cases} D_D = 3\times10^{-6}\cdot\left(\dfrac{1.5-\lambda}{R_t^{2.5}\exp(11.5N/N_y)}+783.333\right)^2-1.923 \\ D_H = 2\times10^{-6}\cdot\left(\dfrac{1.5-\lambda}{R_t^{2.6}\exp(12N/N_y)}+1325\right)^2-3.525 \\ D_B = 4\times10^{-7}\cdot\left(\dfrac{2-\lambda}{R_t^{2.4}\exp(14N/N_y)}+375\right)^2-0.0547 \end{cases} \quad \text{for circular section at } 0.95H_{\max} \text{ state} \tag{9}$$

$$\begin{cases} D_D = 8\times10^{-6}\cdot\left(\dfrac{1.2-\lambda}{R_t^{2.5}\exp(11N/N_y)}+337.5\right)^2-91.132 \\ D_H = 7\times10^{-6}\cdot\left(\dfrac{1.2-\lambda}{R_t^{2.6}\exp(11.5N/N_y)}+442.857\right)^2-1.387 \\ D_B = 5\times10^{-7}\cdot\left(\dfrac{1.2-\lambda}{R_t^{2.6}\exp(11.5N/N_y)}+400\right)^2-0.0786 \end{cases} \quad \text{for circular section at } 0.90H_{\max} \text{ state} \tag{10}$$

$$\begin{cases} D_D = 9.0362\cdot\left\{(R_{\mathrm{R}}-2.0)\cdot\ln(\lambda)\cdot(\alpha-2.0)\cdot\left[(N/N_{\mathrm{y}})^2-0.1\right]-0.047\right\}^2+0.129 \\ D_H = 1.876\cdot\exp\left\{(R_{\mathrm{R}}-0.6)\cdot(\ln\lambda+0.5)\cdot\left[(N/N_{\mathrm{y}}+0.25)^2-0.5625\right]\cdot(\alpha-2.0)\right\} \\ D_B = 0.0044\cdot\exp\left\{(R_{\mathrm{R}}-1.0)\cdot\left[(N/N_{\mathrm{y}}-0.05)^2+0.1475\right]\cdot(\alpha-2.0)\right\} \end{cases} \quad \text{for rectangular section at } 1.00H_{\max} \text{ state} \tag{11}$$

$$\begin{cases} D_D = 0.1146\cdot\exp\left\{\dfrac{12.13\cdot\left(R_{\mathrm{R}}^2-0.6R_{\mathrm{R}}\right)\cdot\left[\ln(N/N_y)+1.0\right]\cdot(1.5-\alpha)}{\lambda^{0.6}}\right\} \\ D_H = 0.7435\cdot\exp\left\{\dfrac{(R_{\mathrm{R}}-0.6)\cdot(\alpha-1.2)}{\lambda^{2.4}\cdot\left[\ln(N/N_{\mathrm{y}})\right]^2}\right\} \\ D_B = 0.0013\cdot\left[\dfrac{\left(R_{\mathrm{R}}^2-0.7R_{\mathrm{R}}\right)\cdot(\alpha-2.4)}{(N/N_{\mathrm{y}})^{1.5}}+0.077\right]^2-0.0111 \end{cases} \quad \text{for rectangular section at } 0.95H_{\max} \text{ state} \tag{12}$$

$$\begin{cases} D_D = 0.173\cdot\left(\dfrac{\left(R_R^{\ 2}-0.6R_R\right)\cdot(\alpha-1.5)}{\lambda^{0.7}\cdot(N/N_y)^{1.6}}\right)-0.0261 \\ D_H = 0.848\cdot\exp\left(\dfrac{1.2-\alpha}{\lambda^{2.6}\cdot R_R^{\ 3.5}\cdot(N/N_y)^{2.2}}\right) \\ D_B = 9.0\cdot\exp\left[\dfrac{2.4-\alpha}{(N/N_y)^{1.8}}\right] \end{cases} \quad \text{for rectangular section at } 0.90H_{\max} \text{ state} \tag{13}$$

5. Comparison of the predicted index and the test results

The results of the experimental tests carried out on the thin-walled steel piers were selected from the studies performed by Ge et al. [31-32]. Therefore, in this section, three steel piers with hollow rectangular sections are numerically analyzed. Then, the crack location and initiation time are compared with the experimental results.

Cross-sectional details of the specimens with rectangular sections are shown in Fig. 7. Table 2 presents the geometric dimensions and design parameters of the specimens. One end of the steel specimen is bolted directly to the fixed-base plate, and the other end is attached to a moving device. A constant vertical load (N/N_y=0.1), together with a similar cyclic horizontal loading as shown in Fig. 2, was applied to the top end. Crack initiation is defined at the time when the crack length extends 1∼2 mm according to observations.

The same technique described in Section 3 is adopted here. In particular, shell elements were used to model the steel plates within a distance of 3 times the length of the transverse diaphragm spacing near the base. Parts with slight or no seismic damage above the third diaphragm from the base were modeled by fiber beam elements. The dimensions of shell and solid elements in the areas of concern are less than 0.25 mm. For the hybrid element model, approximately 30,000 elements were used. For the solid element model, approximately 23,000 elements were used.

The comparisons of the lateral load-displacement hysteretic curves obtained by the test and the numerical analysis are shown in Fig. 8, in which the solid and dotted lines donate the hysteretic curves obtained by the test and the numerical analysis, respectively. The ULCF crack points are indicated in these figures. The load-displacement curves are identical in most cycles of load, while differences are observed in the last several cycles of the load. After the initiation, the crack propagated. Therefore, the hysteretic curves of specimens UB25-35 and UB35-35 obtained from the tests show a significant decrease. Because the strength deterioration caused by the ULCF crack is not considered in the numerical analysis, the difference can be observed between the hysteretic curves obtained by the test and the numerical analysis, especially in the last

load cycle. In addition, the cracks in the test and the numerical analysis initiated at the heat-affected zones. It can be concluded that the numerical results fit very well with the test results.

Table 2
Parameters and dimensions of test specimens

Specimen No.	B (mm)	D (mm)	t (mm)	h (mm)	R_R	λ
UB25-35C3P1	112	103	9.02	568	0.26	0.37
UB35-45C3P1	152	143	9.02	998	0.37	0.47

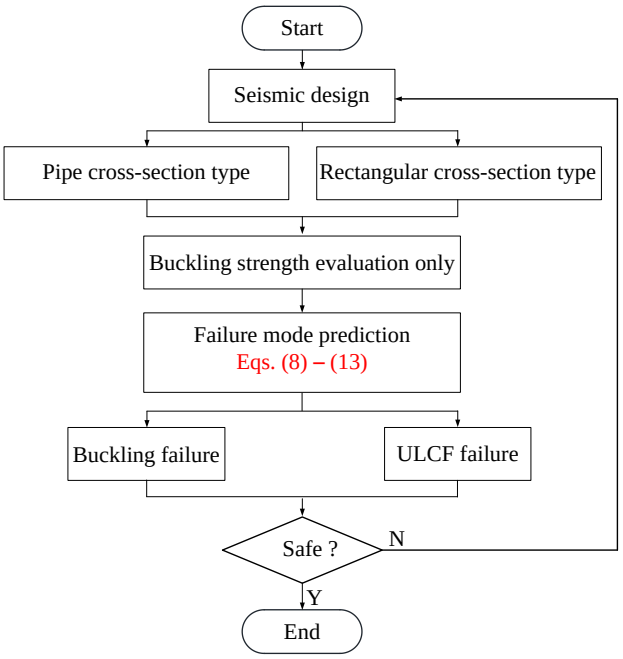

Fig. 7 Flowchart of the simplified seismic design procedure

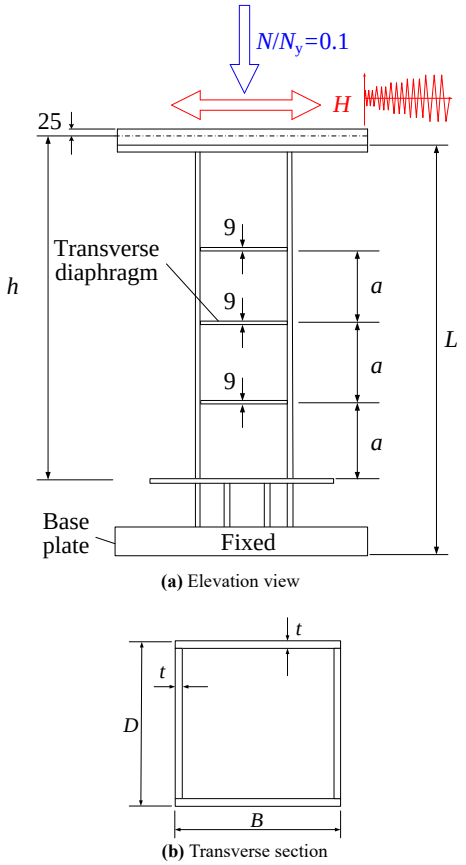

(a) Elevation view

(b) Transverse section

Fig. 8 Test specimen (Unit: mm)

Fig. 9 shows the evolution of the ULCF damage indices along with the load cycles obtained from the numerical analysis. Both the crack initiation point and the ultimate strength state point are indicated in the figure. Fig. 10 shows the envelope curves of the load-displacement hysteretic loops obtained from the numerical analysis, in which the peak value of the strength and the ULCF crack points are indicated. The results show that the ULCF damage index of the heat-affected zone grew faster than those of the base metal and the deposited metal; therefore, the crack initiated in this region. In addition to specimen UB25-35, the bottoms of specimens U35-35 and UB35-45 cracked before the ultimate strength state, which means they first experienced ULCF failure rather than buckling failure. For specimen UB25-35, the crack initiated when the strength of the member exceeded its peak value and decreased to 98% of the ultimate strength. At the crack initiation moment, apparent buckling of the steel plates was not observed for the piers, as shown in Fig. 11.

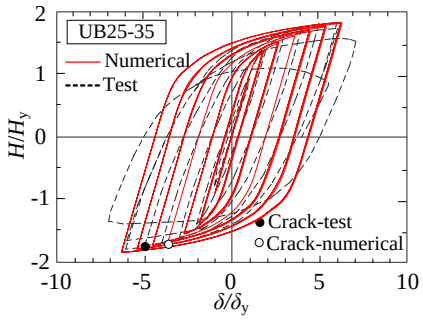

(a) UB25-35

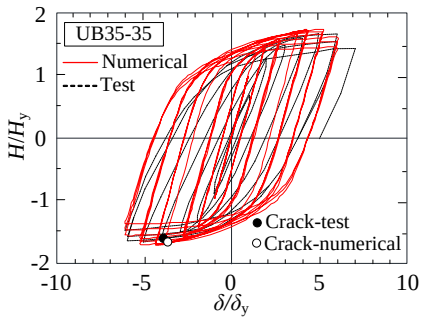

(b) UB35-35

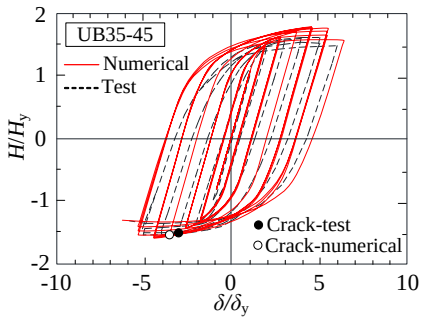

(c) UB35-45

Fig. 9 Comparison of the lateral load-displacement hysteretic curves

Table 3 compares the crack initiation points during loading. The differences between the numerical and experimental results are less than 2 cycles, and the errors between them are 8.1%~14.2%. This means that the ULCF damage index is effective in predicting ULCF crack initiation.

Table 3
Comparison of the crack initiation points

Specimen	Crack initiation		
	Test results	Numerical results (D_0=1.0)	Error
UB25-35C3P1	—26.0 half-cycles	—22.3 half-cycles	14.2%
UB35-35C3P1	—22.0 half-cycles	—20.2 half-cycles	8.1%
UB35-45C3P1	—18.0 half-cycles	—20.4 half-cycles	13.3%

To verify the applicability of the prediction formulas proposed in this study, the ULCF damage indices, which are obtained by the prediction formulas and the numerical analysis, at the ultimate strength state are compared as shown in Fig. 12. The prediction formulas, the numerical results and the test results all show that the most vulnerable region for the ULCF crack is the heat-affected zone near the base. The prediction formulas are reliable for predicting the ULCF damage index of thin-walled steel bridge piers.

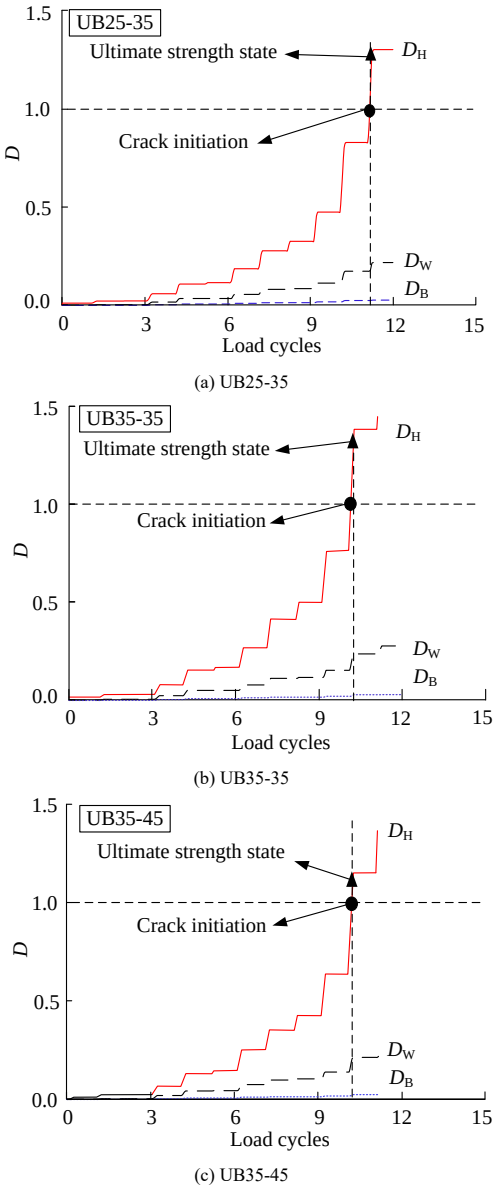

Fig. 10 Evolution of the ULCF damage indices during cyclic loading

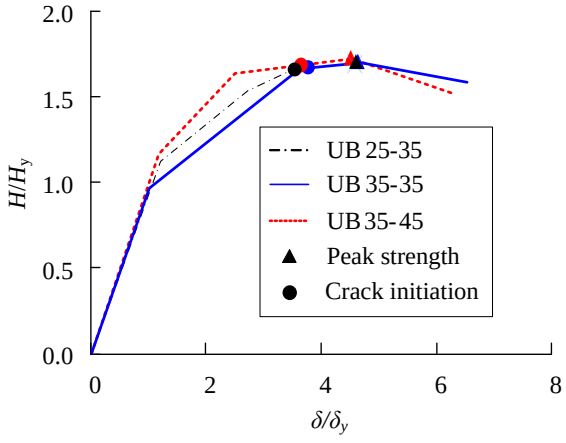

Fig. 11 ULCF failure points and the ultimate strength points of the piers

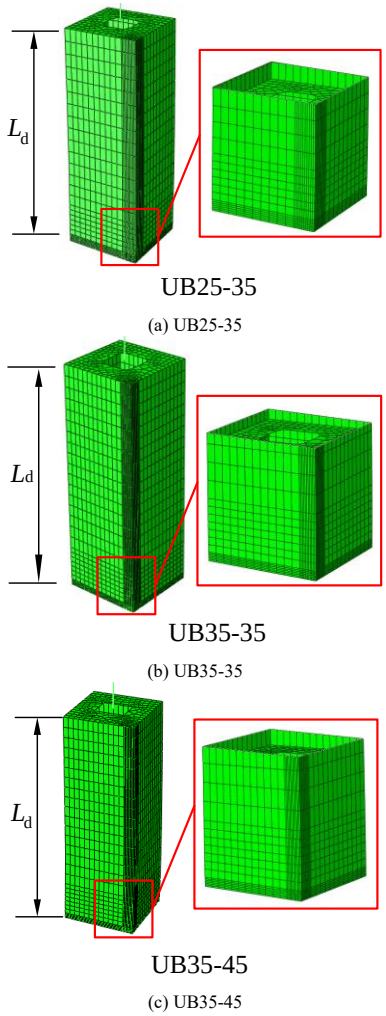

Fig. 12 Local deformation of the steel plate at the ULCF failure point

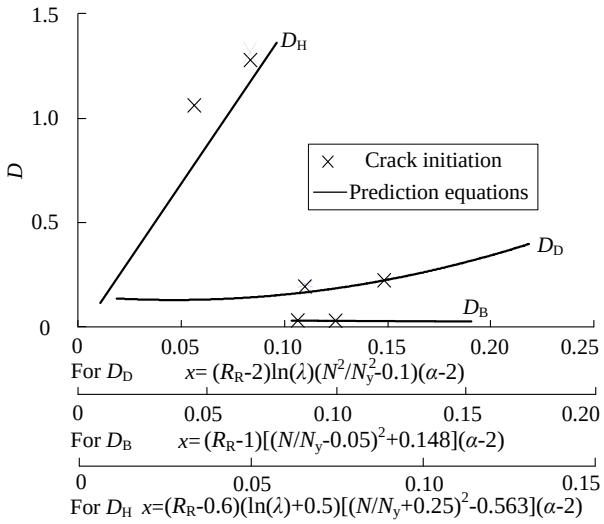

Fig. 13 Comparison between the calculated results and the numerical analysis

6. Conclusions

Parametric analysis of steel bridge piers with hollow boxes or pipe sections was carried out in this study. The influence of the design parameters on the ULCF damage evolution of steel piers was studied. Practical formulas to predict the ULCF damage index were proposed. Some main conclusions can be drawn as follows.

(1) The ULCF damage indices gradually increase as the horizontal resistance of the piers reaches the peak value and then decreases. The heat-affected zone is more vulnerable to ULCF failure than the base metal and the deposited metal.

(2) If one of the structural parameters of the axial compression ratio, the radius-to-thickness ratio and the width-to-thickness ratio is large enough (e.g., N/N_y>0.3, R_t>0.05, or R_R>0.5), the buckling failure mode will play a dominant role in steel bridge piers under cyclic loading.

(3) For piers with circular sections, if the radius-to-thickness ratio is rather small (e.g., R_t<0.03), the ULCF failure may occur at the heat-affected zone near the base when the horizontal strength on the envelope curve just exceeds its peak value. For piers with rectangular sections, when the width-to-thickness ratio of the flange plate, the slenderness ratio, and the diaphragm spacing ratio

are all small enough (e.g., R_R<0.3, λ<0.3 and α<0.8), ULCF failure will occur before the ultimate strength state.

(4) Practical formulas to predict the ULCF damage index of steel piers under cyclic loading are proposed in this study. The satisfactory accuracy of regression analysis can be achieved since the determination coefficients of the estimations are all above 0.8. Comparisons between the predicted results and the tests show that the proposed formulas are effective in predicting the ULCF crack of the steel piers.

References

[1] E. Watanabe, K. Sugiura, K. Nagata, Y. Kitane. Performances and damages to steel structures during the 1995 Hyogoken-Nanbu earthquake. Engineering Structures, 1998, 20(4):282-290.

[2] T. Usami. Interim guidelines and new technologies for seismic design of steel structures. Tokyo: Committee on New Technology for Steel Structures (CNTSS), JSCE, 1996.

[3] J. J. Liang, H. B. Ge. Ultra-low-cycle fatigue failure of metal structures under strong earthquakes. Singapore: Springer Nature Singapore Pte Ltd, 2019.

[4] Y. Zheng, T. Usami, H. B. Ge. Ductility of thin-walled steel box stub-columns Journal of Structural Engineering, 2000, 126(11): 1304-1311.

[5] T. Kono, H. B. Ge, T. Usami. Re-examination of the ultimate strain formula for steel box stub-columns and its application in steel arch bridges. Proceedings of the 6th Symposium on Ductility Design Method for Bridges, Ductility Design Subcommittee, Tokyo, 2003: 323-328.

[6] H. B. Ge, S. B. Gao, T. Usami. Stiffened steel box columns. Part 1: cyclic behavior. Earthquake Engineering and Structural. Dynamics, 2000, 29(11): 1691-1706.

[7] T. Usami, H. B. Ge, S. B. Gao. Stiffened steel box columns. Part 2: ductility evaluation. Earthquake Engineering and Structural. Dynamics. 2000, 29(11): 1707-1722.

[8] H. B. Ge, S. B. Gao, T. Usami. Numerical study on cyclic elasto-plastic behavior of steel bridge piers of pipe-sections without stiffeners. Japan Society of Civil Engineers, 1997, 577(41): 181-190. (In Japanese)

[9] Japanese Road Association. Specifications for highway bridges, Part V: Seismic design. Tokyo: Maruzen, 2012.

[10] AASHTO. Guide specifications for LRFD seismic bridge design. Washington DC: American Association of State Highway and Transportation Officials, 2nd edition, 2011.

[11] H. B. Ge, X. Q. Luo. A seismic performance evaluation method for steel structures against local buckling and extra-low cycle fatigue. Journal of Earthquake and Tsunami, 2011, 05(02):83-99.

[12] H. B. Ge, L. Kang. A damage index-based evaluation method for predicting the ductile crack initiation in steel structures. Journal of Earthquake Engineering, 2012, 16(5):623-643.

[13] L. Kang, H. B. Ge. Predicting ductile crack initiation of steel bridge structures due to extremely low-cycle fatigue using local and non-local models. Journal of Earthquake Engineering, 2013, 17(3):323-349.

[14] J. R. Rice, D. M. Tracey. On the ductile enlargement of voids in triaxial stress fields. Journal of the Mechanics and Physics of Solids, 1969, 17(3): 201-217.

[15] A. M. Kanvinde, G. G. Deierlein. Void growth model and stress modified critical strain model to predict ductile fracture in structural steels. Journal of Structural Engineering, ASCE, 2006, 132(12): 1907-1918.

[16] A. M. Kanvinde, G. G. Deierlein. Finite-element simulation of ductile fracture in reduced section pull-plates using micromechanics-based fracture models. Journal of Structural Engineering, ASCE, 2007, 133(5): 656-664.

[17] A. M. Kanvinde, G. G. Deierlein. Cyclic void growth model to assess ductile fracture initiation in structural steels due to ultra-low cycle fatigue. Journal of Engineering Mechanics, ASCE, 2007, 133(6), 701-712.

[18] A. M. Kanvinde, I. R. Gomez, M. Roberts. Strength and ductility of fillet welds with transverse root notch. Journal of Constructional Steel Research, 2009, 65(4): 948-958.

[19] F. F. Liao, W. Wang, Y. Chen. Parameter calibrations and application of micromechanical fracture models of structural steels. Structural Engineering and Mechanics, 2012, 42(2): 153-174.

[20] F. F. Liao, M. Q. Wang, L. S. Tu. Micromechanical fracture model parameter influencing factor study of structural steels and welding materials. Construction and Building Materials, 2019, 215: 898-917.

[21] Y. Yin, S. Li, Q. Han, P. Lei. Calibration and verification of cyclic void growth model for 20Mn5QT cast steel. Engineering Fracture Mechanics, 2019, 206, 310-329.

[22] S. L. Li, X. Xie, Y. H. Liao. Improvement of Cyclic Void Growth Model for Ultra-Low Cycle Fatigue Prediction of Steel Bridge Piers. Materials, 2019, 12(10): 153-174.

[23] H. Zhou, Y. Wang, L. Yang. Seismic low-cycle fatigue evaluation of welded beam-to-column connections in steel moment frames through global–local analysis. International Journal of Fatigue, 2014, 64(7): 97-113.

[24] H. Zhou, Y. Wang, Y. Shi. Extremely low cycle fatigue prediction of steel beam-to-column connection by using a micro-mechanics-based fracture model. International Journal of Fatigue, 2013, 48(2): 90-100.

[25] Y. Wang, H. Zhou, Y. Shi. Fracture behavior analyses of welded beam-to-column connections based on elastic and inelastic fracture mechanics. International Journal of Steel Structures, 2010, 10(3): 253-265.

[26] X. Xie, H. Q. Zhuge, Z. Z. Tang. Damage characteristics of thin-walled steel arch bridges subjected to in-plane earthquake action. Journal of Constructional Steel Research, 2018, 151:70-82.

[27] H. Kuwamura, K. Yamamoto. Ductile Crack as Trigger of Brittle Fracture in Steel. Journal of Structural Engineering, 1997, 123(6):729-735.

[28] W. F. Chen, L. Duan. Bridge engineering handbook, Second edition: Seismic design, CRC Press: 2014.

[29] Y. H. Liao. Research on ultra-low cycle fatigue properties and fracture mechanism of steel bridge welded joint. Master's Thesis, Zhejiang University, Hangzhou, China, 2018. (In Chinese).

[30] S. Yamada, Y. Jiao, H. Narihara. Plastic deformation capacity of steel beam-to-column connection under long-duration earthquake. International Journal of High-Rise Buildings, 2014, 3(3): 231-241.

[31] H. B. Ge, L. Kang, Y. Tsumura. Extremely Low-Cycle Fatigue Tests of Thick-Walled Steel Bridge Piers. Journal of Bridge Engineering, 2013, 18 (9): 858-870.

[32] H. B. Ge, L. Kang. Ductile crack initiation and propagation in steel bridge piers subjected to random cyclic loading. Engineering Structures, 2014, 59(2):809-820.

Acknowledgments

The work described in this paper was financially supported by the grants from the National Natural Science Foundation of China (No. 51708485), the Natural Science Foundation of Fujian Province (No. 2021J011062), the Jiangsu Planned Projects for Postdoctoral Research Funds (No. 1701191B) and the China Postdoctoral Science Foundation (No. 2017M611925), and their support is gratefully acknowledged by the authors.

Advanced Steel Construction – Vol. 17 No. 4 (2021) 412–424
DOI:10.18057/IJASC.2021.17.4.10

SIMPLIFIED MODELLING OF NOVEL NON-WELDED JOINTS FOR MODULAR STEEL BUILDINGS

Kashan Khan [1], Zhi-Hua Chen [1, 2, 3], Jia-Di Liu [1, *] and Jia-Bao Yan [1, 3]

[1] *Department of Civil Engineering, Tianjin University, Tianjin, China*
[2] *State Key Laboratory of Hydraulic Engineering Simulation and Safety, Tianjin, China*
[3] *Key Laboratory of Coast Civil Structure and safety, Ministry of Education, Tianjin University, Tianjin, China*
** (Corresponding author: E-mail: jdliu@tju.edu.cn)*

ABSTRACT

Prefabricated modular steel (PFMS) construction is a more efficient and safe method of constructing a high-quality building with less waste material and labour dependency than traditional steel construction. It is indeed critical to have a precise and valuable intermodular joining system that allows for efficient load transfer, safe handling, and optimal use of modular units' strength. Thus, the purpose of this study was to develop joints using tension bolts and solid tenons welded into the gusset plate (GP). These joints ensured rigid and secure connectivity in both horizontal and vertical directions for the modular units. Using the three-dimensional (3D) finite element (FE) analysis software ABAQUS, the study investigated the nonlinear lateral structural performance of the joint and two-storey modular steel building (MSB). The solid element FE models of joints were then simplified by introducing connectors and beam elements to enhance computational efficiency. Numerous parameters indicated that column tenons were important in determining the joint's structural performance. Moreover, with a standard deviation (SD) of 0.025, the developed connectors and beam element models accurately predicted the structural behaviour of the joints. As a result of their simplification, these joints demonstrated effective load distribution, seismic performance, and ductility while reducing computational time, effort, and complexity. The validity of the FE analysis was then determined by comparing the results to the thirteen joint bending tests performed in the reference.

ARTICLE HISTORY

Received: 14 November 2020
Revised: 10 May 2021
Accepted: 10 May 2021

KEYWORDS

Novel joints;
Modular steel building;
Finite element analysis;
Simplified model;
Parametric study

1. Introduction

The construction of prefabricated modular steel (PFMS) structures makes use of modular blocks that are manufactured in the factory as corner-supported or load-bearing modules, transported to the site, and then installed into an MSB [1,2]. Offsite construction decreases construction period, waste generation, onsite noise and dust while increasing productivity, quality, and onsite worker safety [3,4]. The PFMS construction has become more important for new urban development than traditional onsite construction [5,6]. The connection mechanism, construction, and design are unique to PFMS, while the lower energy consumption, deadweight, and increased bearing capacity distinguish PFMS from conventional construction [7–9]. Because of its development and performance, the use of MSB in a repeated type of building has attracted construction companies' attention [10,11]. Based on the load transmission path, the MSB is primarily divided into two types. The first is load-bearing, which uses C-section walls to transmit gravity loads. In the second type, gravity and lateral loads are transferred to the base via corner posts [12,13]. Proper connections between interconnected modular units and lateral stabilising members, such as concrete core and corrugated plates, are necessary to withstand lateral forces [14,15]. Due to the increased number of connections in MSB, the resistance to collapse is exceptional; this results in increased structural integrity and alterative load transfer routes; if members sustain accidental damage [14,16]. Several previous studies reported intermodular connection techniques and evaluated their performance under lateral loadings. For instance, one study proposed a vertical intermodular connection via onsite welding of columns, while a horizontal connection via onsite clip bolting [8]. Then, a seismic design for a multistorey braced frame was proposed using these welded joints. However, complete welding of the joint is impossible, resulting in the upper and lower modules rotating differently. Additionally, braced frames greatly reduce lateral sway, which overestimates joint performance and results in an unrealistic load transfer mechanism. The seismic response of blind bolted beam-column joints was investigated through experiments, accompanied by their simplistic theoretical analysis in MSB. The study, however, did not address the lack of space for screwing bolts into interior modular units [17]. The seismic performance of a joint composed of a hollow steel box and a pre-tensioned threaded rod was determined through eight cyclic loading tests [18]. However, the study was limited to corner module joints and did not look into the impact of parametric variations on interior modular joints. Furthermore, static and cyclic load tests were performed to determine the structural performance of an MSB's cross-shaped cover plate joint. However, aside from column weakening caused by access holes, the difficulty of screwing the cover plate in the interior module was not addressed [19]. Several studies adapted the FE method to investigate newly formed MSB joints in addition to the experimental studies mentioned above [20,21]. For example, the axial compression and lateral performance of the VectorBloc joints were evaluated [22,23]. However, the study's findings were limited to corner modules in an elastic regime. It was also unable to discuss elastoplastic mode and the influence of adjacent modules by looking into interior modules. The self-locking interaction system was created to withstand shear forces in MSBs, and the robustness of the system was confirmed through dynamic analysis [5]. However, the joining system was unable to withstand tensile or bending forces. The fully-bolted joints using long beam bolts and column bolts were developed for low-storey MSB [24]. Their seismic performance was investigated using FE analysis, followed by the simplification to conduct dynamic analysis on multistorey buildings [25,26]. Similarly, in addition to joint studies, researchers used finite element models to analyse the rigidity of individual and combined modular units with corrugated walls subjected to lateral loads and contribute to making design recommendations [27]. However, because the study focused on corrugated shear walls as the primary lateral stabilising members, the study prioritised their performance, and seismic behaviour of joints was avoided by simplifying them. It is evident that the majority of previous studies identified joints for cold-formed or C-sections or joints that required access holes in columns or beams to operate bolt screwing, resulting in a weakened cross-section or joints unable to connect interior modules. Similarly, most studies concentrated primarily on the lateral performance of corner frames and the development of simplified models for them, ignoring the actual performance of middle and interior joints, as well as the rotational stiffness of intermodular joints [28–30]. Furthermore, the majority of simplified models were capable of simulating joint elastic behaviour without accounting for elastic-plastic performance. Simultaneously, few studies have investigated the lateral performance of complex forms of modular frames or modular blocks; however, the influence of adjacent bare frames and intermodular joints was not considered. Thus, the current study intended to examine the behaviour of various types of joints, such as corner, middle, and interior joints, and to develop simplified models of these joints for use in future practical engineering applications. Following this, extensive parametric analysis was performed, as well as the application of the developed simplified models in modular units to determine their computational efficiency and accuracy in MSB.

As a result, a new type of joint for connecting hot-rolled structural hollow sections (SHS) with superior torsional resistance is being developed in this study. These joints can avoid compromising the bearing capacity of the structural members by creating access holes or using weaker structural

C-sections. At the same time, they can also maintain an aesthetically pleasing appearance by avoiding diagonal stiffening plates on columns and beams to prevent brittle weld failure between them. The lateral structural performance of these joints and their detailed simplifications with the connector and beam-element model has been researched using FE software ABAQUS. The developed simplified models can simulate the elastoplastic behaviour of corner, middle and interior joints in MSB. The accuracy of FE analysis results is validated by comparing them to similar experimental studies [31–33]. These analyses lead to a more profound indulgence of the joint's behaviour and their contribution to an MSB.

2. Detailing and force transfer mechanism of joint

Fig. 1(a) describes an MSB with various connection systems, while Fig. 1(b) depicts the assembly of SHS members with established joints (b). Modules are produced by welding columns and beams to the upper and lower parts of joints. In contrast, the middle part (tenons with welded GP) and tension bolts are used for the horizontal and vertical combination of adjacent modular units to form an MSB. The dimensions of the joint components are illustrated in Fig. 2(a). Because the depth of the floor beam is slightly more than the ceiling beam; therefore, the length of the middle tenon is more above than below the GP.

The vertical and lateral loads applied to an unbraced multistorey MSB with a clear storey height of h are depicted in Fig. 2(b). The intermodular space is preserved to facilitate module assembly and allow for the passage of MEP systems through the MSB during its life cycle. When vertical and lateral loads are applied, the deflected shape of the unbraced multistorey frame with its inflection point is highlighted. The lengths of the columns and beams are then determined in the MSB using these contra flexure points. The centreline distances of the subassembly are determined using the column's mid-height (h/2) and the beam's mid-length (L/2). Furthermore, these unbraced frames' displacements and sidesway directions are denoted as positive (+Δ) and negative displacement (-Δ). Since the moment distribution capacity of a vertical intermodular connection is dependent on their moment capacity (M_0) in these semi-structured unbraced frames, this capacity has to be deducted in this study. Whereas beam-column welded intramodular connections are fabricated using the fillet welding process, so they are considered rigid.

The upper column is assumed to be free to facilitate sidesway of the unbraced frame. The bottom column was pinned, allowing the base rotation while preventing its translational; however, the upper column's sidesway was maintained. Beams were supported by sliding roller boundary conditions, allowing for lateral displacements and in-plane rotation in the event of a sidesway.

The load transfer mechanism of the joint in its practical application in unbraced MSB against combined lateral loads, such as wind, earthquake, and gravity, is illustrated in Fig. 2(c). The detailed FE analysis determined that when the lateral load (V) and the vertical load (P) is applied at the middle top of the modular columns, the lateral displacement can be measured as a sidesway, such as Δ_c in columns and Δ_b in beams. At the same time, columns and beams bend against joint tenons, resulting in the columns and beams resisting shear stresses (i.e., V_c and V_b) while resisting bending moments (i.e., M_c and M_b). Additionally, joints resist bending moments in proportion to their moment capacity (M_0) in the upper and lower modules. The connection bolts are primarily subjected to slight tension forces, which result in a gap formed between the upper and lower components.

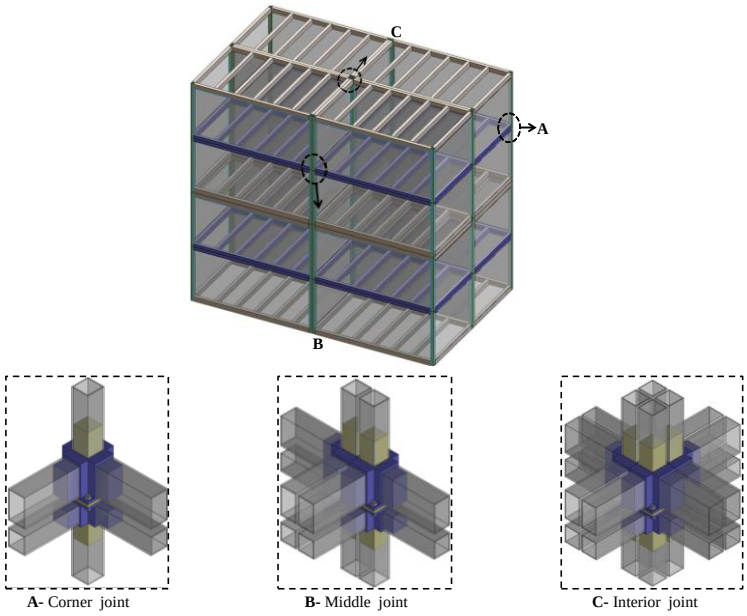

(a) Details of joints in MSB

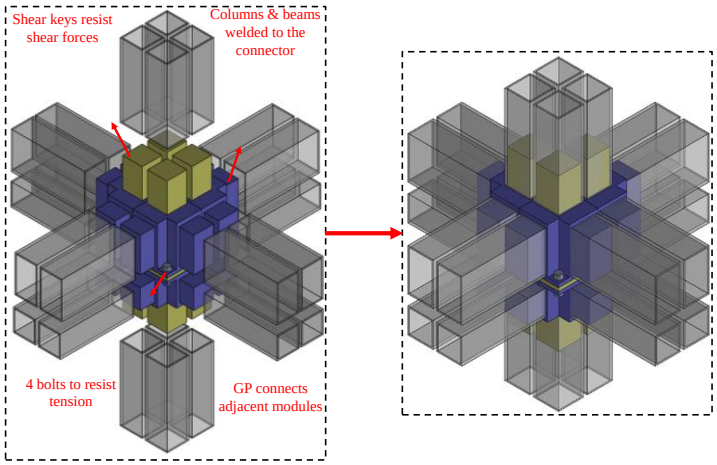

(b) Assembly of the newly developed joint

Fig. 1 A developed joint connecting mechanism in an MSB

3. Experimental studies on joints in MSB

Previously conducted research examined the seismic behaviour of corner and middle joints under static and cyclic loading conditions. The structural behaviour of the joints was compared when diagonal stiffeners were used versus when they were omitted. The joints were created by hollow plugins and screwing long beam bolts to support the upper and lower modules [31,32]. Additionally, the rotational stiffness of the rotary joint was examined [33]. The current study validated the FE analysis and conducted additional nonlinear finite element analyses on a joint developed in this study using the experimental findings from the studies mentioned above.

3.1. Test details

The joint design in the studies mentioned above was compatible with the main author's five-storey MSB project in Tianjin, China. The experiments' primary objective was to evaluate the joints' nonlinear structural performance, load-bearing capacity, seismic response, and rotational rigidity. All tests were conducted at Tianjin University's Structural Engineering laboratory. The static and quasi-static loadings, the effect of diagonal stiffening plates, the beam cross-section, and axial force ratios (AFR) were taken into account. Under static load, the ultimate capacities and failure mechanism of two corner and middle frames with and without stiffeners were investigated. Four additional specimens of the corner and middle frames were subjected to cyclic loading to assess joints' energy consumption and seismic behaviour. The four specimens that were not stiffened were considered standard, whereas the remaining eight specimens that were stiffened were considered parametric. The column end loading technique was adapted to apply the 100t force to the upper free column, with the floor beam (FB), ceiling beam (CB), and lower column supposed to act as the rotational hinge. The experiments used the Chinese standard (JGJ101-96) for cyclic loading [31,32]. Similarly, the rotary joint was used in another MSB project (Ziya Shanglinyuan) in Tianjin, China; thus, the mechanical properties of the joint were similar to those of the actual project. However, the study treated the rotary fitting as a regular bolt [33].

3.2. Material properties

Mild steel Q345B was used for columns, floor beams, ceiling beams, cover plates, diagonal stiffening plates, and beam bolts. On the other hand, joint components were made of cast steel, including ZG35, G20Mn5QT, and ZG310-570. The columns and beams were welded using groove welds, while the stiffeners were welded using fillet welding. Table 1 contains a list of material properties for structural components (i.e., symbols S/SC/QS denote joints with the plugin, while TS denotes rotary joint) that were evaluated compared to the materials used in actual MSB projects.

Table 1
Test specimens' material properties

Type of sp.	Structural Component	Thickness (mm)	Yield strength f_y(MPa)	Ultimate strength f_u(MPa)	Elongation in % age
S/SC/QS	Column, beam plate	8	425	575	30
-	Stiffeners	16	350	510	26
-	Cast plugin device	-	330	350	22.5
TS	Column	18	410	575	26
-	Corner fitting	16	355	515	32.5
-	Connecting plate	-	390	560	35
-	Rotating part	-	340	590	18

4. Numerical modelling technique

4.1. General

ABAQUS/CAE was used to develop FE models, while ABAQUS/Standard type solver was used for nonlinear analysis of detailed solid element and simplified beam element models [34]. The samples used to examine the lateral response of the joints developed in the study are listed in Table 4. The FE models included columns, beams, tension bolts, and joint components.

4.2. Materials model of steel

A nonlinear isotropic/kinematic hardening model is used for all structural members. The model is an elastic-plastic isotropic model that uses the von Mises yielding criteria to define isotropic yielding. For the columns, beam members, and mid-part of the joint, the FE simulation uses Q345B mild steel material properties obtained from the previously mentioned test studies. The upper and lower joint parts, on the other hand, are made of ZG35 cast steel. Tensile stress-strain behavioural patterns of structural steel use a three-linear stress-strain behaviour that takes strain hardening into account, as shown in Fig. 2(c). [35]. Elastic material properties such as Poison's ratio "ν" and modulus of elasticity "E_s", whereas plastic material properties such as yield strength "f_y", ultimate strength "f_u", and strain values "ε" for SHS members and joints are listed in Table 1. Engineering stress and strain are described in Table 1, whereas true stress and strain are inputted in ABAQUS. Consequently, Eqns. (1) and (2) are introduced to convert engineering stress and strain to true stress and strain.

$$\sigma_T = \sigma_E(1 + \varepsilon_E) \tag{1}$$

$$\varepsilon_T = \ln(1 + \varepsilon_E) - \frac{\sigma_T}{E_s} \tag{2}$$

where, σ_T and σ_E denote true and engineering stress, while ε_T and ε_E indicate true and engineering strain.

4.3. Formation of the FE model

To resolve convergence issues, reduce contact surfaces, and improve computational efficiency, numerous simplifications are made to the FE modelling, including circular modelling of bolt heads and nuts, ignoring threads on bolts and nuts, and overlooking spaces between bolts and bolt holes. The welded cover plates, stiffening plates, and beam-column frame skeleton is modelled as a single part for validation purposes, resulting in improved accuracy and fewer complications.

4.3.1. Mesh technique

High-order contact analysis on three-dimensional deformable solid parts such as SHS members and joint components was performed using hexagonally structured mesh controls with an eight-node linear brick, reduced integration, and Hourglass Control Element Type (C3D8R). Corners and areas with geometrical changes, joint regions, bolts, bolt holes, and other high-stress areas and components were finely meshed. The most reliable validation of FE with test results was achieved using four different mesh densities: very fine, fine, coarse, and very coarse. Then the most precise mesh density was used. To simplify FE models, columns and beams had been substituted with three-dimensional beam elements with cross-sections similar to those of detailed solid elements. The beam element sections were meshed using a two-node linear beam element (B31) and the same mesh size as the detailed models.

4.3.2. Contacts and interactions properties

The contact between the column and the tenon, the beam and the tenon, and the joints and bolts were simulated as surface-to-surface contact (standard), with "hard contact" as the normal behaviour and "finite sliding" as the tangential behaviour through the use of the "penalty friction formulation." The hard contact formulation allows two contacting surfaces to share pressure while they are in contact, but no pressure transfer occurs after the contact surfaces are separated. Alternatively, the penalty friction formulation uses a friction coefficient to account for the relative motion of the contact surfaces and calculate the frictional force. After validating the FE results with experimental data, an accurate friction coefficient was chosen. The interaction between columns, beams, and neighbouring joint faces was modelled as hard contact in middle and interior frame samples to maintain consistent force transfer between neighbouring modules. Because columns and beams were welded to their respective joint components, the "Tie constraint" was used to model the interactions between a column and joint and a beam and joint. A tie constraint is a connection between the two distinct surfaces that prevents them from moving relative to one another. The fusion of two regions is achievable with this constraint, even if the meshes created on their surfaces are different.

4.3.3. Boundary conditions and loading mechanism

The study used the test arrangement outlined in the previous studies and the sway frame criteria described in Fig. 2(b) to analyse the nonlinear lateral performance of joints. Therefore, the movement of the lower column at the bottom was restricted in all directions. In contrast, the upper column only restrained out-of-plane movement, and beams were restricted in the vertical and

out-of-plane directions. Besides, the out-of-plane rotation of beams was restricted, allowing them to exhibit only in-plane rotation. The upper column was subjected to lateral displacement-controlled loading as a predicted sidesway and vertical axial loading as a percentage of the column's designed bearing capacity, as calculated from Eqn. (1) to observe the elastoplastic behaviour and simulate the actual force transmission of members in unbraced MSB [36]. Additionally, floor beams were subjected to a factored dead load as the structure's self-weight and a live load calculated according to ASCE 7-10 to investigate the nonlinear lateral bearing capacity of a multistorey modular block with developed joint [14,37]. Furthermore, the modular block's base was assumed to be fixed, while displacement-controlled loading was applied to the middle of the ceiling beam along the modular block's longer direction [38]. During the validation of FE simulation, the following Eqn. (4) was used to predict the pretension force of beam bolts.

$$N = (AFR) f_{yc} A_s \tag{3}$$

$$P = \frac{(0.9)^3}{1.2} A_e f_{tv} \tag{4}$$

where, N denotes the axial load, AFR denotes the axial force ratio, A_s denotes the area of the column, P denotes the bolt's pretension force, A_e denotes the bolt's effective area, and f_{tv} denotes the bolt's tensile strength, which is taken as180 MPa.

4.3.4. Failure criteria in FE modelling

The ABAQUS library included stress criteria and total equivalent plastic strain (PEEQ) criteria for analysing the yielding or fracture condition of ductile material and the distribution of plastic or permanent strain [39]. The equivalent stress and plastic strain were specified as follows:

$$\sigma_{EQ} = \sqrt{\frac{(\sigma_1-\sigma_2)^2+(\sigma_2-\sigma_3)^2+(\sigma_3-\sigma_1)^2}{2}} \tag{5}$$

$$\text{PEEQ} = \int_0^t \sqrt{\frac{2}{3}\dot{\varepsilon}_{ij}^p \dot{\varepsilon}_{ij}^p}\, dt \tag{6}$$

where, σ_{EQ} stands for von Mises stress or equivalent stress; σ_1, σ_2 and σ_3 stand for principal stresses; PEEQ stands for permanent strain, and $\dot{\varepsilon}_{ij}^p$ stands for rate of plastic strain.

4.3.5. A convergence of FE simulation

The experimental results were used to determine the exact solution for FE analysis convergence to obtain the value with the smallest error tolerance. The convergence study took into account strain hardening, bolt friction, mesh sizes, and friction coefficients. As shown in Table 2, specimen S1 was chosen for strain hardening, QS4 for bolt friction, and SC1 for four different mesh sizes and friction coefficients.

The load-carrying capacities of FE models with varying convergence criteria were compared in Fig. 3. Fig. 3(a) illustrates the initial stiffness, yielding, and load-carrying path for models with and without strain hardening. The figure illustrates that strain hardening increased the model's bearing capacity. However, the increase in ultimate bearing capacity observed was only 1%. Similarly, using the same loading criteria, two models were used to analyse the bolt friction. As shown in Fig. 3, a pretty small change in load-carrying capacity of 0.006% was observed when bolt friction was included in the FE model. Additionally, four models with very fine, fine, coarse, and very coarse mesh densities were analysed against lateral loading using sizes of 25, 30, 40, and 50 mm. It was found that as the mesh expanded from very fine to coarse, the ultimate strength increased too. Nevertheless, the very coarse mesh demonstrated a slight reduction in capacity compared to the coarse mesh model, as illustrated in Fig. 3(c). However, no recognisable discrepancy in capacity was observed between coarse and very coarse mesh density models. In contrast, a model with a very fine mesh was incapable of sustaining a load greater than 73 mm, resulting in non-convergence. A fourth convergence study was conducted on friction coefficients. Finite element models with four different values, 0.3, 0.4, 0.5, and 0.6, were analysed, and Fig. 3(d) demonstrated that models with a higher friction coefficient had a greater bearing capacity. Moreover, the capacity increase between modelling techniques with friction coefficients of 0.3 and 0.6 was only 1.5%.

Based on a detailed analysis of the different convergence criteria and the test results, strain hardening was taken into account, but bolts were modelled as frictionless. The structural components have meshed with a 30 mm size, the joint region with a 10 mm size, and the hole area with an 8 mm size. Moreover, the friction coefficient was set to be 0.3.

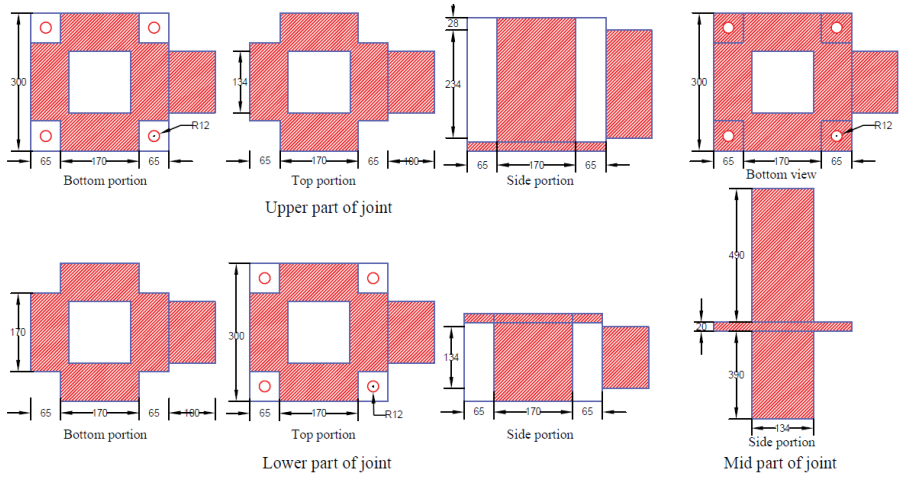

(a) Dimensions of the developed joint (unit: mm)

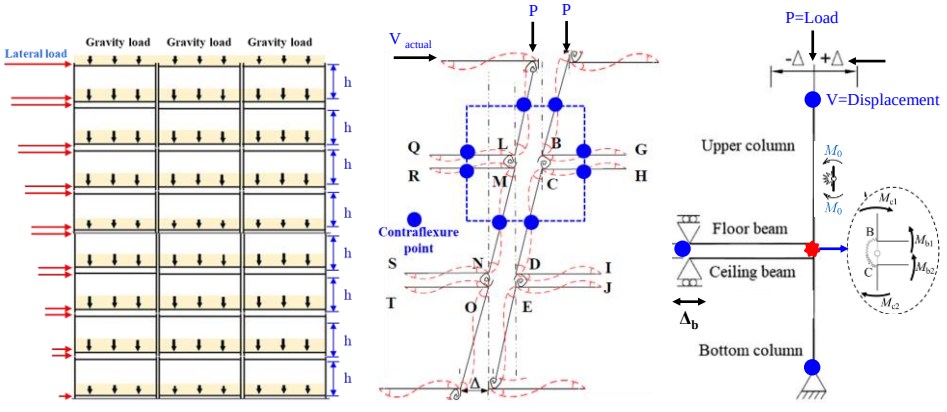

(b) Forces transfer mechanism & frame classification in MSB

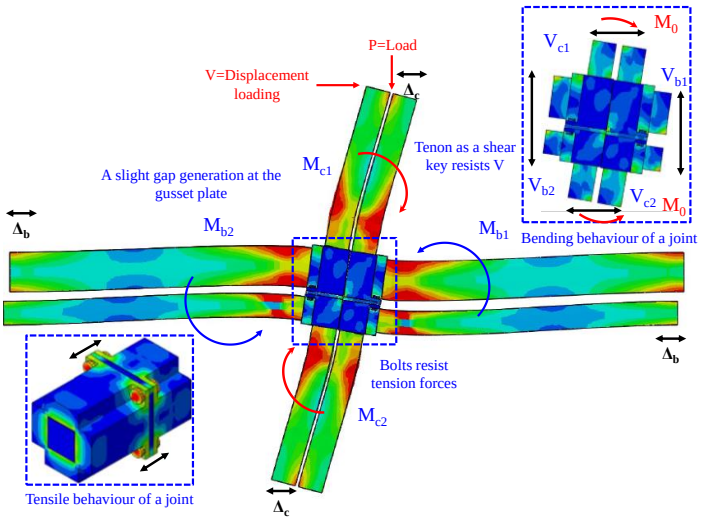

(C) Forces transfer mechanism of the developed joint unbraced MSB (deflection scaled 5times)

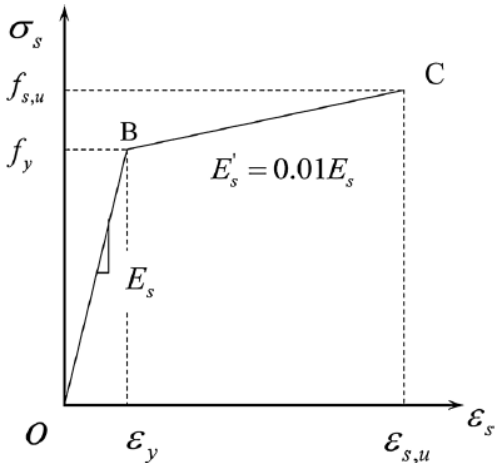

(d) The true bi-linear elastic-plastic material model used in FE analysis [35]

Fig. 2 Forces transfer & material model details for joints in a FE study

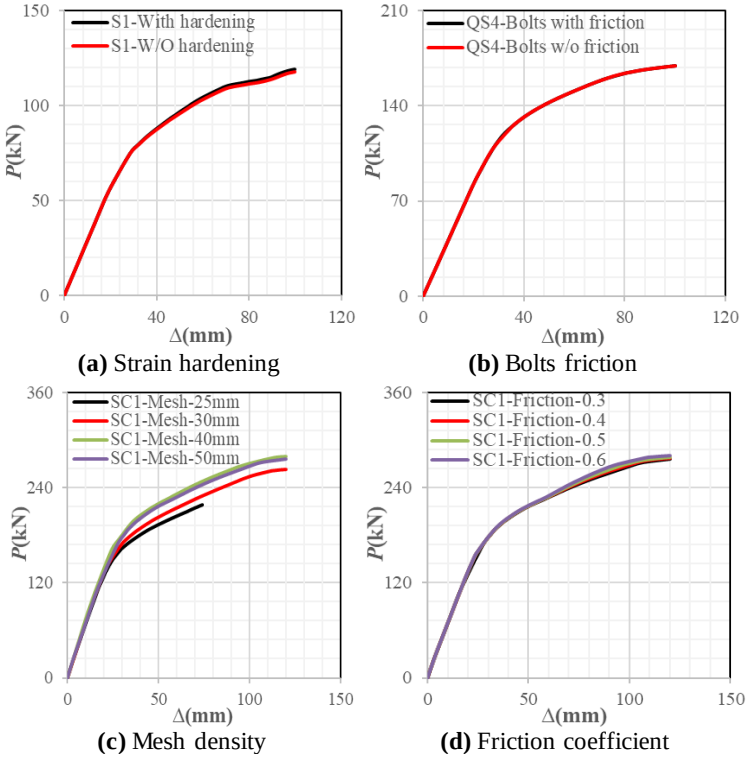

(a) Strain hardening **(b)** Bolts friction

(c) Mesh density **(d)** Friction coefficient

Fig. 3. Comparison of load-displacement curves obtained from convergence studies

Table 2
Detailing of test specimens

Sp. No	Type of joint	CB (mm)	FB (mm)	Column (mm)	Stiffener size (mm)	Bolt (mm)	AFR	Load application
S1	Exterior	150x150x8	150x250x8	150x150x8	None	24	0.2	Static
SC1	Interior	150x150x8	150x250x8	150x150x8	None	24	0.2	Static
S2	Exterior	150x150x8	150x250x8	150x150x8	10	24	0.2	Static
SC2	Interior	150x150x8	150x250x8	150x150x8	10	24	0.2	Static
QS1	Exterior	150x150x8	150x250x8	150x150x8	None	24	0.2	Cyclic
QSC1	Interior	150x150x8	150x250x8	150x150x8	None	24	0.2	Cyclic
QS2	Exterior	150x150x8	150x150x8	150x150x8	10	24	0.2	Cyclic
QSC2	Interior	150x150x8	150x150x8	150x150x8	10	24	0.2	Cyclic
QS3	Exterior	150x150x8	150x250x8	150x150x8	10	24	0.2	Cyclic
QSC3	Interior	150x150x8	150x250x8	150x150x8	10	24	0.2	Cyclic
QS4	Exterior	150x150x8	150x250x8	150x150x8	10	24	0.1	Cyclic
QSC4	Interior	150x150x8	150x250x8	150x150x8	10	24	0.1	Cyclic
TS	Corner	-	-	200x200x18	-	-	-	Bending

4.4. Validations of FE simulation

The results of FE static analysis were compared to the *P-Δ* relationships and failure events of test specimens (such as S/SC/QS/QSC) of plugin joints against static (four models) and cyclic (eight models) loadings. As shown in Table 3, the lateral load resistance of a rotary corner joint specimen (TS) was also validated.

4.4.1. Validations of bending test results with FE analysis

Finite element analysis results were compared to the lateral *P-Δ* curves of twelve test specimens of plugin joint and moment-rotation curves of a rotary joint, as shown in Fig. 4. The results of cyclic loading tests on plugin joint envelope curves were compared to the results of static FE analysis. It was discovered that FE models accurately simulated test specimens' ultimate capacity, stiffness, and ductility. There have been some discrepancy and inconsistency on a minor scale in stiffness or strengths between test and FE. This could be because of differences in material models, sectional imperfections during production, soft supports, or simplifications to the FE model.

Experiment failure modes were compared to von Mises stress distributions in FE models, as illustrated in Fig. 5. Gap development and enlargement, slicing of column or beam welds, stiffener breakdown, local column buckling, and beam tearing were the primary failure events in plugin joint test specimens. The stress localisations observed in FE models, including corner and middle joints, exhibited outward and inward buckling, high stress welded areas and gap generation that was entirely consistent with test results. Similarly, the test results were accompanied by accurate simulations of gap generation of 25 mm between corner fittings and their outward buckling, such as the gap generation of 27 mm demonstrated by FE models for rotary joints.

The comparison of the capacities of the tests specimens and FE models are shown in Table 3. It demonstrates that the average test-to-FE ratio (mean) and coefficient of variation (Cov) are 1.02 and 0.12, respectively. Table 1 summarises the ultimate compressive strengths predicted by the Test-to-FE prediction ratios, indicating that when the ratios exceed 1.0, the FE was marginally underestimated, implying that structural behaviour predictions are secure. Conversely, ratios less than 1.0 indicate that actual behaviour is overestimated, implying that structural behaviour estimations are unsafe. Hence, these comparisons of *P-Δ* curves and predicted P_u values demonstrate that FE analysis can accurately simulate lateral structural performance for newly developed joints and modular blocks when both axial compression and lateral loading are applied. As a result of the FE simulation's accuracy and efficiency, it is recommended to conduct additional parametric studies on joints and a modular block.

Table 3
Comparison of test specimens and FE models' ultimate capacities

Sp. No	Type of joint	Load application	Ultimate load (Test)/P_{Test}(kN)	Ultimate load (FE)/P_{FE}(kN)	P_{Test}/P_{FE}
S1	Corner	Static	112.0	118	0.95
SC1	Middle	Static	248.0	262	0.95
S2	Corner	Static	183.0	162	1.13
SC2	Middle	Static	396.0	392	1.01
QS1	Corner	Cyclic +ve	81.0	79	1.02
		Cyclic -ve	-102.0	-118	0.86
QSC1	Middle	Cyclic +ve	205.0	261	0.79
		Cyclic -ve	231.0	263	1.13
QS2	Corner	Cyclic +ve	118.0	121	0.97
		Cyclic -ve	-137.0	-127	1.07
QSC2	Middle	Cyclic +ve	255.0	261	0.98
		Cyclic -ve	-305.0	-260	1.17
QS3	Corner	Cyclic +ve	161.0	122	1.32
		Cyclic -ve	-183.0	-162	1.13
QSC3	Middle	Cyclic +ve	329.0	391	0.84
		Cyclic -ve	-364.0	-389	0.94
QS4	Corner	Cyclic +ve	141.0	129	1.09
		Cyclic -ve	-168.0	-169	0.99
QSC4	Middle	Cyclic +ve	377.0	387	0.97
		Cyclic -ve	-411.0	-388	1.05
TS	Corner	Bending	33.74.0	33.80	0.99
Mean					1.02
Cov					0.12

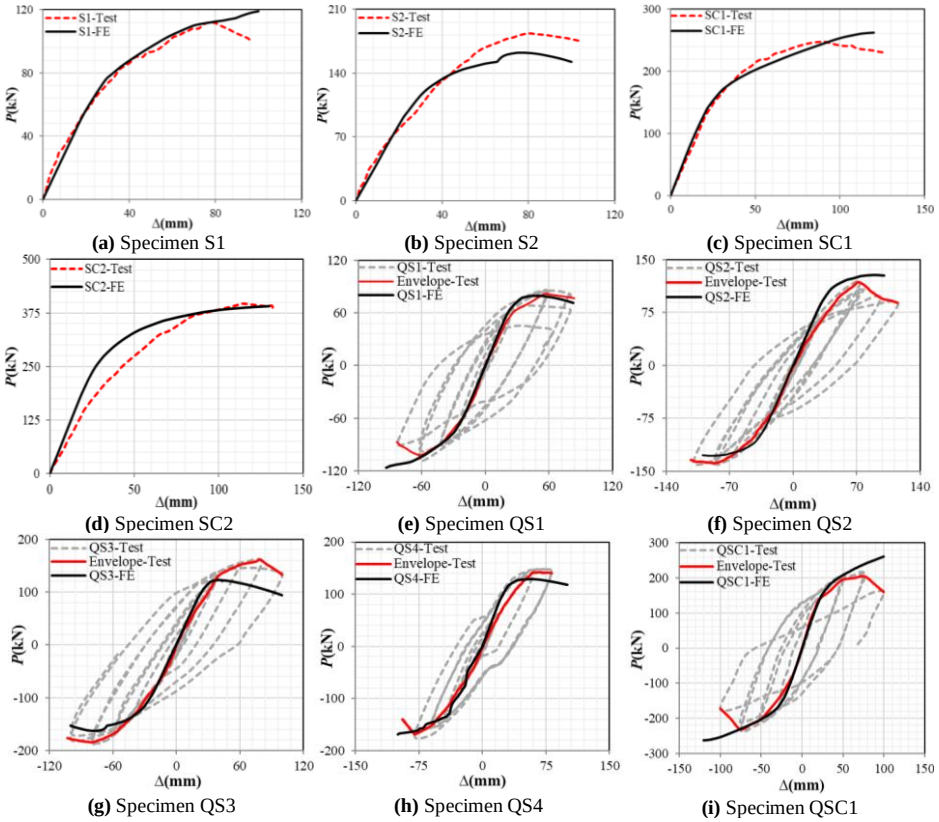

(a) Specimen S1 **(b)** Specimen S2 **(c)** Specimen SC1

(d) Specimen SC2 **(e)** Specimen QS1 **(f)** Specimen QS2

(g) Specimen QS3 **(h)** Specimen QS4 **(i)** Specimen QSC1

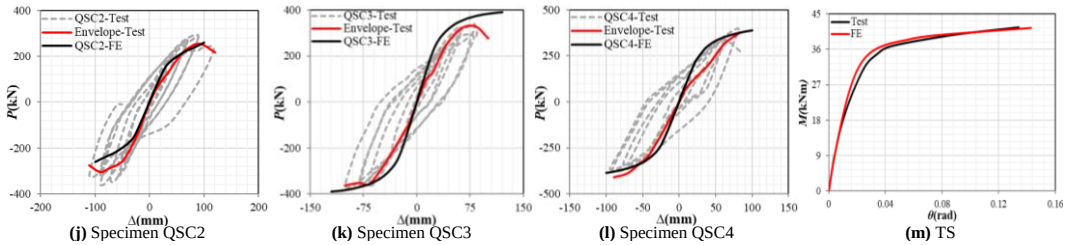

(j) Specimen QSC2 **(k)** Specimen QSC3 **(l)** Specimen QSC4 **(m)** TS

Fig. 4 Validation curves of FE models and test specimens

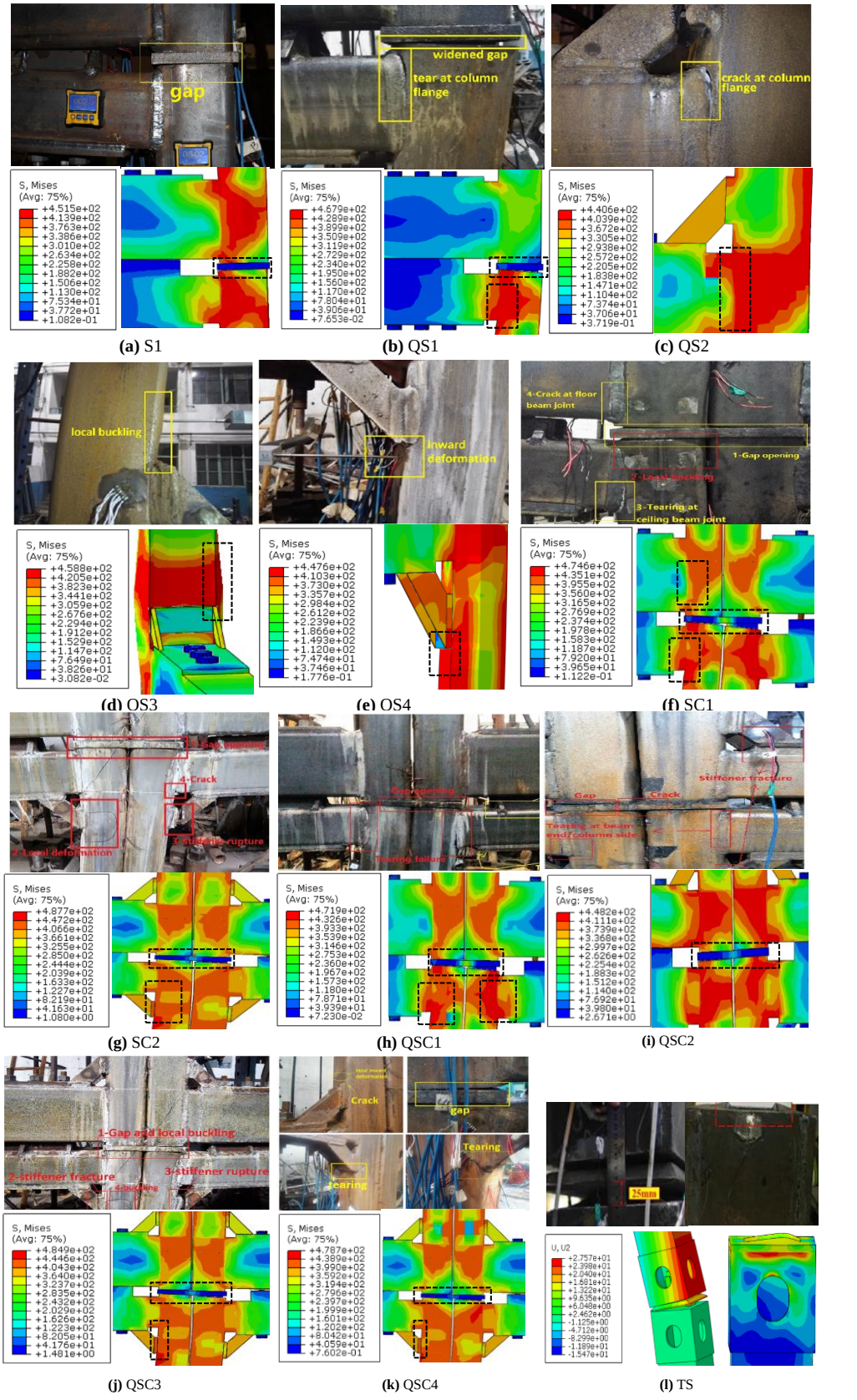

(a) S1 **(b)** QS1 **(c)** QS2

(d) QS3 **(e)** QS4 **(f)** SC1

(g) SC2 **(h)** QSC1 **(i)** QSC2

(j) QSC3 **(k)** QSC4 **(l)** TS

Fig. 5 Validation of failure modes of FE models and test specimens

Table 4
Details of FE models for lateral behaviour of the developed joint

Sp. No	CB (mm)	FB (mm)	Column (mm)	Bolts (mm)	AFR (%)	Loading method
S1	150x150x8x1900	150x250x8x1900	150x150x8x1000	24	0.2	Static
S2	150x150x8x1900	150x250x8x1900	150x150x8x1000	24	0.1	Static
S3	150x150x8x2900	150x250x8x2900	150x150x8x1000	24	0.2	Static
S4	150x150x8x1000	150x250x8x1000	150x150x8x1000	24	0.2	Static
S5	150x250x8x1900	150x250x8x1900	150x150x8x1000	24	0.2	Static
S6	150x150x8x1900	150x150x8x1900	150x150x8x1000	24	0.2	Static
Block-S	150x150x8x1000	150x250x8x1000	150x150x8x1000	24	-	Static
Block-L	150x150x8x3000	150x250x8x3000	150x150x8x1000	-	-	-

5. FE studies on the joints in MSB

5.1. Geometry and detailing

The joint assembly and dimensions of each component used in performance evaluation are depicted in Figs. 1(b) and 2(a). The structural performance of MSB with the established joint is evaluated using a small-scale two-storey modular block scaled to the recommended size. The specimens and structural components are described in detail in Table 4.

5.2. Bending behaviour of the joints

5.2.1. Corner joint

Six FE models of the corner joint supporting an upper and lower modular unit were analysed with varying AFR, beam lengths, and beam cross-sections. Fig. 6 shows that S6 exhibited the lowest bending moment capacity and initial stiffness, whereas S2 showed the largest bending capacity, and S4 exhibited the highest initial stiffness. It was found that an increase in the cross-sections of the beams increases bending capacity and vice versa, whereas the decrease in beam lengths increases the stiffness of the joint. Comparing the permanent plastic strain of models in Fig. 7(a) declares that all other models showed permanent allocation of strain in the upper column except specimen S6 (demonstrated strong column-weak beams). All models demonstrated different plastic strain distribution in FB, but S6 showed the failure of both beams, whereas S5 lacked beams yielding due to stiffer and stronger beams.

5.2.2. Middle joint

For studying the detailed bending performance of the middle joint, six models were analysed supporting four modules, such as two uppers and two lowers. Axial compression and lateral displacement loads were applied to the centre of the upper columns. In comparing the moment-rotation curves of models, the middle joint models behaved similarly to that of the corner joint, both in bending moment capability and initial stiffness, as shown in Fig. 6. The capacity and stiffness were increased by increasing the cross-section (model S5) and reducing the lengths of beams (model S4), which can be considered an upper bound. Meanwhile, reducing the cross-section (model S6) and lengthening of beams (model S3) reduced capacity and stiffness and can be regarded as a lower bound. Whether failure occurred in beams or columns, the effective distribution of stresses to adjacent members on the opposite side was evident, implying that the joint between adjacent modules performed effectively.

5.2.3. Interior joint

The bending capacity of six interior joint models supporting eight modular units was analysed. The upper four columns' centre was subjected to axial and lateral loads. The interior joint specimens all exhibited the same patterns of bending capacities and stiffness as the corner and middle joints. However, the capacities and stiffnesses of models S1 and S2 were slightly different from those of other models. Model S2 demonstrated a greater bending capacity than S1 but a lower stiffness than S1. The relationship between stiffness and capacity was more pronounced in interior joints than in corner and middle joints. Models S4 and S5 demonstrated the highest bending capacities and stiffnesses, while S3 and S6 demonstrated the lowest. As illustrated in Fig. 7, model S3 encountered stresses in the beams, preventing the load-taking operation from continuing. Except for S4 and S5 (which demonstrated high capacity and rigidity), all specimens indicated beam failure; however, equivalent stress propagation was observed in other structural components.

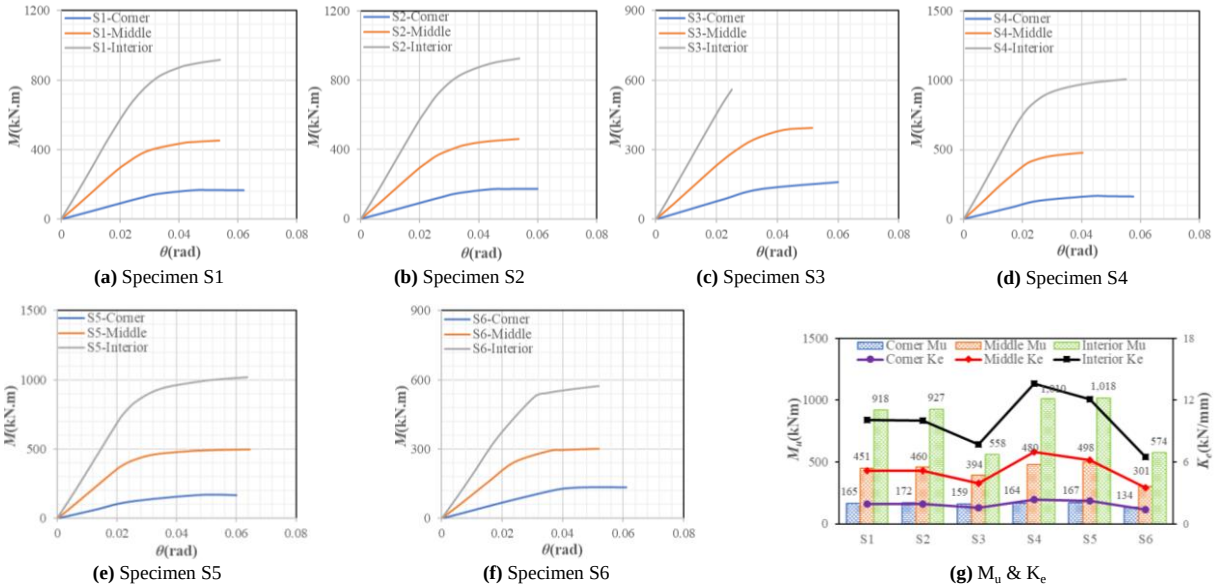

(a) Specimen S1 **(b)** Specimen S2 **(c)** Specimen S3 **(d)** Specimen S4

(e) Specimen S5 **(f)** Specimen S6 **(g)** M_u & K_e

Fig. 6 Moment versus rotation curves and scatters of FE models of joints

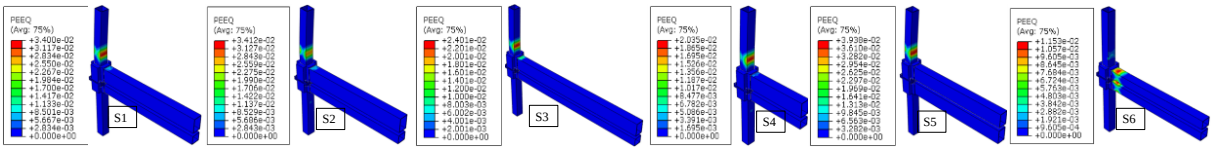

(a) Corner joint

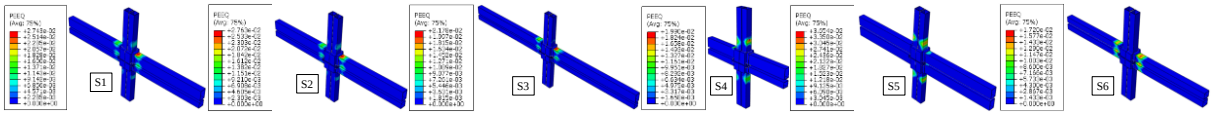

(b) Middle joint

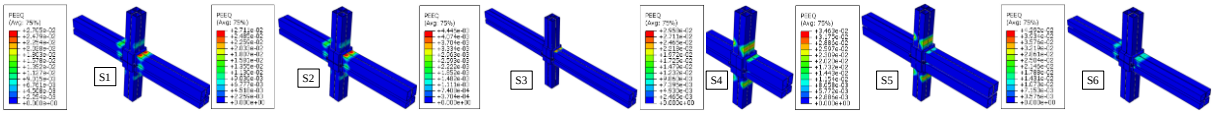

(c) Interior joint

Fig. 7 Plastic strain distribution of joints against lateral loads

5.3. Seismic performance of joints

The seismic performance of each joint model was evaluated using the special moment frame (SMF) parameters, which were found to be consistent with the 0.04 rad rotational deformation capacity with a strength of $0.8M_P$ [28,40]. All corner joint models met the drift angle accumulation criteria of 0.04 rad and the required bending moment capacity (except S3 with a 0.92 ratio). While model S3 met the specified requirements for rotation angle accumulation of at least 0.04 rad, the corresponding value of the bending capacity ratio did not meet the SMF criteria. Similarly, models S6 (1.25, 1.88), S2 (1.75, 1.19), and S5 (1.25, 1.18) demonstrated a greater tendency to resist seismic loads. Thus, beam lengths significantly affected the joint seismic performance compared to the other five specimens that were substantially safer. As shown in Table 5, all middle joint specimens met the criteria for the ultimate angle of rotation greater than 0.04 rad and the moment ratio greater than 1.30. Additionally, all interior joint models met the seismic performance criteria for SMF by having a minimum ultimate rotation angle (θ_u) of 0.05 rad and M_O (obtained moment) and $0.8M_P$ ratios greater than 1.0.

Model S6 demonstrated superior seismic performance for all joints with a maximum moments ratio of 2.0 and beams with no permanent strain distribution to columns (i.e., strong column-weak beam criteria).

Table 5
Seismic performance of joints by SMF criteria

Sp. No	Type of joint	θ_u (rad)	$\theta_{0.04}$ (rad)	M_O (kNm)	$0.8M_P$ (kNm)	$\theta_u/\theta_{0.04}$	$M_O/0.8M_P$
S1	Corner	0.05	0.04	164	142	1.25	1.15
S2	Corner	0.07	0.04	169	142	1.75	1.19
S3	Corner	0.06	0.04	130	142	1.50	0.92
S4	Corner	0.05	0.04	163	142	1.25	1.15
S5	Corner	0.05	0.04	167	142	1.25	1.18
S6	Corner	0.05	0.04	130	69	1.25	1.88
S1	Middle	0.05	0.04	438	284	1.25	1.54
S2	Middle	0.05	0.04	450	284	1.25	1.58
S3	Middle	0.05	0.04	385	284	1.25	1.36
S4	Middle	0.04	0.04	480	284	1.00	1.69
S5	Middle	0.06	0.04	485	284	1.50	1.71
S6	Middle	0.05	0.04	299	139	1.25	2.15
S1	Interior	0.05	0.04	877	568	1.25	1.54
S2	Interior	0.05	0.04	896	568	1.25	1.58
S4	Interior	0.05	0.04	825	568	1.25	1.45
S5	Interior	0.06	0.04	992	568	1.50	1.75
S6	Interior	0.05	0.04	556	278	1.25	2.00
Mean						1.30	1.52

5.4. Bending behaviour of MSB

5.4.1. Two-storey small-scale modular block

The displacement-controlled loading was applied to the top ceiling beam of the two-storey small-scale modular block fixed at the base to analyse the lateral bending efficiency of the joint. Tenons at the top and the bottom of the modular block were not passed through the lower and upper connection components. The modular block demonstrated a high bearing capacity, decent force transmission behaviour and initial stiffness of over 17 kN/mm, as illustrated in Fig.9(g). As illustrated in Fig. 10(d), the developed joint exhibits a superior force distribution tendency between the structural components of the same modular unit and the adjacent modular units. All the columns on the bottom and beams on the two welded ends showed maximum stress concentration with a load restriction. On the other hand, the bottom-storey beams exhibited no stress concentration due to their fixed boundary conditions in both longitudinal and transverse directions. It was noted that ceiling beams along the longer directions of a modular block posed the most significant risk of failure.

5.5. Parametric study on the bending behaviour of joint

5.5.1. Length of column tenon

Five corner joint models with column tenon lengths of 0, 100, 200, 300, and 400 mm were chosen to investigate the effect of column tenon on the joint's bending behaviour. As illustrated in Figs. 8(a) and (f), increasing the length of the column tenon increased both bending capacities and stiffnesses. Although capacity and stiffness were raised, the rise was decreased by 25, 16, 11, and 10%, and 38, 21, 12, and 9%. With a strong column-weak beam pattern, increasing the length of the column tenon increased the moment capacity and stiffness. Additionally, models with tenon lengths of 0 and 100 mm demonstrated unsatisfactory seismic performance, whereas models with tenon

lengths of 200, 300, and 400 mm demonstrated satisfactory seismic performance.

5.5.2. Length of beam tenon

Four corner joint models with beam tenon lengths of 0, 100, 200, and 300 mm revealed a slight increase (<5%) in bending capacity and stiffness as beam tenon length increased, as shown in Fig. 8(b) and (g).

5.5.3. Thickness of gusset plate (GP)

Four different GP thicknesses were chosen, such as 20, 30, 40, and 50 mm, to investigate GP thickness effect on the joint's structural performance. There was no distinguishable increase in capacity, stiffness, or seismic performance was observed as the thickness of GP was increased, as shown in Fig. 8© and (h).

5.5.4. Thickness of beams

On average, beams (FB and CB) of three different thicknesses (i.e., 6, 8, and 10 mm) increased the capacity and stiffness of the joint by 5%, as shown in Fig. 8(d) and (i). Additionally, the model with the most significant beam thickness exhibited plastic deformation only in the column (model S1), whereas the model with the most negligible beam thickness also exhibited an accumulation of plastic strain in the beams.

5.5.5. Inter-modular gap

The bending moment of four models of middle joint with an inter-modular gap of 20, 40, 60, and 80 mm were compared to determine the effect of the constructional gap on the lateral performance of joints. A nonapparent rise in a moment carrying capacity and stiffness (<5%) was illustrated in Figs. 8(e) and (j), whereas permanent strain accumulation was only limited to beams.

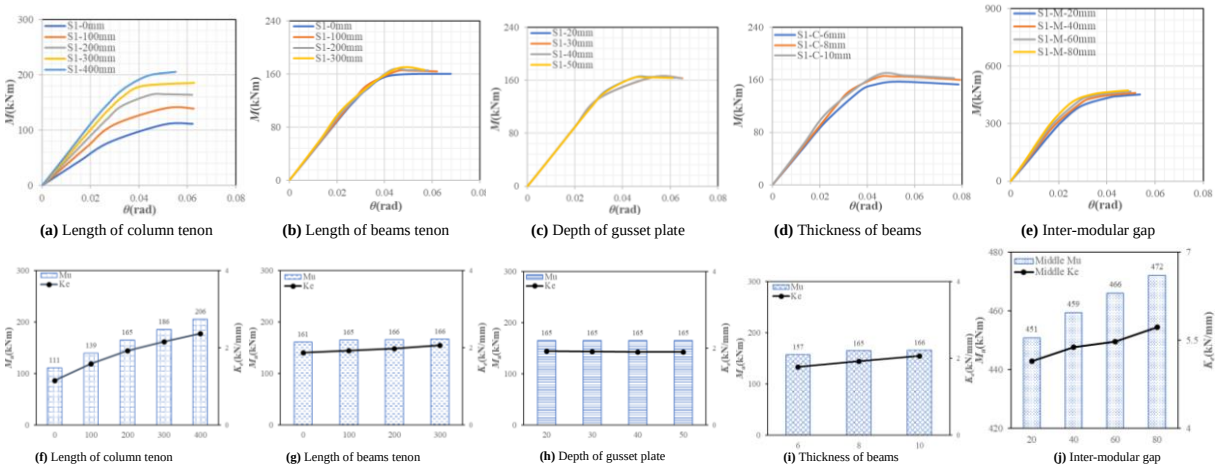

(a) Length of column tenon **(b)** Length of beams tenon **(c)** Depth of gusset plate **(d)** Thickness of beams **(e)** Inter-modular gap

(f) Length of column tenon **(g)** Length of beams tenon **(h)** Depth of gusset plate **(i)** Thickness of beams **(j)** Inter-modular gap

Fig. 8 Parametric studies on the lateral behaviour of joints

5.6. Simplification of joint

To save considerable computational time and accurately simulate the elastoplastic behaviour of a solid model of the joints, a beam model based on nonlinear spring connectors and beam elements was developed. The deformable solid elements of structural members, such as beams and columns, were replaced with three-dimensional beam elements, and the detailed joint model was replaced with nonlinear spring connectors. The connector's rotational stiffness was determined using the momentum versus rotation curves generated by the detailed FE model. Boundary conditions, material properties, cross-section characteristics, and loading conditions were maintained in the same way as the detailed FE analysis. Fig. 9 illustrates the comparison of the eighteen detailed and developed simplified joint models of the corner, middle, and interior joints and a two-storey modular block. It is worth noting that the curves obtained from simplified models accurately predicted the elastic stiffness, ultimate capacity, and plastic behaviour of detailed models, except for model S3, which failed to converge when detailed solid element modelling was used. Table 6 compares the ultimate moments of detailed and simplified FE models and evaluates mean and Cov, which indicates that the mean and Cov are 0.99 and 0.025, respectively. Additionally, the table summarises the moment capacities of detailed-to-simplified models using moment ratios $\left(\frac{M_{Det}}{M_{Sim}}\right)$. It indicated that when the ratios exceed 1.0, the simplified model was slightly underestimated, implying that structural behaviour predictions are safe. In comparison, ratios less than 1.0 indicate that actual behaviour is overestimated by simplified models, implying that structural behaviour estimations are slightly unsafe. These comparisons of moment-rotation curves and predicted moment ratios demonstrate that a simplified beam and connector model can accurately simulate the lateral behaviour of developed joints in MSB when both axial compression and lateral loading are applied. Additionally, Fig. 10 compares the stresses contours of the corresponding models. It was demonstrated that the simplified model accurately predicted the developed joints' structural behaviour and failure initiation. As a result of their accuracy, prediction of nonlinear structural behaviour, and increased computational efficiency, these simplified models are recommended for practical applications.

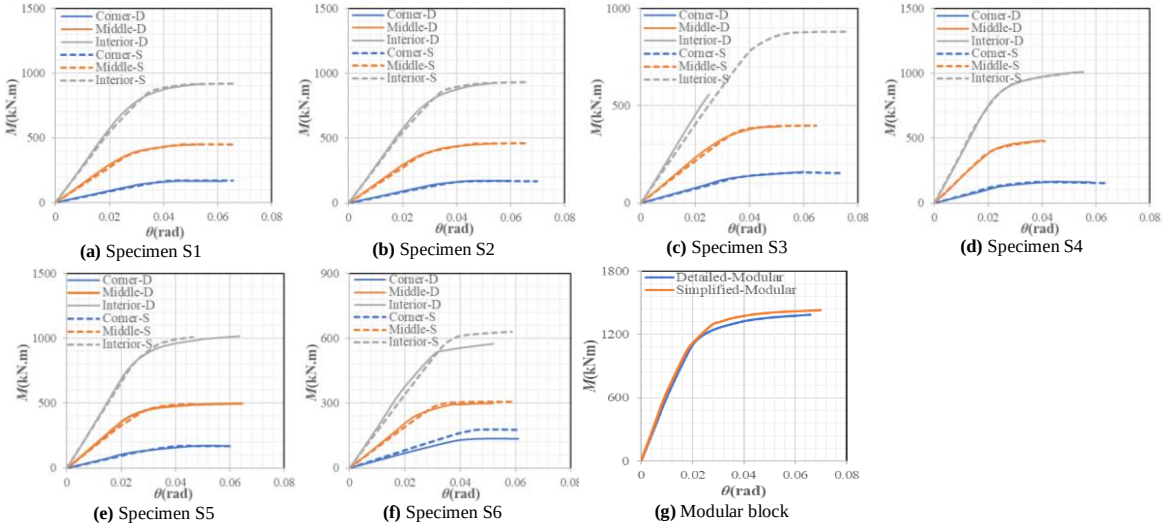

(a) Specimen S1 **(b)** Specimen S2 **(c)** Specimen S3 **(d)** Specimen S4

(e) Specimen S5 **(f)** Specimen S6 **(g)** Modular block

Fig. 9 Comparison of moment-rotation curves of detailed (D) and simplified (S) FE models

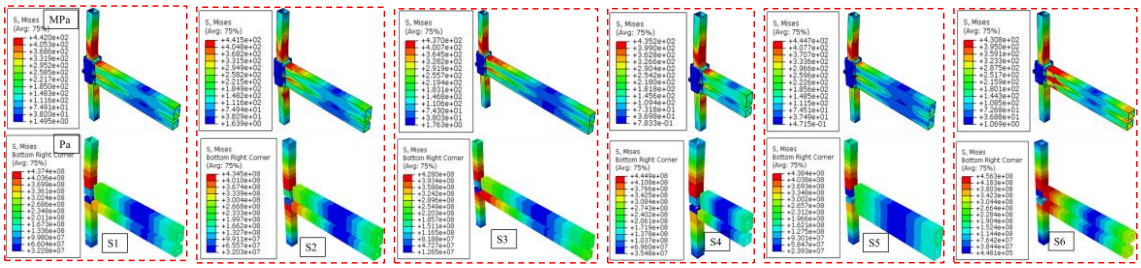

(a) FE models of corner joint

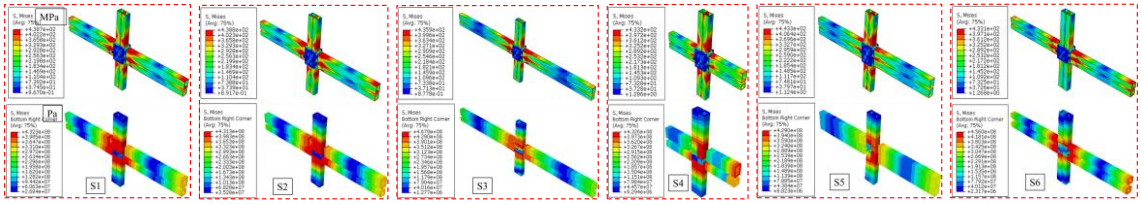

(b) FE models of middle joint

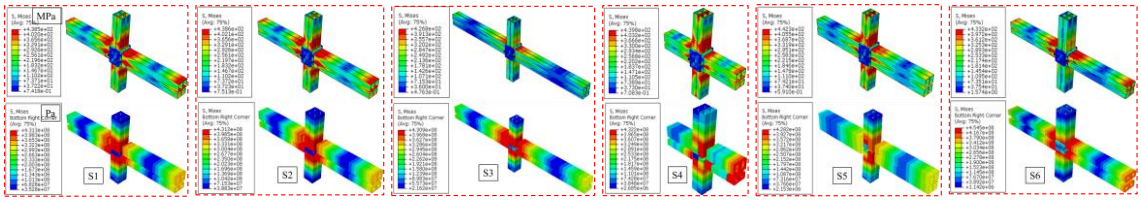

(c) FE models of interior joint

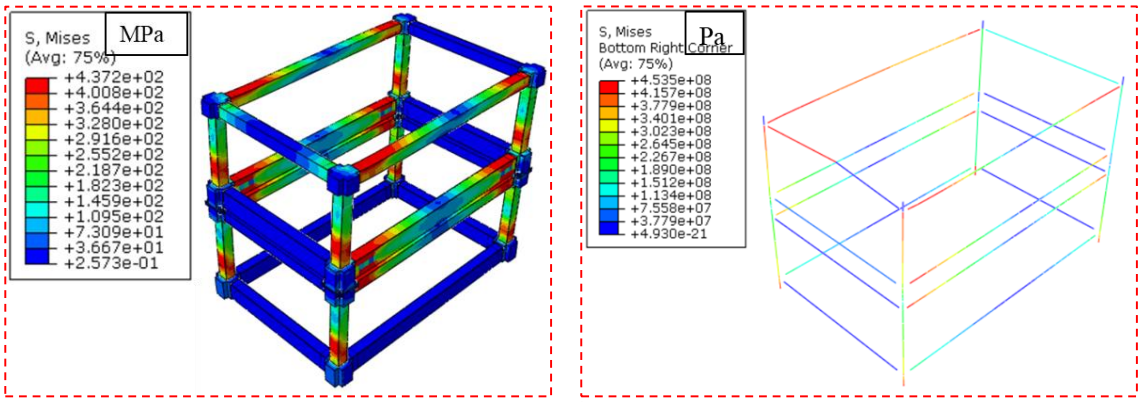

(d) FE models of two-storey modular block

Fig. 10 Comparison of stress distribution of detailed (D) and simplified (S) FE models

Table 6
Comparison of ultimate capacities of detailed and simplified FE models

Sp. No	Type of joint	Ultimate moment $M_{Detailed}$(kNm)	Ultimate moment $M_{Simplified}$(kNm)	M_{Det}/M_{Sim}
S1	Corner	165	168	0.98
S2	Corner	172	171	1.00
S3	Corner	159	155	1.02
S4	Corner	164	163	1.00
S5	Corner	167	170	0.98
S6	Corner	174	179	0.97
S1	Middle	450	448	1.00
S2	Middle	460	459	1.00
S3	Middle	393	398	0.98
S4	Middle	479	476	1.00
S5	Middle	497	491	1.01
S6	Middle	301	306	0.98
S1	Interior	918	919	0.99
S2	Interior	927	931	0.99
S4	Interior	1009	1006	1.00
S5	Interior	1018	1009	1.00
S6	Interior	573	630	0.90
Block	Block	1389	1428	0.97
Mean				0.99
Cov				0.025

6. Discussions

Previous research has emphasised the critical role of joints as a lateral force-resistant system in ensuring the integral and reliable nature of MSBs during catastrophic events. [14–16]. As reported in the literature, the present study proposed a joint for SHS, as illustrated in Fig. 1, to avoid the use of weaker sections, drilling holes in sections, sacrificing aesthetics, and stiffening joints. Fig. 6 shows the lateral bending capacity of joints. The procedure for determining the bending capacity of each joint was identical to that reported previously [17,28,31,32]. The developed joints were found to have a significantly higher lateral load-carrying capacity and seismic response than previously proposed joints [41,42]. According to previous research, semi-rigid frames with a drift ratio greater than 0.032 rad were found appropriate for use in earthquake-prone zones [43]. In comparison, the American Steel Construction Institute's (AISC) seismic provisions require that the lowest possible drift ratio by joints in special moment frames (SMF) be larger than 0.04 rad for capacities greater than $0.8M_p$ [40]. As shown in Table 5, the developed joints fulfilled high seismic performance requirements with $\theta_u/\theta_{0.04} \geq 1$ and $M_O/0.8M_P \geq 1$ and can be used as a lateral force resistant system in MSB. Increased column tenon length resulted in superior seismic performance of the joint (with $\theta_u/\theta_{0.04} \geq 1$ and $M_o/0.8M_P \geq 1$). At the corresponding rotational angle, the corner joint with a tenon length of 0 or 100 mm did not meet current requirements, but the models with a length of 200, 300, or 400 mm met AISC criteria for use in SMF.

The strength, i.e., $0.25M_P \leq M_j \leq M_P$ and stiffness classification criteria, i.e., $0.5EI_b/L_b \leq S_{ji} \leq 25EI_b/L_b$ for the unbraced semi-rigid frames used in the study, have been widely adopted previously [44,45]. According to the criteria, the corner joint with a single FB exhibited semi-rigid behaviour with strength $>0.5M_P$ and a rotational stiffness $>0.5EI_b/L_b$. The middle and interior joints with two and four FBs behaved as rigid joints in the strength classification with strength $>M_P$ and semi-rigid with rotational stiffness $>0.5EI_b/L_b$, except for S6. Such variations in joint behaviour due to beam length and the effect of adjacent modular units on strength and stiffness had received less attention; therefore, a detailed study was conducted in this context. Previously published research has demonstrated the contribution of shear walls, different loading scenarios, and the impact of wall openings on the response and rigidity of modular units [46–48]. On the other hand, the participation of joints in the overall lateral effectiveness of modular units received relatively less attention. The results of the specific bending analysis indicated that when the members' strengths were adequately utilised, the joint in a double-storey module acquired a greater tendency for bearing lateral loads [38]. Previous studies examined simplified models of multistorey modular frames, but there was no stepwise simplified representation and affirmation of the models' appropriateness [8,30]. Likewise, the developed simplified models of joints could simulate only elastic responses with a wide range of plastic regime variation. As illustrated in Fig. 9 and 10, the current study validated the step-by-step comparative efficacy of simplified models and their effectiveness in stimulating the complex detailed models.

7. Conclusions

This study aimed to develop new joints in MSB for SHS members, addressing issues with previously established joints. A detailed 3D FE analysis was performed to simulate the bending performance of the developed joints. Then, in-depth parametric analyses were performed to determine the effect of various parameters on the joints' overall structural performance. Simultaneously, the response of the developed joint in the two-storey small-scale modular block was investigated to mimic its contribution in multistorey MSB. Following that, joints were simplified using connector and beam elements to predict the elastoplastic response of complex joints. Finally, the FE modelling accuracy was confirmed by comparing it to thirteen tests on MSB joints. These studies on joints and a modular block justify the following conclusions:

1) Comparing FE results to thirteen joint bending tests revealed that the developed FE models accurately captured initial stiffness, ultimate bearing capacity, and failure behaviour.
2) The stiffness, lateral capacity, seismic performance, and ductility of the corner, middle, and inner joints were adequate. Beam tenons, GP thickness, and the intermodular gap had no noticeable impact on capacity and stiffness, whereas column tenon length had a significant influence. Beam failure was observed in models with longer and smaller cross-section beams. Columns from middle and inner joints and models of corner joints with weaker beams demonstrated strong-column and weak-beam responses, making them consistent with successful seismic behaviour.
3) The modular block showed a stable lateral load-carrying capacity, rotational stiffness, load distribution, and ductility. The ceiling beams of the upper storey were permanently deformed, but the columns remained safe, meeting strong-column and weak-beam criteria for adequate seismic behaviour.
4) By accurately simulating the elastoplastic behaviour and ultimate bearing capacity of detailed models with a Cov of 0.025, the development of simplified joints with nonlinear spring connector and beam element reduced modelling effort and increased computational efficiency.

Acknowledgment

The authors gratefully acknowledge the research grant received from the China Postdoctoral Science Foundation (Grant No. 2020M670655), the National Natural Science Foundation of China (Grant No. 51978457), and the Science and Technology Project of Tianjin (Grant No. 17ZXCXSF00050). The authors would like to express their profound gratitude for the financial support. The authors would also like to acknowledge the China Scholarship Council for funding the first author's studies at Tianjin University in China.

Nomenclature

σ_T= True stress
σ_E= Engineering stress
ε_E= True strain
ε_T=Engineering strain
E_s= Steel's modulus of elasticity
N= Axial force
A_s= Cross-section are
A_e= Bolts effective area
f_{tv}= Bolts tensile strength
σ_{EQ}= Equivalent stress
σ_1, σ_2 and σ_3= Principal stresses
$\dot{\varepsilon}_{ij}^{p}$= Rate of plastic strain
M_O= Obtained moment
M_P= Plastic moment
K_e= Initial/elastic stiffness
d_b= Diameter of bolt
$\frac{M_{Det}}{M_{Sim}}$= Moment capacities ratios of detailed and simplified models
P= Pretension of a bolt
Δ= Lateral displacement
θ= Rotation angle (rad)
μ= Coefficient of friction
P_{Test}= Ultimate strength of test specimens
P_{FE}= Ultimate strengths of FE models
ν= Poisson's ratio
f_y= Yield strength
f_u= Ultimate strength

References

[1] Smith RE. Prefab Architecture: A Guide to Modular Design and Construction. 2011. https://doi.org/10.1017/CBO9781107415324.004.
[2] Alembagheri M, Sharafi P, Hajirezaei R, Samali B. Collapse capacity of modular steel buildings subject to module loss scenarios: The role of inter-module connections. Eng Struct 2020;210. https://doi.org/10.1016/j.engstruct.2020.110373.
[3] Lawson M, Ogden R, Goodier C. Design in Modular Construction. 2014. https://doi.org/10.1201/b16607.
[4] Kamali M, Hewage K. Life cycle performance of modular buildings: A critical review. Renew Sustain Energy Rev 2016;62:1171–83. https://doi.org/10.1016/j.rser.2016.05.031.
[5] Sharafi P, Mortazavi M, Samali B, Ronagh H. Interlocking system for enhancing the integrity of multi-storey modular buildings. Autom Constr 2018;85:263–72. https://doi.org/10.1016/j.autcon.2017.10.023.
[6] Jiang R, Mao C, Hou L, Wu C, Tan J. A SWOT analysis for promoting off-site construction under the backdrop of China's new urbanisation. J Clean Prod 2018;173:225–34. https://doi.org/10.1016/j.jclepro.2017.06.147.
[7] Lacey AW, Chen W, Hao H, Bi K. Review of bolted inter-module connections in modular steel buildings. J Build Eng 2019;23:207–19. https://doi.org/10.1016/j.jobe.2019.01.035.
[8] Annan CD, Youssef MA, El Naggar MH. Seismic vulnerability assessment of modular steel buildings. J Earthq Eng 2009;13:1065–88. https://doi.org/10.1080/13632460902933881.
[9] Zhang JF, Zhao JJ, Yang DY, Deng EF, Wang H, Pang SY, et al. Mechanical-property tests on assembled-type light steel modular house. J Constr Steel Res 2020;168:105981. https://doi.org/10.1016/j.jcsr.2020.105981.
[10] Lawson RM, Ogden RG, Bergin R. Application of Modular Construction in High-Rise Buildings. J Archit Eng 2012;18:148–54. https://doi.org/10.1061/(ASCE)AE.1943-5568.0000057.
[11] Jellen AC, Memari AM. The state-of-the-art application of modular construction to multi-story. 1st Resid Build Des Constr Conf 2013:284–93.

[12] Lacey AW, Chen W, Hao H, Bi K. Structural response of modular buildings – An overview. J Build Eng 2018;16:45–56. https://doi.org/10.1016/j.jobe.2017.12.008.
[13] Liew JYR, Chua YS, Dai Z. Steel concrete composite systems for modular construction of high-rise buildings. Structures 2019:0–1. https://doi.org/10.1016/j.istruc.2019.02.010.
[14] Lawson PM, Byfield MP, Popo-Ola SO, Grubb PJ. Robustness of light steel frames and modular construction. Proc Inst Civ Eng Struct Build 2008;161:3–16. https://doi.org/10.1680/stbu.2008.161.1.3.
[15] Ding Y, Deng EF, Zong L, Dai XM, Lou N, Chen Y. Cyclic tests on corrugated steel plate shear walls with openings in modularized-constructions. J Constr Steel Res 2017;138:675–91. https://doi.org/10.1016/j.jcsr.2017.08.019.
[16] Chua YS, Liew JYR, Pang SD. Robustness of Prefabricated Prefinished Volumetric Construction (PPVC) High-rise Building 2018. https://doi.org/10.4995/asccs2018.2018.6955.
[17] Cho BH, Lee JS, Kim H, Kim DJ. Structural performance of a new blind-bolted frame modular beam-column connection under lateral loading. Appl Sci 2019;9. https://doi.org/10.3390/app9091929.
[18] Sanches R, Mercan O, Roberts B. Experimental investigations of vertical post-tensioned connection for modular steel structures. Eng Struct 2018;175:776–89. https://doi.org/10.1016/j.engstruct.2018.08.049.
[19] Deng EF, Zong L, Ding Y, Dai XM, Lou N, Chen Y. Monotonic and cyclic response of bolted connections with welded cover plate for modular steel construction. Eng Struct 2018;167:407–19. https://doi.org/10.1016/j.engstruct.2018.04.028.
[20] Azizi Naserabad A, Ghasemi MR, Shabakhty N, Ghohani Arab H. Design of a Novel Prefabricated Bolted I-Beam to Box-Column Connection Using Numerical Analysis Under Cyclic Load. Int J Steel Struct 2019;19:1431–45. https://doi.org/10.1007/s13296-019-00222-6.
[21] Azizi Naserabad A, Ghasemi MR, Shabakhty N, Ghohani Arab H. Evaluation of Three Support Shapes on Behavior of New Bolted Connection BBCC in Modularized Prefabricated Steel Structures. Int J Steel Struct 2018;18:1639–53. https://doi.org/10.1007/s13296-018-0051-9.
[22] Dhanapal J, Ghaednia H, Das S, Velocci J. Structural performance of state-of-the-art VectorBloc modular connector under axial loads. Eng Struct 2019;183:496–509. https://doi.org/10.1016/j.engstruct.2019.01.023.
[23] Dhanapal J, Ghaednia H, Das S, Velocci J. Behavior of thin-walled beam-column modular connection subject to bending load. Thin-Walled Struct 2019:106536. https://doi.org/10.1016/j.tws.2019.106536.
[24] Khan K, Yan J-B. Numerical studies on seismic behaviour of a prefabricated multi storey modular steel building with new type bolted joints. Adv Steel Constr n.d.;17(1):1–9. https://doi.org/10.18057/IJASC.2021.17.1.1.
[25] Khan K, Yan J-B. Development and Study on the Seismic Behavior of Novel Joint in Pre-fabricated Modular Steel Building. Tianjin University, 2017. https://doi.org/10.1017/CBO9781107415324.004.
[26] Khan K, Yan JB. Finite Element Analysis on Seismic Behaviour of Novel Joint in Prefabricated Modular Steel Building. Int J Steel Struct 2020. https://doi.org/10.1007/s13296-020-00320-w.
[27] Zuo Y, Zha X. FEM and Experimental Study on Mechanical Property of Integrated Container Building. Int J Steel Struct 2018;18:699–718. https://doi.org/10.1007/s13296-018-0065-3.
[28] Lee S, Park J, Kwak E, Shon S, Kang C, Choi H. Verification of the seismic performance of a rigidly connected modular system depending on the shape and size of the ceiling bracket. Materials (Basel) 2017;10. https://doi.org/10.3390/ma10030263.
[29] Annan CD, Youssef M, Naggar MH. Seismic performance of modular steel braced frames. 9h Can Conf Earthq Eng 2007. https://doi.org/10.13140/2.1.2132.2241.
[30] Fathieh A, Mercan O. Seismic evaluation of modular steel buildings. Eng Struct 2016;122:83–92. https://doi.org/10.1016/j.engstruct.2016.04.054.
[31] Chen Z, Liu J, Yu Y, Zhou C, Yan R. Experimental study of an innovative modular steel building connection. J Constr Steel Res 2017;139:69–82. https://doi.org/10.1016/j.jcsr.2017.09.008.
[32] Chen Z, Liu J, Yu Y. Experimental study on interior connections in modular steel buildings. Eng Struct 2017;147:625–38. https://doi.org/10.1016/j.engstruct.2017.06.002.
[33] Chen Z, Liu Y, Zhong X, Liu J. Rotational stiffness of inter-module connection in mid-rise modular steel buildings. Eng Struct 2019;196:109273. https://doi.org/10.1016/j.engstruct.2019.06.009.
[34] ABAQUS (2013). User manual Version 6.13. DS SIMULIA Corp, Provid RI, USA 2013:1–847.
[35] Yan J-B. Finite element analysis on steel–concrete–steel sandwich beams. Mater Struct 2015;48:1645–67. https://doi.org/10.1617/s11527-014-0261-3.
[36] Chen Z, Xu J, Chen Y, Xue J. Axial compression ratio limit values for steel reinforced concrete (SRC) special shaped columns. Steel Compos Struct 2016;20:295–316. https://doi.org/10.12989/scs.2016.20.2.295.
[37] ASCE/SEI. ASCE STANDARD Loads for Buildings. Virginia: 2010.
[38] Chen Z, Li H, Chen A, Yu Y, Wang H. Research on pretensioned modular frame test and simulations. Eng Struct 2017;151:774–87. https://doi.org/10.1016/j.engstruct.2017.08.019.
[39] Yan JB, Chen Y, Lin X. Finite element analysis and parametric studies on hysteretic behaviours of high strength steel T-joints with damage-control fuses. Thin-Walled Struct 2020;148. https://doi.org/10.1016/j.tws.2019.106574.
[40] ANSI/AISC 341-16. Seismic Provisions for Structural Steel Buildings. 2016. https://doi.org/10.1201/b11248-8.
[41] Sup S, Woong K, Sung K, Yub S. An Experimental Evaluation of Structural Performance for the Beam to Column Joints in Unit Modular System. J Korean Soc Steel Constr 2013;25:255–65. https://doi.org/10.7781/kjoss.2013.25.3.255.
[42] Lee. Behavior of C-Shaped Beam to Square Hollow Section Column Connection in Modular Frame. J Korean Soc Steel Constr 2015;27:471. https://doi.org/10.7781/kjoss.2015.27.5.471.
[43] Liu XC, Pu SH, Zhang AL, Xu AX, Ni Z, Sun Y, et al. Static and seismic experiment for bolted-welded joint in modularized prefabricated steel structure. J Constr Steel Res 2015;115:417–33. https://doi.org/10.1016/j.jcsr.2015.08.036.
[44] EN 1993-1-1. Eurocode 3: Design of steel structures - Part 1-1: General rules and rules for buildings. vol. 1. 2011.
[45] Choi K-S, Kim H-J. Analytical Models of Beam-Column joints in a Unit Modular Frame. J Comput Struct Eng Inst Korea 2014;27:663–72. https://doi.org/10.7734/coseik.2014.27.6.663.
[46] Zuo Y, Zha X. FEM and experimental study on mechanical property of container building with holes. Int J Steel Struct 2017;17:175–94. https://doi.org/10.1007/s13296-015-0132-y.
[47] Yu Y, Chen Z. Rigidity of corrugated plate sidewalls and its effect on the modular structural design. Eng Struct 2018;175:191–200. https://doi.org/10.1016/j.engstruct.2018.08.039.
[48] Giriunas K, Sezen H, Dupaix RB. Evaluation, modeling, and analysis of shipping container building structures. Eng Struct 2012;43:48–57. https://doi.org/10.1016/j.engstruct.2012.05.001.